



저작자표시-비영리-변경금지 2.0 대한민국

이용자는 아래의 조건을 따르는 경우에 한하여 자유롭게

- 이 저작물을 복제, 배포, 전송, 전시, 공연 및 방송할 수 있습니다.

다음과 같은 조건을 따라야 합니다:



저작자표시. 귀하는 원저작자를 표시하여야 합니다.



비영리. 귀하는 이 저작물을 영리 목적으로 이용할 수 없습니다.



변경금지. 귀하는 이 저작물을 개작, 변형 또는 가공할 수 없습니다.

- 귀하는, 이 저작물의 재이용이나 배포의 경우, 이 저작물에 적용된 이용허락조건을 명확하게 나타내어야 합니다.
- 저작권자로부터 별도의 허가를 받으면 이러한 조건들은 적용되지 않습니다.

저작권법에 따른 이용자의 권리는 위의 내용에 의하여 영향을 받지 않습니다.

이것은 [이용허락규약\(Legal Code\)](#)을 이해하기 쉽게 요약한 것입니다.

[Disclaimer](#)

공학박사 학위논문

# **Micro/Nanostructured Polymeric Metamaterials**

마이크로/나노구조 고분자 메타물질

2018년 8월

서울대학교 대학원

재료공학부

박 주 혁

Doctoral Dissertation in Engineering

**Micro/Nanostructured Polymeric  
Metamaterials**

by

Juhyuk Park

Advisor: Prof. Jae Ryoun Youn

August 2018

Department of Materials Science and Engineering

Graduate School

Seoul National University

# Micro/Nanostructured Polymeric Metamaterials

마이크로/나노구조 고분자 메타물질

지도 교수 윤재륜

이 논문을 공학박사 학위논문으로 제출함

2018년 6월

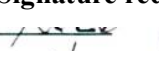
서울대학교 대학원

재료공학부


박주혁

박주혁의 박사 학위논문을 인준함


2018년 6월

위원장 김장주  Signature redacted

부위원장 윤재륜  Signature redacted

위원 서용석  Signature redacted

위원 유웅렬  Signature redacted

위원 송영석  Signature redacted

## **Abstract**

# **Micro/Nanostructured Polymeric Metamaterials**

Juhyuk Park

Department of Materials Science and Engineering

The Graduate School

Seoul National University

Metamaterials are artificially designed and engineered materials to capture the human imagination. Based on mathematical and physicochemical knowledge, manifold metamaterials have been designed with sophisticated polymeric micro/nanostructures. In general, metamaterial design is accomplished by employing micro/nanoscale unit cells that bring out effective media for complex material properties. The metamaterials have been produced as practical devices and have embodied unprecedented phenomena that do not follow the laws of nature. In this dissertation, three classes of metamaterials are proposed by strategic design, numerical analysis, chemical synthesis, fabrication, and experimental characterizations; polymeric rheological metamaterials, shape memory polymeric metasurfaces, and polymeric poroacoustic meta-absorbers.

Chapter 1 provides explanations of what a metamaterial is and what types of metamaterials have been reported so far. Also, the background knowledge required to understand this dissertation is described. Transformation optics and metamaterials based on it are introduced along with the design strategies and encountering challenges. Definition, mechanisms, and applications of shape memory polymers (SMPs) are explained with several specific examples. Sound absorption phenomena and its theoretical models are explicated and general trends of sound absorbing material performance are reviewed. The objectives of this dissertation are briefly described.

Chapter 2 demonstrates the development of the polymeric rheological metamaterials,

which empower unexampled fluid flows through fictitious fluidic space design. Transformation optics has suggested an elaborate way to control electromagnetic waves. Using this theory, coordinate transformations under the Euclidean space were contrived to compress, expand, or rotate specific electromagnetic spaces. The transformed coordinate systems have been experimentally materialized using a metamaterial approach. In the metamaterial approach, micro/nanoscale unit cells capable of realizing unique material properties are designed based on effective medium theory and arranged to manufacture one metamaterial complex. In this study, an idea was conceived to translate transformation optics into rheology in a bid to manipulate fluid dynamic phenomena. Transformation rheology was firstly established mathematically based on Navier-Stokes equations and it was uncovered that fluid viscosity should be transformed into a tensor form with Jacobian transformation matrices for deriving fictitious fluidic spaces. The rheological metamaterials, *i.e.*, cloak, concentrator, and rotator, were designed by mapping effective viscosity unit cells and numerical analysis was carried out to theoretically analyze the metamaterials. The metamaterials were fabricated as microfluidic devices made of polydimethylsiloxane (PDMS). Experimental results portrayed that the metamaterials operate properly as designed.

In Chapter 3, the production process of the shape memory polymeric metasurfaces are explained, which entail sustainable nanopattern-effects by healing the damaged shape. Polymeric nanostructures have been researched for various applications such as antireflection, solar energy harvesting, and photonic sensors. The nanostructures ensure electromagnetic meta-properties due to subwavelength characteristics. This geometrical feature allows the nanostructures to act as an effective material medium rather than the material composition itself. However, vulnerability to mechanical deformation has always been pointed out as the obstacle to the practical applications of nanostructures. In this study, a strategy was built to overcome this drawback by changing the constituent material of the nanostructure to shape memory polymer (SMP). The SMP made of acrylic chemicals was chemically designed and synthesized, which can be triggered by body temperature. The functional metasurfaces for antireflection and biometrics were engineered on the sample surfaces by arranging nanopatterns made of the designed SMP and their meta-properties were verified heuristically. Even though the nanopatterns were deformed by external forces,

they were able to return to their original shape by thermal stimulation. It was ascertained that the impaired performance of each meta-property is restored accordingly.

In Chapter 4, the polymeric poroacoustic meta-absorbers are announced, which facilitate outstanding noise energy dissipation beyond the macroscopic limits. Sound absorbing foams have been studied theoretically and empirically to achieve superior sound absorption performance. In theoretical studies, the internal microstructure of foams was found to be the main contributor to determine sound absorption performance. However, most of previous studies have aimed at controlling macroscopic factors such as thickness, material composition, and density because of elusive microstructural control. Therefore, under the common sense, the main operational frequency and performance of sound absorbing materials are strongly related and proportional to the macroscale factors. In this study, a tactical approach was attempted to yield the meta-absorbers for sound absorption by tuning inner microstructures. Polyurethane (PU) foams with optimal microcell structures, *i.e.*, cell size and cell openness, were fabricated using multiscale numerical simulation and rheology-controlled foaming methods. The fabricated PU foams turned out superior noise absorption performance at low frequencies beyond the limit of density condition. In addition, a novel hybrid microstructure was designed to drive preeminent sound absorption performance as well as high thermal insulation and mechanical characteristics.

In Chapter 5, the conclusion of this dissertation is remarked. The aim of this work is presented with a summary of Chapters 2-4. The employed polymers, design strategies, processing methods, and unique functions of the metamaterials are summarized in order and their potential applications are presented. Problems and limitations of the current technologies are discussed and the solutions for those are offered. Subsequent studies following the metamaterials developed in this dissertation are recommended.

**Keywords:** Metamaterial, polymer, smart material, porous material, materials design, rheology, impedance matching, sound absorption, numerical simulation.

**Student Number:** 2013-23040

# Contents

Abstract.....	i
List of Figures .....	viii
List of Tables.....	xx
<b>Chapter 1. Introduction .....</b>	<b>1</b>
1.1. What is a metamaterial?.....	1
1.2. Research background.....	4
1.2.1. Transformation optics .....	4
1.2.2. Shape memory polymer .....	11
1.2.3. Sound absorption .....	17
1.3. Objectives of present work .....	22
<b>Chapter 2. Polymeric Rheological Metamaterials .....</b>	<b>23</b>
2.1. Overview.....	23
2.2. Transformation rheology.....	25
2.2.1. Introduction.....	25
2.2.2. Theoretical background.....	27
2.2.3. Form invariance of Navier-Stokes equations .....	32
2.2.4. Conclusions.....	39
2.3. Rheological cloak .....	40
2.3.1. Introduction.....	40
2.3.2. Fluidic space modeling .....	42
2.3.3. Numerical analysis.....	49
2.3.4. Metamaterial design.....	58
2.3.5. Experimental realization .....	73
2.3.6. Conclusions.....	83



2.4. Rheological concentrator .....	84
2.4.1. Introduction.....	84
2.4.2. Fluidic space modeling .....	86
2.4.3. Numerical analysis.....	90
2.4.4. Metamaterial design.....	96
2.4.5. Experimental realization .....	107
2.4.6. Conclusions.....	112
2.5. Rheological rotator .....	113
2.5.1. Introduction.....	113
2.5.2. Fluidic space modeling .....	115
2.5.3. Numerical analysis.....	118
2.5.4. Metamaterial design.....	123
2.5.5. Experimental realization .....	134
2.5.6. Conclusions.....	139
2.6. Summary .....	140

### **Chapter 3. Shape Memory Polymeric Metasurfaces..... 141**

3.1. Overview .....	141
3.2. Shape memory polymer synthesis .....	143
3.2.1. Introduction.....	143
3.2.2. Experimental.....	145
3.2.3. Numerical analysis.....	148
3.2.4. Results and discussion .....	154
3.2.5. Conclusions.....	168
3.3. Antireflective SMP nanopattern .....	169
3.3.1. Introduction.....	169
3.3.2. Experimental.....	171
3.3.3. Numerical analysis.....	174
3.3.4. Results and discussion .....	177

3.3.5. Conclusions.....	191
3.4. Biometric SMP nanopattern.....	192
3.4.1. Introduction.....	192
3.4.2. Experimental.....	194
3.4.3. Numerical analysis.....	196
3.4.4. Results and discussion .....	198
3.4.5. Conclusions.....	213
3.5. Summary.....	214

**Chapter 4. Polymeric Poroacoustic Meta-absorbers.....215**

4.1. Overview.....	215
4.2. PU foam with optimum cell size .....	217
4.2.1. Introduction.....	217
4.2.2. Experimental.....	220
4.2.3. Numerical analysis.....	222
4.2.4. Results and discussion .....	228
4.2.5. Conclusions.....	245
4.3. Openness-modulated PU foam.....	246
4.3.1. Introduction.....	246
4.3.2. Experimental.....	249
4.3.3. Numerical analysis.....	250
4.3.4. Results and discussion .....	252
4.3.5. Conclusions.....	268
4.4. Hybrid microstructured PU foam.....	269
4.4.1. Introduction.....	269
4.4.2. Design of syntactic hybrid foams .....	271
4.4.3. Numerical analysis.....	274
4.4.4. Results and discussion .....	276
4.4.5. Conclusions.....	286

4.5. Summary .....287

**Chapter 5. Concluding Remarks .....288**

**Bibliography .....291**

**Korean Abstract .....325**

# List of Figures

**Fig. 1.2.1.** A class of metamaterials; Invisibility cloak [28], negative refraction [2], superlens [5], hologram [16], ultrastiff material [24], Moth eye nanostructure [13], artificial black-hole [10], metahydrogel [23], meta-absorber [29], chiral mechanical metamaterial [30], origami metamaterial [31], and negative Poisson’s ratio [32]. ..... 3

**Fig. 1.2.2.** Schematic illustration of transformation optics. (a) Cartesian coordinate grids in a free space and a distorted coordinate grids (upper). Two and three-dimensional ray trajectories in the cloak (lower) [9]. (b) Optical conformal mapping (left) and ray propagation in the dielectric invisibility device (lower) [8]. ..... 10

**Fig. 1.2.3.** Classification, mechanism, and representative shape-recovery behavior of shape memory polymers. (a) Molecular mechanism of shape memory effect of amorphous SMPs [65]. (b) Overall architecture of SMPs [68]. (c) Shape recovery behavior of the deformed SMP micropillars [112]. ..... 16

**Fig. 1.2.4.** Types of noise and sound absorption principle. (a) Noises generated on automobiles while driving and their frequencies. (b) Mechanism of sound absorption in porous media ..... 21

**Fig. 2.2.1.** Three dimensional differential integration element. it is the modified figure of Fig. 2.3 in ref. [141]. ..... 34

**Fig. 2.3.1.** Schematic illustration of drag-free space creation by a rheological cloak. (a) A flowing fluid without anything in it (the bare case). (b) A flowing fluid with an obstacle in it (the obstacle case). (c) A flowing fluid stabilized by encircling the obstacle with the rheological cloak (the cloaked-obstacle case). (d) A fluid flow with only the rheological cloak (the cloak-only case). ..... 47

**Fig. 2.3.2.** Coordinate grids representing spatial transformation by a cloak. .... 48

**Fig. 2.3.3.** Simulation conditions. (a) A hexahedron geometry and (b) generated meshes in the geometry. .... 48

**Fig. 2.3.4.** Simulation results for (a) the bare case and (b) the obstacle case; (i) pressure fields, (ii) pressure gradient fields ( $p_y$ ), and (iii) velocity fields. .... 51

**Fig. 2.3.5.** Modeling of the ideal case rheological cloak. (a) Spatially varying viscosity tensor components (i) in radial and (ii) azimuthal axes. Simulation results for (b) the cloaked-obstacle case and (c) the cloak-only case of (i) pressure fields, (ii) pressure gradient fields ( $p_y$ ), and (iii) velocity fields. .... 55

**Fig. 2.3.6.** Modeling of the reduced case rheological cloak. (a) Spatially varying viscosity tensor components (i) in radial and (ii) azimuthal axes. Simulation results for (b) the cloaked-obstacle case and (c) the cloak-only case of (i) pressure fields, (ii) pressure gradient fields ( $p_y$ ), and (iii) velocity fields. .... 56

**Fig. 2.3.7.** Profiles of the simulation fields and drag values. Profiles of (a) the pressure gradient field ( $p_y$ ) and (b) velocity field at the center line (the line at  $y=0.5$  cm and  $z=25$   $\mu$ m). (c) Comparison of the drag forces and drag coefficients generated on the obstacle surface with or without the cloak. .... 57

**Fig. 2.3.8.** A constructed geometry of the multilayered cloak and its magnified view. .... 60

**Fig. 2.3.9.** Modeling of the multilayered rheological cloak. (a) Viscosity tensor components of each layer (i) in radial and (ii) azimuthal axes. Simulation results for (b) the cloaked-obstacle case and (c) the cloak-only case of (i) pressure fields, (ii) pressure gradient fields ( $p_y$ ), and (iii) velocity fields. .... 61

**Fig. 2.3.10.** Simulated velocity fields for (a) the bare unit cell for the cloaking shell region and (b) the background unit cell. .... 64

**Fig. 2.3.11.** Simulated velocity fields for the effective viscosity unit cells which are applied to each layer of the rheological metamaterial cloak. The white arrows mean  $r$ -direction and the yellow arrows for  $\theta$ -direction.  $l$  is the length of the micropillar of each unit cell. .... 64

**Fig. 2.3.12.** Viscosity tensor components of the effective viscosity unit cells mapped on the rheological metamaterial cloak (a) in radial and (b) azimuthal axes. .... 65

**Fig. 2.3.13.** Design of the rheological metamaterial cloak of a pillar-arrayed case with detailed configuration and a magnified view. .... 67

**Fig. 2.3.14.** Constructed pillar-arrayed models for the designed rheological metamaterial cloaks and the control groups; (a) the bare, (b) obstacle, (c) cloaked-obstacle, and (d) cloak-only cases. .... 68

**Fig. 2.3.15.** Simulation results of for the designed rheological metamaterial cloaks and the control groups: (a) the bare, (b) obstacle, (c) cloaked-obstacle, and (d) cloak-only cases showing (i) pressure field, (ii) velocity field, and (ii) flow streamlines. ... 69

**Fig. 2.3.16.** Comparison of simulated pressure fields for (a) the bare, (b) obstacle, (c) cloaked-obstacle, and (d) cloak-only cases; (i) continuous media, (ii) multilayer, and (iii) pillar-arrayed cloak cases. .... 70

**Fig. 2.3.17.** Comparison of simulated velocity fields for (a) the bare, (b) obstacle, (c) cloaked-obstacle, and (d) cloak-only cases; (i) continuous media, (ii) multilayer, and (iii) pillar-arrayed cloak cases. .... 71

**Fig. 2.3.18.** Comparison of simulated flow streamlines for (a) the bare, (b) obstacle, (c) cloaked-obstacle, and (d) cloak-only cases; (i) continuous media, (ii) multilayer, and (iii) pillar-arrayed cloak cases. .... 72

**Fig. 2.3.19.** Drawings of the Si masters containing microchannels for the designed rheological metamaterial cloaks and the control groups; (a) the bare, (b) obstacle, (c) cloaked-obstacle, and (d) cloak-only cases..... 75

**Fig. 2.3.20.** A microscale view and configuration of the microchannel drawings; (a) the bare, (b) obstacle, (c) cloaked-obstacle, and (d) cloak-only cases. .... 75

**Fig. 2.3.21.** Fabrication details of the rheological metamaterial cloaks and the control groups. Optical photographs of (a) the patterned Cr masks (b) the fabricated Si masters, and (c) the manufactured microfluidic devices; the bare (Bare), obstacle (Obs), cloaked-obstacle (Clo1), and cloak-only (Clo2) cases, orderly. (d) a chemical structure of PDMS. .... 76

**Fig. 2.3.22.** Comparison of microstructures between the drawings (left) and the fabricated microdevices (right). (a) The bare, (b) obstacle, (c) cloaked-obstacle, and (d) cloak-only cases. .... 76

**Fig. 2.3.23.** Detailed configuration at microscale of (a) the designed rheological metamaterial cloak and (b) the fabricated rheological metamaterial cloak. .... 77

**Fig. 2.3.24.** Experimental set-up for observation of fluorescent microparticle streamlines. (a) A microscope with a fluid-filled syringe, and a microfluidic device. (b) A pressure regulator set to apply 5 kPa. .... 79

**Fig. 2.3.25.** Observed streamlines (left), simulated streamlines (center), and microstructures in the experiment (right) for (a) the bare, (b) obstacle, (c) cloaked-obstacle, and (d) cloak-only cases..... 82

**Fig. 2.4.1.** Coordinate grids representing spatial transformation by a concentrator. .... 89

**Fig. 2.4.2.** Modeling of the ideal case rheological concentrator. (a) Spatially varying viscosity tensor components in (i) radial and (ii) azimuthal axes. Simulation results for (b) the ideal concentrator and (c) the bare case of (i) pressure fields, (ii) pressure gradient fields ( $p_y$ ), and (iii) velocity fields..... 93

**Fig. 2.4.3.** Modeling of the reduced case rheological concentrator. (a) Spatially varying viscosity tensor components in (i) radial and (ii) azimuthal axes. Simulation results for (b) the reduced concentrator and (c) the bare case of (i) pressure fields, (ii) pressure gradient fields ( $p_y$ ), and (iii) velocity fields..... 94

**Fig. 2.4.4.** Profiles of the simulation fields and the calculated flow parameters. Profiles of (a) pressure gradient fields ( $p_y$ ) and (b) velocity fields at the center (the line at

	y=0.5 cm and z=25 μm). (c) Comparison of the hydraulic kinetic energy and mean velocity with or without the concentrator. ....	95
<b>Fig. 2.4.5.</b>	A constructed geometry of the multilayered concentrator and its magnified view. ....	97
<b>Fig. 2.4.6.</b>	Modeling of the multilayered rheological concentrator. (a) Spatially varying viscosity tensor components in (i) radial and (ii) azimuthal axes. Simulation results for (b) the multilayered concentrator and (c) bare cases of (i) pressure fields, (ii) pressure gradient fields ( $p_y$ ), and (iii) velocity fields. ....	98
<b>Fig. 2.4.7.</b>	Simulated velocity fields for (a) the bare unit cell without a microstructure, (b) the background unit cell, and (c) the 10 unit cells which are mapped on each layer of the rheological metamaterial concentrator. The left and right figures in each field show the velocity fields when the pressure field is applied along each axis. Red lines indicate flow streamlines along the flow direction and $l$ means a length of the micropillar. ....	100
<b>Fig. 2.4.8.</b>	Viscosity tensor components of the unit cells mapped on each layer of the rheological metamaterial concentrator; (a) in radial and (b) azimuthal axes. ....	101
<b>Fig. 2.4.9.</b>	Design of the rheological metamaterial concentrator of a pillar-arrayed case with configuration and a magnified view. ....	104
<b>Fig. 2.4.10.</b>	Simulation results for (a) the designed rheological metamaterial concentrator and (b) the bare case of (i) pressure fields, (ii) velocity fields, and (iii) flow streamlines. ....	105
<b>Fig. 2.4.11.</b>	Comparison of the simulation results for (a) the continuous media, (b) multilayered, and (c) pillar-arrayed rheological concentrator cases; (i) pressure fields, (ii) velocity fields and (iii) flow streamlines. ....	106
<b>Fig. 2.4.12.</b>	Magnified images of the simulated velocity fields in the central region; (a) with and (b) without the rheological concentrator. Dashed squares indicate the unit cell. ....	106
<b>Fig. 2.4.13.</b>	A drawing of the Si master containing the microchannels for the designed rheological metamaterial concentrator (left) and rotator (right). The metamaterial rotator is explained in Section 2.5. ....	107
<b>Fig. 2.4.14.</b>	A microscale view and configuration of the microchannel for the designed rheological metamaterial concentrator. ....	108
<b>Fig. 2.4.15.</b>	Fabrication details of the rheological metamaterial concentrator. (a) The patterned Cr mask, (b) the fabricated Si master, and (c) the manufactured microfluidic device. The figures in the blue dashed rectangle are the rheological metamaterial	

concentrators and the others are the metamaterial rotators developed in Section 2.5. ....	108
<b>Fig. 2.4.16.</b> Detailed configuration of (a) the designed rheological metamaterial concentrator and (b) the fabricated rheological metamaterial concentrator.....	109
<b>Fig. 2.4.17.</b> Flow streamlines of the rheological metamaterial concentrator at (a) the entrance, (b) left-side, and (c) central regions; observed streamlines (top), simulated streamlines (middle), and microstructure during the experiment (bottom). ....	111
<b>Fig. 2.5.1.</b> Simulation results of the 180° rheological rotator: (a) transformed coordinate system, (b) pressure fields, (c) pressure gradient fields, and (c) velocity fields.....	121
<b>Fig. 2.5.2.</b> Simulation results of the 90° rheological rotator: (a) transformed coordinate system, (b) pressure fields, (c) pressure gradient fields, and (c) velocity fields.....	121
<b>Fig. 2.5.3.</b> Simulation results of the 30° rheological rotator: (a) transformed coordinate system, (b) pressure fields, (c) pressure gradient fields, and (c) velocity fields.....	122
<b>Fig. 2.5.4.</b> Simulation results of the 1800° rheological rotator as an artificial tornado: (a) transformed coordinate system, (b) pressure fields, (c) pressure gradient fields, and (c) velocity fields.....	122
<b>Fig. 2.5.5.</b> Design of the prototype rheological metamaterial rotator. (a) Total configuration. Configuration of the unit cells mapped on (b) the rotating shell (left: before tilting and right: after tilting) and (c) the background region. ....	127
<b>Fig. 2.5.6.</b> Simulation results of (a) pressure fields, (b) velocity fields, and (c) flow streamlines for (i) the prototype rheological metamaterial rotator and (ii) the ideal rotator of the continuous media. ....	128
<b>Fig. 2.5.7.</b> Design and numerical simulation results for effective viscosity unit cell for the hydrodynamic metamaterial rotator. (a) Configuration of the unit cell. (b) The simulated velocity fields for (i) radial and (ii) azimuthal direction. ....	130
<b>Fig. 2.5.8.</b> Design of the direct-type rheological metamaterial rotator with configuration and magnified views.....	132
<b>Fig. 2.5.9.</b> Simulation results of (a) pressure fields, (b) velocity fields, and (c) flow streamlines for (i) the direct-type rheological metamaterial rotator and (ii) the ideal rotator of the continuous media.....	133
<b>Fig. 2.5.10.</b> Magnified images of the simulated velocity fields in the central region: (a) with	



the rotator and (b) without the rotator. Dashed squares indicate the unit cell. 133

**Fig. 2.5.11.** A microscale view and configuration of the rheological metamaterial rotator. 135

**Fig. 2.5.12.** Fabrication details of the rheological metamaterial rotator. (a) The Cr mask patterned with the designed drawing, (b) the fabricated silicon master, and (c) the manufactured microfluidic device. The figures in the blue dashed rectangle are the rotators and the others are the metamaterial concentrators discussed in Section 2.4. .... 135

**Fig. 2.5.13.** Comparison of microstructure of the rheological metamaterial rotator; (a) the designed drawings and (b) the fabricated devices. Detailed configuration of (a) the designed rheological metamaterial rotator and (b) the fabricated rheological metamaterial rotator at microscale. .... 136

**Fig. 2.5.14.** Flow streamlines of the rheological metamaterial rotator at (a) the entrance region, (b) left-side region, and (c) central region: observed streamlines (top), simulated streamlines (middle), and microstructure during the experiment (bottom). .... 138

**Fig. 3.2.1.** Fabrication scheme of the SMP samples. .... 147

**Fig. 3.2.2.** Constructed geometry for the shape memory simulation. (a) The modeled specimen. (b) The applied boundary conditions. .... 153

**Fig. 3.2.3.** Chemical reaction scheme for the SMPs synthesis. (a) Reaction initiated by UV light irradiation. (b) Generation of pre-polymer chains by free radical electrons. (c) Crosslinking reaction of the pre-polymer chains and the crosslinker. (d) Suggested chemical structure of SMPs. (e) Schematic illustration of shape memory copolymers with monomers (“A” and “B”) and a crosslinker (“C”). 156

**Fig. 3.2.4.** ATR-FTIR spectra of (a) the basic chemicals and (b) the synthesized SMPs. 157

**Fig. 3.2.5.** Chemical formula of the SMPs; (a) S-MMA, (b) S-BMA, (c) S-BA, (d) S-MMA/BMA, and (e) S-BA/BMA. .... 158

**Fig. 3.2.6.** XPS spectra of the SMPs: (a) S-MMA, (b) S-BMA, (c) S-BA, (d) S-MMA/BMA, and (e) S-BA/BMA. .... 159

**Fig. 3.2.7.** DMTA results of the SMPs. (a) Storage modulus as a function of temperature. (b) Tangent delta as a function of temperature. (c) Transition temperature, transition onset temperature, and rubbery modulus of the SMPs. .... 161

**Fig. 3.2.8.** Transient shape recovery tests. (a) Snap shots of the shape recovery process of S-MMA/BMA taken at 40°C and shape recovery ratios measured at (b) 80°C, (c) 40°C, and (d) 0°C. .... 165

**Fig. 3.2.9.** Cyclic shape memory tests. (a) The measured and simulated SST curves of S-

MMA/BMA and S-BA/BMA. 2D plot of the SST curves for (b) S-MMA/BMA and (c) S-BA/BMA. ....	166
<b>Fig. 3.2.10.</b> Numerical simulation results of S-MMA/BMA. ....	166
<b>Fig. 3.2.11.</b> Light transmittance of the SMPs with respect to wavelength. ....	167
<b>Fig. 3.3.1.</b> Experimental set up for the nanopatterning process. (a) Optical photograph of the fabricated Si wafer. (b) Schematic illustration of the used mold. (c) Optical photographs of injecting the SMCPA resin into the mold. ....	173
<b>Fig. 3.3.2.</b> Constructed nanopattern geometry for the shape memory simulation. (a) The 3 by 3 modeled nanopattern array and its configuration. (b) The applied boundary conditions to the nanopattern geometry. ....	175
<b>Fig. 3.3.3.</b> Unit cells constructed for the EMT analysis; (a) the original nanopatterned surface and (b) the deformed nanopattern surface. ....	175
<b>Fig. 3.3.4.</b> Characteristics of the synthesized SMCPA: (a) chemical formula, (b) schematic representation of polymer chain networks, (c) thermomechanical behaviors, (d) measured and simulated cyclic SST curves, (e) measured optical transmittance, and (f) viscosity of the SMCPA resin. ....	179
<b>Fig. 3.3.5.</b> Replica molding method for SMCPA nanopattern array: (i) injection of the precursor resin into the mold, (ii) the polymerization process by irradiating UV light, and (iii) the nanopattern array of SMCPA. ....	180
<b>Fig. 3.3.6.</b> SEM images of (a) the Si master and (b) the SMCPA nanopattern array on the sample surface. ....	180
<b>Fig. 3.3.7.</b> Shape memory-recovery behavior of the SMCPA nanopatterns. SEM and AFM images of the nanopattern arrays: (a) original (45° tilted), (b) deformed (80° tilted), and (c) recovered (45° tilted) surface. ....	182
<b>Fig. 3.3.8.</b> Numerical simulation results of the SMCPA nanopatterns: (i) original nanopatterns, (ii) deformed patterns at 40°C, (iii) deformed patterns after cooling to 0°C, and (iv) deformed patterns after unloading. The original shape of the nanopatterns is recovered (i) after heating up to 40°C again. ....	182
<b>Fig. 3.3.9.</b> Optical photograph for comparison of surface reflectance between the bare and the nanopatterned surface under (i) solar light and (ii) fluorescent light. ....	186
<b>Fig. 3.3.10.</b> Sustainable antireflection by the SMCPA nanopatterns. (a) Measured (Mea.) and calculated (Cal.) transmittances for each sample. (b) Results of cyclic transmittance tests. (c) Nanopattern volume fraction and (d) calculated effective refractive indices depending on the height-profile. ....	186

<b>Fig. 3.3.11.</b> Omnidirectional antireflection by the SMCPA nanopatterns: angular transmittances of (a) the bare, (b) the original patterned, (c) the deformed, and (d) the recovered samples. ....	187
<b>Fig. 3.3.12.</b> Nanoindentation results for the SMCPA nanopatterns: (a) force-displacement graph and (b) dissipated energy and stiffness for the ground surface and the nanopatterned region. ....	188
<b>Fig. 3.3.13.</b> Recoverable hydrophobicity by the SMCPA nanopatterns: results of the CA analysis for the (a) bare, (b) original, (c) deformed, and (d) recovered surfaces. A water droplet on the 30° tilted samples: the (e) original, (f) deformed, and (g) recovered surfaces.....	190
<b>Fig. 3.4.1.</b> Lab-made touch sensor circuit. The enlarged figure shows the measured electric current when touching the sample with the SMPAC/CNT nanocomposite pattern array.....	195
<b>Fig. 3.4.2.</b> Employed unit cells for the nanoelectronic simulation. (a-c) A 3-D view and (d-f) a yz plane view of the unit cells for the CB, CP, and deformed CP unit cells, orderly. ....	197
<b>Fig. 3.4.3.</b> Schematic illustration of the fabrication process for SMCPA/CNT nanocomposite pattern arrays: (i) injection of the resin mixture into the mold, (ii) polymerization by thermal heating, and (iii) demolding of the samples with nanocomposite pattern array. ....	200
<b>Fig. 3.4.4.</b> Measured viscosity of the SMCPA resin and the SMCPA/CNT resin.....	200
<b>Fig. 3.4.5.</b> Confirmation of presence of CNTs embedded in the nanocomposite pattern with use of (a) XPS (X-ray photoelectron spectroscopy) data and (b) DB-FIB (dual beam focused ion beam microscope). ....	201
<b>Fig. 3.4.6.</b> Measured mechanical properties of the samples. (a) Young’s moduli of the specimens and (b) force-displacement curves, which are macroscopic and nanoscopic mechanical properties, respectively. ....	201
<b>Fig. 3.4.7.</b> Synthetic scheme of SMCPA. (a) Excitation of AIBN by heating. Free radical vinyl polymerization for (b) extending monomer chains and (c) chain crosslinking. (d) A chemical structure and (e) a schematic structure of the synthesized SMCPA.....	202
<b>Fig. 3.4.8.</b> Shape memory-recovery behavior of the SMCPA/CNT nanocomposite patterns arrayed on the CP sample surface. SEM and AFM images of the sample surface on (a) the original, (b) deformed, and (c) recovered states.....	204
<b>Fig. 3.4.9.</b> Topological observation of the CP sample by using SEM. (a) Side view of the	

nanocomposite pattern array at a relatively low magnification. Morphology of the (b) employed CNTs and (c) embedded CNTs in the matrix. ....	204
<b>Fig. 3.4.10.</b> Shape memory behavior of the samples. (a) Thermomechanics of the IP and CP samples. (b) Characterized SST curves of the CP sample. ....	207
<b>Fig. 3.4.11.</b> Numerical simulation results of the SMCPA/CNT nanocomposite patterns; (i) the initial state, (ii) the deformed state after heating up to 40°C, (iii) the cooled state by 0°C, (iv) the unloaded state, and (iv→i) the recovery of a shape of the patterns. ....	207
<b>Fig. 3.4.12.</b> Experimental results of biometric sensing. (a) Schematics of the circuit employed to measure electric signal current passing through the touch pad. The right-hand side figure shows alpha-step profiles before and after touching. (b) Measured and simulated signal current for the IB, IP, CB, and CP samples. (c) Measured signal current according to the shape change of the nanopatterns. ....	210
<b>Fig. 3.4.13.</b> Measured electrical conductivities of the samples and a finger. ....	210
<b>Fig. 3.4.14.</b> Numerical simulation results of the impedance matching nanostructure. The normalized current density fields in (a) yz cut-plane and (b) at bottom. (c) The charge density fields in yz cut-plane; (i) the CB, (ii) original CP, and (iii) deformed CP unit cells. ....	212
<b>Fig. 4.2.1.</b> Acoustic characteristics measurement instruments. (a) A schematic figure of the B&K impedance tube for measuring sound absorption coefficient. (b) A photo of the device for flow resistivity measurement. ....	221
<b>Fig. 4.2.2.</b> Construction process for periodic unit cells (PUCs). (a) A cluster of combined tetrakaidecahedron mimicking the real topology of a fabricated PU foam. (b) Constructed PUC. (c) Free tetrahedron meshes generated in fluid domain of the PUC. ....	223
<b>Fig. 4.2.3.</b> B&K impedance tube geometry used in the macroscale analysis. ....	227
<b>Fig. 4.2.4.</b> Simulation results for microscale flow analyses. (a) A scaled velocity field with streamlines as a solution of the viscous flow problem. (b) A scaled electric field with streamlines as a solution of the inertial flow problem. ....	230
<b>Fig. 4.2.5.</b> Simulated acoustic pressure fields for 400 μm PUC, which are the results of macroscopic acoustic modeling (left: background sound field, right: scattered sound field): at (a) 1000, (b) 2000, and (c) 4000 Hz. The graphs below indicate sound pressure profiles in the tube for each case. ....	231
<b>Fig. 4.2.6.</b> Theoretical sound absorption performance of PU foams according to cell size. (a)	

Sound absorption coefficient curves of the PUCs with various cell sizes. Root mean square values of sound absorption coefficient curves in the frequency range (b) from 0 to 2000 Hz ( $\alpha_{\text{rms},2000}$ ), (c) from 0 to 1000 Hz ( $\alpha_{\text{rms},1000}$ ), (d) from 5000 to 6000 Hz ( $\alpha_{\text{rms},5000-6000}$ ), and (e) from 0 to 6400 Hz ( $\alpha_{\text{rms},6400}$ ). ... 232

- Fig. 4.2.7.** Schematic illustration of the ultrasonic PU foaming method. (a) The state diagram of the reaction resin in the ultrasonic wave excitation (gray dots: generated nuclei, black curves: wave front of ultrasonic waves, and red standing wave mode shape: the amplitude of waves). (b) Microcellular structures foamed after each ultrasonic state. .... 236
- Fig. 4.2.8.** Observation and analysis of microcellular structure of the fabricated PU foams. (a) Observed SEM images of (i) 80-1, (ii) 80-2, and (iii) 80-3. Analyzed (d) average cell diameter, (e) average diameter of interconnecting pores, and (f) cell number density of the samples..... 237
- Fig. 4.2.9.** Measured and simulated poroacoustics parameters of the PUCs representing the fabricated PU foam samples: (a) flow resistivity and (b) characteristic lengths. .... 237
- Fig. 4.2.10.** Simulated normalized complex variables of the PU foam samples: (a) effective bulk density, (b) effective bulk modulus, and (c) complex phase speed. .... 238
- Fig. 4.2.11.** Sound absorption performance of the fabricated PU foams. (a) Measured (solid lines) and simulated (dash lines) sound absorption coefficients from 0 to 6400 Hz. (b) A tendency of max peak shift. Root mean square values (c) from 0 to 2000 Hz and (d) from 2000 to 6400 Hz. (c) Noise reduction coefficient curves. .... 241
- Fig. 4.2.12.** Sensitivity analysis for (a) flow resistivity, (b) viscous characteristic length (VCL), and (c) thermal characteristic length (TCL). .... 242
- Fig. 4.2.13.** 1/3 octave band spectrograms. (a) 1/3 octave bands from #1 band to #25 band. (b-d) Comparisons between the measured and simulated values of bands for each sample. .... 243
- Fig. 4.3.1.** Modeling of PUCs with various cell openness. (a) Production process of PUCs: (i) a cluster consisted of 15 tetrakaidecahedron, (ii) elimination of selected cell walls, (c) imparting the hexahedron into the cluster, and (d) Boolean operation generating PUC. Constructed PUCs having (b) 15%, (c) 25%, (d) 50%, and (e) 100% cell openness. .... 251
- Fig. 4.3.2.** Microscale numerical simulation results using PUCs with (a) 15%, (b) 25%, (c) 50%, and (d) 100% cell openness. (i) and (ii) show the solutions of the viscous flow problem and inertial flow problems. .... 255

- Fig. 4.3.3.** Macroscale pressure acoustics simulation results at (a) 1000 Hz, (b) 2000 Hz, (c) 4000 Hz, and (d) 6000 Hz. (i) means the background pressure field, and (ii-v) mean the scattered pressure fields for 15%, 25%, 50%, and 100% openness PUCs, respectively. The graphs below reveal the profiles of sound pressure field in the tube for each PUC case at each frequency..... 256
- Fig. 4.3.4.** Theoretical complex variables as a function of frequency: (a) effective bulk density, (b) effective bulk modulus, (c) complex phase speed, and (d) characteristic impedance curves normalized with the reference air properties..... 257
- Fig. 4.3.5.** Simulated sound absorption coefficient curves for the various PUCs modeled for 15% and 25% cell openness. .... 257
- Fig. 4.3.6.** Schematic illustration of reactive cell opening mechanism and SEM images of the fabricated PU foams. (a) Chemical formulas of (i) a closed cell PU foam and (ii) a semi-open cell PU foam during the foaming reaction. (b-d) SEM images of the fabricated samples; P0 (0% openness), P3 (15% openness), and P6 (22% openness). .... 260
- Fig. 4.3.7.** Cell size distribution of the fabricated PU foam samples..... 260
- Fig. 4.3.8.** Sound absorption performance of the fabricated PU foams: (a) sound absorption coefficient curves, (b) measured and simulated tortuosity as a function of cell openness, (c) RMS values from 0 to 2000 Hz, (d) NRC values, and (e) shift of maximum peak frequency dependent on cell openness..... 264
- Fig. 4.3.9.** 1/3 octave bands for (a) the simulation results and (b) the measurement results. .... 265
- Fig. 4.3.10.** Sensitivity analysis for (a) tortuosity (Tor.), (b) characteristic lengths (CL.), and (c) flow resistivity (Fr.). .... 266
- Fig. 4.3.11.** Comparison of sound absorption performance between the P3 sample and the 80 kg/m<sup>3</sup> sample developed in Section 4.2: (a) sound absorption coefficient curves, (b) RMS values from 0 to 2000 Hz, and (c) NRC values..... 267
- Fig. 4.4.1.** Design strategy for syntactic hybrid foams (SHFs). (a) Schematic illustration of microcellular structures of (i) an open cell bare foam (BF) and (ii) a syntactic hybrid foam (SHF) with PS microbeads. (b) Constructed PUCs showing solid frames (upper) and fluidic domains (lower); (i) PUC of BF, (ii) PUCs of SHFs for SC-SHF, BCC-SHF, and FCC-SHF. .... 273
- Fig. 4.4.2.** Microscale flow analysis results for PUCs of (a) BF, (b) SC-SHF, (c) BCC-SHF, and (d) FCC-SHF. (i) and (ii) show the permeability fields and the scaled electric

fields as a solution to the viscous flow problem and the inertial flow problem, respectively. .... 278

**Fig. 4.4.3.** Macroscale pressure acoustics simulation results for different incident pressure wave frequencies: (a) 1000 Hz, (b) 2000 Hz, and (c) 6400 Hz. (i) shows the background pressure field and (ii-v) show the scattered pressure fields affected by BF, SC-SHF, BCC-SHF, and FCC-SHF, respectively. The line graphs below display pressure profiles for each case. .... 279

**Fig. 4.4.4.** Sound absorption performance of the foams with BF, SC-SHF, BCC-SHF, and FCC-SHF. (a) Sound absorption coefficient curves. (b) Noise damping parameter values; RMS (root mean square) 0-2000, RMS 4000-6400, and NRC (noise reduction coefficient). (c) 1/3 octave band spectrograms. .... 280

**Fig. 4.4.5.** Comparison of the acoustical complex variables of the porous domain; (a) normalized effective bulk density, (b) normalized effective bulk modulus, and (c) normalized complex phase speed. .... 281

**Fig. 4.4.6.** Heat transfer simulation results. Heat flux magnitude in z-direction for (a) BF, (b) SC-SHF, (c) BCC-SHF, and (d) FCC-SHF. (e) Effective thermal conductivities. .... 284

**Fig. 4.4.7.** Microscale structural analysis results. Mises stress contours for (a) BF, (b) SC-SHF, (c) BCC-SHF, and (d) FCC-SHF, after applying 2% compressive strain in z-direction. (e) Effective compressive moduli. .... 284

## List of Tables

<b>Table 2.3.1.</b> Viscosity tensor components of the multilayered cloak given to each layer.	60
<b>Table 2.3.2.</b> Effective viscosity unit cells mapped on each layer of the rheological metamaterial cloak.	65
<b>Table 2.4.1.</b> Viscosity tensor components of the multilayered concentrator given to each layer.	97
<b>Table 2.4.2.</b> Effective viscosity unit cells mapped on each layer of the rheological metamaterial concentrator.	101
<b>Table 3.2.1.</b> Material parameters of the SMCPAs employed in the simulation.	153
<b>Table 3.2.2.</b> Polymeric chain composition of the SMP samples.	156
<b>Table 3.2.3.</b> XPS peak information of the SMP samples.	158
<b>Table 3.2.4.</b> Thermomechanical properties of the fabricated SMPs.	161
<b>Table 3.3.1.</b> Calculated effective refractive indices of SMCPA.	176
<b>Table 3.4.1.</b> Material parameters of SMCPA/CNT employed in the shape memory effect simulation.	197
<b>Table 3.4.2.</b> XPS peak information of the patterned samples, IP and CP.	202
<b>Table 4.2.1.</b> Calculated poroacoustics parameters for JCA model.	230
<b>Table 4.2.2.</b> Microcellular structure information of the fabricated samples.	236
<b>Table 4.2.3.</b> Acoustic damping evaluators of the PUCs for the samples.	243
<b>Table 4.2.4.</b> Band numbers of 1/3 octave band spectrogram.	244
<b>Table 4.3.1.</b> Calculated poroacoustics parameters for JCA model.	254
<b>Table 4.4.1.</b> Material properties employed in the simulations.	273
<b>Table 4.4.2.</b> Calculated poroacoustics parameters for JCA model.	279
<b>Table 4.4.3.</b> Evaluated material properties calculated from poroacoustics, thermal, and mechanical simulation.	284



# Chapter 1.

## Introduction

### 1.1. What is a metamaterial?

A metamaterial, which originated from the Greek word μετά meaning “beyond”, is an artificially engineered material to perform special properties that cannot be normally found in nature [1]. The metamaterial is strategically designed on a theoretical basis and usually made of micro/nanostructured materials made of polymer, metal, ceramic, or composite, to feature extraordinary abilities. As a rapidly emerging research theme, the developed micro/nanostructural metamaterials have enabled a variety of unprecedented phenomena beyond human imagination and have implemented outstanding material properties beyond a stereotype of conventional materials (**Fig. 1.2.1**).

For electromagnetics, negative refraction of light is one of the exceptional phenomena found by metamaterial study where light rays are refracted at the interface in the negative direction opposite to the normal manner [2,3]. A superlens is a metamaterial lens beyond the diffraction limit, which is a characteristic of conventional lenses limiting the resolution [4,5]. A metamaterial absorber is a class of metamaterial to absorb electromagnetic radiation more efficiently than conventional absorbers [6,7]. An invisibility cloak is a fictional theme and has been realized by the usage of metamaterials. This is achieved by controlling and directing the light propagation path in a designed manner and then making an object invisible [8,9]. Even, an artificial black hole using the metamaterial approach was experimentally implemented by mimicking celestial mechanics [10].

A metasurface is a two-dimensional artificial metamaterial architected with subwavelength-scale nanostructures, which are small comparable with the operating wavelength [11]. The metasurface manipulates the electromagnetic behavior in a unique way through the subwavelength feature of the surface. It can be considered as an interface of discontinuity enforcing an abrupt change in both the amplitude and phase of the

impinging light [12]. Antireflective nanostructure mimicking Moth eye is one of the most popular electromagnetic metasurfaces [13,14]. A plasmonic metasurface uses surface plasmon phenomena for optical properties not found in nature [15]. The metasurfaces have also been used to make computer-generated holograms [16].

Recently, transformation optics was reported to produce spatial variations by using a coordinate transformation method and this theory has been applied to design various electromagnetic metamaterials, including cloaks, concentrators, and rotators [8,9,17]. In a theoretical basis similar to general relativity theory, a method of warping coordinate systems for light was devised to guide the light ways in an unprecedented manner. The research for design and materialization of the transformation metamaterials has been attempted through interdisciplinary research in mathematics, physics, nanoscience, materials science, mechanical engineering, and electrical engineering.

Metamaterials that do not aim at electromagnetic wave control have also been developed variously. A seismic metamaterial was theoretically designed to prevent the adverse effects of earthquake [18]. Acoustic metamaterials have been devised to manipulate sound waves at will for cloaking [19], absorbing [20], and diffracting [21] phenomena. Auxetics are mechanical metamaterials that have a negative Poisson's ratio that is a characteristic thickening vertically to the direction of applied force. [22]. A metahydrogel made from a DNA (deoxyribonucleic acid) was reported, which transforms its nature from liquid-like properties to solid-like properties and vice versa [23]. A class of microarchitected materials that maintain a nearly constant stiffness per unit mass density was reported as a mechanical metamaterial [24]. Furthermore, the metamaterials based on transformation optics have been translated into other physics fields beyond the electromagnetics, such as thermodynamics [25], acoustics [26], and mechanical engineering [27].

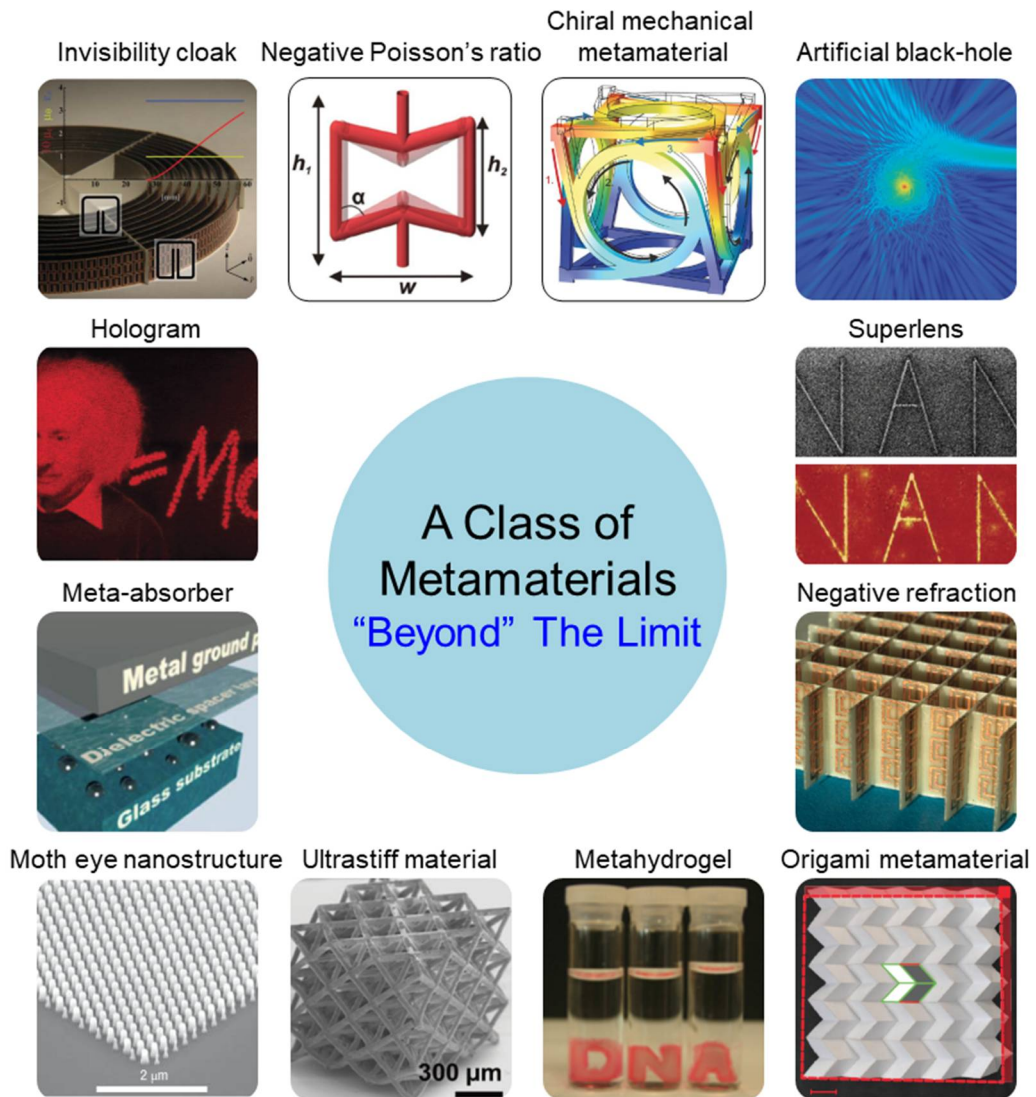


**Figure 1.2.1.** A Class of metamaterials; Invisibility cloak [28], negative refraction [2], superlens [5], hologram [16], ultrastiff material [24], Moth eye nanostructure [13], artificial black hole [10], metahydrogel [23], meta-absorber [29], chiral mechanical metamaterial [30], origami metamaterial [31], and negative Poisson's ratio [32].

## 1.2. Research background

### 1.2.1. Transformation optics

Since development of general relativity theory by Albert Einstein [33] and its follow-up studies [34], the stereotypes of energy transfer in a space have been broken. It was found that the propagation of light can be directed or bent by exterior energy fields, *i.e.*, gravity fields originated from planets. Various phenomena of spatial distortions based on this theory, such as black holes, wormholes, and warp systems, have been observed and theoretically analyzed.

In 2006, two groundbreaking theoretical papers [8,9] on cloaking electromagnetic waves opened a new scientific field called “transformation optics”. The mathematics that underpins transformation optics is very similar to the Albert Einstein’s general relativity that describes how gravity warps space and time. Merely, transformation optics defines a way to manipulate light propagation in a desired manner as warping an electromagnetic coordinate space, instead of the space and time for the general relativity. The two papers suggest the way how to conceal an object electromagnetically by detouring light lays. The metamaterials based on transformation optics have been developed through interdisciplinary research such as mathematics, electromagnetics, mechanical engineering, nanoscience, and materials science.

Pendry *et al.* [9] showed how electromagnetic fields can be redirected at will and proposed a design strategy by using the freedom of design which metamaterials provides (**Fig. 1.2.2(a)**). The electromagnetic fields are all displaced in a consistent manner even in the distorted coordinate system. They presented a simple example of concealing a space left to completely exclude all electromagnetic fields, the electromagnetic cloak. The distortion of electromagnetic fields is achieved by a coordinate transformation, which is used to obtain transformed electrical permittivity and magnetic permeability. The transformed material parameters still satisfy Maxwell’s equations in the distorted coordinate system. They insisted that almost any desired electromagnetic waves can be implemented with this method. In the same issue, Leonhardt [8] reported a general recipe to design media that create perfect invisibility within the accuracy of geometrical optics

(Fig. 1.2.2(b)).

Transformation optics was established with a form invariance of the Maxwell's equations under coordinate transformations. The development process of scaling the material parameters of the Maxwell equations is briefly given below [9]. The proof starts from the Maxwell's equations defined in a Cartesian coordinate system.

$$\nabla \times \tilde{\mathbf{E}} = -\mu \partial \tilde{\mathbf{H}} / \partial t \quad (1.1)$$

$$\nabla \times \tilde{\mathbf{H}} = \varepsilon \partial \tilde{\mathbf{E}} / \partial t \quad (1.2)$$

, where  $\tilde{\mathbf{E}}$  is the electric field,  $\tilde{\mathbf{H}}$  is the magnetic field,  $\mu$  is the permeability, and  $\varepsilon$  is the permittivity. They performed a coordinate transformation to a general system defined by  $u(x, y, z)$ ,  $v(x, y, z)$ , and  $w(x, y, z)$ . If a set of points is defined by equal increments along the  $u$ ,  $v$ , and  $w$  axes, the coordinate meshes would appear distorted in the original Cartesian frame.

The Maxwell's equations in the new coordinate system ( $u$ ,  $v$ ,  $w$ ) become as

$$\nabla' \times \tilde{\mathbf{E}}' = -\tilde{\boldsymbol{\mu}}' \cdot \partial \tilde{\mathbf{H}}' / \partial t \quad (1.3)$$

$$\nabla' \times \tilde{\mathbf{H}}' = \tilde{\boldsymbol{\varepsilon}}' \cdot \partial \tilde{\mathbf{E}}' / \partial t \quad (1.4)$$

, where  $\tilde{\boldsymbol{\mu}}'$ ,  $\tilde{\boldsymbol{\varepsilon}}'$  are the general tensors, and  $\tilde{\mathbf{E}}'$ ,  $\tilde{\mathbf{H}}'$  are the renormalized vector fields. From this relationship, they found that the mathematical form of the Maxwell's equations is preserved after coordinate transformations when the  $\tilde{\boldsymbol{\mu}}'$  and  $\tilde{\boldsymbol{\varepsilon}}'$  are properly defined according to the new coordinate system. Kelvin-Stokes theorem ( $\oint \tilde{\boldsymbol{x}} \cdot d\tilde{\boldsymbol{l}} = \int \nabla \times \tilde{\boldsymbol{x}} \cdot d\tilde{\boldsymbol{a}}$ ) was used for the coordinate transformation of curl operation. After mathematical derivation, the materials tensors are defined as a 2<sup>nd</sup>-order inhomogeneous anisotropic tensor like

$$\tilde{\boldsymbol{\varepsilon}}' = \det(\boldsymbol{\Lambda}^{-1}) \boldsymbol{\Lambda} \boldsymbol{\varepsilon} \boldsymbol{\Lambda}^T \quad (1.5)$$

$$\tilde{\boldsymbol{\mu}}' = \det(\boldsymbol{\Lambda}^{-1}) \boldsymbol{\Lambda} \boldsymbol{\mu} \boldsymbol{\Lambda}^T \quad (1.6)$$

, where  $\boldsymbol{\Lambda}$  is the Jacobian matrix for a backward transformation, which transforms the

coordinate basis from new to old. The renormalized vector fields are also defined as

$$\widetilde{\mathbf{E}}' = \det(\mathbf{\Lambda}^{-1})\mathbf{\Lambda}\widetilde{\mathbf{E}} \quad (1.7)$$

$$\widetilde{\mathbf{H}}' = \det(\mathbf{\Lambda}^{-1})\mathbf{\Lambda}\widetilde{\mathbf{H}} \quad (1.8)$$

The representative application of transformation optics is the invisibility cloak. Cummer *at el.* [35] performed full electromagnetic simulations of the cloaking structure for a cylindrical case. The simulation was conducted by using experimentally realizable electromagnetic parameters, which require modest spatial variation of permittivity and permeability. In addition to discovering electromagnetic cloaking effects, they also proposed a simple reduced set of parameters and a stepwise approximation strategy.

A theoretical study on transformation optics has spread to the experimental realization through an artificial metamaterial design. For the first realization of the invisibility cloak [28], the metamaterial cloak was designed by using a reduced set of material parameters and was made by mapping split-ring resonator (SRR) unit cells to implement the anisotropic inhomogeneous materials parameters. The SRR consisted of a polymeric composite (Duroid 5870) covered with a copper film. A copper cylinder was successfully hidden from electromagnetic waves at microwave frequencies. As a follow-up study, the metamaterial design of a non-magnetic cloak operating at optical frequencies was presented [36]. By inserting metal wires of subwavelength size in a dielectric matrix, the optical metamaterial cloak was theoretically designed and its performance was demonstrated by using numerical analysis.

A new strategy of concealing objects beneath the carpet was established by quasiconformal mapping refractive indices spatially varying but isotropic [37]. This strategy gains the advantages that the cloak parameters can be made of isotropic values without singular matrix problem. The carpet cloak was designed to mimic a flat ground plane and no extreme values are required in the material profile.

Different types of metamaterials have been reported in addition to invisibility cloaks. An electromagnetic concentrator was demonstrated [38] and unlike the invisibility cloak, the spatial distortion for the concentrator requires simultaneous compression and expansion. It was insisted that the concentrator allows a very large concentration of magnetic energy

in the encircled region and it can be utilized for increasing the sensitivity of magnetic sensors [39]. Unfortunately, experimental realization of the electromagnetic concentrator has not been reported so far.

An electromagnetic field rotator is another type of metamaterials that rotates propagating waves. A way to direct electromagnetic waves was suggested by introducing a rotation mapping of coordinates [40]. By twisting the space of the shell surrounding the central region, the external information, electromagnetic waves in this case, was rotated as if coming from another angle. The metamaterial rotator was designed by mapping unit cells that contain a tilted pillar and the experimental results showed that the designed rotator can guide electromagnetic waves in the desired direction regardless of the light source [41].

Much research has been performed on whether transformation optics can be translated into and applied to wave equations other than optics. Development of transformation acoustics was one of the researches on these attempts. Numerical analysis of a two dimensional acoustic wave cloak was carried out with an inhomogeneous bulk modulus and an anisotropic-inhomogeneous mass density by time harmonic simulations [26]. It was figured out that the exact equivalence in two-dimensions between fluid acoustics and single polarization electromagnetics holds for anisotropic materials. This anisotropic isomorphism enables transformation optics to be realized acoustically. A three dimensional acoustic cloak was developed by deriving the mass density and bulk modulus for the spherical cloaking shell [42]. The Helmholtz equation for fluid acoustics should be form invariant under coordinate transformations on the basis of this study.

A theoretical design was proposed for a cloak to control ultrabroadband elastic waves propagating in isotropic heterogeneous thin plates [43]. An elastic metamaterial was designed through homogenization of a multilayered concentric circle possessing the piecewise constant isotropic elastic material property, *i.e.*, Young's modulus. The cloak exhibited no phase shift for both backward and forward scattering of elastic waves. Invariant transformation for quantum mechanical systems was proposed by modifying the potential and effective mass of the space for cloaking of matter waves [44]. This system could be achieved due to a form invariance of the Schrödinger equation.

Relatively recently, several research groups have investigated how governing equations behave under geometric transforms in other nonharmonic physics, *i.e.*,

conduction problems [45]. The metamaterials for scalar fields have emerged, which are mostly governed by Laplace equation [46]. Transformation optics tools were adapted to thermodynamics which is governed by the parabolic heat equation [45]. A transformed heat conduction equation was mathematically derived and a heterogeneous anisotropic thermal conductivity tensor was calculated from this equation. Thermal cloaking effect was shown numerically, which reduces the temperature inside an arbitrary cloaked region. For static electromagnetic fields, anisotropic electrical conductivities were constructed in three-dimensions that give rise to the same voltage and current measurements on the boundary as those of a homogeneous and isotropic conductivity [47].

A concept for manipulation of fluid flow was introduced based on coordinate transformations of Darcy's pressure equation [48]. The cloak with anisotropic permeable porous media was theoretically analyzed. It was insisted that this cloak would remove downstream wakes, complement the viscous drag, and suggest the possibility of a new propulsion technique.

Experimental realization of the various transformation physics, such as acoustic waves, elastic waves, heat transfer, and electric current transfer, has been attempted. The cylindrical cloak for linear surface liquid waves was realized and it was experimentally found that backscattering of acoustic waves from an obstacle surrounded by the cloak decreases [49]. A metamaterial cloak for elastic waves was designed, manufactured, and characterized [27]. The cloak consisted of twenty concentric rings, each of which is a custom polymeric composite made of polyvinyl chloride and polydimethylsiloxane. The good cloaking behavior was observed for carrier frequencies in the range from 200 to 400 Hz.

Metamaterials for conduction problems have also been developed. The thermodynamic metamaterial cloak was experimentally realized by designing, fabricating, and characterizing a microstructured composite plate composed of a copper and polydimethylsiloxane [25]. This metamaterial allows for transient heat protection while maintaining the same downstream heat flow in background region. The first experimental demonstration of a dc electric cloak was presented, which can hide an object from static current fields [50]. The dc cloak can smoothly guide electric currents around the cloaked area and keep perturbations only inside the cloak.



In addition, the metamaterial cloaks for elastic-solid mechanics whose underlying equations are not form invariant under coordinate transformations were introduced. An elasto-mechanical unfeelability cloak was designed and experimentally realized using pentamode polymeric metamaterials [51]. The same research group proposed the mechanical cloak designed by using a direct lattice transformation [52].

Based on a similar rationale to transformation optics, transformation physics (acoustics, thermodynamics, *etc.*) can be applied to other types of metamaterials such as concentrators or rotators. The spatial relationship between an original virtual space and a distorted physical space is identical to the other electromagnetic metamaterials.

Several metamaterial concentrators have been reported. A thermodynamic concentrator was theoretically demonstrated, which gathers heat fluxes in a desired region and concentrating thermal energy to the central region of the device [53]. It was mentioned that the concentrator could be potentially applied in solar thermal panels and thermal-electric devices to enhance energy harvesting efficiency. A thermodynamic metamaterial concentrator was designed and fabricated [54]. The experimental thermal concentrator is made of a single hollow cylindrical shaped polymeric composite metamaterial with highly anisotropic effective thermal conductivities in both radial and azimuthal directions. The central area enclosed by the concentrator exhibited a significantly increased temperature gradient up to 83.1% compared to the applied value. A dc electric concentrator was devised to enhance the electric field and current density for steady current fields [55].

Metamaterial rotators also have been studied. An acoustic metamaterial rotator that manipulates acoustic wave front by a certain angle was theoretically designed and experimentally realized [56]. The designed rotator was simply composed of an array of identical polymeric plates and the rotation effect was confirmed. A thermodynamic metamaterial rotator was designed and constructed by fabricating the multilayered polymer composite, which can invert heat flux direction by  $204^\circ$  [57].

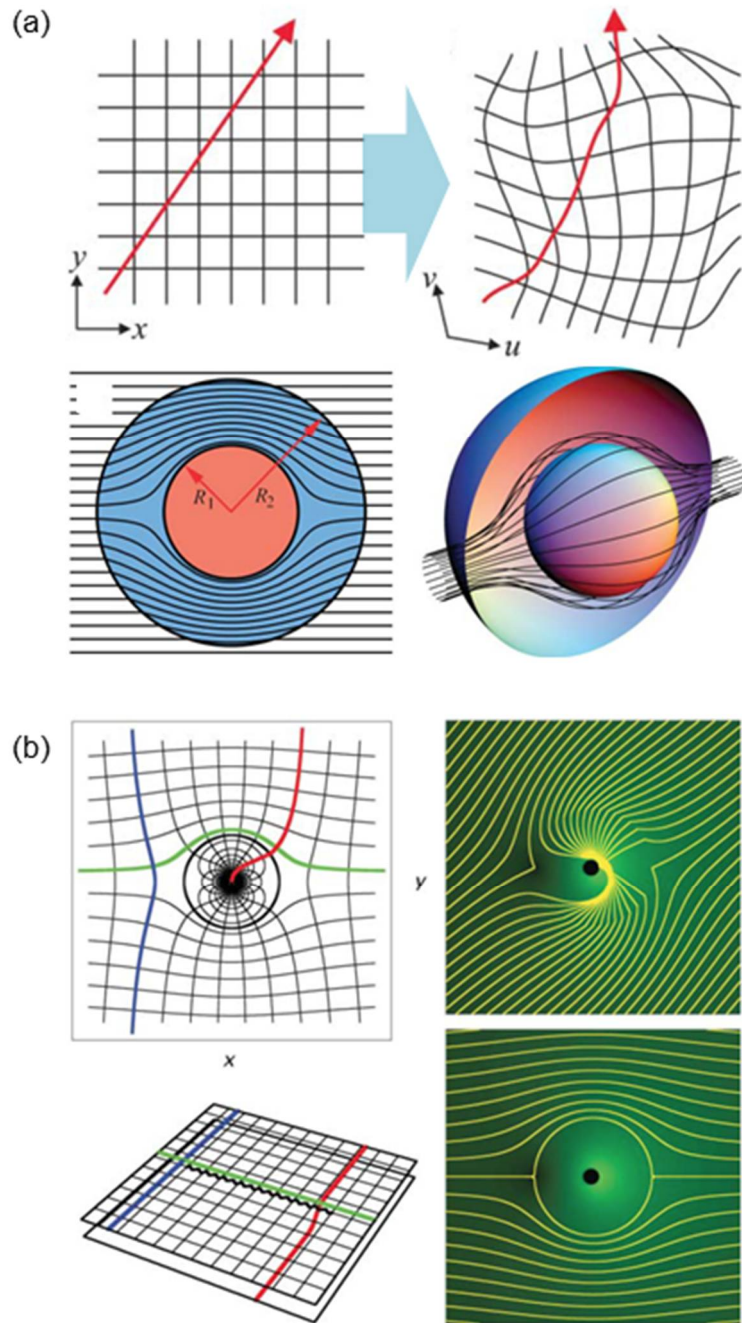


**Figure 1.2.2.** Schematic illustration of transformation optics. (a) Cartesian coordinate grids in a free space and a distorted coordinate grids (upper). Two and three-dimensional ray trajectories in the cloak (lower) [9]. (b) Optical conformal mapping (left) and ray propagation in the dielectric invisibility device (lower) [8].

### 1.2.2. Shape memory polymer

Scientists and engineers involved in chemistry and materials science have followed the principles developed by nature over millions of years for the design of new synthetic materials to mimic the outstanding properties of natural materials [58]. Among them, smart materials, also called intelligent materials or stimulus-responsive materials, are peculiar materials that change their characteristics according to the surrounding environment [59]. These materials are sensitive to a variety of stimuli such as light, heat, acidity, humidity, or external fields and react in a variety of ways, such as changing color, light transmission, or shape. Using these characteristics, the smart materials have been applied to broad academic fields including biomedical engineering, optical devices, electro-circuits, self-healing technology, and aerospace engineering [60].

Shape memory materials (SMMs) have been widely developed and received a great deal of attention in the past few decades, as one of the most significant branches of smart materials. The term “shape memory” was first suggested by Vernon in 1941 [61] but the importance of SMPs was not recognized until the 1960s. The SMMs include shape memory alloys (SMAs), shape memory ceramics (SMCs), shape memory polymers (SMPs), and shape memory composite materials (SMCMs) [62]. Among them, the SMPs have attracted more research attention than other SMMs, due to their biocompatibility, lightweight, low cost, and broad applicability.

The SMPs respond by an external stimulus with a shape-transformation from a temporary shape to a permanent original shape. A unique and interesting feature of SMPs is that the original shape is remembered in the macromolecular system of SMPs even after deformation. Hence, the original shape can be restored by the external stimulus without additional mechanical aid. This shape memory effect of SMPs is a bio-inspired mechanism found in spider draglines [63].

The SMPs possess the following advantages for practical uses and materials design [62]. In addition to heating, the SMPs can utilize various external stimuli and triggers, including light, magnetic fields, chemicals, and electricity. Highly flexible shape-programming is possible through single or multistep processes. There is an abundance of approaches to design crosslinking net-points and switching segment in the molecular

structure of SMPs, so a wide variety of SMPs can be synthesized. The characteristics of SMPs can be easily and precisely adjusted using composites, blending, and synthesis methods. The SMPs offer unique opportunities for smart medical, biological, and garment-integrated devices because they are biodegradable and biocompatible. The SMPs are lightweight and can be easily fabricated as a porous foam structure.

The shape memory behavior of SMPs can be demonstrated in various polymeric systems with greatly different molecular structures. The mechanism of shape memory effects (SMEs) has been described in various theoretical models according to each type of SMP. A molecular mechanism of thermal-triggered SMPs was proposed in which the network structure is chemically or physically crosslinked and the switching units are made of a semi-crystalline or amorphous phase (**Fig. 1.2.3(a)**) [64,65].

Two athermal SMP models were proposed with assumption of supramolecular switches. One model is designed to generate a light-sensitive SMP in which the chromophores are covalently grafted onto a crosslinked polymer network. The light-sensitive SMEs can be achieved through efficient photoreversible (2+2) cycloaddition reactions between chromophore molecules, namely cinnamic acid-type molecules [66]. Another athermal system is the water-sensitive SMP made from a nanocomposite containing nanocellulose whiskers in an elastomer matrix [67].

A three-dimensional SMP model was proposed based on the molecular mechanisms, which can describe any type of SMPs (**Fig. 1.2.3(b)**) [68]. In the model, the SMPs are composed of a switching segment and crosslinking net-points. An original permanent shape of SMPs are determined by the net-points which are made of chemical or physical crosslinks. Meanwhile, the switching segment controls the shape fixity and recovery according to the surrounding environment and external forces. The driving force triggering strain recovery of SMPs is assumed as the entropic elasticity stored in the polymeric network chains while deforming. Therefore, the design and implementation of physical or chemical net-points through intermolecular forces or covalent bonding is at the heart of the SMP driving principle.

The SMPs were classified by Hu *et al.* [62] according to various standards, such as chemical composition, types of stimuli, and shape memory functionality. Depending on the chemical composition, the following SMPs can be categorized; chemically crosslinked

SMPs [69–71], SMP composites [72,73], interpenetrating polymer networks [74–76], SMP blends [77,78], copolymer networks [79,80], and supramolecular SMP networks [81]. According to the stimuli triggering SMEs, the SMPs can be assorted in the following groups; thermal-induced, water sensitive, light sensitive, electrically sensitive, and redox sensitive types. The SMEs have been researched from the conventional one-way SMEs to two-way, triple, and even multiple SMEs. Additionally, multi-functionality has been achieved in the SMP chemicals [82].

The study and use of theoretical modeling facilitate molecular design of new SMP systems and have provided new knowledge of various SME mechanisms. Specifically, modeling of thermal-induced SMPs has been widely studied from microscale, macroscale, mesoscale, molecular, and quantum-chemical models to structural analysis. The modeling can be used to predict shape memory behavior of SMPs depending on time, temperature, applied stresses, constraints, and other factors. A deeper understanding of the mechanisms and principles can be obtained from the modeling.

In the macroscale modeling, the thermodynamics of entropic elasticity and energy was employed to interpret the shape memory behavior of SMPs without considering molecular interactions. Generally, linear viscoelastic models are used for a simplified phenomenological approach. A mesoscale model was proposed that consider an SMP composed of two different continuous substructural components [83]. The SMPs were modeled with a resistant component that maintains elasticity with a constant Young's modulus and a compliant component that deforms in a time/temperature dependent elastic–plastic–viscous manner. This model can provide a detailed understanding of the SMP mechanisms. Another mesoscale model was reported that demonstrates a nonlinear material response and contains phenomenological three dimensional formulations for SMPs [84]. This model decomposes the strain into thermal, elastic, and stored components and uses two internal variables, which are the frozen volume fraction and the stored strain, to explain the evolution of the microstructure. It reasonably captures the essential shape memory responses to temperature events at the continuum level but cannot deal with the time dependence. In addition, various studies for microscale modeling [85], molecular dynamic simulation [86], quantum chemical calculations [87], and device-structure modeling [88,89] have been performed.

Due to the unique performance of SMPs, many applications have been reported in industry and academia. Applications of SMPs can be categorized by the following groups [58]; industrial applications, biomedical, self-healing, and tunable surface characteristics. As an example of the industrial applications, heat shrinkable tubings have been developed to overcome difficulty in processing [90,91]. Self-deployable functions of SMP-based devices have contributed to smart aerospace engineering with their lightweight advantages [92–94].

The SMPs for the biomedical engineering applications must be possible to heat up inside human body. These issues have been solved by using IR(infrared)-Lasers [95] and magnetic-sensitive nanoparticles [96,97]. Also, biocompatibility and non-toxicity of SMPs have been proven showing low cytotoxicity, cytokine activation, low thrombogenicity, and low *in-vivo* inflammatory response [98–100]. Based on these properties, the SMPs have been applied in a myriad of biomedical fields, such as cardiac valves [101], endovascular strokes [102,103], vascular stents [104–106], orthopedics [107], kidney dialysis [108], neuroprosthetics [109], and endoscopic surgery [110].

Self-healing ability of materials is an innovative characteristic that can recover mechanical damage and deformation. A reversible plasticity of the self-healing polymers was reported and self-healing using SMPs under unconfined conditions can be applied to external scratches, damage to thin films, or internal cracks and small defects [111]. A strategic system called “shape memory assisted self-healing (SMASH)” was proposed and the excellent self-healing effect by the SMASH system was proved [74]. In addition, a variety of self-healing SMPs have been developed, which will serve as a solution to break the stereotypes of conventional material preservation.

Micro/nanostructured surface patterns facilitate various unique properties such as super-hydrophobicity, self-cleaning, structural coloring, adhesion, friction, lubrication, and drag reduction. Therefore, the technique of injecting shape memory ability into micro/nanostructures is one of the most attractive topics in the field of smart materials. Tunable wetting by SMPs was investigated by studying water droplet spreading on the SMP micropillars (**Fig. 1.3(c)**) [112,113]. Localized structural colors were demonstrated by depositing an Au film on the sub-nanoscale wrinkled SMP surface [114]. Switchable micro-optics devices were possible by patterning microstructures made of a transparent shape

memory elastomer [115]. A reversibly switchable optical window was developed by fabricating tilted micropillar arrays [116]. Cell mechanobiology was controlled by using a tunable nanogeometry made of SMP and the cell fate could be regulated as intended [117–119]. A reversible self-peeling function was suggested for a dry adhesive system by using microstructured SMP surfaces [120–122].

In addition, a variety of applications using SMPs have been studied such as shape memory fibers [62], shape memory textiles [68,123], and artificial muscles [124,125]. Many researchers involved in smart materials have reported synthesis, modeling, and applications of SMPs, but there are still many unexplored areas and limitations of SMPs to be studied.

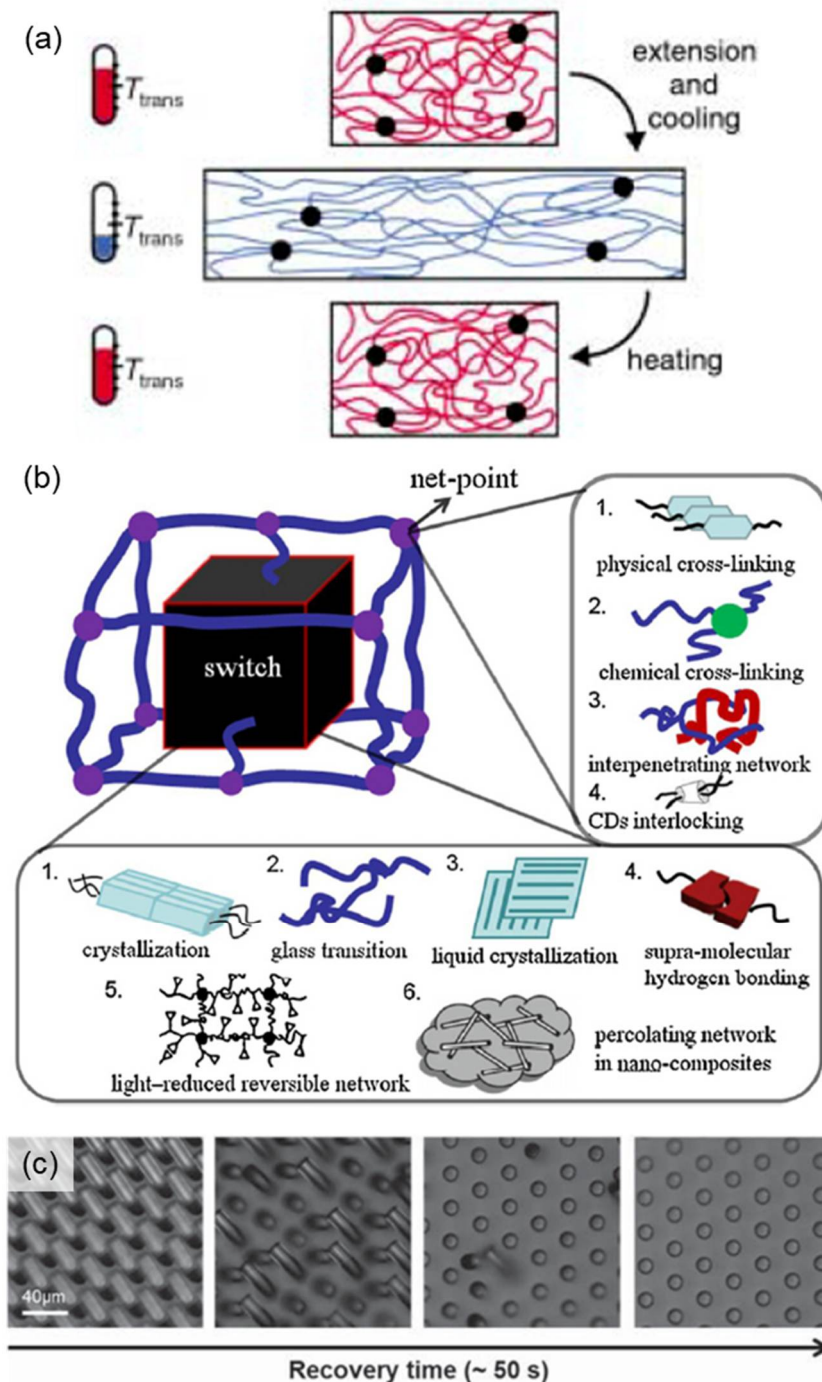


**Figure 1.2.3.** Classification, mechanism, and representative shape-recovery behavior of shape memory polymers. (a) Molecular mechanism of shape memory effect of amorphous SMPs [65]. (b) Overall architecture of SMPs [68]. (c) Shape recovery behavior of the deformed SMP micropillars [112].



### 1.2.3. Sound absorption

Sound is an audible pressure wave propagating through transmission media. As a class of sound, noise is unwanted annoying sound judged in brain to be unpleasant, loud or disruptive to hearing. Hence, noise control is one of the major factors that detracts from the quality of life from our daily life as well as the operation of any machinery (**Fig. 1.2.4(a)**). Hence, the control and elimination of noise by soundproofing is significant consideration when designing and manufacturing artificial substances requiring noise control such as vehicles and buildings.

The soundproofing is means of reducing noise by reflecting or absorbing the energy of sound waves. Sound absorption is a phenomenon that uses a specific mechanism to convert some portion of the sound energy into heat energy instead of being transmitted or reflected. Sound absorption materials are selected and used according to the frequency distribution of the main noise to be absorbed. Sound insulation materials are massive substances having high surface characteristic impedance, which can reflect the sound energy to the incident direction [126–128]. In addition, noise cancellation generators have been developed for active noise control. The active noise control is possible through destructive interference using sound waves with opposite polarity to the target noise.

Effective air media made of micro/nanostructured porous materials have been used with two mechanisms assigned to the interface between the solid frame and air. One mechanism originates from viscous dissipation in the viscous boundary layer near the solid frame surface, where non-slip behavior of sound waves causes large relative motions. The other mechanism is based on heat conduction through the solid surfaces, which derives the breakdown of the adiabatic characteristic of sound waves. According to these mechanisms, a sound absorbing material should be composed of a porous structure, and the inner micro/nanostructure is a factor much more important than the materials properties in sound absorption performance. Porous sound absorbers are designated as a noise absorber in a wide range of medium frequencies and are less impressive at low frequencies. In the meanwhile, resonant sound absorbers are effective at low-medium frequencies and operate only in a narrow frequency range.

Sound absorption coefficient ( $\alpha$ ) is a parameter for sound absorption performance of a material and is defined as a ratio of the absorption energy to the incident energy, which represents the amount of sound energy absorbed by the material. When an acoustic wave is incident on the surface of a sound absorbing material, the wave is divided into an incident wave, a reflected wave, and a transmission wave [129]. The sound absorption coefficient is generally measured by using a B&K two-microphone standing wave tube which is a circular tube having a constant cross-section. A loud speaker is fixed at the end of the tube generating a plane wave, and a sample is mounted at the other end of the tube with rigid backing. A phase-matched microphone is located in the tube and the sound pressure at each point was measured. To obtain the sound absorption coefficient, the sound pressure at microphone positions is represented by

$$P_1 = (Ae^{-jkx_1} + Be^{jkx_1})e^{j\omega t} \quad (1.9)$$

$$P_2 = (Ae^{-jkx_2} + Be^{jkx_2})e^{j\omega t} \quad (1.10)$$

, where  $A$  and  $B$  represent the amplitude of incident and reflected waves in the tube respectively,  $k$  is the wavenumber, and  $x_1$  and  $x_2$  are the distances from the sample to microphones 1 and 2. The transfer function which is the sound pressure ratio between the two microphones is represented by

$$H_{12} = \frac{P_1}{P_2} = \frac{Ae^{-jkx_1} + Be^{jkx_1}}{Ae^{-jkx_2} + Be^{jkx_2}} = \frac{e^{-jkx_1} + Re^{jkx_1}}{e^{-jkx_2} + Re^{jkx_2}} \quad (1.11)$$

, where  $R$  is the reflection coefficient which is the ratio of  $A$  and  $B$ . The reflection coefficient is expressed by the transfer function ( $H_{12}$ ) by the following equation.

$$R = \frac{-e^{-jkx_1} + H_{12}e^{-jkx_2}}{e^{jkx_1} - H_{12}e^{jkx_2}} \quad (1.12)$$

Finally, the sound absorption coefficient ( $\alpha$ ) is calculated through the reflection coefficient as  $\alpha = 1 - |R|^2$ . The absorption coefficient ( $\alpha$ ) has a value of between 0 and 1 and if the value is close to 1, it can be evaluated that the material well-absorbs the sound energy.

Poroacoustics modeling at microscale has been studied numerically and analytically to demonstrate sound propagating phenomena theoretically. The poroacoustics models are classified into three types of models; diphasic models, motionless skeleton models, and uniform pressure models. The diphasic model, represented by Biot's model, describes sound wave propagation and interaction in both fluidic and solid phases of porous materials. It is the most comprehensive model to explain the vibro-acoustic phenomena of porous media, but it is too complicated for intuitive interpretation because many parameters have to be considered. The motionless skeleton model, represented by Johnson-Champoux-Allard (JCA) model, interprets the solid phase of a porous medium as being immobile under certain acoustical and material conditions. On the contrary, the uniform pressure model assumes that no sound wave propagates in the fluid phase.

In the motionless skeleton model, a solid material frame can be considered rigid and motionless if the incident sound frequency is much higher than the phase decoupling frequency and the porous material has much greater stiffness or weight than air. The wave equation for the motionless skeleton model is defined as

$$\nabla^2 p + \omega^2 \frac{\rho(\omega)}{K(\omega)} p = 0 \quad (1.13)$$

, where  $p$  is the pressure of sound waves,  $\rho(\omega)$  and  $K(\omega)$  are the effective bulk density and effective bulk modulus,  $\nabla$  is the nabla operator, and  $\omega$  is the angular frequency of sound waves [130]. **Equation 1.13** is very similar with the simple Helmholtz equation but the two complex variables ( $\rho(\omega)$  and  $K(\omega)$ ) describing porous media make a difference.  $\rho(\omega)$  is modeled for considering the viscous friction performance and  $K(\omega)$  demonstrates the thermal exchange in porous media (**Fig. 1.2.4(b)**). The models aim to calculate the complex variables from microstructural characteristics for certain frequency range, and predict macroscopic acoustical performance of porous materials, *e.g.*, sound absorption coefficients. Using these models, microstructural influence on sound absorption has been studied for cell size [131] and cell openness [132].

On the other hand, macroscopic parameters of sound absorbing materials such as thickness, density, and porosity also significantly affect the sound absorption performance [133]. Among them, the thickness of materials is directly related to the sound absorption

performance in low frequency range from 100 Hz to 2000 Hz [134]. As the thickness of materials increases, the sound absorption performance at low frequencies improves significantly [135]. This change is because low-frequency noise has a higher wavelength, so that thicker materials can cancel the sound waves by inducing destructive interference between the noises. The density of materials is another significant macroscopic parameter defined as mass per unit volume. The density determines the acoustical surface characteristic impedance of materials, which affects the degree of surface reflection of sound waves. Generally, a more complex inner microcellular structure is formed inside the higher density foam. Hence, the sound absorbing performance is enhanced by increasing the density of materials [136], because Inside the complex sound propagating media, sound waves more contact the solid surface, increasing the airflow friction and inducing more heat exchange [137].

In summary, in common sense, thicker sound absorbing materials exhibit higher sound absorbing performance at low frequency, and higher density sound absorbing materials show the higher sound absorbing performance in entire frequency domain. However, the use of thin sound absorbing materials is much more economical when designing any material or building because it takes up less space to install. Also, the use of a low-density sound absorbing material can contribute greatly to enhance fuel efficiency in applications such as automobile driving. Therefore, the development of poroacoustic meta-absorbers that can get beyond reasonable bounds of conventional sound absorbing materials is capable of leading to a very innovative advance in the field of NVH (noise, vibration, and harness) control.

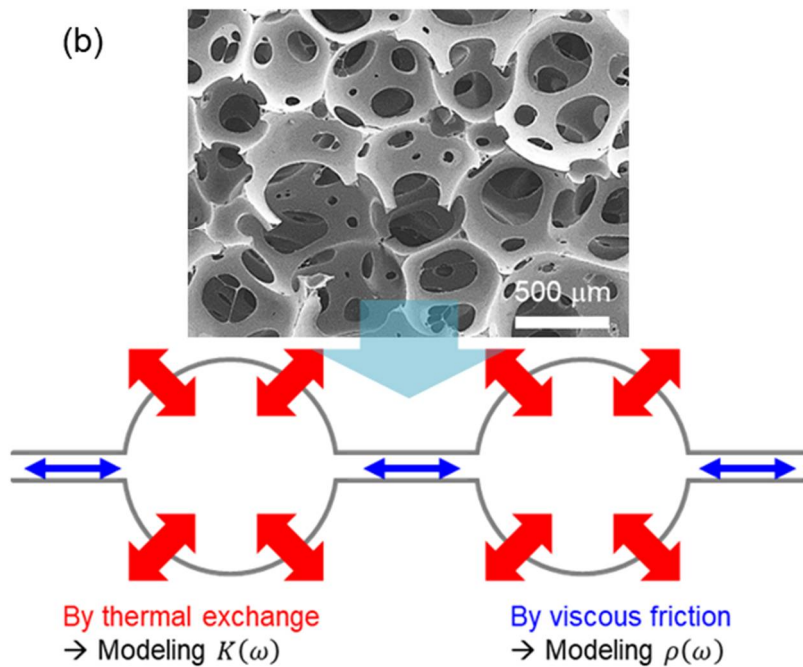
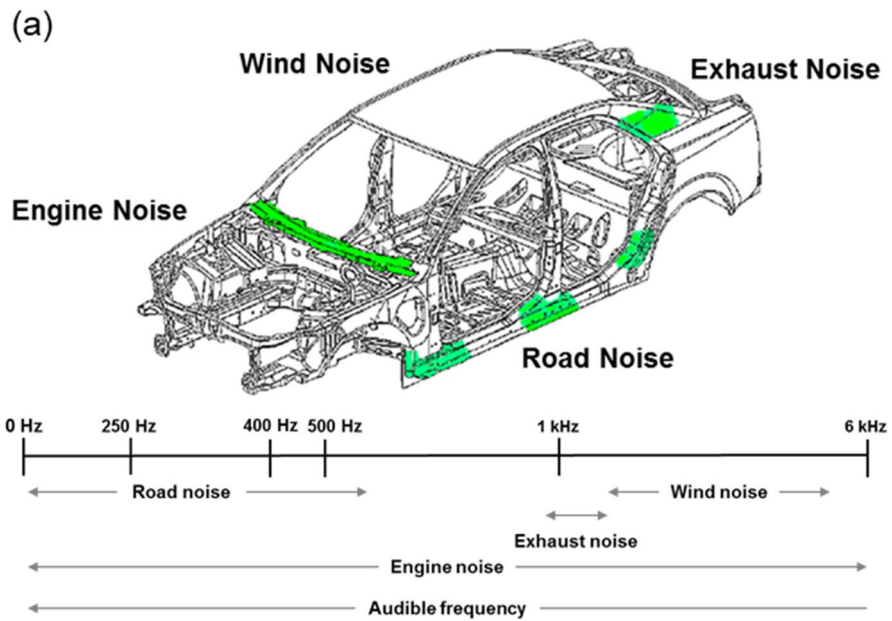


**Figure 1.2.4.** Types of noise and sound absorption principle. (a) Noises generated on automobiles while driving and their frequencies. (b) Mechanism of sound absorption in porous media.

### **1.3. Objectives of present work**

Overall, this dissertation aims to present new insights into polymeric metamaterials. Three types of metamaterials are proposed in each chapter; polymeric rheological metamaterials in Chapter 2, shape memory polymeric metasurfaces in Chapter 3, and polymeric poroacoustic meta-absorbers in Chapter 4. Strategies for developing the metamaterials were established based on the background knowledge which is demonstrated in Chapter 1.

The rheological metamaterials provide a source of technology that demonstrates the possibility of manipulating fluid momentum such as detour or coalescence by effective viscosity control. Development of the shape memory polymeric metasurfaces was aimed at imparting smart functions to the nanostructured materials to resolve the mechanical vulnerability. The polymeric poroacoustic meta-absorbers were expected to overcome the mass density limit of sound absorbing foams through microcellular structure control.

Based on the strategic approaches, novel metamaterials were synthesized, designed, manufactured, and analyzed to confirm whether the desired phenomena are implemented and what novel features appear. To validate the obtained experimental results, the underlying mechanisms and discussion about such phenomena were specifically presented by carrying out numerical analyses based on a finite element method. Finally, limitations, potential applications, and follow-up studies of the developed metamaterials are presented.

# Chapter 2.

## Polymeric Rheological Metamaterials

### 2.1. Overview

In this chapter, rheological metamaterials made of precisely designed polymeric microstructures are proposed, which modulate fluid fluxes by fluidic space distortion. The fluidic spaces required for a cloak, a concentrator, and a rotator were mathematically developed, and the corresponding metamaterials were designed and experimentally realized.

In Section 2.2, transformation rheology based on Navier-Stokes equations was mathematically developed by transforming fluidic coordinate systems. After defining the coordinate systems, a form invariance of the Navier-Stokes equations was proved by using divergence theorem. Transformed Navier-Stokes equations were derived as a result of the mathematical process. The most important finding in this section is that the information on spatial deformation of coordinate systems can be applied to fluidic viscosity, deriving a transformed viscosity tensor.

Drag-free technology to preclude drag on objects in a flowing fluid has long been a dream of scientists and engineers involved in fluid mechanics. Recently, transformation optics has provided mathematical solutions and ways to design metamaterials that steer energy fields. In Section 2.3, a rheological metamaterial cloak that conceals an object from fluid momentum was devised based on transformation theory. Transformation rheology developed in Section 2.2 yielded a transformed viscosity tensor for cloaking a fluidic space. The rheological metamaterial cloak was designed by mapping effective viscosity unit cells and fabricated as a microfluidic device. Numerical simulation and experiments confirmed that the metamaterial cloak can render a drag-free space in it. The rheological cloak will offer a systematic strategy that can manipulate fluid dynamic behavior which is not found in nature.

Hydropower is a means of harvesting energy from a fast flowing fluid. The technology of condensing hydraulic forces is a long-felt desire of engineers involved in fluid mechanics for efficient electricity production. In Section 2.4, a rheological metamaterial concentrator was demonstrated that focuses a hydraulic energy in the desired space. A mathematical solution for compressing a fluidic space, *i.e.*, a transformed viscosity tensor, was derived from transformation rheology. Numerical simulations were performed to theoretically visualize and demonstrate the concentrated pressure and velocity fields. The metamaterial concentrator was designed by mapping the unit cells that implement the transformed viscosity tensor as effective values, and it was numerically simulated, fabricated, and experimentally characterized. The rheological metamaterial concentrator developed in this section is expected to help dramatically improve the efficiency of energy harvesting of hydroelectricity.

An energy field rotator is a class of metamaterials that change direction of energy. In Section 2.5, a rheological metamaterial rotator was developed, which can control the direction of fluid flow differently from the direction of a given pressure field. Transformed viscosity tensors for rotating fluid flows by  $180^\circ$ ,  $90^\circ$ , and  $30^\circ$  were calculated from transformation rheology. Three rotators were numerically simulated and the pressure and velocity fields were analyzed numerically. The metamaterial rotator was designed by mapping the unit cells that have effective anisotropic viscosity, and experimentally characterized. The rheological metamaterial rotator has the potential to develop a disaster prevention technique that can change the direction of hydrological and meteorological disasters.



## 2.2. Transformation rheology

### 2.2.1. Introduction

Transformation optics [8,9,138] has offered great flexibility for manipulating electromagnetic waves and presented groundbreaking solutions for how to design metamaterials. This theory could be established by a form invariance of Maxwell's equations under curvilinear coordinate transformations between different spaces [36]. The transformation approach has been translated into other physics, such as acoustics, thermodynamics, electrostatics, and quantum mechanics. For transformation physics to operate, the underlying equations of each physics, *i.e.*, Helmholtz equation, Schrodinger equation, and heat conduction equation, should be form invariant under coordinate transformations.

Transformation acoustics was reported by calculating a coordinate-transformed bulk modulus and mass density of air [42,139]. Transformation quantum mechanics was developed by yielding an effective mass tensor [44]. Development of transformation thermodynamics involved the derivation of spatially inhomogeneous and anisotropic heat conductivity tensors [45]. Notwithstanding, metamaterials for fluid flow control have rarely been reported except for a few papers. In a previous study [48], a porous flow cloak was devised only theoretically by exploiting a transformed permeability tensor in Darcy's pressure equation. However, as the authors mentioned in the paper, the transformed permeability tensor is unable to be experimentally implemented due to extremely varying anisotropic components.

As a governing equation for fluid dynamics, Navier-Stokes equations describe the motion of Newtonian fluids with the assumption that the stresses in a fluid consist of a diffusing viscous term and a pressure term [140]. Fluidic viscosity is a major material parameter of the equations that determines fluid flow. These equations are Poisson's equations which are partial differential equations of elliptic type, mathematically similar with the Maxwell's equations for transformation optics. Hence, if the Navier-Stokes equations are form invariant under coordinate transformations, a spatially varying viscosity tensor can materialize rheological metamaterials that embody artificial fictitious fluidic

spaces inside them.

In this section, transformation rheology was developed, as a mathematical design tool of fluidic spaces. After defining bases of coordinate systems and transformation coordinates, a coordinate transformation for the divergence of the stress tensor was figured out. Using the found relationship, transformed Navier-Stokes equations were mathematically derived based on their form invariance. As a result, a mathematical relationship was demonstrated that viscosity as a rheological characteristic of fluids should be set to a tensor form depending on the space distortion.

## 2.2.2. Theoretical background

### 2.2.2.1. Coordinate transformation

A coordinate system is a system that uniquely determines the location of geometric elements on Euclidean space. As the simplest example, a Cartesian coordinate system, *i.e.*, a rectangular coordinate system, is the most commonly used system with three mutually perpendicular coordinate axes,  $x$ ,  $y$ , and  $z$  axes. There are also other coordinate systems such as a polar coordinate system, a cylindrical coordinate system, and a spherical coordinate system.

Coordinate transformation is a mathematical method for representing points in different coordinate systems when they are given in a coordinate system. This method has two uses: to change only the coordinate system in the same space and to display the deformed space with the same coordinate system. Industrial applications of the coordinate transformation method include numerical modeling of an injection molding process, which simulates the flow of polymer melts deforming in real time.

The bases of coordinate transformation should be established before the development of transformation rheology. The definitions about coordinate transformation, which are described in the Pu Zhang's dissertation [141], were referred to this section. The usage of index should be stated in order to avoid confusion caused by the error of index notations. A single index is generally intended to represent the entire set of physical quantities by taking all possible index values, 1, 2, and 3. A same index that occurs twice is the sum of the indices on all possible values by following the Einstein summation notation. In mathematical description, such as linear algebra and physics, the Einstein notation achieves simplicity of the index notation because this rule implies the sum over a set of index terms in a formula [33].

Mathematically, transformation physics has a basis for the relationship between physical quantities in two different spaces. The coordinate systems of two spaces do not obey how they transform. Therefore, the Cartesian coordinate system was selected as a base coordinate system for achieving the simplicity. Two spaces are named as a physical space and a virtual space, and their physical quantities are coded with or without a prime symbol ( $'$ ), orderly. For example,  $\tilde{\mathbf{x}}'$  is a vector in the physical space and  $\tilde{\mathbf{x}}$  is a vector in the

virtual space. For convenience of notation, the coordinate system in the physical space is also represented by a new coordinate system and the coordinate system in the virtual space is expressed to an old coordinate system.

A position vector is a Euclidean vector that indicates the position of a point  $P$  related to a reference origin  $O$  [142]. It correlates to the straight line distance and direction between the origin  $O$  and the point  $P$ . Let's define a position vector in the virtual space as  $\tilde{\mathbf{r}}$ . Then a position vector in the physical space is expressed with the prime symbol as  $\tilde{\mathbf{r}}' = \tilde{\mathbf{r}}'(\tilde{\mathbf{r}})$ . Each position vector is composed of a contravariant component ( $p^i$  or  $p'^i$ ) and a unit covariant vectors ( $\tilde{\mathbf{x}}_i$ ) as

$$\tilde{\mathbf{r}} = p^i \tilde{\mathbf{x}}_i \quad (2.2.1)$$

$$\tilde{\mathbf{r}}' = p'^i \tilde{\mathbf{x}}'_i \quad (2.2.2)$$

In **Eqns. 2.2.1-2**, the contravariant components have the transformation relationship as  $p'^i(p^1, p^2, p^3)$ .

A physical quantity of space has a different component depending on coordinate systems, and a connection between them are established through coordinate-independent elements such as a Jacobian matrix. With the unit vector  $\tilde{\mathbf{r}}$  as a example vector, the relationship between the two spaces can be defined by using a chain rule of derivative as

$$\tilde{\mathbf{x}}_i = \frac{\partial \tilde{\mathbf{r}}}{\partial p^i} = \frac{\partial \tilde{\mathbf{r}}}{\partial p'^j} \frac{\partial p'^j}{\partial p^i} = \frac{\partial p'^j}{\partial p^i} \tilde{\mathbf{x}}'_j \quad (2.2.3)$$

In the relationship above (**Eqn. 2.2.3**), the Jacobian matrix ( $\Lambda$ ) is defined as a set of the derivatives which connect the two unit vectors  $\tilde{\mathbf{x}}_i$  and  $\tilde{\mathbf{x}}'_j$ .

$$\Lambda = \Lambda_i^{j'} = \frac{\partial p'^j}{\partial p^i} \quad (2.2.4)$$

In this chapter, the Jacobian matrix ( $\Lambda$ ) as a backward transformation matrix was used, which transforms a coordinate basis from new (the physical space) to old (the virtual space). In the meanwhile, the new coordinate system (the physical space) can also be obtained by

using a forward transformation matrix  $(\Lambda_{i'}^j)$ , which transforms the coordinate system from an old basis to a new basis like

$$\widetilde{x}^i = \Lambda_{i'}^j \widetilde{x}^j \quad (2.2.5)$$

### 2.2.2.2. Navier-Stokes equations

Navier-Stokes equations describe the motion of Newtonian fluids with the assumption that the stresses in a fluid consist of a diffusing viscous term and a pressure term [140]. These equations were named after Claude-Louis Navier and George Gabriel Stokes and produced by applying the Newton's second law to fluid motion. The solution of the Navier-Stokes equations is the fluid velocity and it is also calculated in other forms such as pressure, energy, or temperature.

The Navier-Stokes equations have been applied for practical uses in many academic and industrial fields. There are some examples of the applications; prediction of weather and ocean states, design of automobiles and airplanes, and pipeline design for factory establishment. Meanwhile, in mathematical concerns, the Navier-Stokes equations have not yet been proven in three dimensions without any mathematical singularity, although these equations have been extensively used to describe and predict fluid dynamic and rheological phenomena. It is called the existence and smoothness problems of Navier–Stokes equations.

The Navier-Stokes equations consist of two differential equations for balances, the momentum equation for a force balance (**Eqn. 2.2.6**) and the continuity equation for a mass balance (**Eqn. 2.2.7**). These equations are expressed in vector differential forms as

$$\frac{\partial}{\partial t}(\rho \widetilde{\mathbf{u}}) + \nabla \cdot (\rho \widetilde{\mathbf{u}} \otimes \widetilde{\mathbf{u}}) = \nabla \cdot (\widetilde{\boldsymbol{\tau}} - p \widetilde{\boldsymbol{\delta}}) + \rho \widetilde{\mathbf{g}} \quad (2.2.6)$$

$$\frac{\partial \rho}{\partial t} + \nabla \cdot (\rho \widetilde{\mathbf{u}}) = 0 \quad (2.2.7)$$

,where  $\nabla$  is the nabla operator,  $\rho$  is the mass density of a fluid,  $\tilde{\mathbf{u}}$  is the velocity field,  $\tilde{\boldsymbol{\tau}}$  is the deviatoric stress tensor (second order),  $p$  is the hydrostatic pressure,  $\tilde{\boldsymbol{\delta}}$  is the unit identity tensor,  $\tilde{\mathbf{g}}$  is the term about body acceleration (generally, gravity),  $\otimes$  is the tensor product,  $\cdot$  is the scalar product symbol, and  $t$  is the time.

The momentum equation (**Eqn. 2.2.6**) is another form of the Cauchy momentum equation which is a partial differential equation (PDE) to account for nonrelativistic momentum transfer in continuum media. Each term in the momentum balance equation indicates following meanings per unit volume;  $\partial(\rho\tilde{\mathbf{u}})/\partial t$  is the increase rate of momentum,  $\nabla \cdot (\rho\tilde{\mathbf{u}}\otimes\tilde{\mathbf{u}})$  is the rate of momentum added by convection,  $\nabla \cdot (\tilde{\boldsymbol{\tau}} - p\tilde{\boldsymbol{\delta}})$  means the rate of momentum added by molecular transport, and  $\rho\tilde{\mathbf{g}}$  is the external force term acting on a fluid. The left-hand-side (LHS) of **Eqn. 2.2.6** describes acceleration of a fluid, which is composed of transient and convective values. In the meanwhile, the right-hand-side (RHS) of **Eqn. 2.2.6** is the summation of force terms such as a hydrostatic force, divergence of the deviatoric stress, and a gravity force. The continuity equation is developed by a mass balance over unit volume.  $\partial\rho/\partial t$  is the increase rate of mass per unit volume and  $\nabla \cdot (\rho\tilde{\mathbf{u}})$  is the net mass rate added by convection in unit volume.

By assuming an incompressible fluid and no external forces, the Navier-Stokes equations can be simplified by neglecting the inertia term ( $\nabla \cdot (\rho\tilde{\mathbf{u}}\otimes\tilde{\mathbf{u}})$ ), the term about time-derivative of density ( $\tilde{\mathbf{u}}(\partial\rho/\partial t)$ ), and the external force term ( $\rho\tilde{\mathbf{g}}$ ).

$$\nabla \cdot \tilde{\boldsymbol{\tau}} = \nabla p + \rho \frac{\partial \tilde{\mathbf{u}}}{\partial t} \quad (2.2.8)$$

$$\nabla \cdot \tilde{\mathbf{u}} = 0 \quad (2.2.9)$$

The simplified form of the momentum equation (**Eqn. 2.2.8**) originates from the assumption on the Cauchy stress tensor [143]. The stress tensor is Galilean invariant that depends only on the spatial derivative of flow velocity,  $\nabla\tilde{\mathbf{u}}$ . Therefore, the deviatoric stress term ( $\tilde{\boldsymbol{\tau}}$ ) of **Eqn. 2.2.8** can be expressed as

$$\tilde{\boldsymbol{\tau}} = 2\mu\tilde{\boldsymbol{\epsilon}} \quad (2.2.10)$$

,where  $\mu$  is the dynamic viscosity of a fluid and  $\tilde{\boldsymbol{\epsilon}}$  is the strain rate tensor defined as  $\tilde{\boldsymbol{\epsilon}} = (\nabla\tilde{\mathbf{u}} + \nabla\tilde{\mathbf{u}}^T)/2$ . Following this relationship, the Stokes' stress constitutive equation for incompressible viscous fluids can be represented as

$$\tilde{\boldsymbol{\tau}} = \mu(\nabla\tilde{\mathbf{u}} + \nabla\tilde{\mathbf{u}}^T) \quad (2.2.11)$$

## 2.2.3. Form invariance of Navier-Stokes equations

### 2.2.3.1. Coordinate transformation of tensor divergence

For transformation optics, curl and divergence of vector fields of the Maxwell's equations should be defined under curvilinear coordinate transformations. Hence, for development of transformation optics, the researchers attempted to prove the form invariance of the Maxwell's equations by using Kelvin-Stokes theorem and divergence theorem. Unfortunately, this mathematical approach cannot be directly applied to transformation rheology based on the Navier-Stokes equations since the momentum equation (**Eqn. 2.2.8**) contains the divergence of the second order stress tensor ( $\nabla \cdot \tilde{\boldsymbol{\tau}}$ ), unlike the curl or divergence of the first-order tensors.

Accordingly, the coordinate transformation of the divergence of the stress tensor is defined in this section. To prove that, a new set of the stress tensor was constructed in the new coordinate system (the physical space). The transformation medium is designated as a new set in the physical space. The index form of the stress tensor is defined as  $\tilde{\boldsymbol{\tau}} = \tau^{ij}x_i x_j$  in the old coordinate system and  $\tilde{\boldsymbol{\tau}}' = \tau'^{ij}x'_i x'_j$  in the new coordinate system.

The target point is to figure out the relationship parameter of the divergence of the stress tensor between the old and new coordinate systems. The proof process started with the divergence theorem, similar to the case of transformation optics, except for the order of tensor. By the divergence theorem, the divergence of the stress tensor can be expressed by following integral formation.

$$\iint_s \tilde{\boldsymbol{\tau}} \cdot d\tilde{\boldsymbol{s}} = \iiint_V \nabla \cdot \tilde{\boldsymbol{\tau}} dV \quad (2.2.12)$$

,where  $\tilde{\boldsymbol{s}}$  is the surface vector and  $V$  is the volume of an arbitrary three dimensional unit element as shown in **Fig. 2.2.1**. If the surface integration is considered about the unit element, the left-hand-side of **Eqn. 2.2.12** can be transformed as



$$\begin{aligned}
\iint_S \tilde{\mathbf{t}} \cdot d\tilde{\mathbf{s}} &= dp'^3 \frac{\partial}{\partial p'^3} [\tilde{\mathbf{t}} \cdot (\tilde{\mathbf{x}}'_1 \partial p'^1 \times \tilde{\mathbf{x}}'_2 \partial p'^2)] + dp'^1 \frac{\partial}{\partial p'^1} [\tilde{\mathbf{t}} \cdot (\tilde{\mathbf{x}}'_2 \partial p'^2 \times \tilde{\mathbf{x}}'_3 \partial p'^3)] \\
&\quad + dp'^2 \frac{\partial}{\partial p'^2} [\tilde{\mathbf{t}} \cdot (\tilde{\mathbf{x}}'_3 \partial p'^3 \times \tilde{\mathbf{x}}'_1 \partial p'^1)] \\
&= \left[ \frac{\partial \tilde{\mathbf{t}} \cdot (\tilde{\mathbf{x}}'_1 \times \tilde{\mathbf{x}}'_2)}{\partial p'^3} + \frac{\partial \tilde{\mathbf{t}} \cdot (\tilde{\mathbf{x}}'_2 \times \tilde{\mathbf{x}}'_3)}{\partial p'^1} + \frac{\partial \tilde{\mathbf{t}} \cdot (\tilde{\mathbf{x}}'_3 \times \tilde{\mathbf{x}}'_1)}{\partial p'^2} \right] \partial p'^1 \partial p'^2 \partial p'^3 \\
&= \left[ \frac{\partial \tau'^{3i} \tilde{\mathbf{x}}'_i \tilde{\mathbf{x}}'_3 \cdot (\tilde{\mathbf{x}}'_1 \times \tilde{\mathbf{x}}'_2)}{\partial p'^3} + \frac{\partial \tau'^{1j} \tilde{\mathbf{x}}'_j \tilde{\mathbf{x}}'_1 \cdot (\tilde{\mathbf{x}}'_2 \times \tilde{\mathbf{x}}'_3)}{\partial p'^1} + \frac{\partial \tau'^{2k} \tilde{\mathbf{x}}'_k \tilde{\mathbf{x}}'_2 \cdot (\tilde{\mathbf{x}}'_3 \times \tilde{\mathbf{x}}'_1)}{\partial p'^2} \right] \partial p'^1 \partial p'^2 \partial p'^3 \\
&= \left[ \frac{\partial \tau'^{3i} \tilde{\mathbf{x}}'_i \det(\mathbf{\Lambda}^{-1})}{\partial p'^3} + \frac{\partial \tau'^{1j} \tilde{\mathbf{x}}'_j \det(\mathbf{\Lambda}^{-1})}{\partial p'^1} + \frac{\partial \tau'^{2k} \tilde{\mathbf{x}}'_k \det(\mathbf{\Lambda}^{-1})}{\partial p'^2} \right] \partial p'^1 \partial p'^2 \partial p'^3 \\
&= \nabla \cdot \tilde{\mathbf{t}}' \partial p'^1 \partial p'^2 \partial p'^3 \tag{2.2.13}
\end{aligned}$$

The right-hand-side of **Eqn. 2.2.12** which describes the volumetric integral of the element can be expressed as

$$\begin{aligned}
\iiint_V \nabla \cdot \tilde{\mathbf{t}} dV &= \tilde{\mathbf{x}}'_1 dp'^1 \cdot (\tilde{\mathbf{x}}'_2 dp'^2 \times \tilde{\mathbf{x}}'_3 dp'^3) \nabla \cdot \tilde{\mathbf{t}} \\
&= \tilde{\mathbf{x}}'_1 \cdot (\tilde{\mathbf{x}}'_2 \times \tilde{\mathbf{x}}'_3) \nabla \cdot \tilde{\mathbf{t}} \partial p'^1 \partial p'^2 \partial p'^3 \\
&= \nabla \cdot \tilde{\mathbf{t}} \det(\mathbf{\Lambda}^{-1}) \partial p'^1 \partial p'^2 \partial p'^3 \tag{2.2.14}
\end{aligned}$$

Consequently, from the mathematical processes above (**Eqns. 2.2.13-14**), the following relationship was obtained.

$$\nabla \cdot \tilde{\mathbf{t}} = (\det(\mathbf{\Lambda}) \mathbf{\Lambda}^{-1}) \nabla' \cdot \tilde{\mathbf{t}}' \tag{2.2.15}$$

,where the coordinate transformation of the del operator ( $\nabla$ ) is defined as  $\nabla = \mathbf{\Lambda}^{-1} \nabla'$ . Therefore, the divergence of the stress tensor in the physical space (new coordinate system)

is defined by using the equation in the virtual space (old coordinate system) as

$$\nabla' \cdot \tilde{\boldsymbol{\tau}} = \det(\boldsymbol{\Lambda}^{-1}) \boldsymbol{\Lambda} \nabla \cdot \tilde{\boldsymbol{\tau}} \quad (2.2.16)$$

The meaning of **Eqn. 2.2.16** is that the tensor divergence term in the new coordinate system is derived by multiplying  $\det(\boldsymbol{\Lambda}^{-1}) \boldsymbol{\Lambda}$  to the term in the old coordinate system.

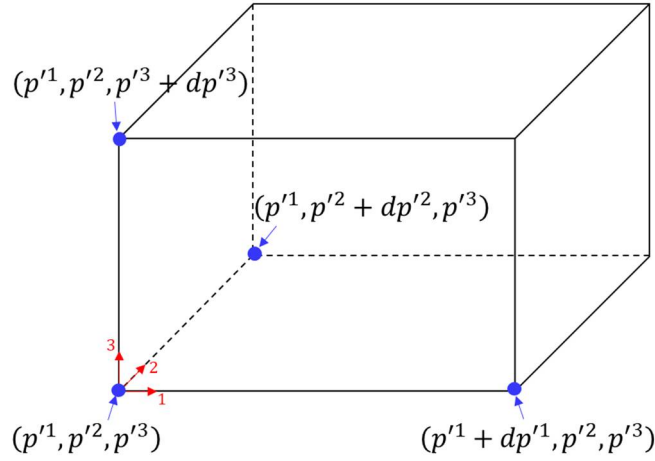


**Figure 2.2.1.** Three dimensional differential integration element. it is the modified figure of Fig. 2.3 in ref. [141].

### 2.2.3.2. Transformed viscosity tensor

In the previous sections, the relationship of the divergence of the stress tensor between two coordinate systems was proved in the three dimensional unit element. The next step is to derive transformed Navier-Stokes equations which are established in the physical space and to figure out which is a material parameter to be transformed into a tensor form. A spatial transformation must be reflected in different material properties depending on the physical phenomena targeted. For example, transformation optics require a spatial variation in permeability and permittivity, thermal conductivity in transformation thermodynamics, and mass density and bulk modulus in transformation acoustics.

At first, the divergence of the stress tensor of **Eqn. 2.2.8** is expressed in the new coordinate system with the relationship parameter  $(\det(\mathbf{\Lambda}^{-1})\mathbf{\Lambda})$ ,

$$\nabla' \cdot \tilde{\boldsymbol{\tau}} = \det(\mathbf{\Lambda}^{-1})\mathbf{\Lambda}\nabla p + \det(\mathbf{\Lambda}^{-1})\mathbf{\Lambda}\rho \frac{\partial \tilde{\mathbf{u}}}{\partial t} \quad (2.2.17)$$

The right-hand-side of **Eqn. 2.2.17** can be changed with the pressure gradient and velocity terms in the new coordinate system as  $\nabla p = \mathbf{\Lambda}^T \nabla' p$  and  $\tilde{\mathbf{u}} = \det(\mathbf{\Lambda})\mathbf{\Lambda}^{-1}\mathbf{u}$ , orderly.

$$\nabla' \cdot \tilde{\boldsymbol{\tau}} = \det(\mathbf{\Lambda}^{-1})\mathbf{\Lambda}\mathbf{\Lambda}^T \nabla' p + \det(\mathbf{\Lambda}^{-1})\mathbf{\Lambda}\rho \det(\mathbf{\Lambda})\mathbf{\Lambda}^{-1} \frac{\partial \tilde{\mathbf{u}}}{\partial t} \quad (2.2.18)$$

By the relationships of  $\det(\mathbf{\Lambda}^{-1})\det(\mathbf{\Lambda})=\tilde{\boldsymbol{\delta}}$  and  $\mathbf{\Lambda}\mathbf{\Lambda}^{-1} = \tilde{\boldsymbol{\delta}}$ , **Eqn. 2.2.18** can be simplified as

$$\nabla' \cdot \tilde{\boldsymbol{\tau}} = \det(\mathbf{\Lambda}^{-1})\mathbf{\Lambda}\mathbf{\Lambda}^T \nabla' p + \rho \frac{\partial \tilde{\mathbf{u}}}{\partial t} \quad (2.2.19)$$

Meanwhile, the stress tensor in the physical space ( $\tilde{\boldsymbol{\tau}}$ ) in **Eqn. 2.2.19** can be expressed with the stress tensor in the virtual space ( $\tilde{\boldsymbol{\tau}}$ ) as

$$\nabla' \cdot \tilde{\boldsymbol{\tau}} = \nabla' \cdot (\det(\mathbf{\Lambda}^{-1})\mathbf{\Lambda}\tilde{\boldsymbol{\tau}}\mathbf{\Lambda}^T) \quad (2.2.20)$$

The stress tensor in the virtual space ( $\tilde{\boldsymbol{\tau}}$ ) of **Eqn. 2.2.20** can be stated as the Stokes' stress constitutive equation like

$$\nabla' \cdot \tilde{\boldsymbol{\tau}} = \nabla' \cdot (\det(\mathbf{\Lambda}^{-1})\mathbf{\Lambda}\mu(\nabla\tilde{\mathbf{u}} + \nabla\tilde{\mathbf{u}}^T)\mathbf{\Lambda}^T) \quad (2.2.21)$$

The derivative of the velocity term in the virtual space ( $\nabla\tilde{\mathbf{u}}$ ) in **Eqn. 2.2.21**, *i.e.*, the strain rate tensor term ( $\tilde{\boldsymbol{\epsilon}}$ ), can be replaced with the derivative of the velocity term in the physical space ( $\nabla'\tilde{\mathbf{u}}$ , equal to  $\tilde{\boldsymbol{\epsilon}}$ ) by the relationship of  $(\nabla\tilde{\mathbf{u}} + \nabla\tilde{\mathbf{u}}^T) = \mathbf{\Lambda}^{-1}(\nabla'\tilde{\mathbf{u}} + \nabla'\tilde{\mathbf{u}}^T)\mathbf{\Lambda}^{-T}\det(\mathbf{\Lambda})$ .

$$\nabla' \cdot \tilde{\boldsymbol{\tau}}' = \nabla' \cdot \left( \det(\boldsymbol{\Lambda}^{-1}) \boldsymbol{\Lambda} \mu \boldsymbol{\Lambda}^{-1} \left( \nabla' \tilde{\mathbf{u}}' + \nabla' \tilde{\mathbf{u}}'^T \right) \boldsymbol{\Lambda}^{-T} \det(\boldsymbol{\Lambda}) \boldsymbol{\Lambda}^T \right) \quad (2.2.22)$$

The right-hand-side of **Eqn. 2.2.22** can be simplified by offsetting the Jacobian matrix terms as

$$\nabla' \cdot \tilde{\boldsymbol{\tau}}' = \nabla' \cdot \left( \mu \left( \nabla' \tilde{\mathbf{u}}' + \nabla' \tilde{\mathbf{u}}'^T \right) \right) \quad (2.2.23)$$

By combining **Eqns. 2.2.19** and **2.2.23**, the following relationship is accomplished.

$$\nabla' \cdot \left( \mu \left( \nabla' \tilde{\mathbf{u}}' + \nabla' \tilde{\mathbf{u}}'^T \right) \right) = \det(\boldsymbol{\Lambda}^{-1}) \boldsymbol{\Lambda} \boldsymbol{\Lambda}^T \nabla' p + \rho \frac{\partial \tilde{\mathbf{u}}'}{\partial t} \quad (2.2.24)$$

If the inverse matrix of the term of  $\det(\boldsymbol{\Lambda}^{-1}) \boldsymbol{\Lambda} \boldsymbol{\Lambda}^T$ , *i.e.*,  $\det(\boldsymbol{\Lambda}) \boldsymbol{\Lambda}^{-1} \boldsymbol{\Lambda}^{-T}$ , is multiplied on both sides of **Eqn. 2.2.24**, the following equation is yielded.

$$\nabla' \cdot \left( \det(\boldsymbol{\Lambda}) \boldsymbol{\Lambda}^{-1} \mu \boldsymbol{\Lambda}^{-T} \left( \nabla' \tilde{\mathbf{u}}' + \nabla' \tilde{\mathbf{u}}'^T \right) \right) = \nabla' p + \det(\boldsymbol{\Lambda}) \boldsymbol{\Lambda}^{-1} \rho \boldsymbol{\Lambda}^{-T} \frac{\partial \tilde{\mathbf{u}}'}{\partial t} \quad (2.2.25)$$

Finally, the momentum equation in the physical space is derived with the transformed parameters as

$$\nabla' \cdot \left( \tilde{\boldsymbol{\mu}}' \cdot \left( \nabla' \tilde{\mathbf{u}}' + \nabla' \tilde{\mathbf{u}}'^T \right) \right) = \nabla' p + \tilde{\boldsymbol{\rho}}' \cdot \frac{\partial \tilde{\mathbf{u}}'}{\partial t} \quad (2.2.26)$$

,where  $\tilde{\boldsymbol{\mu}}'$  and  $\tilde{\boldsymbol{\rho}}'$  are the fluid viscosity and fluid mass density as a form of the 2nd-order tensor defined as

$$\tilde{\boldsymbol{\mu}}' = \det(\boldsymbol{\Lambda}) \boldsymbol{\Lambda}^{-1} \mu \boldsymbol{\Lambda}^{-T} \quad (2.2.27)$$

$$\tilde{\boldsymbol{\rho}}' = \det(\boldsymbol{\Lambda}) \boldsymbol{\Lambda}^{-1} \rho \boldsymbol{\Lambda}^{-T} \quad (2.2.28)$$

Meanwhile, a mathematical form of the mass balance equation in the physical space (**Eqn. 2.2.29**) is easily satisfied because this equation does not include a high order tensor term but only the velocity vector term.

$$\nabla' \cdot \widetilde{\mathbf{u}}' = 0 \quad (2.2.29)$$

The derived equations by the mathematical processes (**Eqns. 2.2.26** and **2.2.29**) are the transformed Navier-Stokes equations and this theory can be referred to as “transformation rheology” which means rheological theory for spatial distortion. In fact, transformation fluid-mechanics may be more appropriate denotation, but it was named as above taking into account the assumptions and experimental conditions to be demonstrated in later sections.

The most noteworthy feature in transformation rheology is that the fluid density ( $\rho$ ) and the fluid viscosity ( $\mu$ ) are no longer constants and are transformed into the tensor forms ( $\widetilde{\boldsymbol{\rho}}'$  and  $\widetilde{\boldsymbol{\mu}}'$  in **Eqns. 2.2.27-28**) with the Jacobian matrix ( $\Lambda$ ) for specific spatial deformation. Therefore, the two terms are intended to include position-dependent anisotropic components. Another significant point is that the transformed tensors are inversely related with the Jacobian matrix unlike the transformed material parameters developed in transformation optics.

Implementing both transformation parameters ( $\widetilde{\boldsymbol{\mu}}'$  and  $\widetilde{\boldsymbol{\rho}}'$ ) simultaneously is a very challenging experimental condition. Because of this difficulty, only one material parameter was considered in the development of the electromagnetic metamaterial cloak by using a polarized beam in experiment [28]. Therefore, **Equation 2.2.26** should be more simplified by assuming steady-state flow conditions in which the fluid state does not change at any point in the system, regardless of time. Then, the transient term in **Eqn. 2.2.26** ( $\widetilde{\boldsymbol{\rho}}' \cdot (\partial \widetilde{\mathbf{u}}' / \partial t)$ ) is neglected as

$$\nabla' \cdot \left( \widetilde{\boldsymbol{\mu}}' \cdot \left( \nabla' \widetilde{\mathbf{u}}' + \nabla' \widetilde{\mathbf{u}}'^T \right) \right) = \nabla' p \quad (2.2.30)$$

**Equation 2.2.30** is called the Stokes flow equation or the creeping flow equation. Stokes flow is a type of fluid flow with very small advective inertial forces compared to viscous forces. It is defined when Reynolds number ( $Re$ ) is much smaller than 1 ( $Re \ll 1$ ). This Reynolds number condition is established when fluid viscosity is very large, fluid velocity is very slow, or a length scale of fluid flow is micro- or nanoscale.

Design simplicity originates from the fact that the density tensor ( $\tilde{\rho}'$ ) is ignored and the mapping of the viscosity tensor ( $\tilde{\mu}'$ ) is only considered. Consequently, this simplified form of the transformed Navier-Stokes equations (**Eqns. 2.2.29-30**) was used in numerical simulation, design, fabrication, and characterization of all rheological metamaterials in this chapter. The specific tensor components of the transformed viscosity tensor ( $\tilde{\mu}'$ ) are derived in Sections 2.3-5 for each desired spatial deformation, *i.e.*, cloaking, concentrating, and rotating fluid flow.

#### **2.2.4. Conclusions**

In this section, a full mathematical proof process was demonstrated for the development of transformation rheology. The index notation and coordinate transformations were defined firstly. The physical quantities and tensors of each space were expressed by using a prime symbol to distinguish between the physical space (also coded as the new coordinate system) and the virtual space (the old coordinate system). The Jacobian matrix which bridges two spaces (or two coordinate systems) was defined by using a vector-differential expression. The Navier-Stokes equations were briefly explained and the form invariance of these equations was proved under coordinate transformations. Consequently, it was found that the transformed parameters in the transformed Navier-Stokes equations are the transformed viscosity and density tensors. By assuming the Stokes flow, the density tensor among the two transformed material parameters could be neglected, and the viscosity tensor could be considered as the only factor. In conclusion, a method of deriving the transformed viscosity tensor, which can lead to a distorted fluidic space, was established and proved.

## 2.3. Rheological cloak

### 2.3.1. Introduction

Drag is a hydrodynamic resistant force that acts on objects in the opposite direction of a flowing fluid. The drag force is greatly influenced by the velocity magnitude of the surrounding fluid [144] and this phenomenon corresponds to both laminar flow and turbulent flow. Such drag not only significantly reduces the fuel efficiency of vehicles such as automobiles, ships, and aircrafts but also occurs dangerous situations by inducing unpredictable flows while operating vehicles. In addition, natural disasters such as tsunamis and hurricanes are caused by generation of the drag to people or substances. Likewise, the fluidic drag is an inevitable issue in fluid dynamics applications. Hence, a drag-free technology to preclude drag on objects has long been a dream of scientists and engineers involved in fluid mechanics [145–147].

On the other hand, in the field of optics, transformation optics [8,9] has offered great flexibility for manipulating electromagnetic waves. It presents a groundbreaking mathematical solution for how to design a cloak which makes certain substances lying inside not to be recognized from the outside. Based on this theory, there have been a myriad of researches to design and materialize electromagnetic metamaterial cloaks by introducing spatially varying material parameters as a tensor form [28,36,148–152].

Transformation optics and metamaterials have been translated into other physics such as thermodynamics [25], acoustics [26], and quantum mechanics [44]. Each transformation physics applies a spatial transformation of coordinate systems to the material properties, in order to enable unprecedented behaviors for the correlating physical quantities. Especially, metamaterial cloaks aim to induce the spatial transformation that vacates a specific space and bypasses a physical quantity accordingly. Typically, the cloak for optics can make an object placed in it invisible outside. Inspired from these previous studies, transformation rheology was developed and described in Section 2.2 by deriving the form invariance of the Navier-Stokes equations under coordinate transformations with general tensor bases. Hence, a fluidic space defined by a coordinate-transformed viscosity tensor is assumed to



offer a rheological metamaterial cloak that embodies an artificial fictitious fluidic space in it.

In this section, a rheological metamaterial cloak is demonstrated from mathematics, numerical simulation, design of a metamaterial, to experimental realization. By using transformation rheology, a transformed viscosity tensor for cloaking was derived by calculating a Jacobian matrix which enables the desired fluidic space distortion. The function of the rheological cloak was theoretically shown by carrying out numerical simulation based on a finite element method. Unit cells that bring out anisotropic effective viscosity components were designed and constructed at microscale. The rheological metamaterial cloak was designed by mapping the unit cells and fabricated as a microfluidic device. Numerical simulation and experimental characterization of the designed rheological metamaterial cloak were performed to confirm that the cloak can precisely control fluid flow around the obstacle and render a drag-free space in it.

### 2.3.2. Fluidic space modeling

A basic concept of the rheological cloak is illustrated in **Fig. 2.3.1** with the expected pressure contours. The fluid flows as shown in **Fig. 2.3.1(a)** when there is nothing in it (a “bare” case). If an obstacle is situated in the fluid, it is subjected to a frictional force, the drag, as depicted in **Fig. 2.3.1(b)** (an “obstacle” case). We dreamed up a novel strategy to create a drag-free space by wrapping the obstacle in the rheological cloak. This strategy began with an idea that compressing a fluidic space from the cylindrical region ( $0 < r < b$ ) into the annular region ( $a < r' < b$ ) opens the “rheologically” empty space ( $0 < r' < a$ ) in the coordinate system (**Figs. 2.3.1(c-d)**). Regardless of the surrounding fluid flow, no fluid momentum is penetrated into the central empty space. The fluid flows as if nothing is present since the space where the object is placed becomes “rheologically” invisible. Hence, if the obstacle is concealed in the central drag-free space, the drag acting on the obstacle can be prevented (**Fig. 2.3.1(c)**, a “cloaked-obstacle” case). Even if only the obstacle is removed and the cloak is maintained, the surrounding fluid flow is not affected since the central space is empty (**Fig. 2.3.1(d)**, a “cloak-only” case).

A transformation matrix is a linear algebra term that describes the parameters of a linear coordinate transformation as a form of a Jacobian matrix. The Jacobian matrix is a matrix of first-order partial derivatives of a vector-valued function. To calculate the transformed viscosity tensor for a cloaking space, the transformation Jacobian matrix ( $\Lambda$ ) must be mathematically derived, which can mediate the desired spatial deformation. In previous studies, orthogonal coordinate transformations have been generally used for cloaking cylindrical or spherical regions since spatial transformations are possible with simple Jacobian matrices. Furthermore, a cylindrical cloak is much more convenient to achieve experimental realization than a spherical cloak, because of the few variables to be considered when transforming spaces.

Two more coordinate systems for cylindrical coordinate systems in the virtual ( $q^i$ ) and physical spaces ( $q'^i$ ) are needed to be introduced. If the relation between the two spaces is defined as  $q'^i = q'^i(q^1, q^2, q^3)$ , the Jacobian matrix connecting the two spaces ( $\lambda$ ) is specified as  $\lambda = \lambda_j^i = \partial q'^i / \partial q^j$ . Then, the four coordinate systems are established as  $p^i$  for the Cartesian coordinate system in the virtual space,  $q^i$  for the cylindrical coordinate

system in the virtual space,  $p'^i$  for the Cartesian coordinate system in the physical space, and  $q'^i$  for the cylindrical coordinate system in the physical space. Consequently, the total Jacobian matrix ( $\mathbf{\Lambda}$ ) defines the coordinate transformation in the order of  $p'^i \rightarrow q'^i \rightarrow q^i \rightarrow p^i$ , and is defined by a chain rule as,

$$\mathbf{\Lambda} = \left( \Lambda_j^{i'} \right) = \frac{\partial p'^i}{\partial p^j} = \frac{\partial p'^i}{\partial q'^k} \frac{\partial q'^k}{\partial p^j} = \frac{\partial p'^i}{\partial q'^k} \frac{\partial q'^k}{\partial q^l} \frac{\partial q^l}{\partial p^j} = \mathbf{B}'^{-1} \boldsymbol{\lambda} \mathbf{B} \quad (2.3.1)$$

, where  $\boldsymbol{\lambda} (= \lambda_j^{i'} = \partial q'^i / \partial q^j)$  is the Jacobian matrix between the two cylindrical coordinate systems ( $q'^i \rightarrow q^i$ ),  $\mathbf{B} (= \mathbf{B}_j^i = \partial q^i / \partial p^j)$  is the Jacobian matrix between the cylindrical coordinate system and the Cartesian coordinate system in the virtual space ( $q^i \rightarrow p^i$ ), and  $\mathbf{B}' (= \mathbf{B}'_j{}^{i'} = \partial q'^i / \partial p'^j)$  is the Jacobian matrix between the cylindrical coordinate system and the Cartesian coordinate system in the physical space ( $q'^i \rightarrow p'^i$ ). Specific derivation of the Jacobian matrices for spatial distortions, such as cloaking, concentrating, and rotating, is described in each section.

The essence of transformation rheology for the cloak is to compress a fluid dynamic force, *i.e.*, fluid momentum, of the virtual space into a specific area of the physical space. Simultaneously, outside the cloak owns the identity tensor as a transformation Jacobian matrix, resulting that no perturbation of fluid flow occurs in the physical space. Because of this spatial distortion, an object inside the cloak can be hidden from fluid stream without dragging.

Both  $\mathbf{B}$  and  $\boldsymbol{\lambda}$  should be calculated to obtain the  $\mathbf{\Lambda}$  matrix for the cylindrical cloak. Linear geometric transformation, the radial stretch, was assumed under a two-dimensional cylindrical case for space compression. The required transformation between the two spaces is represented by the coordinate grids in **Fig. 2.3.2**. One point in the virtual space expands to the circular region of the physical space ( $r' < a$ ), but the area outside the concentric circle ( $r' > b$ ) remains intact. When the inner radius was  $a$  and the outer radius was  $b$ , the transformation between the two spaces that compresses a space from the cylindrical region ( $0 < r < b$ ) into the annular region ( $a < r' < b$ ) is defined as,

$$r' = \left(\frac{b-a}{b}\right)r + a \quad (2.3.2)$$

$$\theta' = \theta \quad (2.3.3)$$

$$z' = z \quad (2.3.4)$$

Then, the Jacobian matrix for the radial stretch ( $\lambda$  for  $q'^i \rightarrow q^i$ ) is expressed in a matrix form as

$$\lambda = \begin{bmatrix} \frac{\partial r'}{\partial r} & \frac{\partial r'}{\partial \theta} & \frac{\partial r'}{\partial z} \\ \frac{\partial \theta'}{\partial r} & \frac{\partial \theta'}{\partial \theta} & \frac{\partial \theta'}{\partial z} \\ \frac{\partial z'}{\partial r} & \frac{\partial z'}{\partial \theta} & \frac{\partial z'}{\partial z} \end{bmatrix} = \begin{bmatrix} \frac{b-a}{b} & 0 & 0 \\ 0 & 1 & 0 \\ 0 & 0 & 1 \end{bmatrix} \quad (2.3.5)$$

Also, the relationship between the cylindrical coordinate system and the Cartesian coordinate system is defined as

$$r = \sqrt{x^2 + y^2}, \theta = \tan^{-1}(y/x), z = z \quad (2.3.6)$$

$$x = r\cos\theta, y = r\sin\theta, z = z \quad (2.3.7)$$

The corresponding Jacobian matrix for the backward transformation ( $\mathbf{B}$  for  $q^i \rightarrow p^i$ ) is specified as

$$\mathbf{B} = \begin{bmatrix} \frac{\partial r}{\partial x} & \frac{\partial r}{\partial y} & \frac{\partial r}{\partial z} \\ \frac{\partial \theta}{\partial x} & \frac{\partial \theta}{\partial y} & \frac{\partial \theta}{\partial z} \\ \frac{\partial z}{\partial x} & \frac{\partial z}{\partial y} & \frac{\partial z}{\partial z} \end{bmatrix} = \begin{bmatrix} \cos\theta & \sin\theta & 0 \\ -\frac{\sin\theta}{r} & \frac{\cos\theta}{r} & 0 \\ 0 & 0 & 1 \end{bmatrix} \quad (2.3.8)$$

Finally, the total Jacobian matrix for the cylindrical cloak and its determinant are obtained as

$$\mathbf{\Lambda} = \mathbf{B}'^{-1} \boldsymbol{\lambda} \mathbf{B} = \begin{bmatrix} \frac{b-a}{b} & 0 & 0 \\ 0 & \frac{r'}{r} & 0 \\ 0 & 0 & 1 \end{bmatrix} \quad (2.3.9)$$

$$\det(\mathbf{\Lambda}) = \left(\frac{b-a}{b}\right) \left(\frac{r'}{r}\right) \quad (2.3.10)$$

Alternatively, the equations above (**Eqns. 2.3.9-10**) can also be derived by calculating a metric tensor ( $\tilde{\mathbf{g}}$ ) of **Eqn. 2.3.8**. The metric tensor is calculated as

$$\tilde{\mathbf{g}} = (\mathbf{B}\mathbf{B}^T)^{-1} = \begin{bmatrix} 1 & 0 & 0 \\ 0 & r^2 & 0 \\ 0 & 0 & 1 \end{bmatrix} \quad (2.3.11)$$

Then, the total Jacobian matrix for the cylindrical cloak ( $\mathbf{\Lambda}$ ) is obtained with the metric tensor by following relationship.

$$\mathbf{\Lambda} = \tilde{\mathbf{g}}'^{-1/2} \boldsymbol{\lambda} \tilde{\mathbf{g}}^{1/2} = \begin{bmatrix} \frac{b-a}{b} & 0 & 0 \\ 0 & \frac{r'}{r} & 0 \\ 0 & 0 & 1 \end{bmatrix} \quad (2.3.12)$$

The total Jacobian matrix and its determinant ( $\mathbf{\Lambda}$  and  $\det(\mathbf{\Lambda})$ ) can be fully described in terms of the physical space variable ( $r'$ ) by removing the radial variable in the virtual space ( $r$ ).

$$\mathbf{\Lambda} = \begin{bmatrix} \frac{b-a}{b} & 0 & 0 \\ 0 & \left(\frac{r'}{r'-a}\right) \left(\frac{b-a}{b}\right) & 0 \\ 0 & 0 & 1 \end{bmatrix} \quad (2.3.13)$$

$$\det(\mathbf{\Lambda}) = \left(\frac{b-a}{b}\right)^2 \left(\frac{r'}{r'-a}\right) \quad (2.3.14)$$

All pieces required for deriving the transformed viscosity tensor were prepared. For feasible experimental implementation, the steady-state Stokes flow equations (**Eqns. 2.2.29-30**) were chosen not to take into account the mapping of the fluidic density tensor. Following **Eqn. 2.2.27**, the transformed viscosity tensor for the cloak is defined as

$$\tilde{\boldsymbol{\mu}}' = \det(\boldsymbol{\Lambda})\boldsymbol{\Lambda}^{-1}\boldsymbol{\mu}\boldsymbol{\Lambda}^{-T} = \begin{bmatrix} \frac{r'}{r'-a} & 0 & 0 \\ 0 & \frac{r'-a}{r'} & 0 \\ 0 & 0 & \left(\frac{b-a}{b}\right)^2 \left(\frac{r'}{r'-a}\right) \end{bmatrix} \boldsymbol{\mu} \quad (2.3.15)$$

The transformed viscosity tensor for the ideal case ( $\tilde{\boldsymbol{\mu}}'$  in **Eqn. 2.3.15**) is very difficult to be experimentally achieved since the tensor components have infinite values at specific positions of  $r' = a$  and  $r' = 0$  and vary extremely in each principal axial direction. In other words, a matrix singularity of **Eqn. 2.3.15** strictly hinders the design and fabrication of the cloak based on the ideal parameters. Instead of, a “reduced” set of the material parameters has been considered to mitigate this condition in the previous studies [25,28]. The reduced transformed viscosity tensor ( $\tilde{\tilde{\boldsymbol{\mu}}}'$  in **Eqn. 2.3.16**) is obtained by multiplying  $\tilde{\boldsymbol{\mu}}'$  by  $\det(\boldsymbol{\Lambda}^{-1})$ . In **Eqn. 2.3.16**, the z-directional component is not under consideration because 2-D y-directional pressure-driven flow was solved. Detail simulation conditions are explained in Section 2.3.3.1.

$$\tilde{\tilde{\boldsymbol{\mu}}}' = \mu''_{ij} = \begin{bmatrix} \mu''_{rr} & \mu''_{r\theta} \\ \mu''_{\theta r} & \mu''_{\theta\theta} \end{bmatrix} = \begin{bmatrix} \left(\frac{b-a}{b}\right)^2 \left(\frac{r'}{r'-a}\right)^2 & 0 \\ 0 & \left(\frac{b-a}{b}\right)^2 \end{bmatrix} \boldsymbol{\mu} \quad (2.3.16)$$

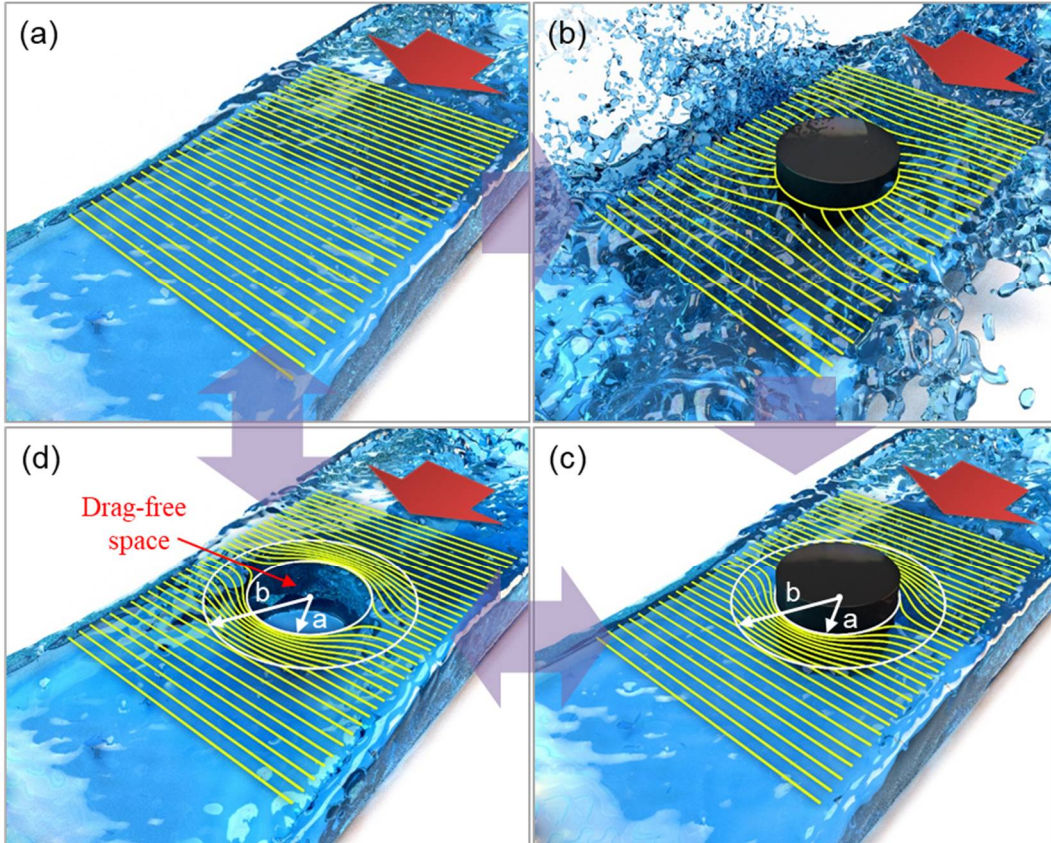


**Figure 2.3.1.** Schematic illustration of drag-free space creation by a rheological cloak. (a) A flowing fluid without anything in it (the bare case). (b) A flowing fluid with an obstacle in it (the obstacle case). (c) A stabilized flowing fluid by encircling the obstacle with the rheological cloak (the cloaked-obstacle case). (d) A fluid flow with only the rheological cloak (the cloak-only case).

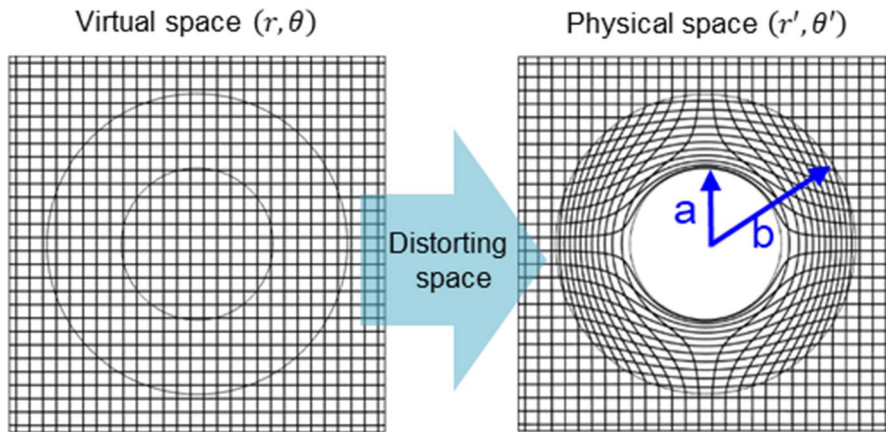


**Figure 2.3.2.** Coordinate grids representing spatial transformation by a cloak.

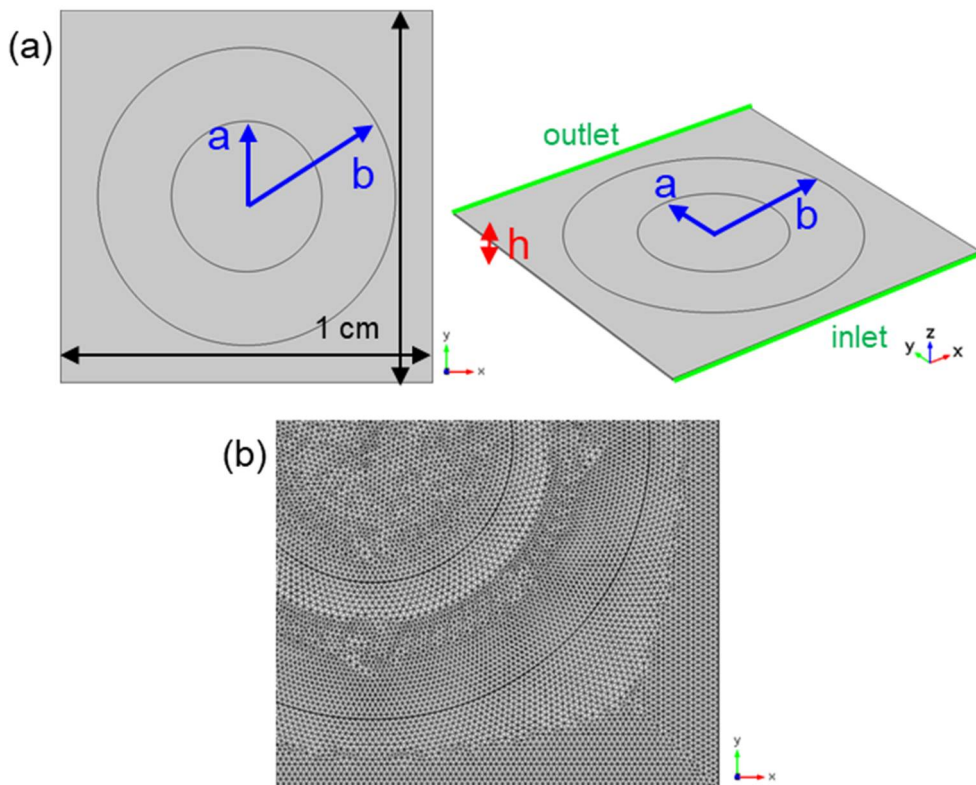


**Figure 2.3.3.** Simulation conditions. (a) A hexahedron geometry and (b) generated meshes in the geometry.



### 2.3.3. Numerical analysis

#### 2.3.3.1. Simulation conditions

Numerical simulation was performed by using COMSOL Multiphysics, the commercial finite-element-based solver, to visualize and analyze pressure and velocity fields of fluid flow. All simulation conditions were set to be consistent with the experimental conditions described later.

Four cases were simulated; the bare, obstacle, cloaked-obstacle, and cloak-only cases. A hexahedron block geometry was generated having a dimension of  $1\text{ cm} \times 1\text{ cm} \times 50\text{ }\mu\text{m}$  (height,  $h$ ) (**Figs. 2.3.3(a)**). A concentric ring meaning the cloaking shell was inserted into the block, whose inner radius  $a$  is 2 mm and outer radius  $b$  is 4 mm. Free tetrahedral meshes were generated in the geometry (**Fig. 2.3.3(b)**). Complete meshes consist of 110989 domain elements, 73084 boundary elements, and 1884 edge elements. The number of iteration and the maximum element to process were four. The maximum and minimum element sizes were  $100\text{ }\mu\text{m}$  and  $30\text{ }\mu\text{m}$ , orderly. The maximum element growth rate was 1.2, the curvature factor was 0.7, and the resolution of narrow regions was 0.6.

Non-slip boundary conditions ( $\tilde{\mathbf{u}} = 0$ ) were applied to the wall of the obstacles, the lateral surfaces of the hexahedron block ( $yz$  planes), and the top-bottom surfaces ( $xy$  planes) of the hexahedron block in  $z$ -axis. A pressure boundary condition ( $\Delta p = 1\text{ kPa}$ ) was applied to simulate Poiseuille flow through the block along  $y$ -axis direction. The employed fluid was water, the most general Newtonian fluid, having  $1\text{ mPa}\cdot\text{s}$  fluid viscosity. Density of the fluid did not need to be considered in the simulation because the equations for the creeping flow were solved.

The fluid flow interface basically built in COMSOL Multiphysics is not available to simulate functions of the rheological cloak that requires a viscosity value as a tensor input, because the fluid viscosity is programmed to be constant only. Therefore, the Navier-Stokes equations (**Eqns. 2.2.29-30**) were modeled as a differential form by customizing a general form PDE (partial differential equation) interface in COMSOL Multiphysics. In the customized interface, the transformed viscosity tensor could be successfully applied in the modeled Navier-Stokes equations by setting appropriate parameters and variables.

It was very important to properly set and optimize the simulation solver conditions of

the program since the newly customized interface was harnessed. Basically, the stationary solver was used by coupling the continuity equation and the momentum equation which were modeled separately. MUMPS (a multifrontal massively parallel sparse direct solver) was coded and used as a basic solver. The memory allocation factor was 1.2. The pivoting condition was used and its threshold was 0.1. The error estimate factor was 400. The double dogleg option was used for a nonlinear method, and the initial damping factor was 1e-4. The simulation was terminated after 50 number of iteration and the tolerance factor was set as 1.

### 2.3.3.2. Simulation results without cloaks

The Navier-Stokes equations can become the simplified forms same as **Eqns. 2.2.8-11** without the transient term ( $\rho \partial \tilde{\mathbf{u}} / \partial t$ ) like

$$\nabla \cdot \tilde{\mathbf{u}} = 0 \quad (2.3.17)$$

$$\nabla \cdot \tilde{\boldsymbol{\tau}} = \nabla p \quad (2.3.18)$$

$$\tilde{\boldsymbol{\tau}} = \mu(\nabla \tilde{\mathbf{u}} + \nabla \tilde{\mathbf{u}}^T) \quad (2.3.19)$$

,where  $\tilde{\boldsymbol{\tau}}$  is the second order stress tensor,  $\tilde{\mathbf{u}}$  is the velocity field,  $p$  is the hydrostatic pressure,  $\mu$  is the viscosity of a fluid, and  $\nabla$  is the nabla operator, under the assumptions of steady-state flow, an incompressible fluid, and neglecting gravity effect. In this section, two general cases without cloaks were simulated and analyzed; the bare case and the obstacle case.

**Figures 2.3.4(a), (i-iii)** show the simulation results for the bare case where no obstacle exists. The parallel pressure contours and the constantly distributed pressure field indicate that no perturbation occurs in the fluid. The parallel flow streamlines, uniform velocity fields, and uniform pressure gradient field imply the same characteristics about the bare case. In the obstacle case (**Figs. 2.3.4(b), (i-iii)**), the dense pressure contours were generated on the obstacle surface. Therefore, the pressure gradient field was perturbed and

a large pressure gradient was applied to the obstacle surface resulting in a drag force. Accordingly, the flow streamlines were disturbed and the obstacle must be subjected to a resistant force by the fluid that strikes the obstacle surface.

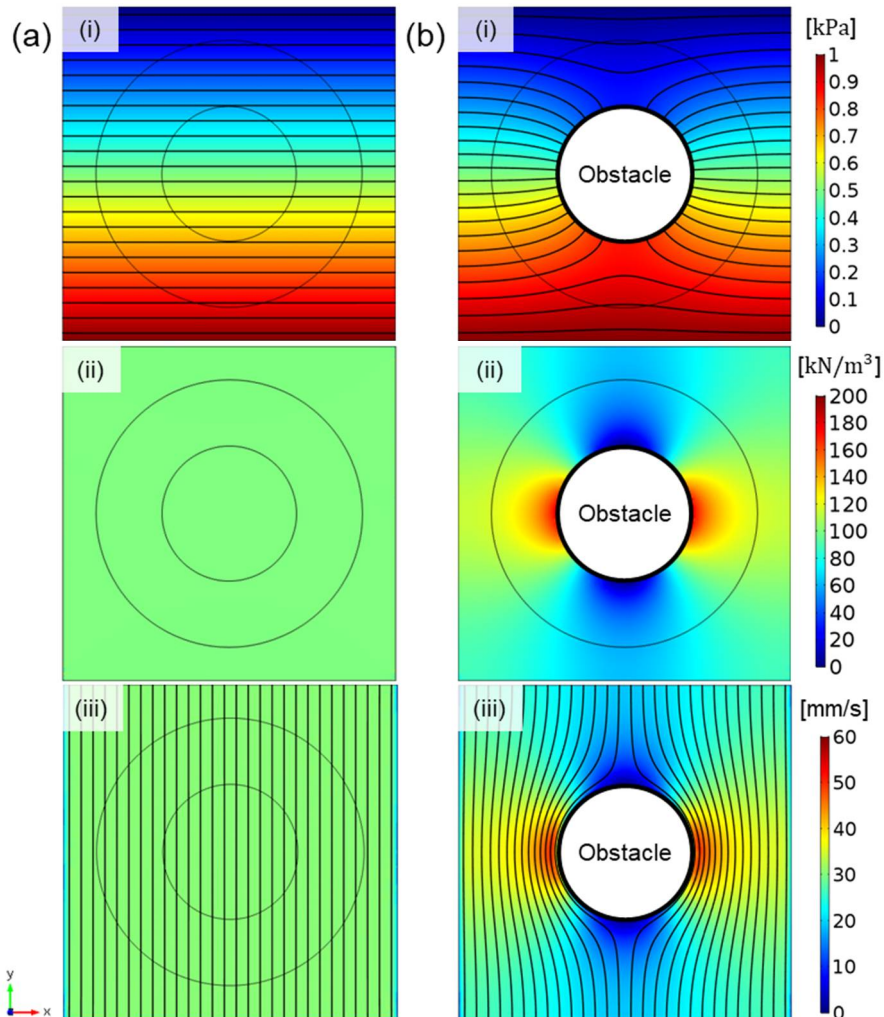


**Figure 2.3.4.** Simulation results for (a) the bare case and (b) the obstacle case; (i) pressure fields, (ii) pressure gradient fields ( $p_y$ ), and (iii) velocity fields.

### 2.3.3.3. Simulation results with cloaks

In this section, the simulation results of the cases with the rheological cloak are shown and discussed. At first, numerical simulation using the transformed viscosity tensor for the ideal case (**Eqn. 2.3.15**) was carried out. The transformed viscosity tensor for the ideal cloak ( $\tilde{\mu}'$ ) has spatially varying components both  $r$  and  $\theta$  axis (**Fig. 2.3.5(a)**). The radial component varies from infinite viscosity at  $r' = a$  to 2 mPa·s at  $r' = b$  and the azimuthal component varies from 0 mPa·s at  $r' = a$  to 0.5 mPa·s at  $r' = b$ . Due to this spatial relationship, impedance at the boundary of the cloak ( $r' = b$ ) is perfectly matched with the background impedance although the space was distorted.

The simulation results with the ideal cloak are shown in **Figs. 2.3.5(b-c)**. In the simulation, the transformed Navier-Stokes equations (**Eqns. 2.2.29-30**) were solved by using the PDE interface customized in COMSOL Multiphysics. The cloaking behavior is discussed later along with the simulation results of the reduced cloak (**Fig. 2.3.6**) because there are so many overlapping parts between the two results.

Unfortunately, the ideal cloak is almost impossible to be realized experimentally due to the extremely varying material parameters at both principal axes,  $r$  and  $\theta$ . Therefore, the reduced set of the transformed viscosity tensor ( $\tilde{\mu}''$ ) was calculated as **Eqn. 2.3.16**. For impedance matching with the background area, the reduced transformed viscosity tensor ( $\tilde{\mu}''$ ) should be scaled up 1.5 times. Each component of the reduced transformed viscosity tensor was plotted in **Fig. 2.3.6(a)**. Unlike the transformed viscosity tensor for the ideal cloak ( $\tilde{\mu}'$ ), it has the radial component varying from infinite at  $r' = a$  to 1.5 mPa·s at  $r' = b$ . More importantly, the azimuthal component does not vary and has a constant value of 0.375 mPa·s.  $\mu''_{rr}$  is the only varying component along the radial distance since  $\mu''_{\theta\theta}$  becomes a constant. Since one of the components of both axes becomes a constant, the experimental conditions can be much more mitigated. Despite this material condition alleviation, the reduced cloak can induce the same dispersion relationship, except for outer boundary of the cloak.

The simulation results of the reduced case rheological cloak are shown in **Figs. 2.3.6(b-c)** for pressure, pressure gradient, and velocity fields. The obstacle encircled by the cloak was not affected by the applied pressure distribution (**Fig. 2.3.6(b), (i)**). In other

words, the deviatoric stress of a flowing fluid cannot penetrate into the central region but rather is directed around the obstacle. As a result, the pressure contour outside the cloak remains parallel. The pressure gradient outside the cloak has a constant value (**Fig. 2.3.6(b), (ii)**), as if there was no obstacle around as same with the bare case. It means that an external observer is unaware of something hidden in the fluid flow from a rheological point of view. Also, this concealment removes the confusion of velocity fields and creates straight streamlines outside the cloak (**Fig. 2.3.6(b), (iii)**). Instead, the fluid momentum, which is excluded from both the center and the background, is compensated in the annular cloak region ( $a < r' < b$ ), inducing a very high flow rate. Since the force of a flowing fluid does not transfer to the rheologically empty space ( $0 < r' < a$ ), it is obvious that the drag to the surface of the placed object must be very small.

This cloaking phenomenon can be understood more intuitively in the simulation results of the cloak-only case that the obstacle is absent (**Figs. 2.3.6(c), (i-iii)**). In the cloaked region, pressure gradient along the flow direction ( $P_y$ ) is almost zero (**Fig. 2.3.7(a)**). Furthermore, the magnitude of velocity field is close to zero unlike the fast flow velocity outside the cloak and it allows us to predict very tranquil flow inside the cloak (**Fig. 2.3.6(c), (iii)** and **Fig. 2.3.7(b)**). Most notably, it could be deduced that the cloaking behavior is independent of a shape of objects within the circular cloaked region. As a result, it was numerically proven that a drag-free fluidic space can be created if the cylindrical space is wrapped with the cloak with the scaled reduced transformed viscosity tensor.

In practice, how much drag is reduced by the cloak was evaluated by calculating and comparing the drag forces applied on the surface of the cylindrical obstacle (**Fig. 2.3.7(c)**). The drag force ( $F_d$ ) acting on the obstacle surface was defined as

$$F_d = \iint_s \tau_y ds \quad (2.3.20)$$

, where  $\tau_y$  is the y-axis stress acting on the obstacle surface and  $s$  is the surface area of the obstacle. Both the viscous force and the pressure force are included in the stress term of  $\tau_y$ . The drag coefficient ( $C_d$ ) was defined as

$$C_d = \frac{2F_d}{\rho_0 u_{inf}^2 A} \quad (2.3.21)$$

, where  $\rho_0$  is the mass density of a fluid,  $u_{inf}$  is the flow velocity of the obstacle relative to a flowing fluid, and  $A$  is the reference area of the obstacle.

The drag force on the obstacle was 120  $\mu\text{N}$ , but it was reduced by 7 times to 18  $\mu\text{N}$  after cloaked. Besides, the drag coefficient, which is a dimensionless quantity, was decreased by 10 times from 4569.7 to 440.8 by cloaking. These calculation results suggest the possibility of applications of the rheological cloak to the drag-free technology. The calculated drag values did not become zero because these are the mathematical iteration results. Naturally, if a smaller obstacle is placed in the cloak, the drag reduction rate will increase much higher (not shown in this dissertation).

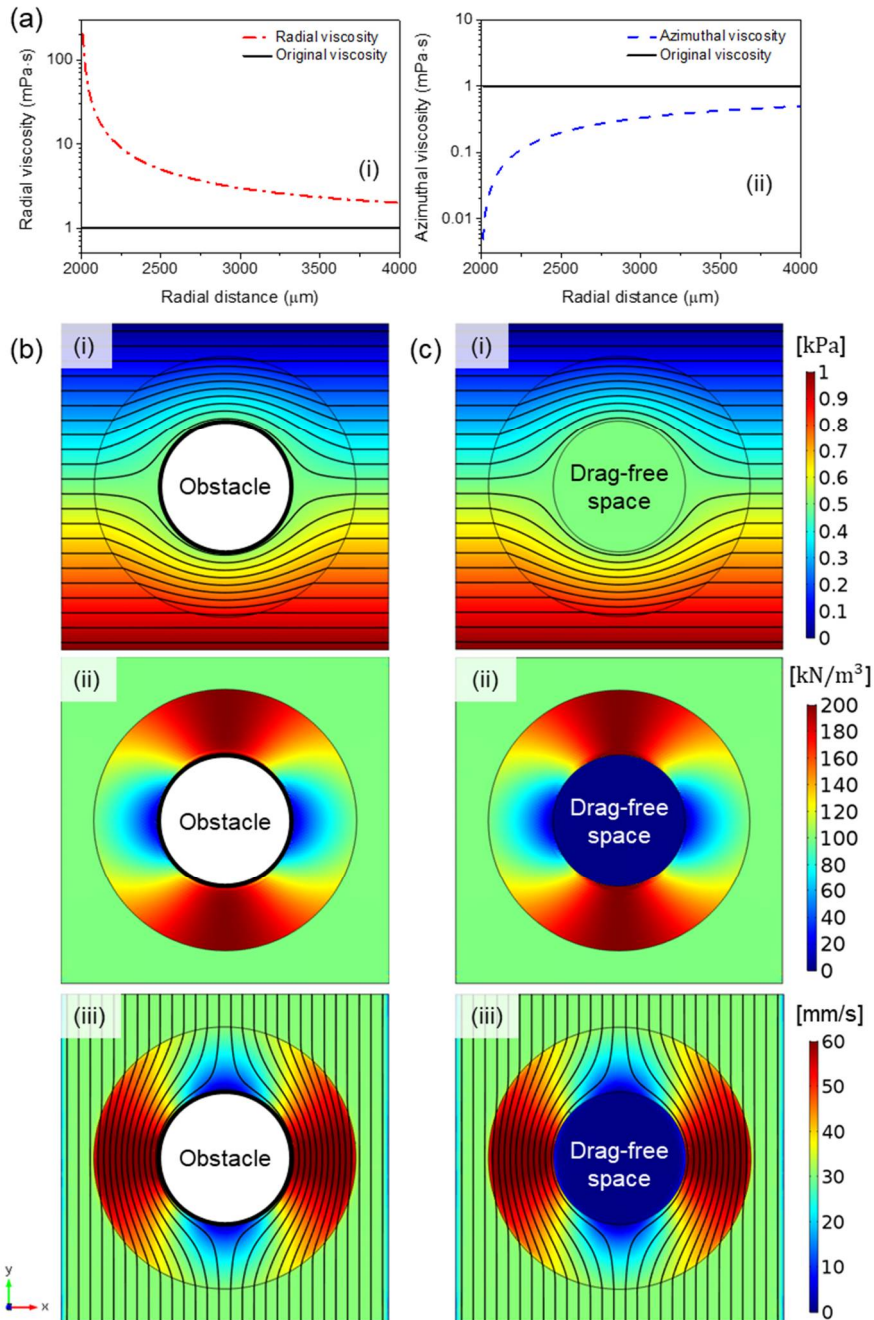


**Figure 2.3.5.** Modeling of the ideal case rheological cloak. (a) Spatially varying viscosity tensor components (i) in radial and (ii) azimuthal axes. Simulation results for (b) the cloaked-obstacle case and (c) the cloak-only case of (i) pressure fields, (ii) pressure gradient fields ( $p_y$ ), and (iii) velocity fields.

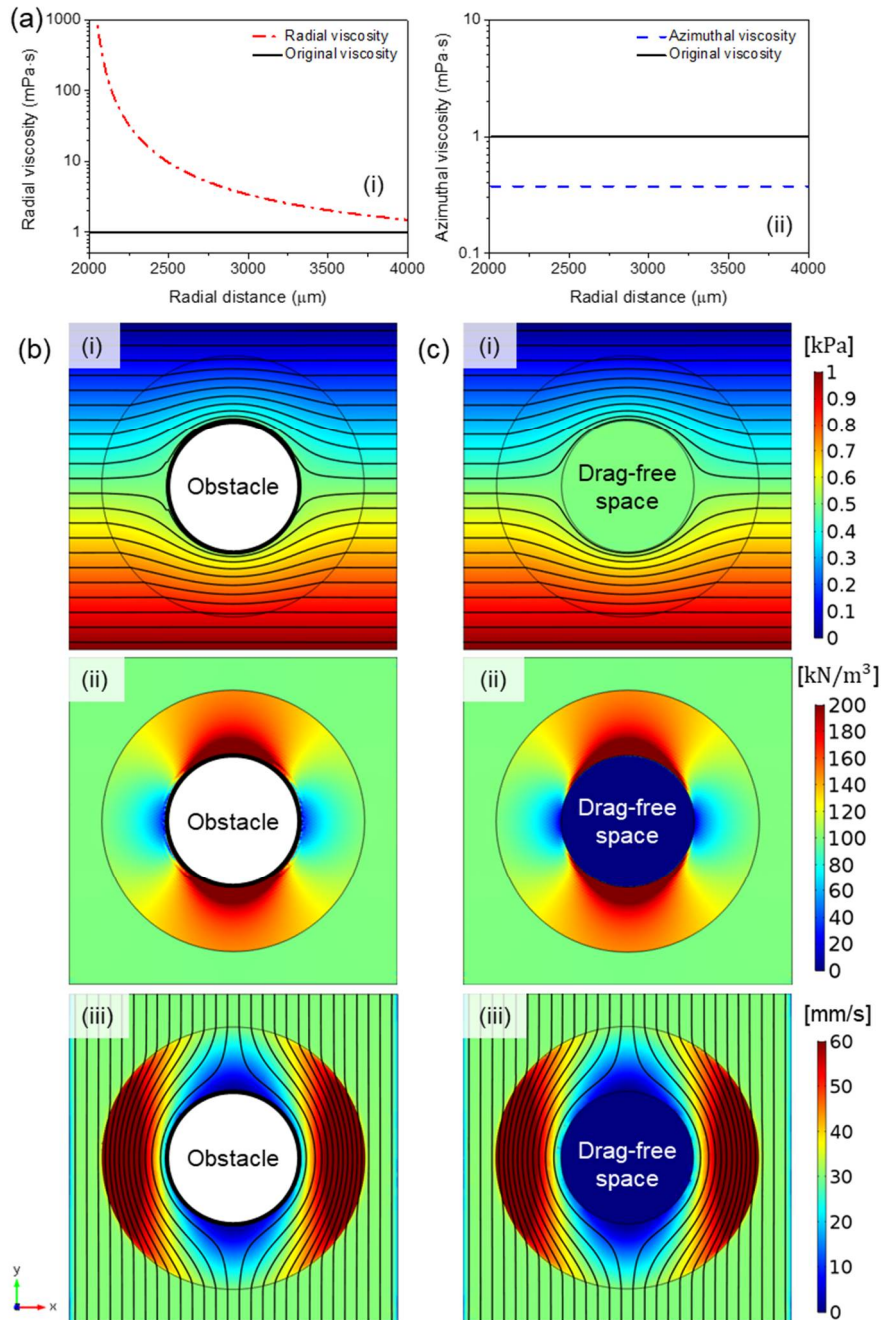


**Figure 2.3.6.** Modeling of the reduced case rheological cloak. (a) Spatially varying viscosity tensor components (i) in radial and (ii) azimuthal axes. Simulation results for (b) the cloaked-obstacle case and (c) the cloak-only case of (i) pressure fields, (ii) pressure gradient fields ( $p_y$ ), and (iii) velocity fields.



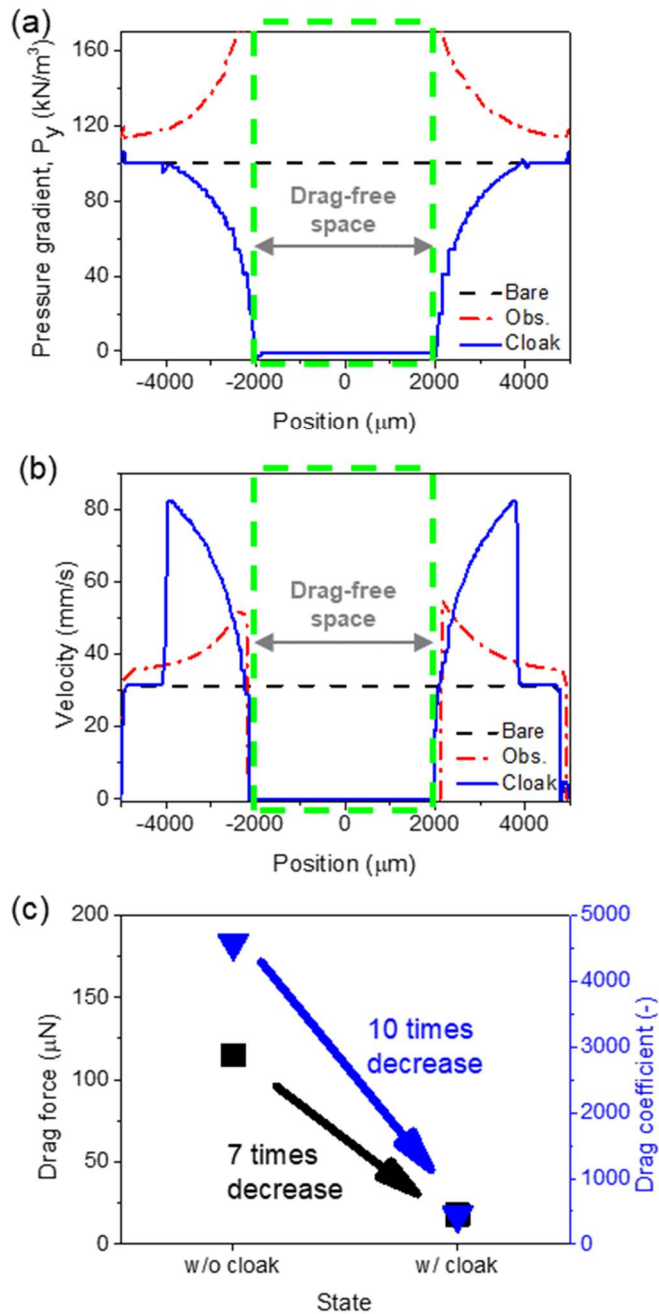


**Figure 2.3.7.** Profiles of the simulation fields and drag values. Profiles of (a) the pressure gradient field ( $p_y$ ) and (b) velocity field at the center line (the line at  $y=0.5$  cm and  $z=25$   $\mu\text{m}$ ). (c) Comparison of the drag forces and drag coefficients generated on the obstacle surface with or without the cloak.

## 2.3.4. Metamaterial design

### 2.3.4.1. Multilayered cloak

As a preliminary step to design the rheological metamaterial cloak, a multilayered cloak was built based on the homogenized layer method [25,28] and it was analyzed theoretically. It is impossible to achieve a seamless continuous viscosity tensor value over the entire area of the cloak. Therefore, this step is a very significant process to compartmentalize the cloak in order to approximate the viscosity values required for experimental implementation.

The annular cloaking shell region ( $a < r' < b$ ) was divided into 10 concentric layers as shown in **Fig. 2.3.8**. Each layer was numbered from 1 to 10 in order from inside to outside. The thickness of all layers is equal to 200  $\mu\text{m}$ , which is one tenth of the total thickness of the cloak ( $b - a$ ). Each layer has anisotropic viscosity tensor components along  $r$  and  $\theta$  axes, but it has a homogeneous value in one layer. The viscosity components of each layer were allocated to the averaged values of the scaled reduced transformed viscosity tensor (1.5 times scaled  $\widetilde{\mu}''$  shown in **Fig. 2.3.6(a)**) for each section.

The viscosity tensor values assigned to each layer are shown in **Fig. 2.3.9(a)** and **Table 2.3.1**. The radial component greatly changes from 511.3 mPa·s for the 1st layer to 1.58 mPa·s for the 10th layer. On the other hand, the azimuthal component does not change for each layer but maintains the constant value of 0.375. However, the viscosity of the central clocked area does not need to be considered since the force of a flowing fluid does not extend inside the cloak (denoted as “None” in **Table 2.3.1**).

Numerical analysis was performed using COMSOL Multiphysics, in order to theoretically verify that the multilayered cloak produced in this way is actually equivalent to the continuous media cloak. The methods and conditions for the numerical analysis were as described in Section 2.3.3.1. First, it could be confirmed that the simulation results of the continuous media cloak (**Fig. 2.3.6**) and the multilayered cloak (**Fig. 2.3.9**) are very similar in the pressure, pressure gradient, and velocity fields. The pressure contours were successfully removed from the obstacle surface and the velocity fields outside the multilayered cloak were stabilized as if there was no obstacle (**Figs. 2.3.9(b-c), (i)**). Furthermore, the drag-free space was successfully created, resulting in the pressure gradient and velocity field approaching zero in the space (**Figs. 2.3.9(b-c), (ii)**). The only

difference between the two cases was that a slight non-uniformity was observed at the interface of each layer where the values of the viscosity components were distinguished.

The drag parameters, the drag force and drag coefficient, also were calculated and compared with the simulation results of the continuous media cases. The same drag equations (**Eqns. 2.3.20-21**) were applied to the multilayered cloak simulations. The drag force acting on the obstacle was 120  $\mu\text{N}$  and it decreased to 18  $\mu\text{N}$  after encircled by the multilayered cloak, as same with the continuous media case. The drag coefficient decreased from 4569.7 to 440.0 by almost 10 times.

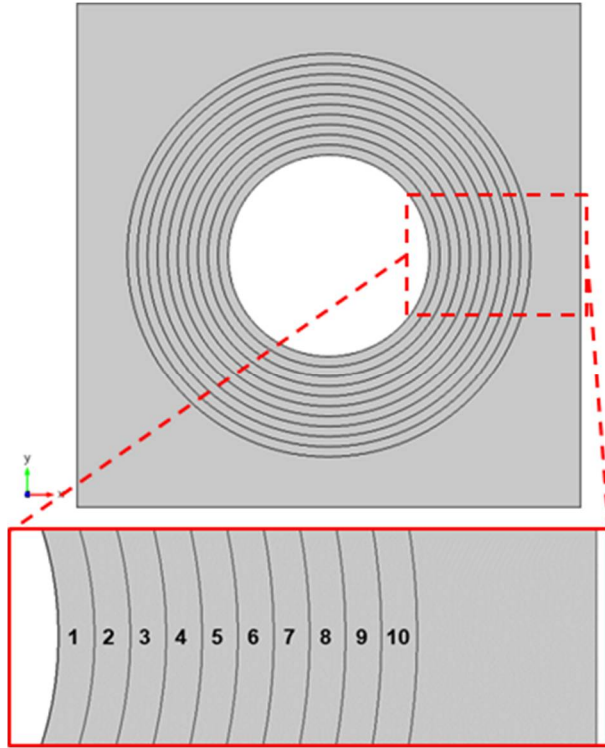


**Figure 2.3.8.** A constructed geometry of the multilayered cloak and its magnified view.

**Table 2.3.1.** Viscosity tensor components of the multilayered cloak given to each layer.

Layer No.	$\mu_{eff,r}$ (mPa·s)	$\mu_{eff,\theta}$ (mPa·s)
Center region	None	None
1	511.29	0.375
2	24.92	0.375
3	9.75	0.375
4	5.67	0.375
5	3.93	0.375
6	2.99	0.375
7	2.42	0.375
8	2.04	0.375
9	1.77	0.375
10	1.58	0.375
Background	1	1

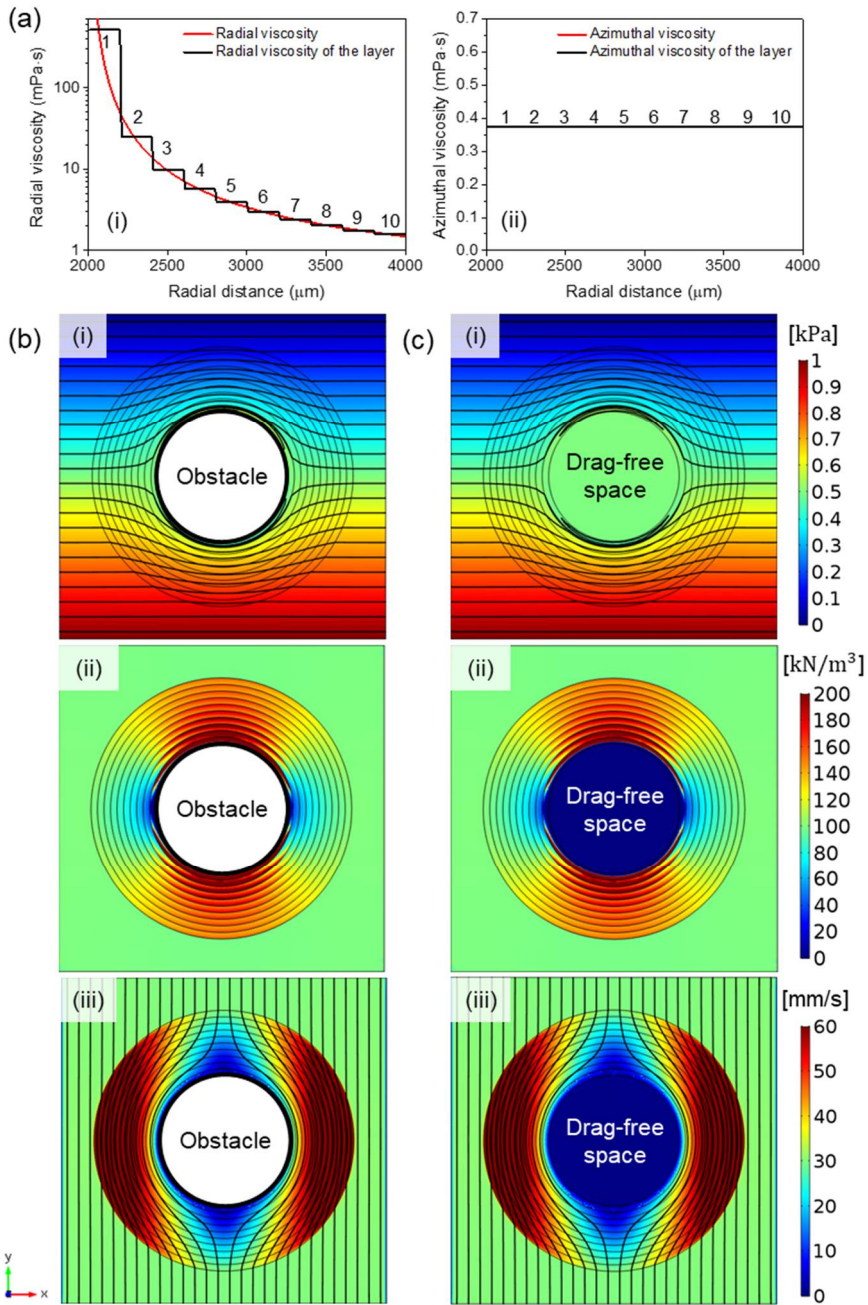


**Figure 2.3.9.** Modeling of the multilayered rheological cloak. (a) Viscosity tensor components of each layer (i) in radial and (ii) azimuthal axes. Simulation results for (b) the cloaked-obstacle case and (c) the cloak-only case of (i) pressure fields, (ii) pressure gradient fields ( $p_y$ ), and (iii) velocity fields.

### 2.3.4.2. Unit cell modeling

Production of the multilayered cloak requires unit cells, which can implement the anisotropic effective viscosity, for mapping on each layer. In the previous metamaterial researches, various unit cells for correlating physics such as thermodynamics and optics have been developed by designing and fabricating composite materials based on effective medium theory [25,36]. The unit cells developed in the previous studies should be able to have anisotropic material properties, *e.g.*, thermal conductivity [25], of tensor components in each direction. And the unit cells can be flexibly designed from a very small value close to zero to a high value of several hundreds or thousands.

Unfortunately, unit cells that materialize effective viscosity have rarely been reported so far, unlike other unit cells that can be easily calculated from the effective medium theory. This concept has been addressed only in porous media flow [153–156] which is governed by Darcy’s pressure equation or Brinkman equation, not as a unit cell concept. A plan for developing effective viscosity unit cells was conceived by considering superficial velocity which is defined as the mean velocity of a specific domain [157–159]. The superficial velocity is inversely proportional to the fluid viscosity if other conditions are identical. From this notion, the effective viscosity of a unit cell for each axis ( $\mu_{eff,pillar}$ ) is defined as

$$\mu_{eff,pillar} = \left( \frac{\langle \tilde{\mathbf{u}}_0 \rangle_S}{\langle \tilde{\mathbf{u}}_{pillar} \rangle_S} \right) \mu \quad (2.3.22)$$

, where  $\langle \tilde{\mathbf{u}}_0 \rangle_S$  and  $\langle \tilde{\mathbf{u}}_{pillar} \rangle_S$  are the superficial velocity values for the bare unit cell and the pillar-placed unit cell, and  $\mu$  is the intrinsic water viscosity.

The effective viscosity unit cells were contrived through superficial velocity control. The superficial velocity was controlled by introducing a microstructure with theoretically designed dimension. Dimension of unit cells is 200 by 200 by 50  $\mu\text{m}^3$  as shown in **Fig. 2.3.10**. The unit cell size needs to be smaller than the scale of water momentum diffusivity, *i.e.*, kinematic viscosity of water (0.9  $\text{mm}^2/\text{s}$ ).

The superficial velocity of unit cells was calculated from the simulated velocity fields by using COMSOL Multiphysics. Non-slip boundary conditions were applied to the upper

and lower surfaces of the unit cell (in z-axis), the surfaces of the cylinder and micropillars. Pressure boundary conditions ( $\Delta p = 10$  Pa) were applied to the side surfaces lying in the flow direction. The value of the pressure condition itself (10 Pa) is not important since only the ratio of the superficial velocity determines the effective viscosity. Periodic boundary conditions were applied to the remaining side surfaces. Each axis of the unit cell is represented by the cylindrical coordinate system  $(r, \theta, z)$  following the circular structure of the cloak to be conclusively mapped.

The simulated velocity field of the bare unit cell is shown in **Fig. 2.3.10(a)**. From the velocity field, the superficial velocity of the bare unit cell ( $\langle \tilde{\mathbf{u}}_{bare,i} \rangle_V$ ) was calculated to be 10.49 mm/s. Before modeling the unit cells, all viscosity components of **Eqn. 2.3.16** were scaled up by a factor of 5.2 to make the azimuthal viscosity larger than 1 mPa·s, from 0.25 mPa·s to 1.3 mPa·s (red lines in **Figs. 2.3.12(a-b)**). In order to realize anisotropic viscosity components in the effective unit cells, micropillars with a large aspect ratio were inserted into each unit cell and then, the superficial velocity along each axis ( $\langle \tilde{\mathbf{u}}_{pillar,i} \rangle_V$ ) can be greatly different within the unit cell.

Nine micropillar-embedded unit cells were devised. The reason why the number of unit cells is nine instead of ten is that the same unit cells are used for the layers 1 and 2 (**Fig. 2.3.11**). In the other eight layers, unit cells with different shaped micropillars were placed. The simulated velocity fields and the calculated effective viscosity of all unit cells were described in **Fig. 2.3.11** and **Table 2.3.2**. The length of the micropillars ( $l$ ) was ranged from 188  $\mu\text{m}$  to 163  $\mu\text{m}$ . In the meanwhile, the thickness of the micropillars was fixed to 50  $\mu\text{m}$  to keep the azimuthal viscosity constant. Hence, the azimuthal viscosity remained fairly constant to 1.3 from 1.292 mPa·s to 1.338 mPa·s, while the radial component was varied broadly from 79.27 mPa·s to 5.3 mPa·s.

The effective viscosity of the background must be taken into account due to the scaling operation by a factor of 3.47 (5.2 divided 1.5). Originally, the background effective viscosity should be 3.47 mPa·s but it should be further adjusted to a value of 2.76 mPa·s to resolve the impedance mismatch problem originated from the error of the effective medium approximation. Therefore, the unit cells having a 150  $\mu\text{m}$  diameter cylinder were arranged on the entire background area in the form of a 50 by 50 rectangular grid.

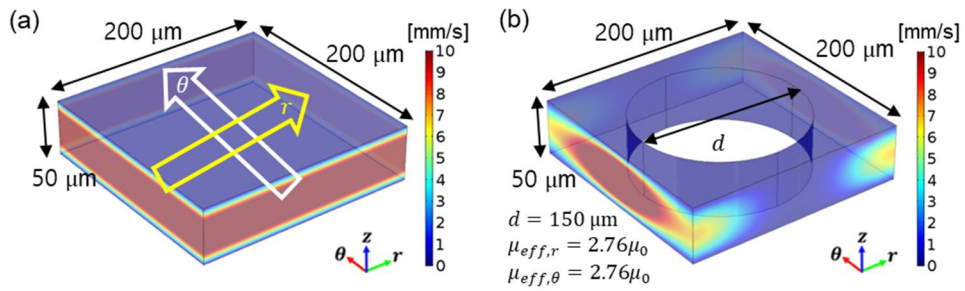


**Figure 2.3.10.** Simulated velocity fields for (a) the bare unit cell for the cloaking shell region and (b) the background unit cell.

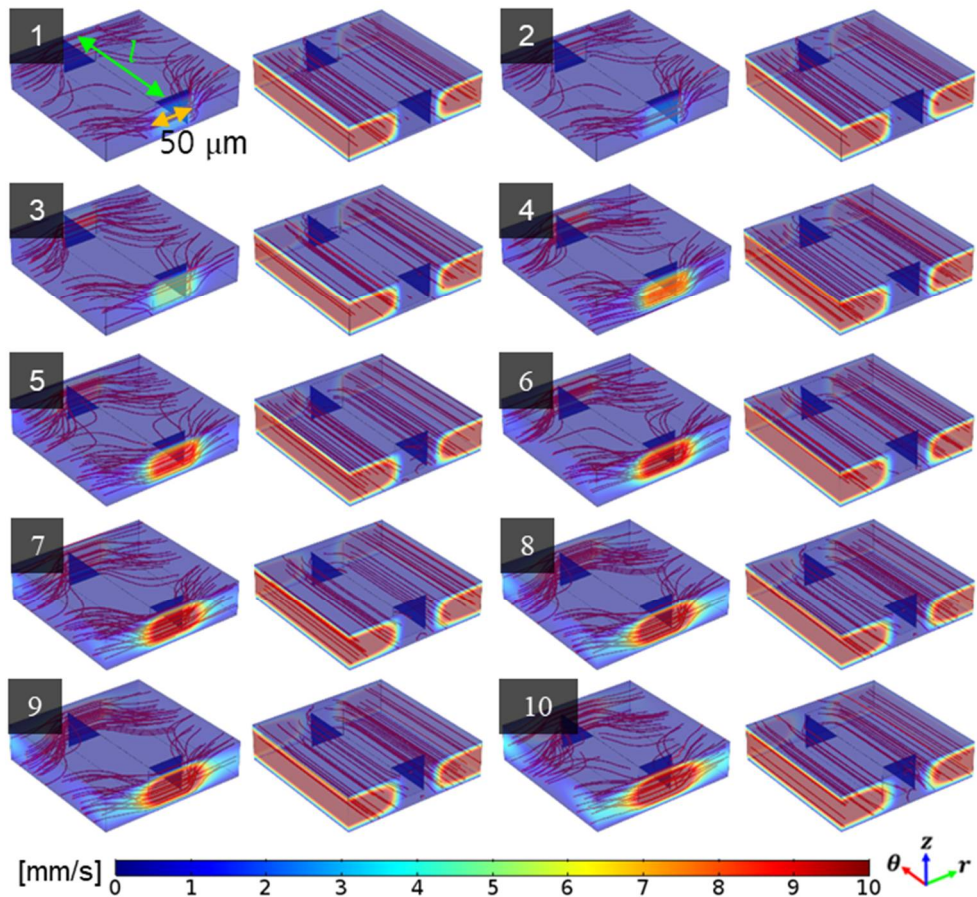


**Figure 2.3.11.** Simulated velocity fields for the effective viscosity unit cells which are applied to each layer of the rheological metamaterial cloak. The white arrows mean  $r$ -direction and the yellow arrows for  $\theta$ -direction.  $l$  is the length of the micropillar of each unit cell.



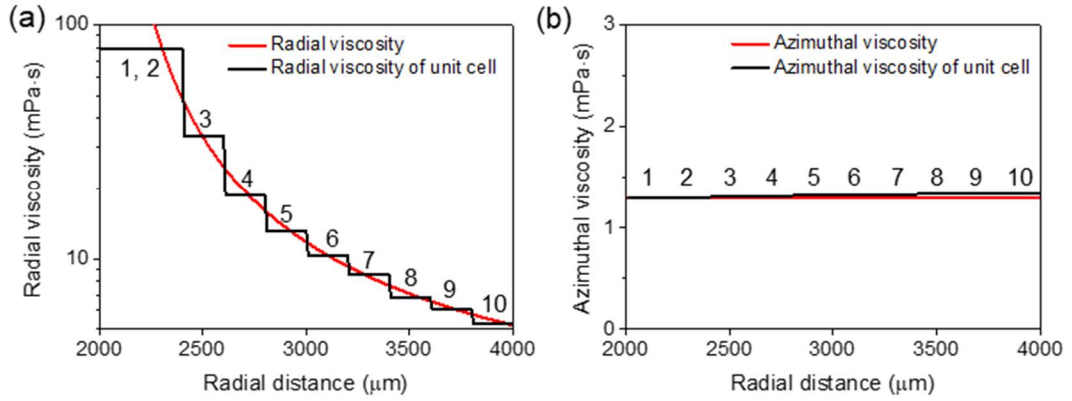


**Figure 2.3.12.** Viscosity tensor components of the effective viscosity unit cells mapped on the rheological metamaterial cloak (a) in radial and (b) azimuthal axes.

**Table 2.3.2.** Effective viscosity unit cells mapped on each layer of the rheological metamaterial cloak.

Layer No.	$l$ ( $\mu\text{m}$ )	$\mu_{eff,r}$ (mPa·s)	$\mu_{eff,\theta}$ (mPa·s)
Center region	-	None	None
1	188	79.269	1.292
2	188	79.269	1.292
3	183	33.623	1.302
4	178	18.760	1.311
5	174	13.126	1.318
6	171	10.374	1.322
7	168	8.551	1.328
8	164	6.803	1.332
9	161	6.094	1.338
10	159	5.300	1.338
Background	$d=150$	2.758	2.758

\* $d$  means the radius of the microcylinder.

#### 2.3.4.3. Designed metamaterial cloak

The rheological metamaterial cloak was designed as a three-dimensional pillar-arrayed model by mapping the designed effective viscosity unit cells (**Fig. 2.3.13**). Each layer of the cloak from 1 to 10 consists of 65, 72, 79, 85, 91, 97, 104, 110, 116, and 120 corresponding unit cells. The total dimensions are the same as for the continuous media and multilayered cases. Four pillar-arrayed models for the designed rheological metamaterial cloaks and their control groups were constructed (**Fig. 2.3.14**). The four models were drawn by using CATIA 5.18. After inserting the models into the hexahedron block, a Boolean operation was harnessed. Then the remaining space inside the block is a fluid domain and the removed empty space is a solid frame. **Figures 2.3.14(a-d)** show the bare, obstacle, cloaked-obstacle, and cloak-only cases.

Numerical simulation was carried out to pre-check cloaking phenomena of the pillar-arrayed models. Unlike the continuous media and multilayer cases, the fluid flow interface basically built in COMSOL Multiphysics was utilized under the creeping flow condition. The following simulation conditions were different from the previous two cases. Non-slip boundary conditions were applied to all surfaces of the microstructures, including the cylinder and anisotropic micropillars. A large number of meshes are required because the models contain very fine structures; 1834961 domain elements, 681580 boundary elements, and 93962 edge elements. The maximum and minimum element sizes were 30  $\mu\text{m}$  and 20  $\mu\text{m}$ , orderly. The maximum element growth rate was 1.15, the curvature factor was 0.6, and the resolution of narrow regions was 0.7. Of course, only a constant water viscosity (1  $\text{mPa}\cdot\text{s}$ ) was given in as a material property.

Simulation results for the four pillar-arrayed models are shown in **Fig. 2.3.15** showing pressure fields, velocity fields, and flow streamlines, orderly. All the simulation results are fairly matched with both the results of the continuous media and the multilayer simulations. **Figures 2.3.16-18** show the direct comparison of all simulation results.

It can be seen in **Figs. 2.3.15(c-d), (i)** that the isopressure lines are formed by completely deflecting the central cloaked area and naturally, no pressure gradient occurred in the cloaked area. For the velocity fields and flow streamlines, a magnified view of the quarter region is depicted to plot the detailed field distribution of the gaps between the microstructures (**Figs. 2.3.15(c-d), (ii)**).

In the cloak-only case, the velocity field of the central encircled zone converges to almost zero and the streamlines rarely invade. Furthermore, the velocity field and flow streamlines outside the cloak are not disturbed at all, regardless of presence of the obstacle. It could be figured out from the velocity fields of the cloaking shell, background, and central cloaked regions that the design strategy of effective viscosity unit cells is theoretically close to perfect for materializing the rheological metamaterial cloak.

Importantly, it could be confirmed that the drag force decreased by 5 times from 110  $\mu\text{N}$  to 23  $\mu\text{N}$  and the drag coefficient by 9 times from  $1.2e5$  to  $1.3e4$ , by covering the obstacle with the pillar-arrayed model cloak. The reduction ratio of the drag force relatively decreased compared to the previous two simulation cases (the continuous media and multilayer cases). This is presumably due to the error of the unit cell approximation, as the resolution of a screen decreases when size of unit pixels is large. Therefore, if the overall dimension of effective viscosity unit cells can be made smaller, the reduction rate of the drag force is expected to approach the ideal simulation results.

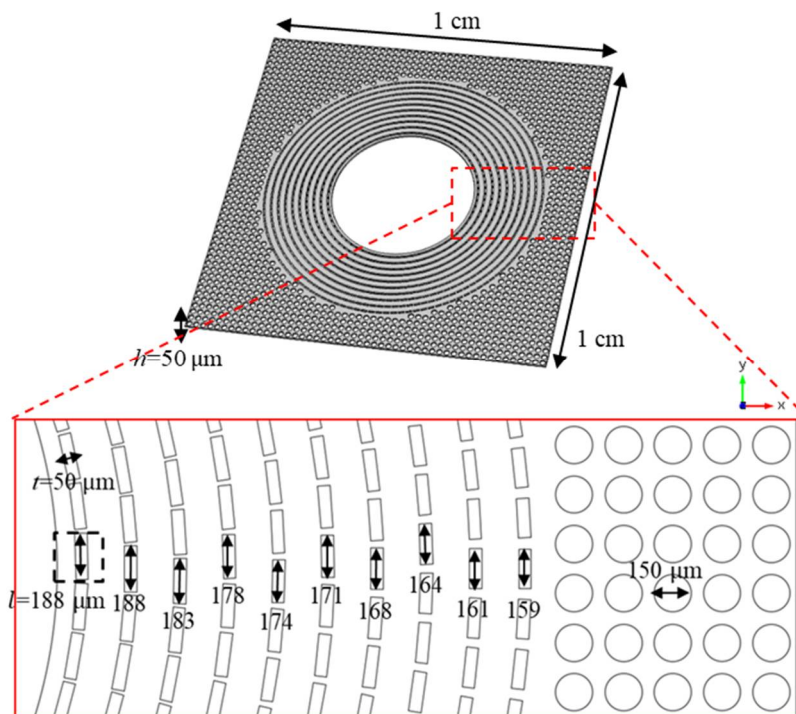


**Figure 2.3.13.** Design of the rheological metamaterial cloak of a pillar-arrayed case with detailed configuration and a magnified view.

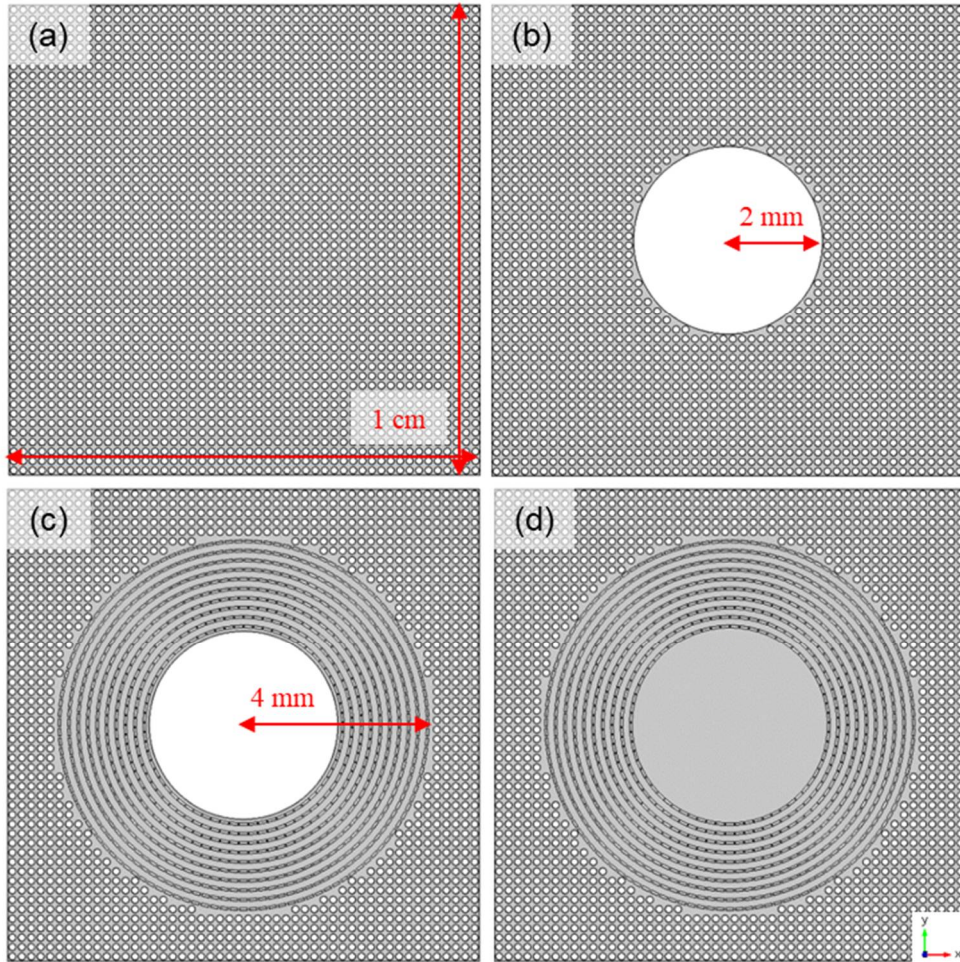


**Figure 2.3.14.** Constructed pillar-arrayed models for the designed rheological metamaterial cloaks and the control groups; (a) the bare, (b) obstacle, (c) cloaked-obstacle, and (d) cloak-only cases.

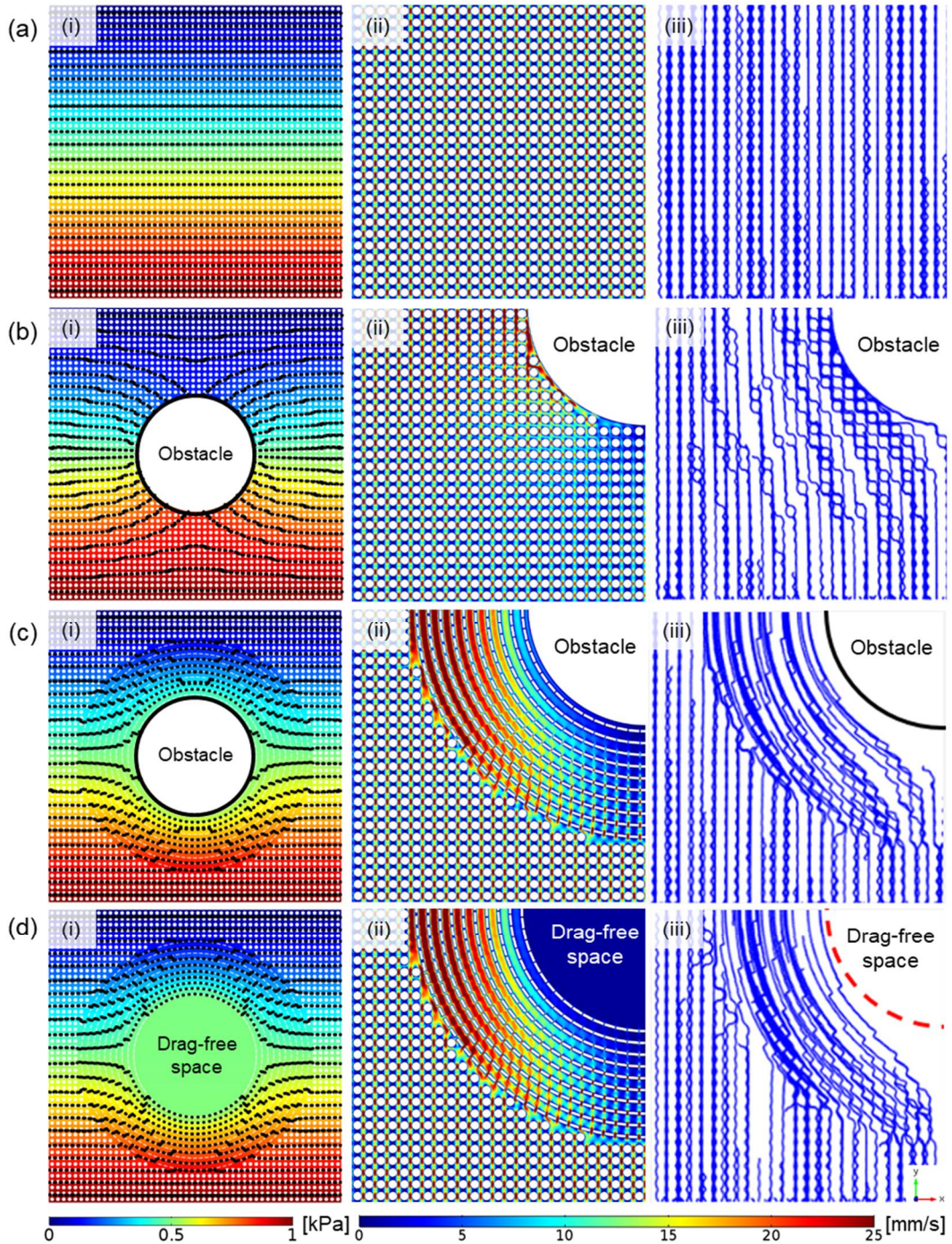


**Figure 2.3.15.** Simulation results of for the designed rheological metamaterial cloaks and the control groups: (a) the bare, (b) obstacle, (c) cloaked-obstacle, and (d) cloak-only cases showing (i) pressure field, (ii) velocity field, and (ii) flow streamlines.

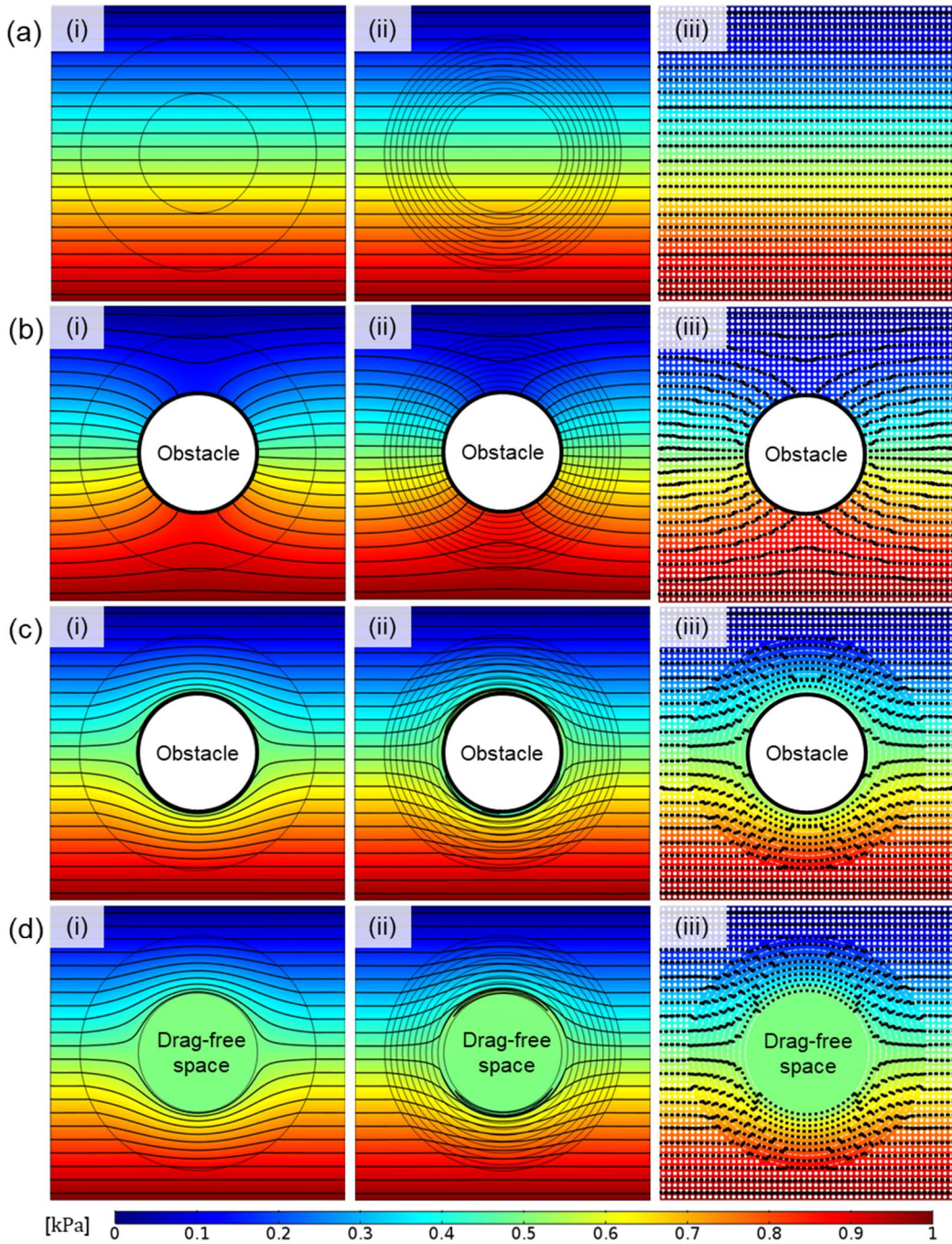


**Figure 2.3.16.** Comparison of simulated pressure fields for (a) the bare, (b) obstacle, (c) cloaked-obstacle, and (d) cloak-only cases; (i) continuous media, (ii) multilayer, and (iii) pillar-arrayed cloak cases.

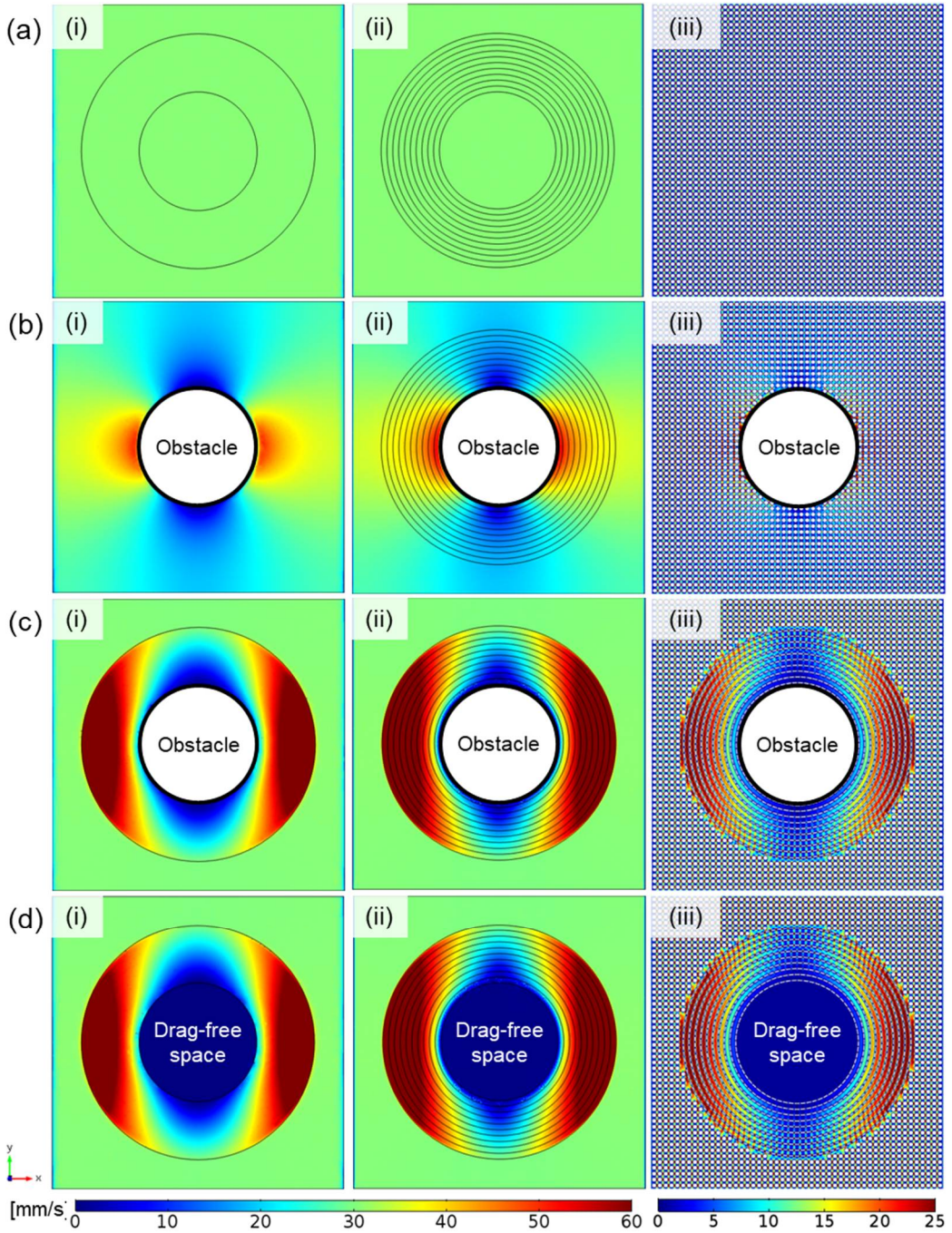


**Figure 2.3.17.** Comparison of simulated velocity fields for (a) the bare, (b) obstacle, (c) cloaked-obstacle, and (d) cloak-only cases; (i) continuous media, (ii) multilayer, and (iii) pillar-arrayed cloak cases.

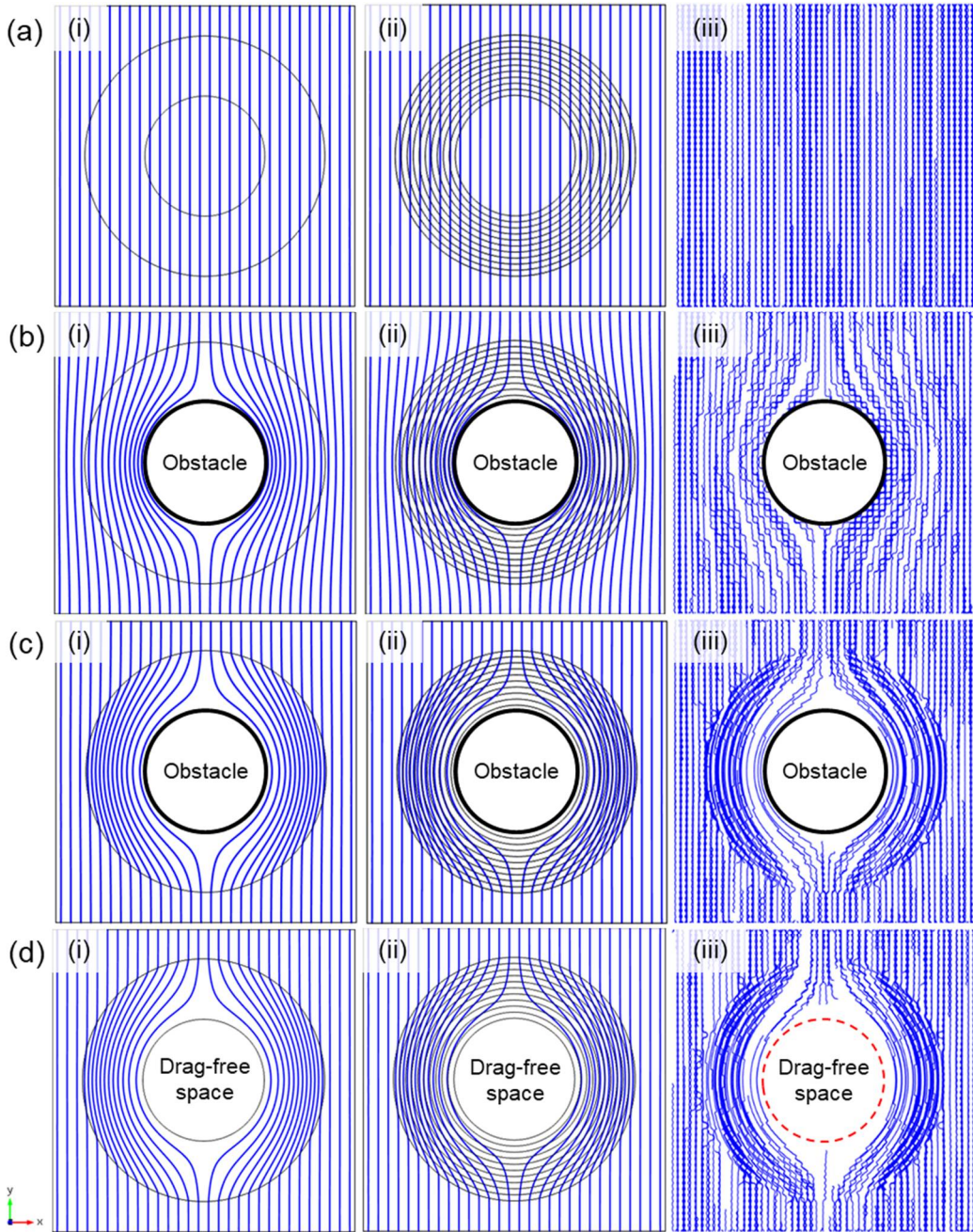


**Figure 2.3.18.** Comparison of simulated flow streamlines for (a) the bare, (b) obstacle, (c) cloaked-obstacle, and (d) cloak-only cases; (i) continuous media, (ii) multilayer, and (iii) pillar-arrayed cloak cases.



## 2.3.5. Experimental realization

### 2.3.5.1. Fabrication method

The designed metamaterial cloaks demonstrated in Section 2.3.4.3 were fabricated into polymeric microstructures by using a replica molding method. At first, the drawings of four microchannels which include the bare, obstacle, cloaked-obstacle, and cloak-only cases were modeled by using a commercial CAD (computer-aided design) program, AutoCAD 2017 (Autodesk, United States) (**Figs. 2.3.19-20**). The four microchannels were arranged in two circles representing a 4-inch silicon (Si) wafer. Two 2 mm holes of each microchannel represent reservoirs for the inlet and outlet to introduce fluid flow. The total length of the channels was 5 cm and the width was 1 cm. The length of a pillar-arrayed section was set to 3 cm, not 1 cm, to eliminate unexpected influences by inlet conditions and create a complete steady-state flow.

The Si wafer used as a replication master was fabricated by using photolithography. The photolithography is a microfabrication process used to pattern fine structures at micro-/nanoscale, also called optical lithography or UV (ultraviolet) lithography. This method employs UV light to transfer geometric patterns of drawings from a photomask, which is a metal-covered opaque plate with transparent holes, to a photoresist which is a light-sensitive chemical. After the Si wafer was covered with SU-8, a commonly used epoxy-based negative photoresist, UV light was irradiated over the patterned chromium (Cr) photomask. The Cr photomask possesses the drawings of the four microchannels as shown in **Fig. 2.3.21(a)**. In the development process for etching, an uppermost layer of the Si wafer that is not protected was removed by using a chemical agent. The etching depth was 50  $\mu\text{m}$ , which is the same height as the hexagonal block used in the simulations. Consequently, the two Si masters were manufactured as shown in **Fig. 2.3.21(b)**.

Soft lithography was used to fabricate the microdevices containing the four microchannels for the microfluidic experiment. The soft lithography is a technique that replicates micro-/nanostructures using a polymeric elastomer. Polydimethylsiloxane (PDMS) is usually used as an elastomeric material for the soft lithography. The microchannels consisted of PDMS were manufactured by replicating the patterned Si masters.

The procedure for PDMS synthesis is as follows. Sylgard 184 A and B (Dow Corning, United States), the prepolymer and the curing agent orderly, were mixed thoroughly at a mass ratio of 10:1. After the Si master attached to a Petri dish container, the Sylgard mixture was poured on the Si master-attached container. The container was placed in a vacuum oven for about 2 hours to remove air bubbles of the Sylgard mixture generated while the mixing process. A curing process of the Sylgard mixture was conducted by placing the degassed container in a heating oven at 60°C for 4 hours.

The cured PDMS was separated from the Si master and rinsed with ethanol (Daejung Chemicals, Republic of Korea) to remove dusts and unreacted residues. The inlet and outlet of the microchannels were created by punching 1.5 mm diameter holes in the cured PDMS. The PDMS was bonded to a slide glass after applying corona treatment to oxidize surface for 5 minutes for surface activation, and then it was heat-treated for 1 hour at 110°C for strong adhesion. The corona treatment was conducted by using a high frequency generator (model BD-10AV, Electro-Technic products Inc., United States). Finally, the microdevices for the microfluidic experiment were prepared as shown in **Fig. 2.3.21(c)**. The microstructures are perfectly the same as those in the drawings (**Fig. 2.3.22**). In addition, the detailed configuration of the fabricated microstructures perfectly coincides with the designed drawings (**Fig. 2.3.23**).

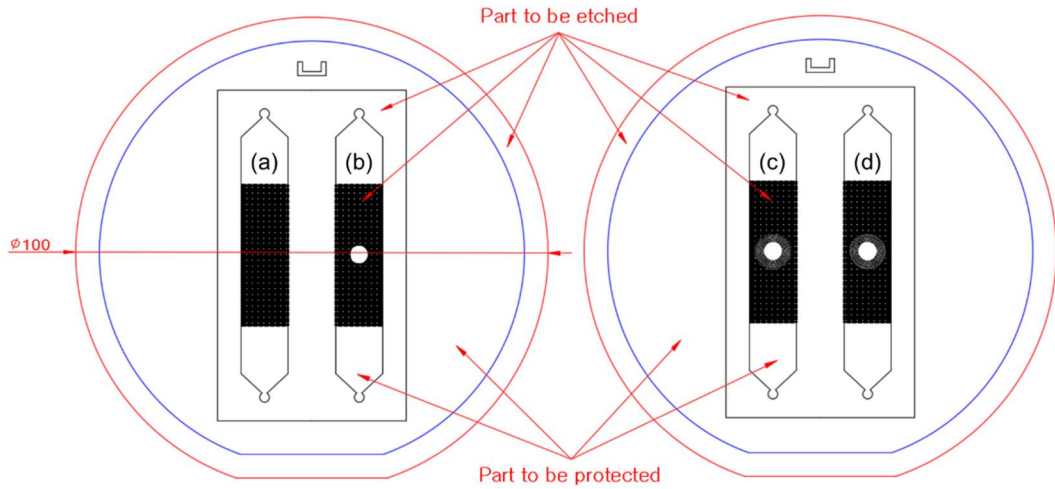


**Figure 2.3.19.** Drawings of the Si masters containing microchannels for the designed rheological metamaterial cloaks and the control groups; (a) the bare, (b) obstacle, (c) cloaked-obstacle, and (d) cloak-only cases.

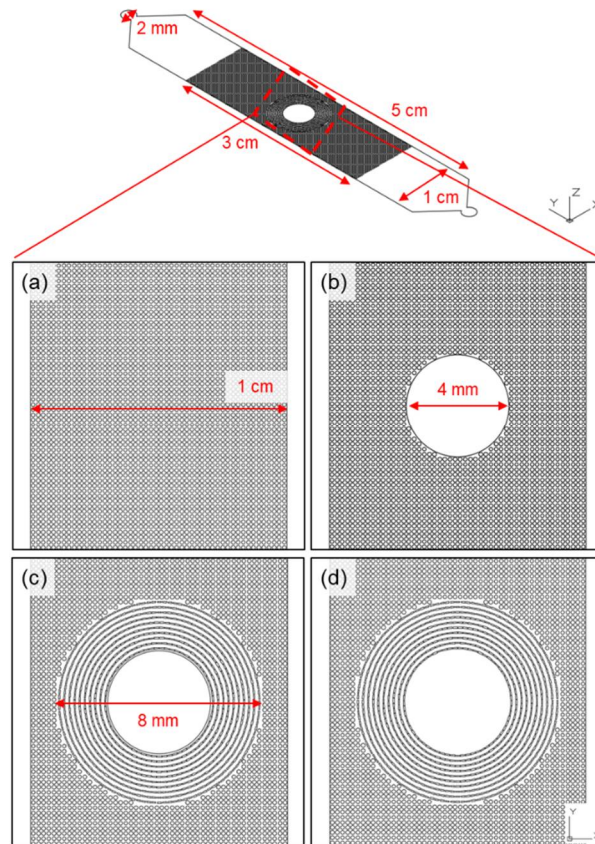


**Figure 2.3.20.** A microscale view and configuration of the microchannel drawings; (a) the bare, (b) obstacle, (c) cloaked-obstacle, and (d) cloak-only cases.

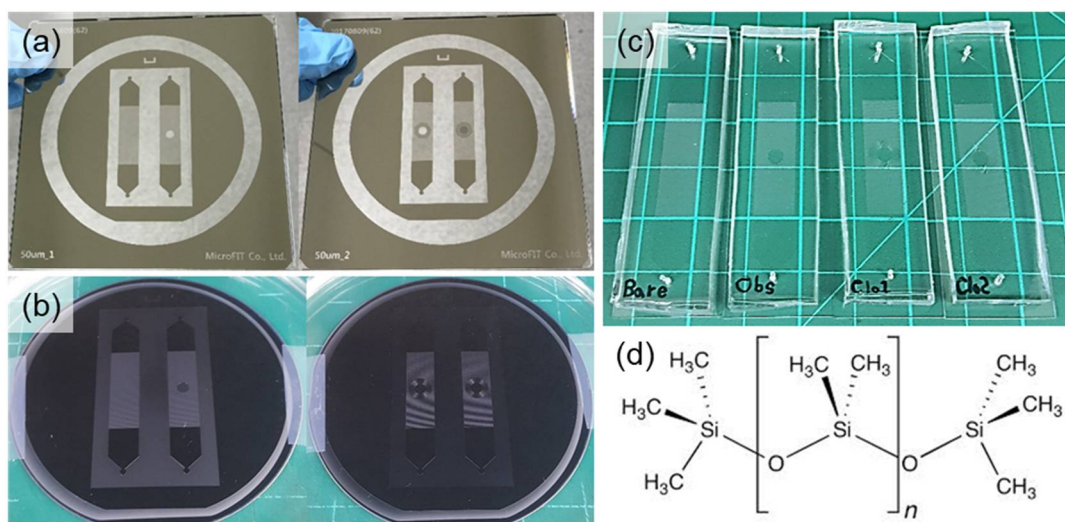


**Figure 2.3.21.** Fabrication details of the rheological metamaterial cloaks and the control groups. Optical photographs of (a) the patterned Cr masks, (b) the fabricated Si masters, and (c) the manufactured microfluidic devices; the bare (Bare), obstacle (Obs), cloaked-obstacle (Clo1), and cloak-only (Clo2) cases, orderly. (d) A chemical structure of PDMS.

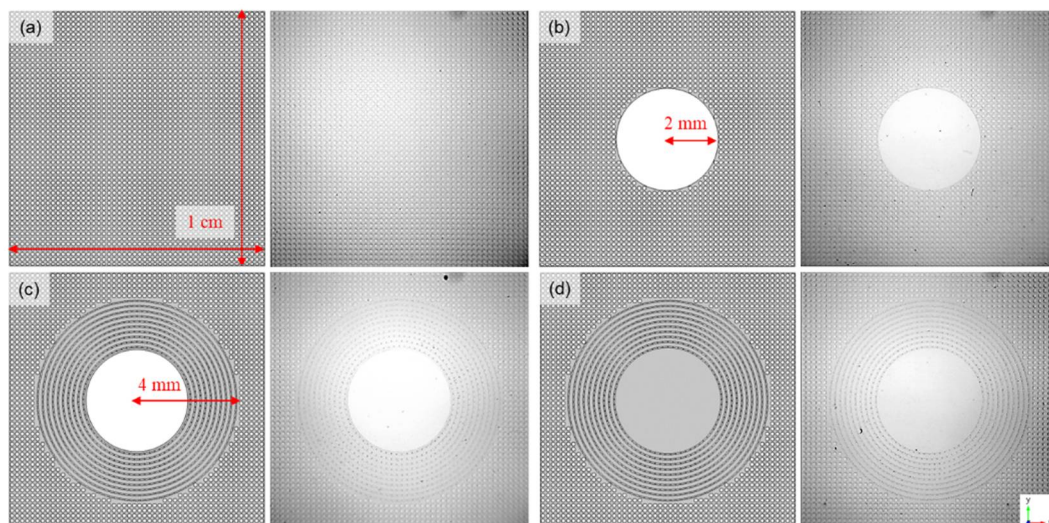


**Figure 2.3.22.** Comparison of microstructures between the drawings (left) and the fabricated microdevices (right). (a) The bare, (b) obstacle, (c) cloaked-obstacle, and (d) cloak-only cases.

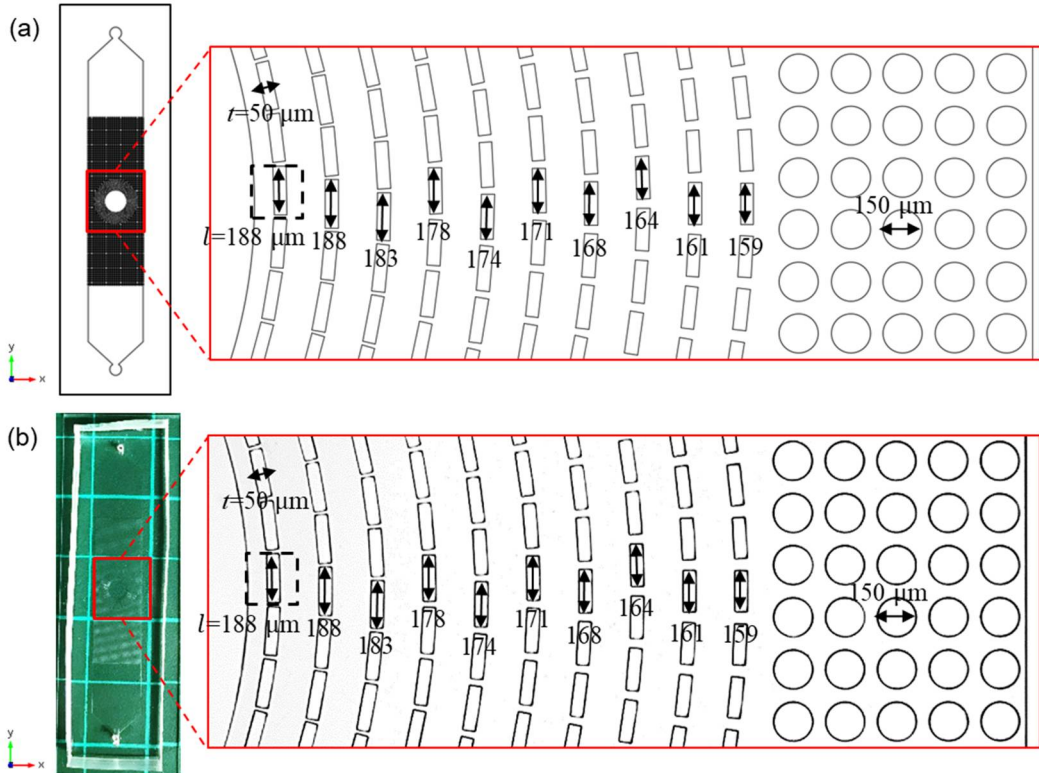


**Figure 2.3.23.** Detailed configuration at microscale of (a) the designed rheological metamaterial cloak and (b) the fabricated rheological metamaterial cloak.

### 2.3.5.2. Experimental method

The rheological cloaking effect was experimentally characterized in the microfluidic devices by observing and capturing flow streamlines. Immediately prior to the experiment, the inlet and outlet of the microchannel were punched with a Harris Uni-Core 1.5-mm-diameter puncher (Ted Pella, Inc., United States). Then flexible plastic tubes (Tygon®, Saint-Gobain Performance Plastics, France) were connected to each entry. The fluid was injected into the reservoirs of the microchannel through a 3 ml syringe (3 ml sterile, non-toxic, and non-pyrogenic Kovax-Syringe, Korea Vaccine Co., Ltd, Republic of Korea) connected to the plastic tubes.

The used fluid in the experiment was water, the typical Newtonian fluid with  $1 \text{ kg/m}^3$  mass density and  $1 \text{ mPa} \cdot \text{s}$  dynamic viscosity at room temperature. Fluorescent

microparticles with a radius of 3.2  $\mu\text{m}$  (Red fluorescent, Fluoro-Max<sup>TM</sup>, CAT.NO.RO300, LOT NO.42259, Thermo Scientific, United States) were dispersed in the water to visualize streamlines of fluid flow. The volumetric concentration of the microparticle/water solution was 0.3  $\mu\text{l/ml}$ . TWEEN<sup>®</sup> 20 (Polyethylene glycol sorbitan monolaurate, Sigma Aldrich, United States), a nonionic detergent, was added to the microparticle/water solution with a volume concentration of 0.1  $\mu\text{l/ml}$  to help dispersion and avoid aggregation of the microparticles.

The total experimental set-up is represented in **Fig. 2.3.24(a)**. Particle streamlines were observed by using an inverted fluorescence microscope (IX53, Olympus corporation, Japan). UPlanFL N 4x/0.13 PhP (Olympus corporation, Japan) was used as a microscope objective lens. A color CCD (charge-coupled device) camera (AcquCAM 23G, JNOpTIC corporation, Republic of Korea) was installed to the microscope with a low-magnification C-mount adapter (U-TV0.5XC, Olympus corporation, Japan). The adapter was necessary to take wider images when shooting the microchannel and flow streamlines.

Pressure-driven fluid flow was generated by using a N<sub>2</sub> gas pressure pump with a pressure of 0.05 bar (5 kPa). Because the total length of the microchannel is set to 5 cm, this pressure condition is consistent with the simulation pressure condition applying 1 kPa to the geometries. A digital pressure gauge (DPG8001-60, OMEGA Engineering, United States) was used to control pressure values with a precision regulator (100LR, ControlAir Inc., United States) (**Fig. 2.3.24(b)**). After filling the syringe with the microparticle/water solution, the pressure exerted by the gas pump caused Poiseuille flow in the microchannel. The streamlines of microparticles could be taken by properly controlling light exposure conditions of the CCD camera. The employed light exposure conditions in the experiment were 40.3 dB grain and 0.125 s exposure time.

Images of the particle streamlines were captured by using a commercial CCD camera-related program, JNOPTIC Capture 2.4 (JNOpTIC corporation, Republic of Korea). The captured images were processed to clearly show the streamlines by using Adobe Photoshop CS6 (Adobe Systems, United States). Color of the streamlines was changed from red to green, brightness and contrast of the images were optimized, and background noise was removed. Also, immobilized fluorescent microparticles that either stick to the microstructures or aggregate each other also removed from the taken images.

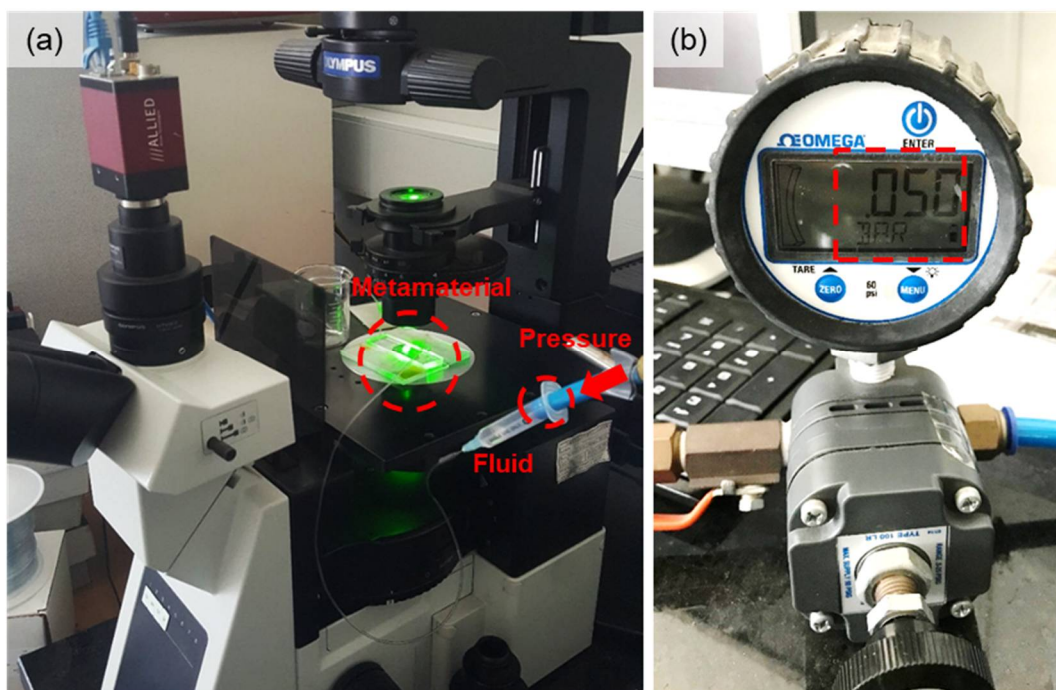


**Figure 2.3.24.** Experimental set-up for observation of fluorescent microparticle streamlines. (a) A microscope with a fluid-filled syringe and a microfluidic device. (b) A pressure regulator set to apply 5 kPa.

### 2.3.5.3. Experimental results

Experimental realization of the rheological cloak was carried out with the fabricated metamaterial devices. The particle streamlines were captured and compared with the corresponding simulation results (**Figs. 2.3.25**). The simulated streamlines shown in **Fig. 2.3.15(iii)** were slightly enlarged and inserted into **Fig. 2.3.25** to compare with the experimental results at the same magnification.

The captured streamlines of the bare case were observed to have a parallel shape in all regions without being bent or interrupted by something, like the simulation result of the bare case (**Fig. 2.3.25(a)**). In the obstacle case, a cylinder obstacle is placed at the center of the microchannel (**Fig. 2.3.25(b)**). Therefore, the streamlines were perturbed by a drag force generated on the surface of the obstacle. The generation of drag was also confirmed by the microparticles striking the obstacle surface. In **Fig. 2.3.25(b)**, the red dotted line indicates the outline of the obstacle. By observing the streamlines near the red line, it was found that the green streamlines are densely formed along the outline of the obstacle. This phenomenon not only means that the presence of an object can be perceived from a rheological point of view, but also indicates that the overall flow rate of the microchannel is slowed by the drag generated when the fluid hits the obstacle surface. The isopressure lines could be expected from the streamlines since these two lines are mathematically orthogonal to each other. In the bare case, the pressure field is expected to be uniformly formed, but in the obstacle case, it is thought to be disturbed due to the drag on the obstacle surface.

This drag generation can be prevented by surrounding the obstacle with the rheological metamaterial cloak. (**Fig. 2.3.25(c)**). The streamlines outside the cloak remained in a parallel shape as if there is no obstacle at the center. The shape of streamlines in the cloaking shell is very similar to that in the simulation results. Also, unlike the obstacle case, it could be confirmed that the green particle streamlines are hardly formed on the red dotted line, the obstacle outline. This is experimental evidence that there is little drag on the obstacle surface. It is noticed from the slowly moving particles in the vicinity of the obstacle that the fluid momentum is successfully bypassed around the obstacle surface without generating drag. The drag-free space could be more clearly validated in the cloak-only case (**Fig. 2.3.25(d)**). In the central cloaked region, the microparticles flowed at about



0.5 mm/s, which is much slower than the flow rate of the background.

In fact, if the cloaking function operates perfectly, the fluid force must be completely precluded from the central region, so there should be no microparticles in it. In development of transformation rheology, the creeping flow condition was assumed for the simplified form of the Navier-Stokes equations. In this process, the fluid inertia effect was completely excluded from the Navier-Stokes equations. Therefore, the metamaterial cloak could not bypass the fluid inertia force penetrating into the central region. In addition, the approximation made during the multilayer compartmentalization and the unit cell mapping might cause problems with the perfect cloaking performance to create a space with a zero flow rate. In summary, the zero flow rate in the cloaked region, which means a perfect drag-free space, is not feasible due to the fluid inertia and the approximate error in effective media.

Since the rheological metamaterial cloak is designed by the unit cell mapping method, its practical uses are limited. The biggest problem is that the effective viscosity should be increased to several times the base fluid viscosity to make the fluid viscosity greater than 1. In the lab scale experiment, this problem was solved by setting the effective viscosity of the background area to 2.78 mPa·s by mapping the microcylinders. Therefore, much advances of the viscosity control technique are essential since the rheological metamaterial cloak itself cannot be used alone. Research for producing arbitrary-shaped cloaks is also very meaningful to widen the application range of this study. Overall, this study presents a new direction for reducing a fluid resistant force through space distortion and is valuable as an original research.

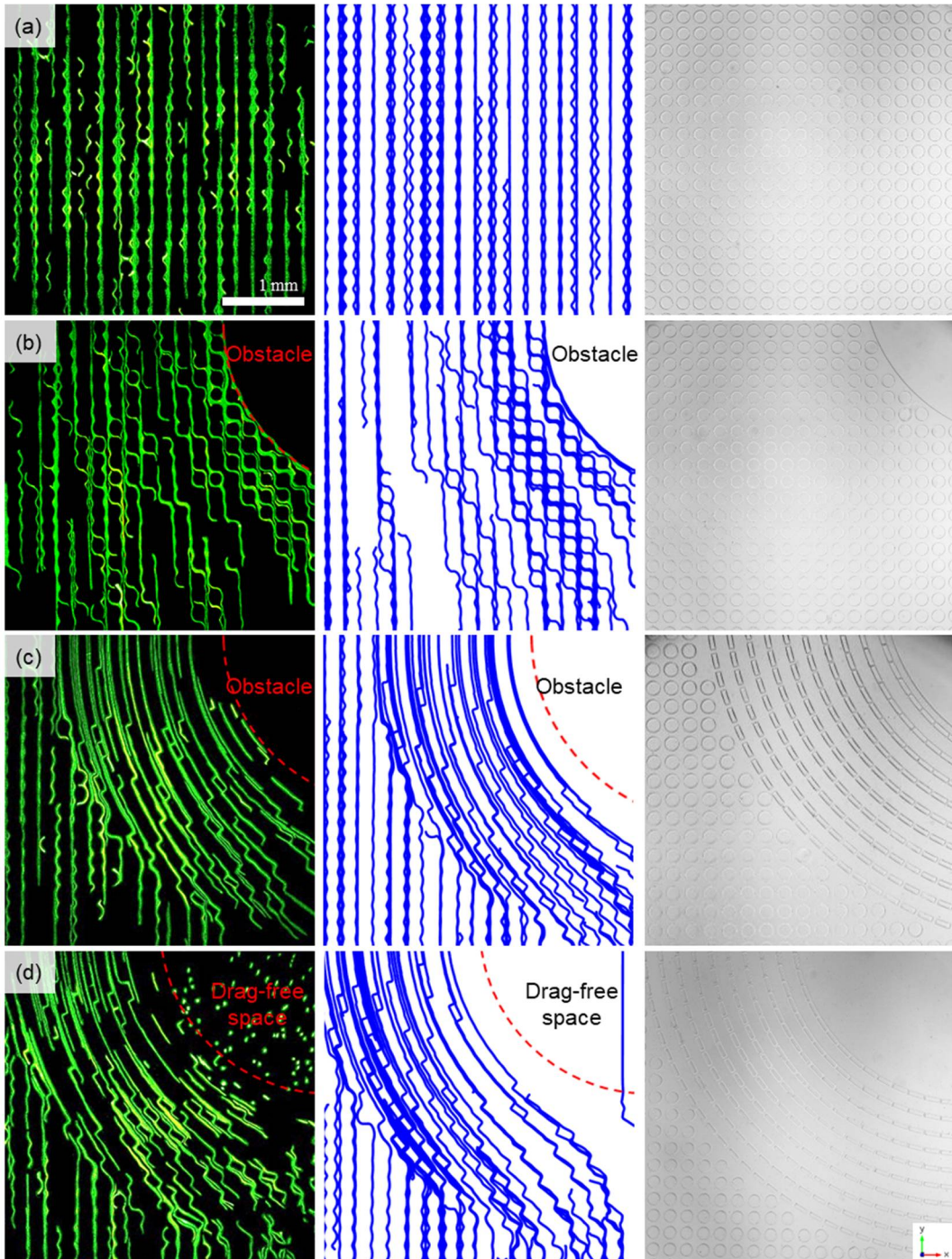


**Figure 2.3.25.** Observed streamlines (left), simulated streamlines (center), and microstructures in the experiment (right) for (a) the bare, (b) obstacle, (c) cloaked-obstacle, and (d) cloak-only cases.

### **2.3.6. Conclusions**

In this section, a novel strategy to minimize drag was proposed by wrapping an obstacle in the rheological cloak. The Jacobian matrix required for cloaking was calculated based on transformation rheology. Numerical analysis was carried out by using the transformed viscosity tensor, and the cloaking behavior was confirmed theoretically. The design of the rheological metamaterial cloak was sequenced by using the multilayer method and the effective viscosity unit cells. The designed cloak was theoretically pre-tested and fabricated as a microfluidic device. It was experimentally confirmed from the captured streamlines that the fabricated metamaterial cloak can successfully guide fluid flow as designed and dramatically reduce the drag on the obstacle surface. The developed rheological cloak is anticipated to open up the new road to unprecedented control of fluid flow not found in nature. The rheological cloak can be used as an artificial architecture to detour natural meteorological or hydrological disasters. Furthermore, if this concept is extended to aerodynamics, drag-free operation of vehicles, such as aircrafts, automobiles, and submarines, will be possible dramatically increasing fuel efficiency.

## 2.4. Rheological concentrator

### 2.4.1. Introduction

Hydropower is a means of harvesting energy from a fast flowing fluid. It is derived from the energy of falling or fast running water, and then also called water power. From ancient to modern times, the hydropower has been harnessed as a renewable energy source for the operation of various machineries by switching its power to electricity, *i.e.*, hydroelectric power. The hydroelectric power accounts for a significant portion of the total electricity generation and particularly, it contributes about half of all renewable energy generation. Improvement of hydroelectricity production efficiency is a long-felt desire of engineers involved in fluid mechanics. There are many factors to achieve this desire but fundamentally, it is essential to speed up the water running a turbine.

So far, various metamaterial cloaks [8,9,26,45] have been reported based on transformation physics [25,28,36,50]. On the other hand, transformation physics has enabled not only the cloaks but also other types of metamaterials, such as negative refraction [160], perfect absorbers [161], rotators [41], superlens [5], and artificial black-holes [162]. An energy field concentrator is one of the significant metamaterial classes that collects and focuses energy in a target space. Several electromagnetic energy concentrators have been reported [38,163] by modeling a space that simultaneously expands and compresses. Improving efficiency of magnetic energy harvesting was suggested as a potential application of the metamaterial concentrator [39]. Furthermore, thermodynamic metamaterial concentrators [45,53] were reported to focus heat flux in the central encircled region, which are potentially applicable in solar thermal panels or thermal-electric devices.

However, there are few examples of metamaterial concentrators that have been experimentally implemented. Moreover, metamaterial concentrators for hydropower have never been reported theoretically or experimentally. Increasing the efficiency of hydroelectric power generation is a meaningful research result in terms of energy harvesting. Therefore, the development of a rheological metamaterial concentrator can provide a breakthrough source technology that can collect fluid energy in an unprecedented way.

In this section, a rheological metamaterial concentrator is demonstrated from mathematical modeling, simulation, metamaterial design, to experimental realization of that. A transformed viscosity tensor for concentrating a fluidic space was derived by calculating a transformation Jacobian matrix based on transformation rheology. Function and performance of the rheological concentrator were investigated theoretically from numerical analysis. Effective viscosity unit cells for the concentrator were theoretically designed and the rheological metamaterial concentrator was designed by mapping them. The designed rheological metamaterial concentrator was numerically simulated, fabricated, and characterized experimentally. It was conformed that the designed metamaterial can concentrate fluid momentum to the inner space of it.

## 2.4.2. Fluidic space modeling

In Section 2.3, the total transformation matrix ( $\mathbf{\Lambda}$ ) for cloaking a space was calculated and applied to the shell region in a form of the transformed viscosity tensor.  $\mathbf{\Lambda}$  is composed of  $\boldsymbol{\lambda}$ ,  $\mathbf{B}$ , and  $\mathbf{B}'$  as described in Eqn. 2.3.1. In this section, a total Jacobian transformation matrix ( $\mathbf{\Lambda}$ ) for concentrating a space was derived by calculating and introducing  $\boldsymbol{\lambda}$  connecting between the virtual and physical spaces.

The most important feature in this space modeling is that the concentrator should compress and simultaneously expand a space without affecting a space outside the concentrator (Fig. 2.4.1). Unlike the coordinate system of the virtual space, much denser coordinate system can be created in the physical space. The space outside the concentrator is not deformed because the space expands as much as the space is compressed in the concentrator.

Mathematical modeling for the concentrator also requires a radial stretch of linear geometric transformation under the two-dimensional cylindrical case assumption. Unlike the cloaking shell, the concentrating shell consists of two concentric rings; the inner radius is  $a$ , the middle radius is  $b$ , and the outer radius is  $c$  (Fig. 2.4.1). The following relationship compresses the space from  $0 < r < b$  into  $0 < r' < a$  and simultaneously expands the space from  $b < r < c$  into  $a < r' < c$ .

$$\begin{cases} r' = \left(\frac{a}{b}\right)r & 0 < r < b \\ r' = \left(\frac{c-a}{c-b}\right)r - \left(\frac{b-a}{c-b}\right)c & b < r < c \end{cases} \quad (2.4.1)$$

$$\theta' = \theta \quad (2.4.2)$$

$$z' = z \quad (2.4.3)$$

By this spatial deformation, the energy flux can be focused on the central region ( $0 < r' < a$ ) by  $b/a$  times while the total amount of energy is unchanged. The Jacobian matrix ( $\boldsymbol{\lambda}$ ) and the determinant of  $\boldsymbol{\lambda}$  for this spatial deformation are defined as

$$\lambda = \begin{bmatrix} \frac{\partial r'}{\partial r} & \frac{\partial r'}{\partial \theta} & \frac{\partial r'}{\partial z} \\ \frac{\partial \theta'}{\partial r} & \frac{\partial \theta'}{\partial \theta} & \frac{\partial \theta'}{\partial z} \\ \frac{\partial z'}{\partial r} & \frac{\partial z'}{\partial \theta} & \frac{\partial z'}{\partial z} \end{bmatrix} = \begin{cases} \begin{bmatrix} \frac{a}{b} & 0 & 0 \\ 0 & 1 & 0 \\ 0 & 0 & 1 \end{bmatrix} & 0 < r < b \\ \begin{bmatrix} \frac{c-a}{c-b} & 0 & 0 \\ 0 & 1 & 0 \\ 0 & 0 & 1 \end{bmatrix} & b < r < c \end{cases} \quad (2.4.4)$$

$$\det(\lambda) = \begin{cases} \frac{a}{b} & 0 < r < b \\ \frac{c-a}{c-b} & b < r < c \end{cases} \quad (2.4.5)$$

With **Eqns. 2.4.4-5**, the total Jacobian matrix ( $\Lambda$ ) and its determinant for the concentrating shell are yielded as

$$\Lambda = \mathbf{B}'^{-1} \lambda \mathbf{B} = \begin{cases} \begin{bmatrix} \frac{a}{b} & 0 & 0 \\ 0 & \frac{r'}{r} & 0 \\ 0 & 0 & 1 \end{bmatrix} & 0 < r' < a \\ \begin{bmatrix} \frac{c-a}{c-b} & 0 & 0 \\ 0 & \frac{r'}{r} & 0 \\ 0 & 0 & 1 \end{bmatrix} & a < r' < c \end{cases} \quad (2.4.6)$$

$$\det(\Lambda) = \begin{cases} \left(\frac{a}{b}\right) \left(\frac{r'}{r}\right) & 0 < r' < a \\ \left(\frac{c-a}{c-b}\right) \left(\frac{r'}{r}\right) & a < r' < c \end{cases} \quad (2.4.7)$$

**Equations 2.4.6-7** can be described in terms of physical space variables only by substituting the radial variable in the virtual space ( $r$ ) to the physical space variable ( $r'$ ) and the geometrical parameters.

$$\mathbf{\Lambda} = \mathbf{B}'^{-1} \boldsymbol{\lambda} \mathbf{B} = \begin{cases} \begin{bmatrix} \frac{a}{b} & 0 & 0 \\ 0 & \frac{a}{b} & 0 \\ 0 & 0 & 1 \end{bmatrix} & 0 < r' < a \\ \begin{bmatrix} \frac{c-a}{c-b} & & 0 \\ 0 & \left( \frac{r'}{r' + \left( \frac{b-a}{c-b} \right) c} \right) \left( \frac{c-a}{c-b} \right) & 0 \\ 0 & & 1 \end{bmatrix} & a < r' < c \end{cases} \quad (2.4.8)$$

$$\det(\mathbf{\Lambda}) = \begin{cases} \left( \frac{a}{b} \right)^2 & 0 < r' < a \\ \left( \frac{r'}{r' + \left( \frac{b-a}{c-b} \right) c} \right) \left( \frac{c-a}{c-b} \right)^2 & a < r' < c \end{cases} \quad (2.4.9)$$

The transformed viscosity tensor for the concentrator was calculated with  $\mathbf{\Lambda}$  and  $\det(\mathbf{\Lambda})$ . Following **Eqn. 2.2.27**, the transformed viscosity tensor ( $\tilde{\boldsymbol{\mu}}'$ ) is calculated as

$$\tilde{\boldsymbol{\mu}}' = \det(\mathbf{\Lambda}) \mathbf{\Lambda}^{-1} \boldsymbol{\mu} \mathbf{\Lambda}^{-T}$$

$$= \begin{cases} \begin{bmatrix} 1 & 0 & 0 \\ 0 & 1 & 0 \\ 0 & 0 & \left( \frac{a}{b} \right)^2 \end{bmatrix} \boldsymbol{\mu} & 0 < r' < a \\ \begin{bmatrix} r' / \left( r' + \left( \frac{b-a}{c-b} \right) c \right) & & 0 \\ 0 & \left( r' + \left( \frac{b-a}{c-b} \right) c \right) / r' & 0 \\ 0 & & \left( \frac{r' + \left( \frac{b-a}{c-b} \right) c}{r'} \right) \left( \frac{c-b}{c-a} \right)^2 \end{bmatrix} \boldsymbol{\mu} & a < r' < c \end{cases} \quad (2.4.10)$$

The radial profiles of  $\tilde{\boldsymbol{\mu}}'$  are plot in **Fig. 2.4.2(a)**.

Unlike the ideal set of the transformed viscosity tensor for the cloaking shell, a matrix singularity is not arisen in **Eqn. 2.4.10**. However, **Equation 2.4.10** is still hard to be



realized experimentally since the components change simultaneously along both axes, especially in the region  $a < r' < c$ . To mitigate this condition, a reduced set of the transformed viscosity tensor ( $\tilde{\boldsymbol{\mu}}''$ ) for the concentrator, similar to the cloak but slightly different, was obtained by multiplying  $\tilde{\boldsymbol{\mu}}'$  by  $\det(\boldsymbol{\Lambda}^{-1})$  as

$$\tilde{\boldsymbol{\mu}}'' = \tilde{\boldsymbol{\mu}}' \det(\boldsymbol{\Lambda}^{-1}) = \begin{bmatrix} \left(\frac{c-b}{c-a}\right)^2 & 0 \\ 0 & \left(\frac{c-b}{c-a}\right)^2 \left\{ \left( r' + \left( \frac{b-a}{c-b} \right) c \right) / r' \right\}^2 \end{bmatrix} \mu \quad (2.4.11)$$

, by referring the previous work conducted by Wang *et al.* [164]. By exploiting this mathematical treatment, the radial component becomes a constant and experimental implementation conditions can be much more relaxed. However, impedance mismatching problem at the outer boundary (at  $r' = c$ ) occurs like the cloak case. This issue was treated by multiplying the viscosity tensor (Eqn. 2.4.11) by a factor of 2. The radial profiles of  $\tilde{\boldsymbol{\mu}}''$  are plot in Figs. 2.4.3(a). In Eqn. 2.4.11, the vertical component was not considered because only y-direction pressure-driven flow was analyzed as in Section 2.3.

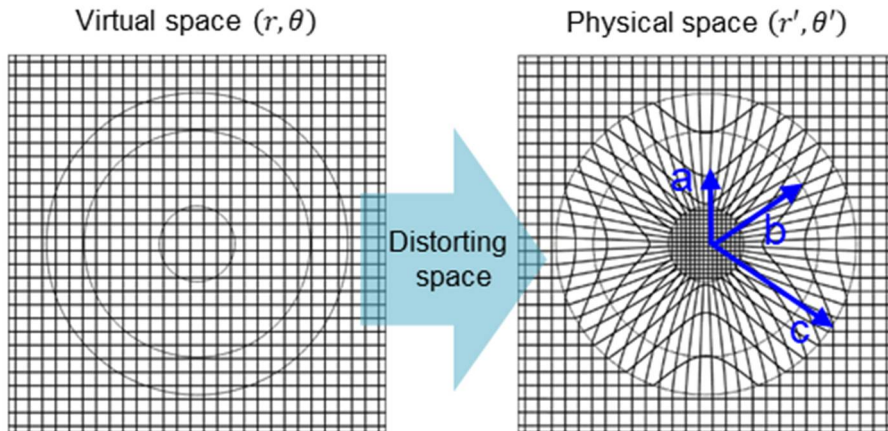


**Figure 2.4.1.** Coordinate grids representing spatial transformation by a concentrator.

### 2.4.3. Numerical analysis

#### 2.4.3.1. Simulation conditions

Numerical simulation was carried out by using COMSOL Multiphysics. As a simulation result, pressure and velocity fields of fluid flow were visualized and analyzed. Basically, most simulation conditions coincide with the conditions described in Section 2.3.3.1.

A hexahedron block geometry shown in **Fig. 2.3.3(a)** was used, which has a dimension of  $1\text{ cm} \times 1\text{ cm} \times 50\text{ }\mu\text{m}$ . A concentric ring that indicates the concentrator was incorporated in the block, whose inner radius  $a$  is 1 mm and outer radius  $c$  is 4 mm. The same boundary conditions and material properties of the cloak case were used in the simulation. The customized PDE (partial difference equation) interface developed in Section 2.3.3.1 was employed to simulate the rheological concentrator that requires tensor components of viscosity as a material property input.

### 2.4.3.2. Simulation results

In this section, the simulation results for the rheological concentrator are shown, compared, and discussed with the bare case. Numerical simulation was carried out to solve fluid flow affected by the ideal concentrator with the transformed viscosity tensor in **Eqn. 2.4.10** and **Fig. 2.4.2(a)**. The radial viscosity gradually increases from 0.111 mPa·s at  $r' = a$  to 0.333 mPa·s at  $r' = c$  and the azimuthal viscosity changes from 9 mPa·s at  $r' = a$  to 3 mPa·s at  $r' = c$ . The impedance between the ideal concentrator and the background is perfectly matched at  $r' = c$ , so the impedance matching treatment is not needed.

The simulation results for the ideal concentrator are shown in **Fig. 2.4.2(b)** with the bare case (**Fig. 2.4.2(c)**). The transformed Navier-Stokes equations (**Eqns. 2.2.29-30**) were solved by using the customized PDE interface built in COMSOL Multiphysics. The explanation of the simulation results for the ideal concentrator is omitted to avoid unnecessarily overlapping description with the reduced case (**Fig. 2.4.3**).

For easier experimental implementation, a reduced set of the transformed viscosity tensor ( $\widetilde{\mu}''$ ) was suggested as **Eqn. 2.4.11**. The reduced concentrator can achieve the similar concentrating performance, but the viscosity tensor should be scaled up with a factor of 2 to resolve the impedance mismatch phenomenon at the boundary. Each viscosity component is plotted in **Fig. 2.4.2(a)**. The radial component becomes a constant value of 0.222 (=2/9) mPa·s while the azimuthal component still varies from 18 mPa·s at  $r' = a$  to 2 mPa·s at  $r' = c$ . In contrast to the cloak case,  $\mu''_{\theta\theta}$  is the only varying component along the azimuthal distance, not  $\mu''_{rr}$ .

The simulation results for the reduced concentrator are shown in **Fig. 2.4.3(b)** with the pressure, pressure gradient, and velocity fields. The simulated fields of the bare case were arranged next to the figures to check the effect of the concentrator through comparison (**Fig. 2.4.3(c)**). The pressure fields are focused on the central region, generating 3 times higher pressure gradient (**Figs. 2.4.3(b-c), (i-ii)**). The magnitude of pressure gradient inside the concentrator was rated at 300 kN/m<sup>3</sup> while the value outside the concentrator was evaluated to 100 kN/m<sup>3</sup> (**Fig. 2.4.4(a)**). As designed in Section 2.4.2, the pressure field was exactly  $b/a$  times compressive in the central deformed fictitious space with a threefold increase in physical quantities. The collected hydraulic force in the central region could accelerate the fluid flow (**Fig. 2.4.3(b), (iii)**). The original flow rate was about 31 mm/s,

but the flow rate of the space surrounded by the concentrator was accelerated to about 93 mm/s, exactly three times the original flow rate (**Fig. 2.4.4(b)**). It is worth noting that the background fields including both pressure and velocity fields are not affected by this spatial change.

Hydraulic kinetic energy ( $E_k$ ) of the central region was calculated to ascertain how much kinetic energy can be increased by the flow rate increase due to the spatial concentration. The hydraulic kinetic energy is a parameter that is directly related to the efficiency of hydropower generation, which is the potential application of the rheological concentrator, so it is worth to calculate it. The hydraulic kinetic energy  $E_k$  is defined as

$$E_k = \frac{\rho V \langle \tilde{\mathbf{u}} \rangle_V^2}{2} \quad (2.4.12)$$

, where  $\rho$  is the mass density of a fluid,  $V$  is the volume of the central region, and  $\tilde{\mathbf{u}}$  is the velocity of the region, and  $\langle \cdot \rangle_V$  is the volume averaging operator. The  $E_k$  value of the area without the concentrator was calculated to be  $1.47 \times 10^{-4}$   $\mu\text{J}$  on the whole region. However, the  $E_k$  value of the area inside the concentrator increased 9 times from  $1.47 \times 10^{-4}$   $\mu\text{J}$  to  $1.32 \times 10^{-3}$   $\mu\text{J}$  (**Fig. 2.4.4(c)**). From these calculation results, it was theoretically verified that the rheological concentrator can collect more hydroelectric power in the space where a flowing fluid is turning a turbine.

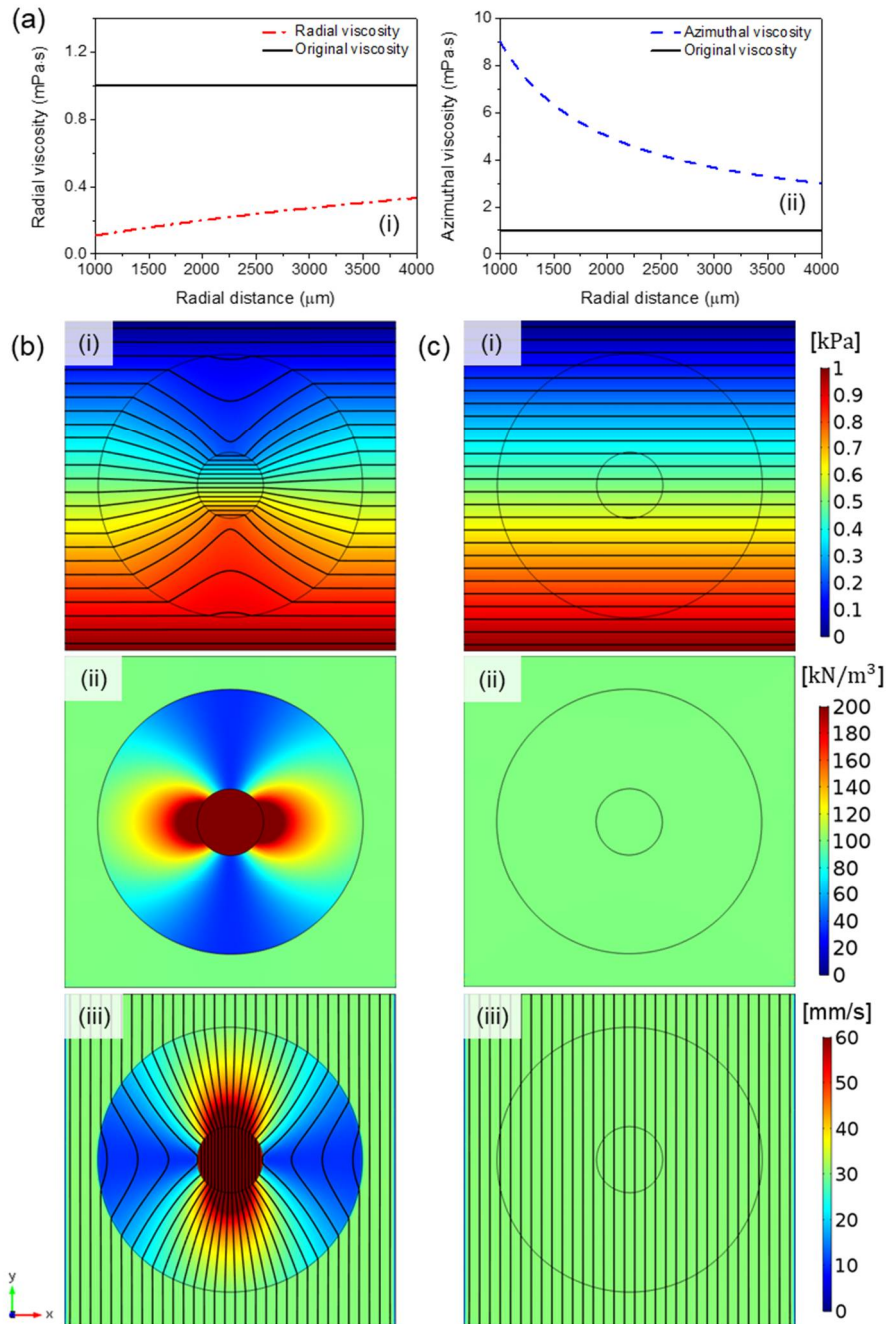


**Figure 2.4.2.** Modeling of the ideal case rheological concentrator. (a) Spatially varying viscosity tensor components in (i) radial and (ii) azimuthal axes. Simulation results for (b) the ideal concentrator and (c) bare case of (i) pressure fields, (ii) pressure gradient fields ( $p_y$ ), and (iii) velocity fields.

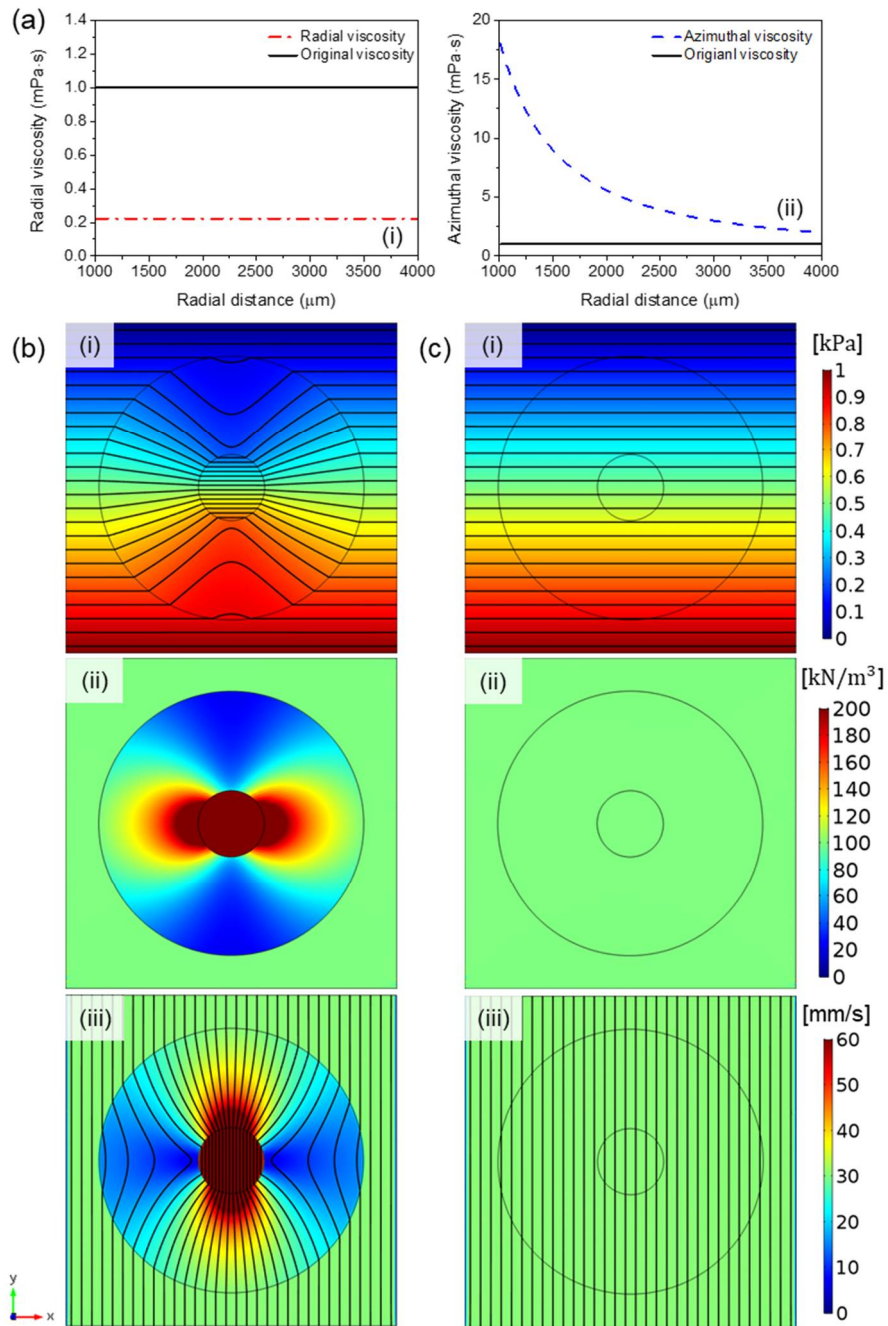


**Figure 2.4.3.** Modeling of the reduced case rheological concentrator. (a) Spatially varying viscosity tensor components in (i) radial and (ii) azimuthal axes. Simulation results for (b) the reduced concentrator and (c) the bare case of (i) pressure fields, (ii) pressure gradient fields ( $p_y$ ), and (iii) velocity fields.

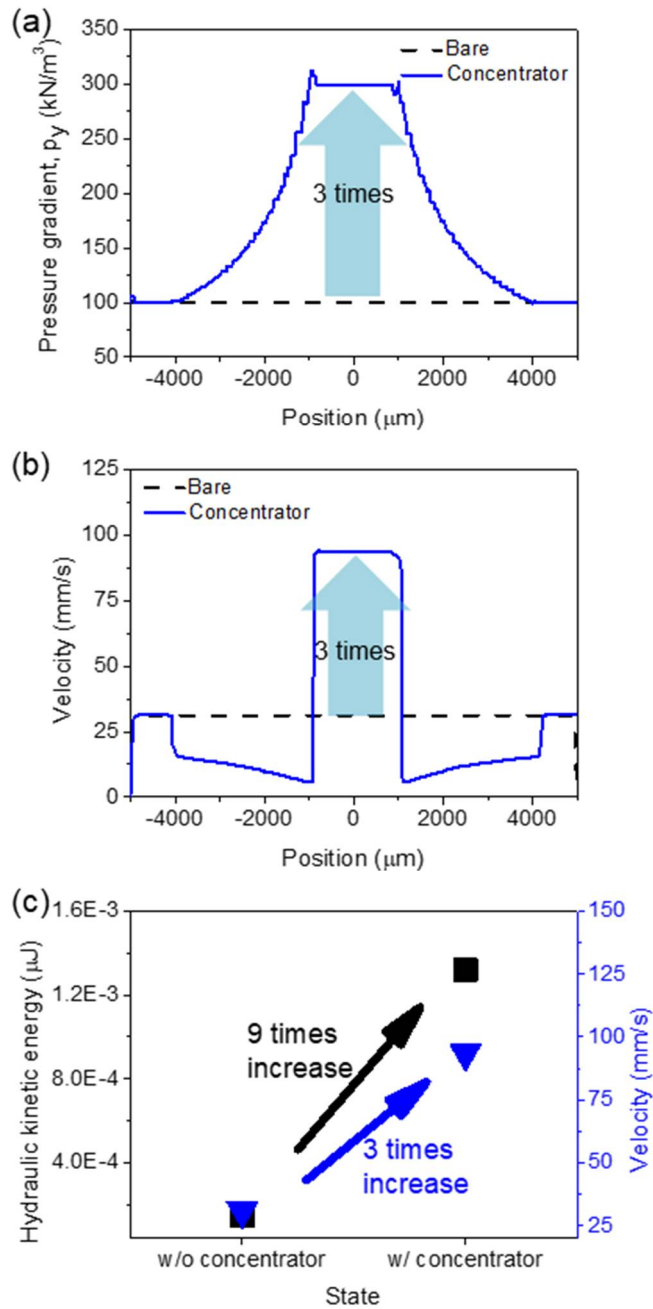


**Figure 2.4.4.** Profiles of the simulation fields and the calculated flow parameters. Profiles of (a) pressure gradient fields ( $p_y$ ) and (b) velocity fields at the center (the line at  $y=0.5$  cm and  $z=25$   $\mu\text{m}$ ). (c) Comparison of the hydraulic kinetic energy and mean velocity with or without the concentrator.

## 2.4.4. Metamaterial design

### 2.4.4.1. Multilayered concentrator

Before proceeding with design of the metamaterial concentrator, a multilayered rheological concentrator was theoretically constructed and simulated by using a homogenized layer method [25,28]. It is experimentally impossible to implement a perfect viscosity gradient seamlessly in all-region of the concentrator shell.

The shell region of the concentrator ( $a < r' < c$ ) was separated to 10 annular layers (**Fig. 2.4.5**). The layers were numbered from 1 to 10 in order from inside to outside and the thickness of each layer was 300  $\mu\text{m}$ , which is one tenth of the total thickness of the concentrator shell, 3000  $\mu\text{m}$  ( $c - a$ ). The material parameters of each layer were allocated to the averaged components (in  $r$  and  $\theta$  axes) of the scaled transformed viscosity tensor (**Fig. 2.4.3(a)**). The spatial profiles of the contributed viscosity value are shown in **Fig. 2.4.6(a)** and **Table 2.4.1**. While the radial viscosity component maintains a constant value of 0.111, the azimuthal component varies from 14.38 mPa·s at  $r' = a$  to 2.1 mPa·s at  $r' = c$ .

Numerical analysis was carried out by using COMSOL Multiphysics with the multilayered concentrator and its materials properties. The purpose of this numerical study was to verify whether the multilayered concentrator can function similar to the continuous medium concentrator. The simulation conditions were consistent with the conditions for the multilayered cloak. The simulated pressure, pressure gradient, and velocity fields are shown in **Fig. 2.4.6(b)**. The simulated fields of the multilayered concentrator accord with the results of the continuous media case (**Figs. 2.4.3** and **2.4.6**). Not only distribution of the velocity and pressure fields coincide, but also the concentration degree of the fields is three times as high. Naturally, the degree of hydraulic kinetic energy could be also increased accordingly by a factor of 9 (**Eqn. 2.4.12**). Through the multilayered concentrator design and its numerical analysis results, it was theoretically confirmed that even when the concentrating shell is divided into several layers, the desired performance is maintained except for a few minor differences.



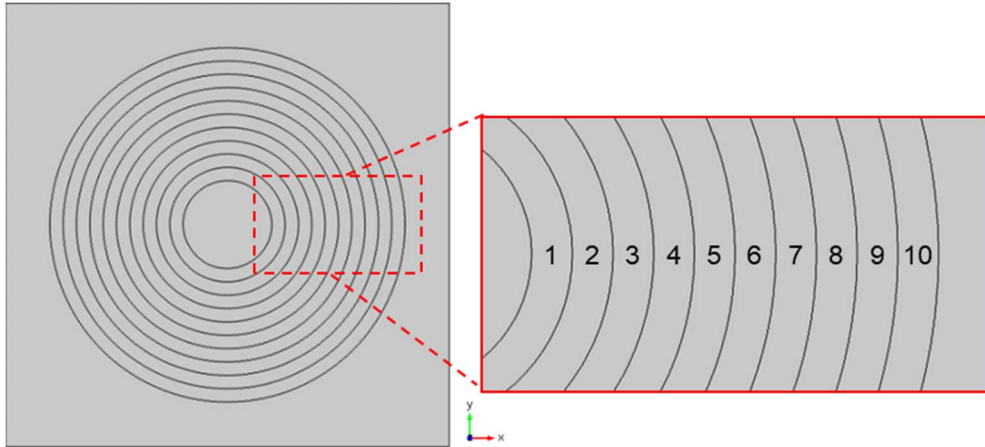


**Figure 2.4.5.** A constructed geometry of the multilayered concentrator and its magnified view.

**Table 2.4.1.** Viscosity tensor components of the multilayered concentrator given to each layer.

Layer No.	$\mu_{eff,r}$ (mPa·s)	$\mu_{eff,\theta}$ (mPa·s)
Center region	1	1
1	0.222	14.38
2	0.222	9.56
3	0.222	6.96
4	0.222	5.36
5	0.222	4.32
6	0.222	3.6
7	0.222	3.06
8	0.222	2.66
9	0.222	2.36
10	0.222	2.1
Background	1	1

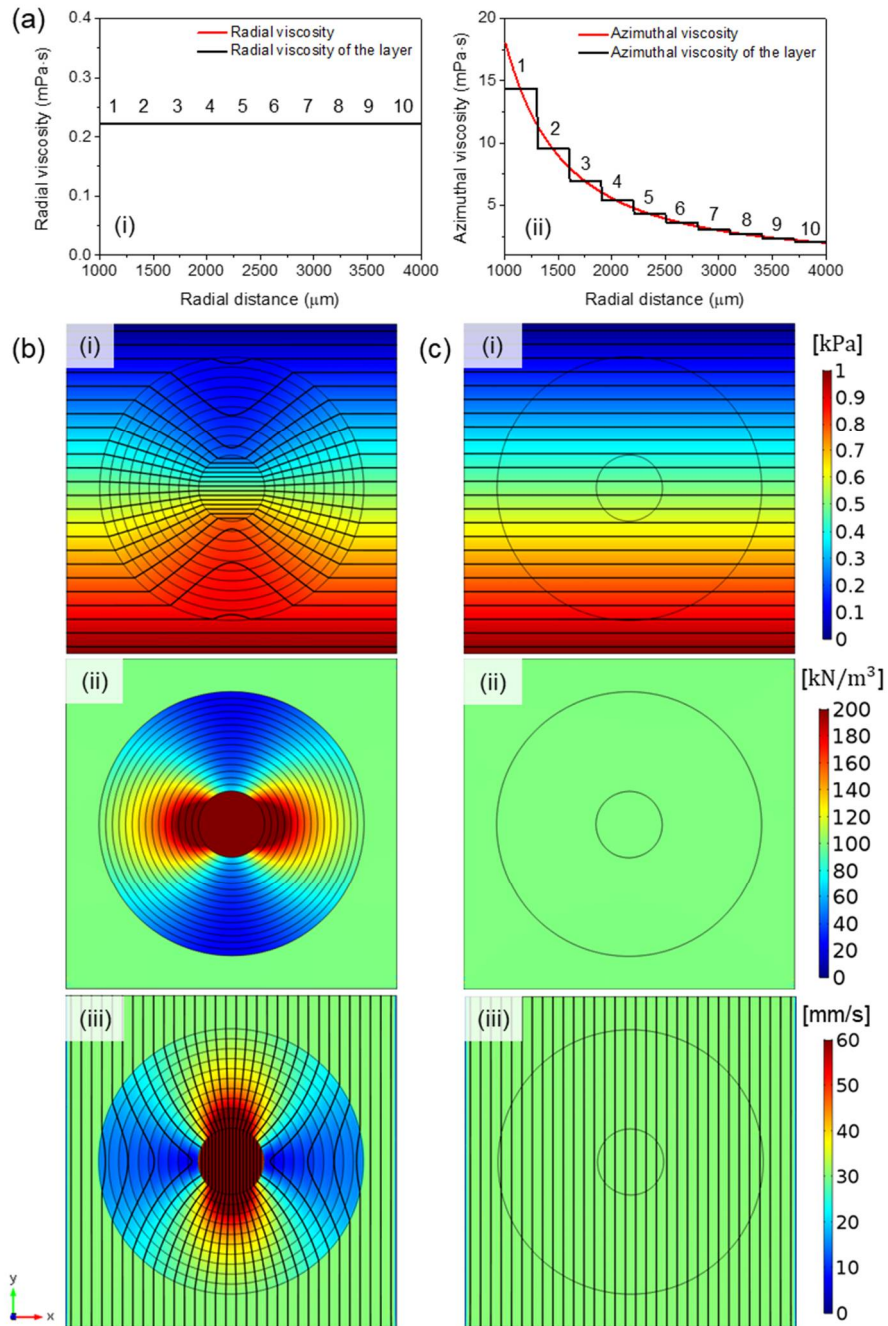


**Figure 2.4.6.** Modeling of the multilayered rheological concentrator. (a) Spatially varying viscosity tensor components in (i) radial and (ii) azimuthal axes. Simulation results for (b) the multilayered concentrator and (c) bare cases of (i) pressure fields, (ii) pressure gradient fields ( $p_y$ ), and (iii) velocity fields.

#### 2.4.4.2. Unit cell modeling

The same strategy used in Section 2.3.4.2 was employed for designing effective viscosity unit cells and mapping the rheological metamaterial concentrator with the unit cells. In the unit cells for the metamaterial cloak, the length in  $\theta$  axis was designed to be much longer than the length in  $r$  axis for embodying anisotropic viscosity components. On the other hand, the unit cell required for the metamaterial concentrator should have a longer length on  $r$  axis than  $\theta$  axis. In accordance with the layer thickness of the multilayered concentrator, 300 by 300 by 50  $\mu\text{m}^3$  unit cells were modeled with theoretically shape-determined micropillars. The velocity field of the bare unit cell without any microstructure is shown in **Fig. 2.4.7(a)** and the effective viscosity of this unit cell is identical with the pristine water viscosity, 1 mPa·s. **Figure 2.4.7(b)** shows the velocity field of the same background unit cell used for the rheological metamaterial cloak.

The viscosity components given to each layer (**Table 2.4.1**) were multiplied by a factor of 5.4 to make the radial viscosity larger than 1 mPa·s, from 0.222 mPa·s to 1.2 mPa·s (red lines in **Fig. 2.4.8**). Ten unit cells with micropillars of different shapes were constructed and their simulated velocity fields are shown in **Fig. 2.4.7(c)**. The effective viscosity components embodied by each unit cell and mapping information are tabulated in **Table 2.4.2**. The length of the micropillars ( $l$ ) was distributed from 285  $\mu\text{m}$  to 265  $\mu\text{m}$ , which functions to diversify the effective viscosity in  $\theta$  axis from 72.06 mPa·s to 11.66 mPa·s. On the other hand, thickness of all micropillars was set to 80  $\mu\text{m}$ , and hence the azimuthal components varies only from 1.204 mPa·s to 1.244 mPa·s irrespective of the layer while remaining constant at almost 1.2 mPa·s. The designed unit cells were mapped on the shell region ( $a < r' < c$ ) and acted as an element of the rheological metamaterial concentrator. The background region ( $r' > c$ ) was mapped with the 150  $\mu\text{m}$  microcylinder to achieve impedance matching.

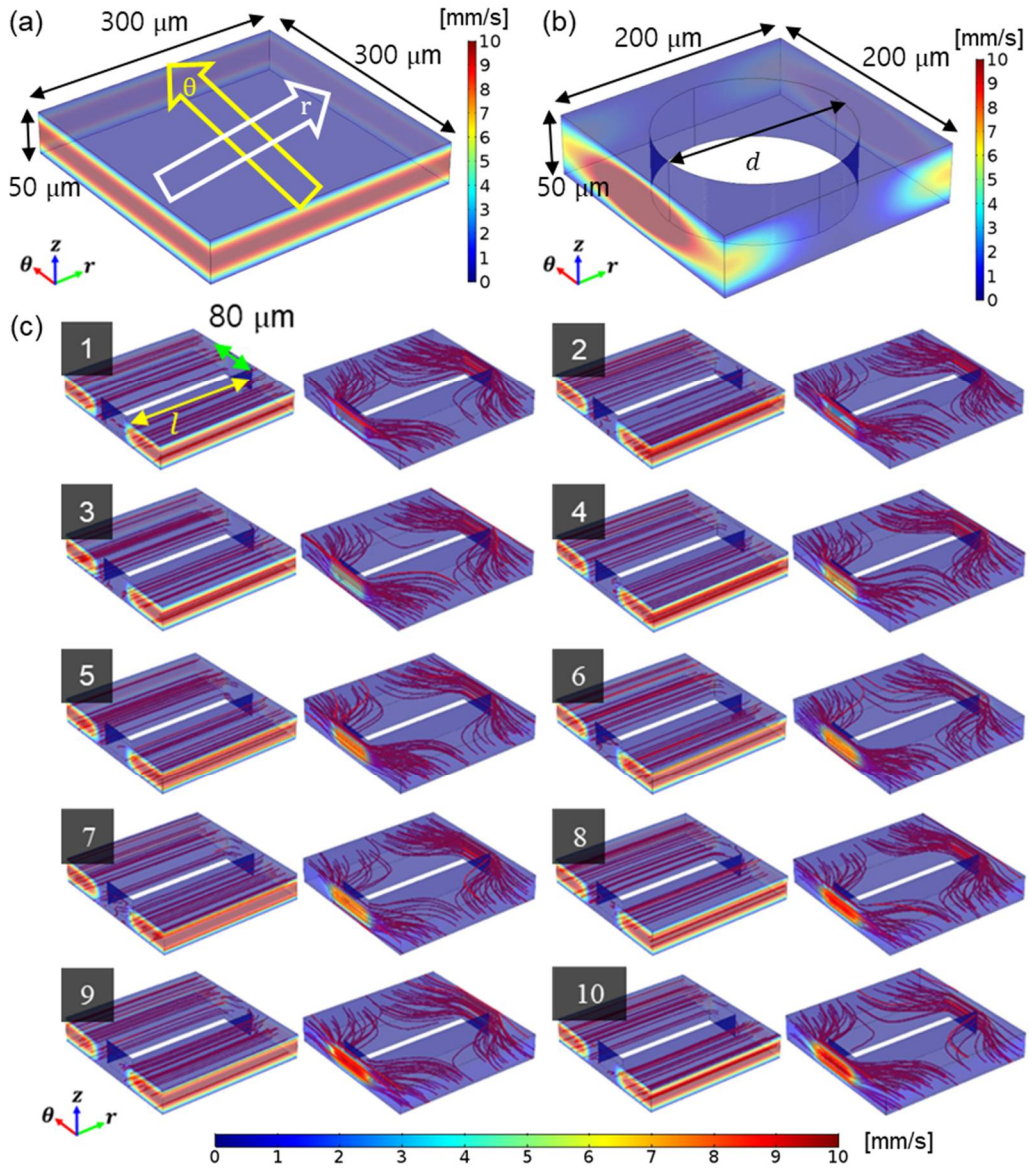


**Figure 2.4.7.** Simulated velocity fields for (a) the bare unit cell without a microstructure, (b) the background unit cell, and (c) the 10 unit cells which are mapped on each layer of the rheological metamaterial concentrator. The left and right figures in (c) show the velocity fields when the pressure field is applied along each axis. Red lines indicate flow streamlines along the flow direction and  $l$  means a length of the micropillar.

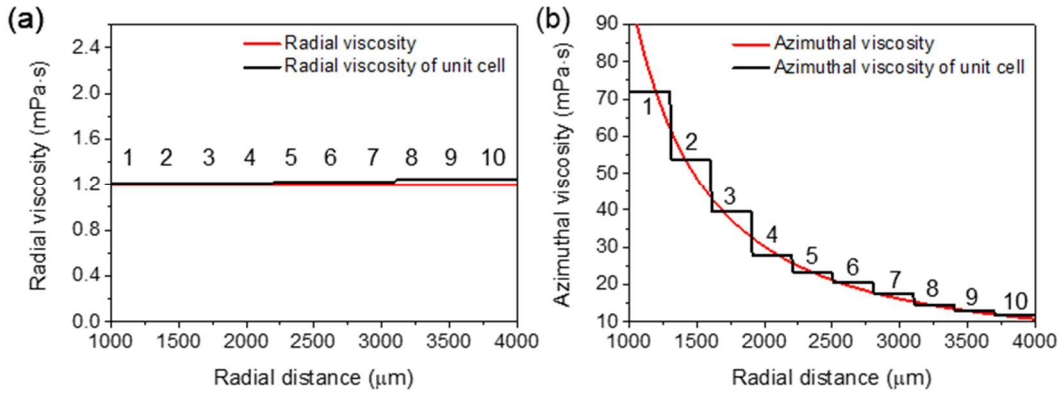


**Figure 2.4.8.** Viscosity tensor components of the unit cells mapped on each layer of the rheological metamaterial concentrator; (a) in radial and (b) azimuthal axes.

**Table 2.4.2.** Effective viscosity unit cells mapped on each layer of the rheological metamaterial concentrator.

Layer No.	$l$ ( $\mu\text{m}$ )	$\mu_{eff,r}$ (mPa·s)	$\mu_{eff,\theta}$ (mPa·s)
Center region	$d=150$	2.758	2.758
1	285	1.2037	72.061
2	283	1.2059	53.617
3	281	1.2122	39.555
4	278	1.2145	27.785
5	276	1.2223	23.224
6	274	1.2240	20.568
7	272	1.2269	17.576
8	269	1.2421	14.653
9	267	1.2443	12.925
10	265	1.2444	11.655
Background	$d=150$	2.758	2.758

\* $d$  means the radius of the microcylinder.

### 2.4.4.3. Designed metamaterial concentrator

The rheological metamaterial concentrator was designed by arranging the 10 anisotropic unit cells developed in Section 2.4.4.2 (**Fig. 2.4.9**). The layers 1 to 10 of the metamaterial concentrator consist of 24, 30, 37, 43, 49, 55, 62, 68, 74, and 81 correlating unit cells. 50×50 number of the isotropic unit cells composed of 150 μm cylinders were mapped in the background for impedance matching. The overall size of the designed concentrator is the same as for the continuous media and multilayered cases. The pillar-arrayed model of the designed metamaterial concentrator was drawn by using CATIA 5.18. After inserting the designed pillar-arrayed concentrator into the hexahedron block, the Boolean operation removed the patterned space, creating a fluid domain model with solid microstructures.

Numerical simulation for the designed metamaterial concentrator was carried out to confirm the concentrating effect. Almost the same simulation conditions as those described in Session 2.3.4.3 were used. The other conditions are described as follows. Completed free tetrahedral meshes consisted of 1304955 domain elements, 553384 boundary elements, 77321 edge elements. The maximum and minimum element size were 52 μm and 10 μm, orderly. The maximum element growth rate was 1.13, the curvature factor was 0.5, and the resolution of narrow regions was 0.8.

**Figure 2.4.10** shows the simulation results of pressure fields, velocity fields, and flow streamlines for the designed metamaterial concentrator. All simulation results are consistent with the previous simulation results of the continuous media and multilayer cases as shown in **Fig. 2.4.11**. The concentrated pressure field in the central region is found in **Fig. 2.4.10(a), (i)**, while the uniformly distributed pressure field in the bare case is shown in **Fig. 2.4.10(b), (i)**. The pressure contours are also created more densely in the central compressed space. It could be seen that the velocity field of the central region inside the metamaterial concentrator greatly increased compared to the outside region or the region without the concentrator (**Figs. 2.4.10(a-b), (ii)**). A number of streamlines were condensed in the central region, which represents concentrated fluid momentum (**Figs. 2.4.10(a-b), (iii)**). As in the cloaking metamaterial, the velocity field and flow streamlines outside the metamaterial concentrator were not perturbed at all, regardless of the spatial variation. The unit cell strategy used to create the rheological metamaterial concentrator can be evaluated as successful from the simulation results of fluid flow fields that are concentrated in the

central region and have no effect on the surrounding space.

The magnified view of the velocity fields shows the increased flow rate more clearly (**Fig. 2.4.12**). To quantitatively analyze the concentrating effect, the average velocity of the unit cell ( $\langle \tilde{\mathbf{u}} \rangle_{unit}$ ) was calculated for the region with or without the concentrator, where  $\langle \cdot \rangle_{unit}$  means the volume averaging operator for the unit cell. The dashed rectangles in **Fig. 2.4.12** indicate the unit cells subject to the calculation of the velocity fields. The mean velocity value ( $\langle \tilde{\mathbf{u}} \rangle_{unit}$ ) increased about 2 times by encircling the central region by the metamaterial concentrator, from 8 mm/s to 17 mm/s.

Unfortunately, the degree of amplification was lower than the 3-fold increase of the ideal concentrator performance, calculated from the continuous media simulation results. It is speculated that the approximation error in the effective viscosity unit cell design might cause this inconsistency, on a similar rationale that can not to create the space of a perfect zero flow rate in the metamaterial cloak development. Obviously, the error in the assumptions can be reduced if the metamaterial concentrator is designed and built with smaller unit cells. However, in this dissertation, the metamaterial concentrator was designed under the present unit cell conditions due to fabrication and experimental limitations.

From the velocity analyses, theoretical hydraulic kinetic energy of the unit cell region ( $E_{k,unit}$ ) could be calculated based on **Eqn. 2.4.13** as

$$E_{k,unit} = \frac{\rho V \langle \tilde{\mathbf{u}} \rangle_{unit}^2}{2} \quad (2.4.13)$$

, where  $\rho$  is the mass density of a fluid, and  $V$  is the volume of a unit cell. After the calculation, the  $E_k$  value in the bare region was evaluated to be  $1.44\text{e-}7$   $\mu\text{J}$ . And the  $E_k$  value in the central concentrated region was estimated to be  $6.50\text{e-}7$   $\mu\text{J}$ , which is a 4.5 times higher value than that of the bare region. Naturally, the relatively low increase rate of  $E_k$  originates from the same reason as in the velocity field calculation.

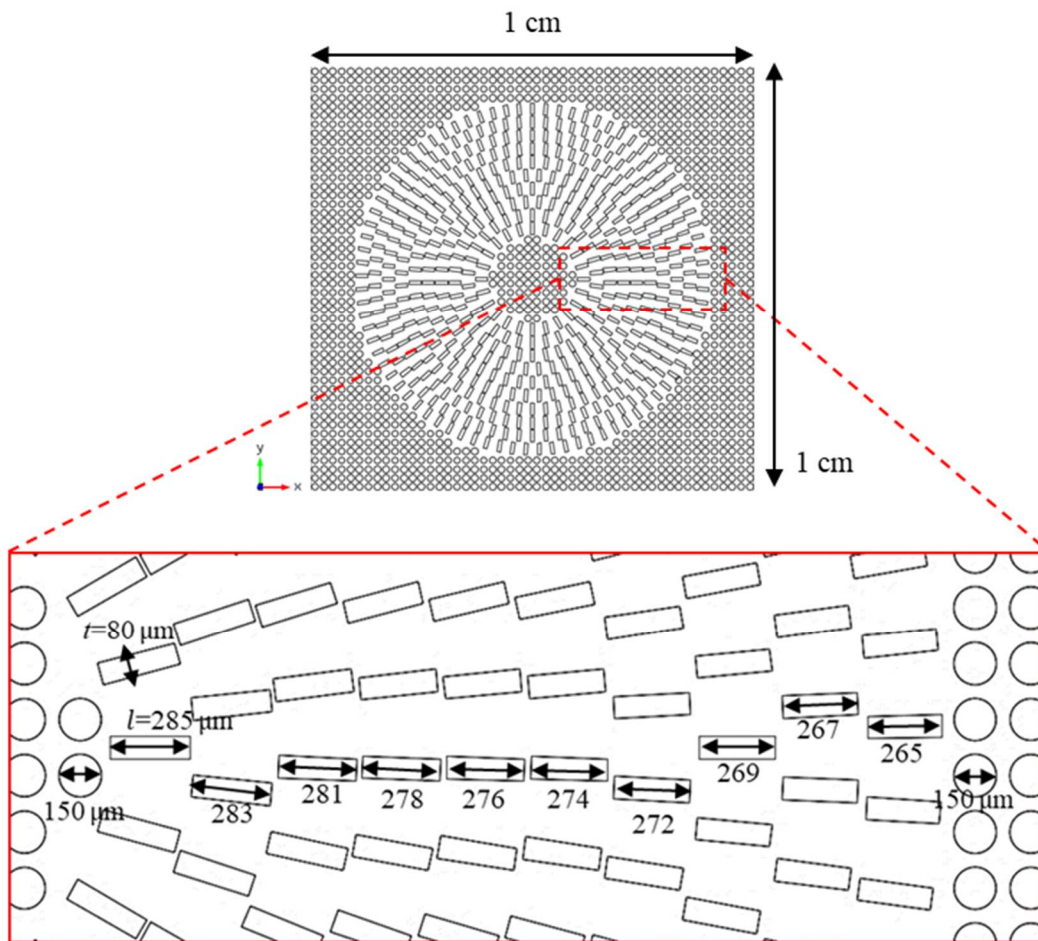


**Figure 2.4.9.** Design of the rheological metamaterial concentrator of a pillar-arrayed case with configuration and a magnified view.



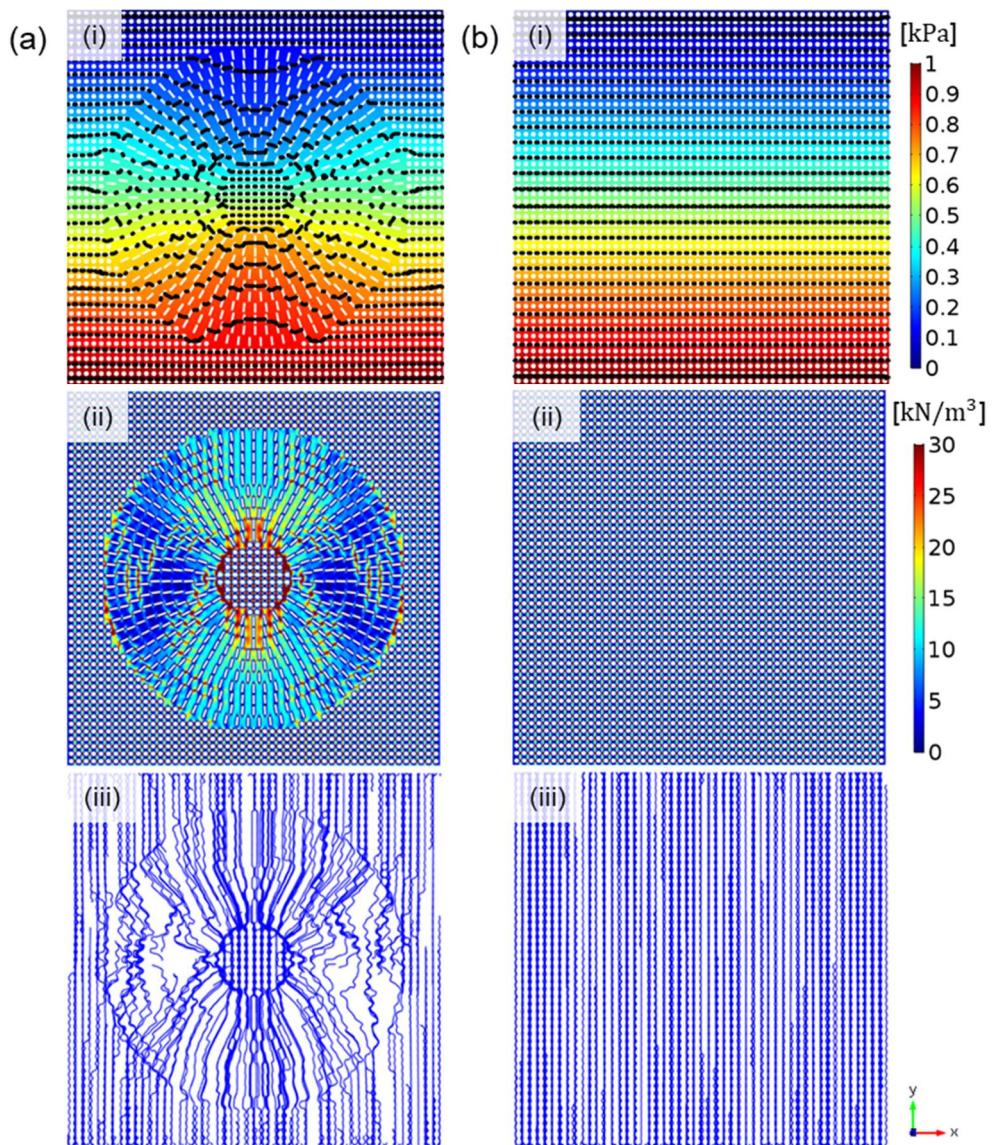


**Figure 2.4.10.** Simulation results for (a) the designed rheological metamaterial concentrator and (b) bare cases of (i) pressure fields, (ii) velocity fields, and (iii) flow streamlines.

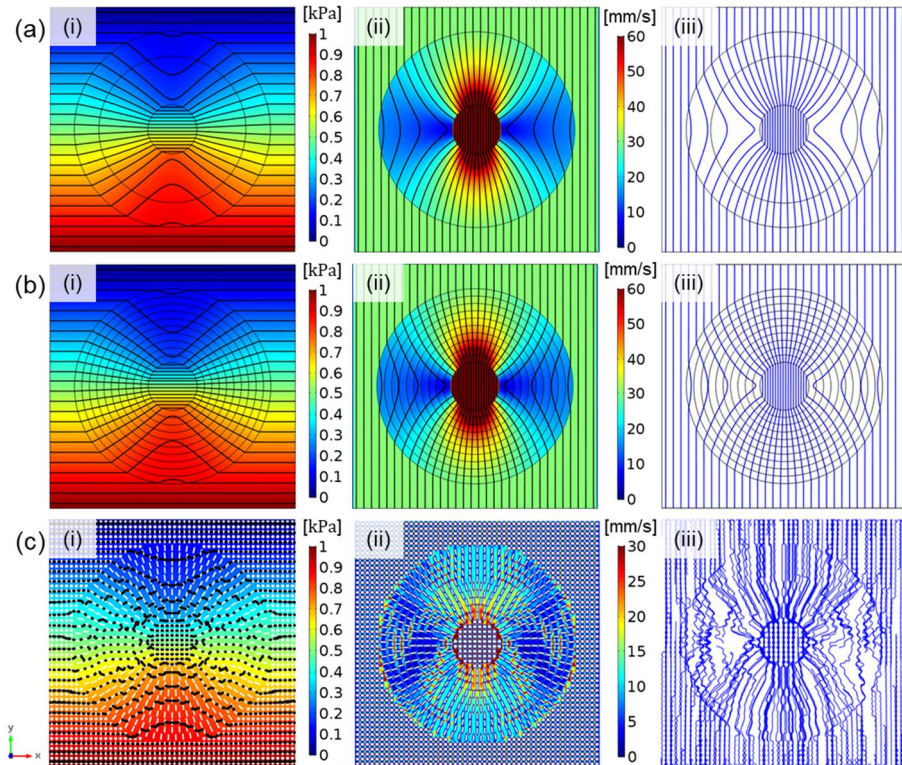


**Figure 2.4.11.** Comparison of the simulation results for (a) the continuous media, (b) multilayered, and (c) pillar-arrayed rheological concentrator cases; (i) pressure fields, (ii) velocity fields and (iii) flow streamlines.

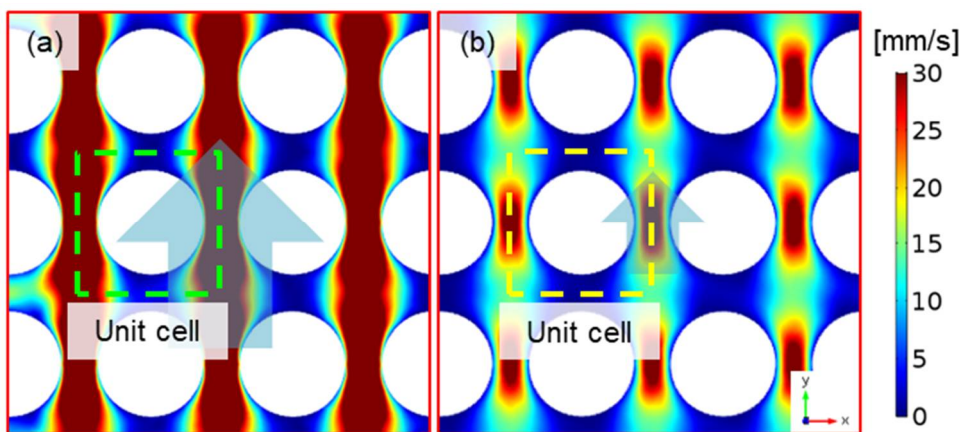


**Figure 2.4.12.** Magnified images of the simulated velocity fields in the central region; (a) with and (b) without the rheological concentrator. Dashed squares indicate the unit cell.

## 2.4.5. Experimental realization

### 2.4.5.1. Fabrication method

The rheological metamaterial concentrator designed in Section 2.4.4 was drawn using AutoCAD 2017 and shown in **Figs. 2.4.13-14**. The overall configuration and dimensions of the microchannels were identical to those of the metamaterial cloak.

The detail fabrication method used for a polymeric microfluidic device is demonstrated in Section 2.3.5.1. In order to proceed with the photolithography, a photomask was produced by covering with a chromium (Cr) and it contained the metamaterial concentrator design (**Fig. 2.4.15(a)**). The Si master with the metamaterial concentrator design was manufactured as shown in **Fig. 2.4.15(b)**. The microdevice for the metamaterial concentrator was fabricated as shown in **Fig. 2.4.15(c)**. By observing the fabricated microdevice through a microscope, the configuration of the fabricated metamaterial concentrator was confirmed to be in perfect agreement with the drawing (**Fig. 2.4.16**).

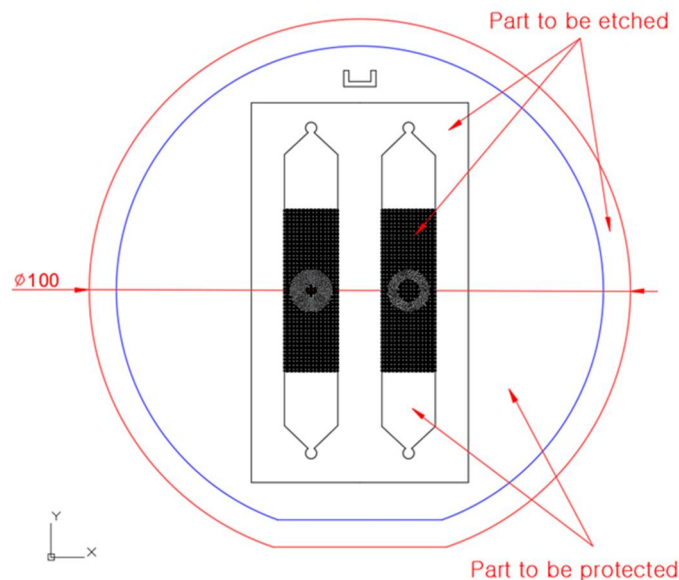


**Figure 2.4.13.** A drawing of the Si master containing the microchannels for the designed rheological metamaterial concentrator (left) and rotator (right). The metamaterial rotator is explained in Section 2.5.

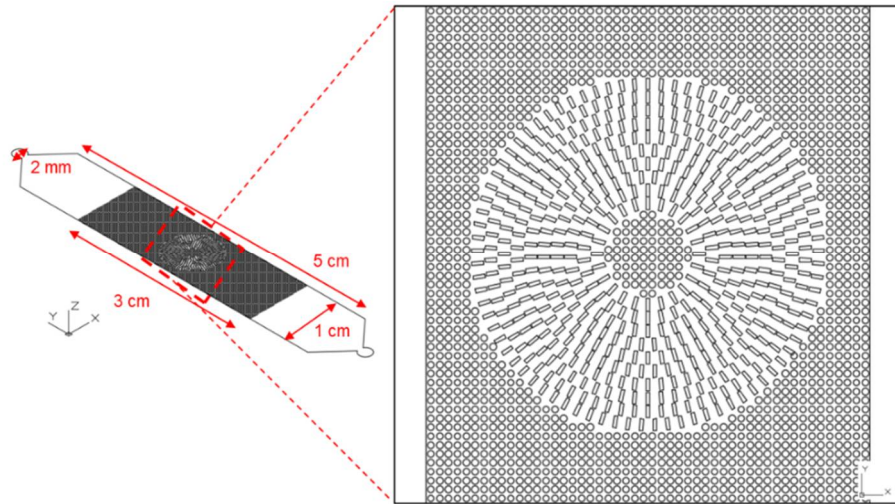


**Figure 2.4.14.** A microscale view and configuration of the microchannel for the designed rheological metamaterial concentrator.

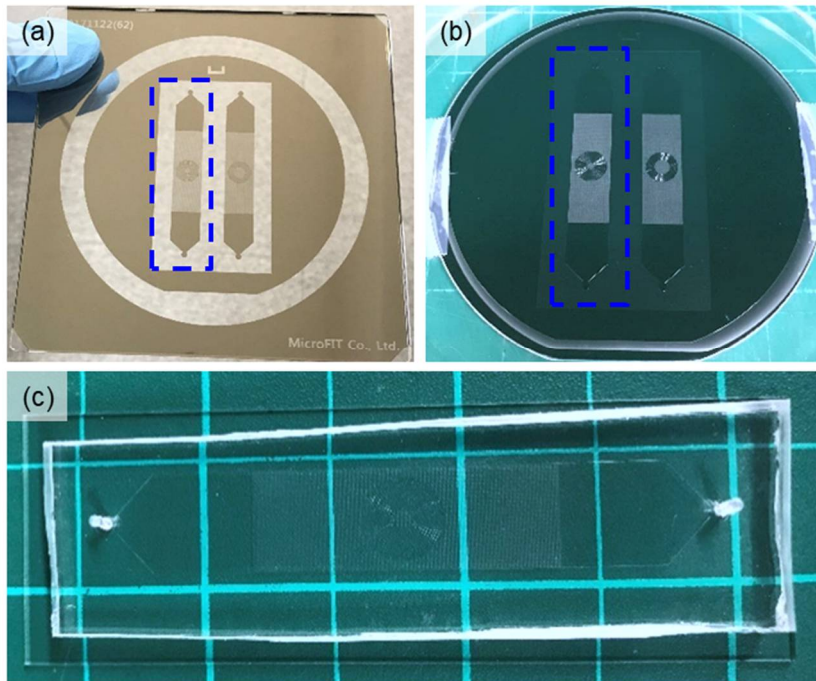


**Figure 2.4.15.** Fabrication details of the rheological metamaterial concentrator. (a) The patterned Cr mask, (b) the fabricated Si master, and (c) the manufactured microfluidic device. The figures in the blue dashed rectangle are the rheological metamaterial concentrators and the others are the metamaterial rotators developed in Section 2.5.

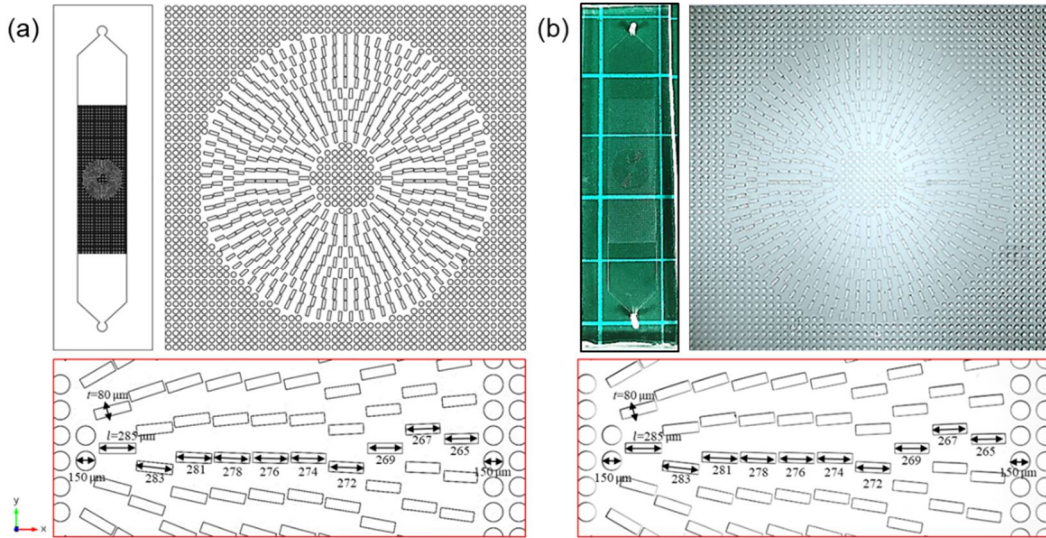


**Figure 2.4.16.** Detailed configuration of (a) the designed rheological metamaterial concentrator and (b) the fabricated rheological metamaterial concentrator.

### 2.4.5.2. Experimental method

The rheological concentrating function by the fabricated metamaterial was experimentally verified in the microfluidic device by visualizing flow streamlines of the fluorescent microparticles. The experimental method used for the rheological metamaterial concentrator is described in Section 2.3.5.2 and **Fig. 2.3.24**.

### 2.4.5.3. Experimental results

Experiment for the rheological metamaterial concentrator was performed with the fabricated polymeric microfluidic device. The observed particle streamlines are shown in **Fig. 2.4.17**. Three separate parts of the metamaterial concentrator were photographed to identify streamlines more clearly. The captured images of flow streamlines were compared with the simulation results, and the microstructures of each part during the experiment were shown.

In all the parts observed through the experiment, the captured flow streamlines show almost perfect agreement with the simulated results. **Figure 2.4.17(a)** shows the entry part of the metamaterial concentrator where the fluidic force begins to gather. The left-side part of the metamaterial is shown in **Fig. 2.4.17(b)**, where the difference in density of streamlines is clearly verified between the expanded and compressed spaces. The most important part in this experiment is the central part surrounded by the rheological metamaterial concentrator. It was confirmed in **Fig. 2.4.17(c)** that the central part possesses much denser flow streamlines than those outside the metamaterial concentrator. This phenomenon indicates a much faster flow rate of the fluid formed in the central region.

Although this spatial distortion was induced, the surrounding fluidic space was not distorted at all as in the previous simulations and designs. The flow streamlines in the background region remained a straight shape. It is a very meaningful phenomenon because the hydraulic energy of the fluid was concentrated in the desired space by only distorting and rearranging the fluidic space without the aid of external forces or energy to be applied.

The design of the rheological metamaterial concentrator faces the same limitation as the metamaterial cloak design. Likewise, it is essential to develop an advanced method of viscosity control for application to hydroelectric plants, since the unit cell method of microstructure mapping has various problems in practical use. Notwithstanding, this study is valuable of being the first study to coalesce hydropower as designed by using a fluidic space transformation.

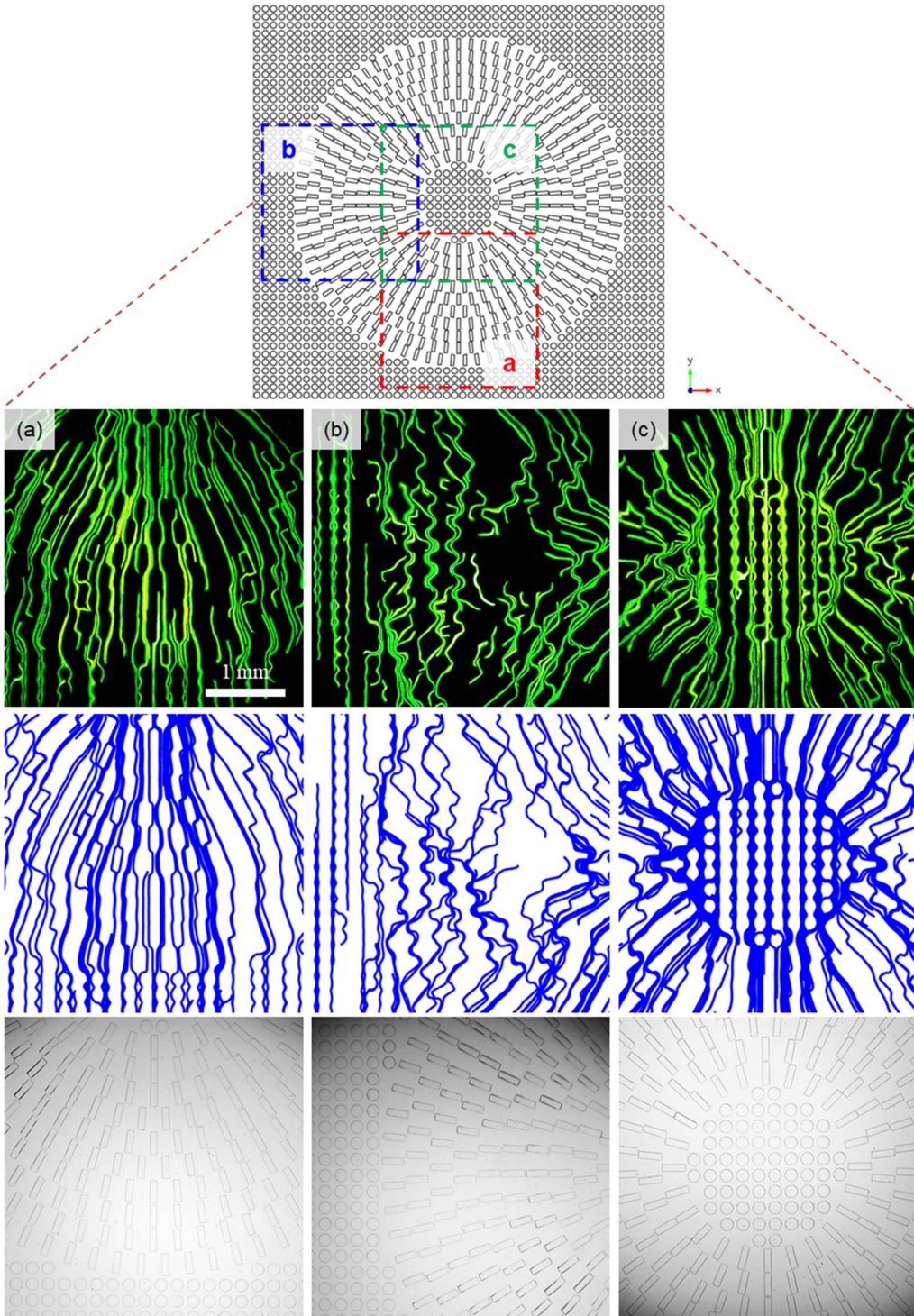


**Figure 2.4.17.** Flow streamlines of the rheological metamaterial concentrator at (a) the entrance, (b) left-side, and (c) central regions; observed streamlines (top), simulated streamlines (middle), and microstructure during the experiment (bottom).

#### **2.4.6. Conclusions**

In this section, the rheological metamaterial concentrator was proposed. Similar with Section 2.3, the field-concentrating shell was defined as a form of the Jacobian transformation matrix based on transformation rheology. The transformed viscosity tensor for concentrating was used for numerical analysis and its function was verified. The rheological concentrator was designed by mapping the effective viscosity unit cells. The metamaterial design was numerically simulated for visualizing pressure and velocity fields and produced experimentally as a microfluidic device. The observed flow streamlines perfectly coincided with the simulated streamlines, representing the fluid momentum successfully focused on the target area. It is expected that the technology capable of collecting hydraulic kinetic energy will dramatically improve the efficiency of hydroelectric power generation. In addition, the amount of fuel consumed in sailing submarines or ships can be dramatically reduced by accelerating the space of seaway or canal. Furthermore, if the scope of this study extends to aerodynamics described by the governing equations of the same kind, it can also provide an outstanding idea for designing takeoff runways for airplanes.



## 2.5. Rheological rotator

### 2.5.1. Introduction

It is so natural that a fluid flows along the direction of an applied pressure. Adjusting the flowing fluid direction to desired direction is not feasible without changing the applied pressure direction. Because of this law of nature, an object moving in the opposite direction of a flowing fluid receives a large drag force. In addition, even in the case of wind or hydraulic power generation, there is a big difference in the harvesting efficiency level depending on the direction of a flowing fluid. Therefore, if a metamaterial is developed that can control the direction of fluid flow regardless of external pressure or velocity fields, it can provide a breakthrough solution for a variety of problems in fluid dynamic technology.

It was already confirmed that transformation rheology inspired from transformation optics [8,9,138] can provide a way to control fluid momentum in an unprecedented manner in the previous sections. The form invariance of Navier-Stokes equations under the curvilinear coordinate transformation allows transformed viscosity tensors to bring about fictitious spaces for cloaking and concentrating fluid flows, in Sections 2.2-3, representatively.

The metamaterial design based on transformation optics has been applied to the rotation of physical fields, in addition to cloaking and concentrating. After the first demonstration of the transformation electromagnetic rotating media by Chen *et al.* [40], the experimental realization of the metamaterial rotator was reported by the same research group [41]. As a follow-up study, the metamaterial rotators that change the direction of heat transfer [57,165–167] and propagation of sound waves [56] have been developed.

In this section, a rheological metamaterial rotator was developed, which can control the direction of fluid flow differently from the direction of given external fields. The required material tensor, *i.e.*, the transformed viscosity tensor, was calculated from transformation rheology based on the transformed Navier-Stokes equations. The rheological rotators for changing flow direction by  $180^\circ$ ,  $180^\circ$ ,  $90^\circ$ , and  $30^\circ$  were simulated numerically to visualize and analyze the pressure and velocity fields of flowing fluid. The rheological metamaterial rotator was designed by mapping the effective viscosity

unit cells that are designed by tilting a micropillar at a specific angle. Comparison of the simulated and experimentally observed streamlines of the metamaterial rotator shows that the constructed strategy is successful and the designed metamaterial rotator can guide the direction of fluid flow as intended.

## 2.5.2. Fluidic space modeling

The total transformation matrices ( $\Lambda$ ) for the cloaking and concentrating shells developed in Sections 2.2-3 were calculated as a Jacobian matrix form to procure the transformed viscosity tensors.  $\lambda (= \lambda_j^{i'} = \partial q^{i'}/\partial q^j)$ ,  $B (= B_j^i = \partial q^i/\partial p^j)$ , and  $B' (= B_{j'}^{i'} = \partial q^{i'}/\partial p'^j)$  compose  $\Lambda$  as demonstrated in **Eqn. 2.3.1**. The metamaterial rotators require a total Jacobian matrix ( $\Lambda$ ) that allows for rotational space design by introducing new  $\lambda$  which enables spatial twist.

Unlike the space design of the shells for the concealment and concentrating, the rotating shell should be able to fulfil the spatial twist rather than compression or expansion. The twisted internal space of the rotating shell serves to change the enclosed coordinate space by a certain desired angle. The momentous point here is that the space inside and outside the rotating shell should have unchanged physical quantity except for the direction of that. With this spatial design, the fluid flow direction of the inner enclosed space can be manipulated independently of the external field through setting of the desired rotation angle.

As aforementioned, design of the rotating space requires not the radial stretch but the spatial twist. When the inner radius is  $a$  and the outer radius is  $b$ , the space is twisted by the angle  $\theta_0$  as compared with the background region by the coordinate relationship described below.

$$r' = r \quad (2.5.1)$$

$$\theta' = \begin{cases} \theta + \theta_0 & r < a \\ \theta & r > b \\ \theta + g(r) & a < r < b \end{cases} \quad (2.5.2)$$

$$z' = z \quad (2.5.3)$$

, where  $g(r) = \theta_0 \{(f(b) - f(r))/(f(b) - f(a))\}$ . As the radius ( $r$ ) approaches  $b$ , the rotation angle decreases to zero. In the above relationship (**Eqns. 2.5.1-3**), the rotation angle  $\theta_0$  must always be positive. The function  $f(r)$  of  $g(r)$  can be any continuous function whose variation is defined by a radial distance.

From the above relationship, the Jacobian matrix ( $\lambda$ ) for twisting space by  $\theta_0$  ( $a <$

$r < b$ ) can be derived as

$$\lambda = \begin{bmatrix} \frac{\partial r'}{\partial r} & \frac{\partial r'}{\partial \theta} & \frac{\partial r'}{\partial z} \\ \frac{\partial \theta'}{\partial r} & \frac{\partial \theta'}{\partial \theta} & \frac{\partial \theta'}{\partial z} \\ \frac{\partial z'}{\partial r} & \frac{\partial z'}{\partial \theta} & \frac{\partial z'}{\partial z} \end{bmatrix} = \begin{bmatrix} 1 & 0 & 0 \\ r \frac{dg(r)}{dr} & 1 & 0 \\ 0 & 0 & 1 \end{bmatrix} \quad (2.5.4)$$

If the function  $f(r)$  is set as  $f(r) = \ln(r)$ , the term  $\lambda_{\theta'r} (= \partial\theta'/\partial r)$  can be defined as  $\lambda_{\theta'r} = r(dg(r)/dr) = -\{\theta_0/\ln(b/a)\}$  with the constant values only. Then, the Jacobian matrix ( $\lambda$ ) is expressed as

$$\lambda = \begin{bmatrix} 1 & 0 & 0 \\ -\frac{\theta_0}{\ln(b/a)} & 1 & 0 \\ 0 & 0 & 1 \end{bmatrix} = \begin{bmatrix} 1 & 0 & 0 \\ -t & 1 & 0 \\ 0 & 0 & 1 \end{bmatrix} \quad (2.5.5)$$

, where  $t = \theta_0/\ln(b/a)$ . By combining **Eqn. 2.5.5** with  $\mathbf{B}'^{-1}$  and  $\mathbf{B}$ , the total Jacobian matrix ( $\Lambda$ ) between the virtual space ( $a < r < b$ ) and the physical space ( $a < r' < b$ ) is derived as

$$\Lambda = \mathbf{B}'^{-1} \lambda \mathbf{B} = \lambda = \begin{bmatrix} 1 & 0 & 0 \\ -t & 1 & 0 \\ 0 & 0 & 1 \end{bmatrix} \quad (2.5.6)$$

$$\det(\Lambda) = 1 \quad (2.5.7)$$

, where  $\mathbf{B}$  is the backward transformation matrix that changes a coordinate system from cylindrical to Cartesian. Consequently, the transformed viscosity tensor ( $\tilde{\mu}'$ ) is calculated as

$$\tilde{\mu}' = \det(\Lambda) \Lambda^{-1} \mu \Lambda^{-T} = \begin{bmatrix} 1 + t^2 & t \\ t & 1 \end{bmatrix} \mu \quad (2.5.8)$$

The notable point of **Eqn. 2.5.8** is that the tensor does not have a spatially varying component and has a constant value independent of its radial position. In other words, unlike other metamaterials, the metamaterial rotator can be achieved with a homogeneous

material. Hence, the transformed viscosity tensor for the rotator does not need to be a reduced set unlike the tensors for cloaking or concentrating and can be used in an ideal form without impedance mismatching issue at the outer boundary of the rotator. The vertical component of **Eqn. 2.5.8** was not considered in modeling because only 2D y-directional flows were simulated. Another unusual feature, unlike the two derived viscosity tensors in Sections 2.3-4, is that the tensor of **Eqn. 2.5.8** has off-diagonal components. In the preceding chapters, the unit cells are modeled considering the effective viscosity only in  $r$  and  $\theta$  axes, however, the off-diagonal terms lead to a more complicated process for the metamaterial rotator.

Four transformed viscosity tensors for rotating space ( $\widetilde{\mu}'$ ) were modeled as expressed in **Eqns. 2.5.9-12** from **Eqn. 2.5.8**. These equations show the transformed viscosity tensors for rotating space at  $180^\circ$ ,  $90^\circ$ , and  $30^\circ$ , orderly.

$$\widetilde{\mu}'_{180^\circ} = \begin{bmatrix} 21.5 & 4.53 \\ 4.53 & 1 \end{bmatrix} \mu \quad (2.5.9)$$

$$\widetilde{\mu}'_{90^\circ} = \begin{bmatrix} 6.14 & 2.27 \\ 2.27 & 1 \end{bmatrix} \mu \quad (2.5.10)$$

$$\widetilde{\mu}'_{30^\circ} = \begin{bmatrix} 1.57 & 0.76 \\ 0.76 & 1 \end{bmatrix} \mu \quad (2.5.11)$$

Each tensor was derived by substituting the angles of rotation for  $\theta_0$  and calculating  $t$ .  $t$  for  $\widetilde{\mu}'_{180^\circ}$  is 4.53, for  $\widetilde{\mu}'_{90^\circ}$  is 2.27, and for  $\widetilde{\mu}'_{30^\circ}$  is 0.76. The extreme case rotator was modeled to show a unique phenomenon such as an artificial tornado. For this case,  $t$  for rotating  $180^\circ$  was calculated at 5.29 and the corresponding transformed viscosity tensor was calculated as

$$\widetilde{\mu}'_{180^\circ} = \begin{bmatrix} 36.2 & 5.29 \\ 5.29 & 1 \end{bmatrix} \mu \quad (2.5.12)$$

### 2.5.3. Numerical analysis

#### 2.5.3.1. Simulation conditions

In this section, simulation results of the four rotators using the viscosity tensors described in **Eqns. 2.5.9-12** are explained. Most simulation conditions used in this section are same with the conditions demonstrated in Section 2.3.3.1. For the three rotators, the hexahedron block geometry and the concentric ring in Section 2.3 (**Fig. 2.3.3**) were used, and for the artificial tornado case, the inner radius  $a$  was set to a small value of 10  $\mu\text{m}$ . Free tetrahedral meshes consisted of 111567 domain elements, 73272 boundary elements, and 1884 edge elements. The used element size parameters and control entities are same with the those described in Section 2.3.3.1.

The same customized PDE (partial difference equation) interface suggested in Section 2.3.3.1 solved the Navier-Stokes equations with the transformed viscosity tensors of the rheological rotators. The solver, boundary conditions, and material properties used in the analysis are the same for the rheological cloak.

### 2.5.3.2. Simulation results

Using the transformed viscosity tensors developed in Section 2.5.2, the feasibility of the rheological rotators was demonstrated with numerical simulation results. The simulation results of the four rheological rotators were analyzed with transformed coordinate grids, pressure fields, pressure gradient fields, and velocity fields with flow streamlines.

**Figure 2.5.1** shows the numerical simulation results for the  $180^\circ$  rotator with  $\widetilde{\mu}'_{180^\circ}$  (Eqn. 2.5.9). From **Fig. 2.5.1(a)**, it can be found that the coordinate system of the rotating shell ( $a < r' < b$ ) is largely warped while the inside and outside the  $180^\circ$  rotator maintains their original shape. A red point on the outer circle of the rotating shell is connected to a blue point on the inner circle on the opposite side through the shell with the twisted space. Hence, the inner space surrounded by the  $180^\circ$  rotator has a physical quantity in opposite direction to that of the surrounding space.

**Figure 2.5.1(b)** shows the  $180^\circ$  inverted pressure field in the central region ( $r' < a$ ). The pressure gradient in the central region is formed as a positive number from top to bottom, as opposed to the pressure gradient condition applied in the simulation. Therefore, the negative pressure gradient field (about  $-96 \text{ kN/m}^3$ ) is found in the central region (**Fig. 2.5.1(c)**). It should be noted that the pressure gradient of the central region has the same magnitude as the surrounding pressure gradient (about  $96 \text{ kN/m}^3$ ), but only the sign becomes opposite.

Due to the negative pressure gradient, the flow direction of fluid is reversed as shown in **Fig. 2.5.1(d)**. The length and direction of the black arrows indicate the flow rate and direction, respectively. When the flowing fluid enters the outer boundary of the  $180^\circ$  rotator, it accelerates greatly in a helical direction with spiral patterns and reaches the farthest side of the inner circle. The velocity magnitude of the central region and the background region was matched with each other at  $30 \text{ mm/s}$ .

The  $90^\circ$  rotator with  $\widetilde{\mu}'_{90^\circ}$  (Eqn. 2.5.10) was demonstrated in **Fig. 2.5.2**. Similarly with the  $180^\circ$  rotator, the coordinate grid of the rotating shell is twisted to connect a red point on the outer circle of the rotating shell to another blue point on the inner circle on the perpendicular side. Due to this spatial distortion, the pressure gradient in the central region is aligned along negative x-direction that is perpendicular to the applied pressure fields (**Fig.**

**2.5.2(b)**). Because the pressure fields are directed by  $90^\circ$ , the pressure gradient in y-axis ( $P_y$ ) has an almost zero value (**Fig. 2.5.2(c)**) and that in x-axis ( $P_x$ ) was calculated at about  $-97 \text{ kN/m}^3$ . According to this pressure gradient, the fluid in the central region flows in the direction of negative  $x$  axis (**Fig. 2.5.2(d)**).

The two rotators for  $180^\circ$  and  $90^\circ$  rotation require excessive space warpage, which is not feasible experimentally. For this reason, the  $30^\circ$  rotator  $\widetilde{\mu}_{30^\circ}$  (**Eqn. 2.5.11**) was modeled for experimental realization (**Fig. 2.5.3**). The inner and outer points of the rotating shell are connected to one another through much more gentle spiral patterns than in the previous two cases. Along the transformed coordinate space, the pressure, pressure gradient, and velocity fields were formed in an inclined direction of  $30^\circ$  (**Figs. 2.5.3(a-c)**).

A tornado is a rapidly rotating whirlwind that rotates very vigorously. By setting the center region very small ( $a=10 \text{ } \mu\text{m}$ ) and the rotation angle to be very large ( $\theta_0=1800^\circ$ ), the artificial tornado was modeled with an extremely distorted fluidic space as an extreme case (**Fig. 2.5.4**). Not only the flow rate in the  $1800^\circ$  rotator is very fast, but also the swing angle is also very large, since the fluid inside the rotator must be rotated by  $1800^\circ$  before reaching the inner central region. In spite of very severe distortion of the space, it can be seen that the surrounding space is not affected and maintains a uniform pressure and velocity fields.



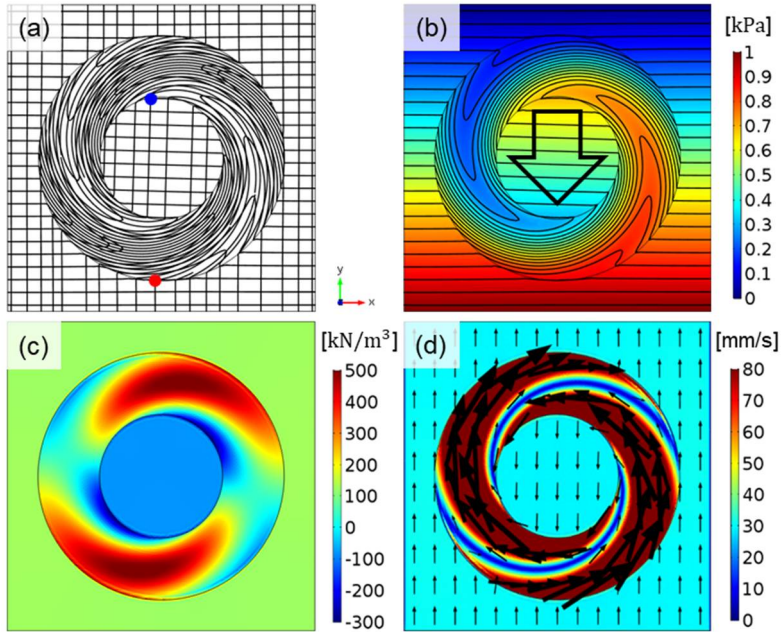


**Figure 2.5.1.** Simulation results of the 180° rheological rotator: (a) transformed coordinate system, (b) pressure fields, (c) pressure gradient fields, and (c) velocity fields.

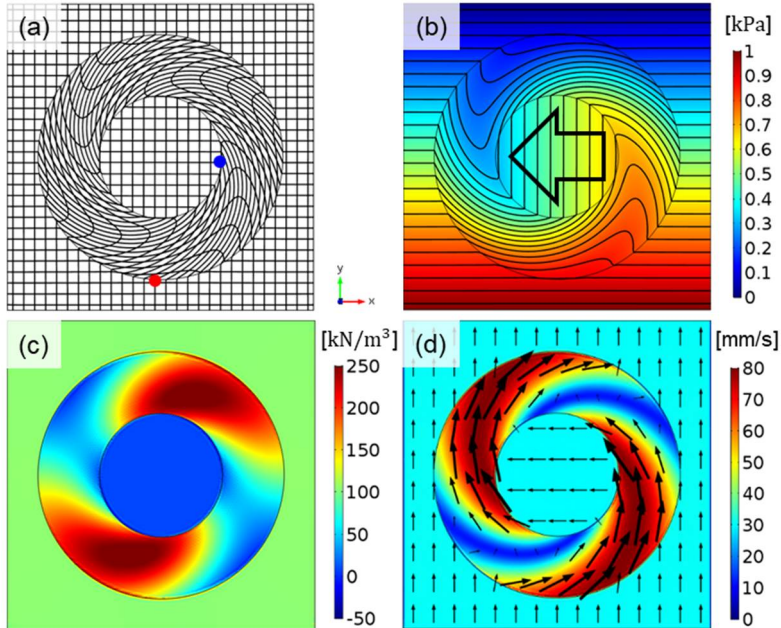


**Figure 2.5.2.** Simulation results of the 90° rheological rotator: (a) transformed coordinate system, (b) pressure fields, (c) pressure gradient fields, and (c) velocity fields.

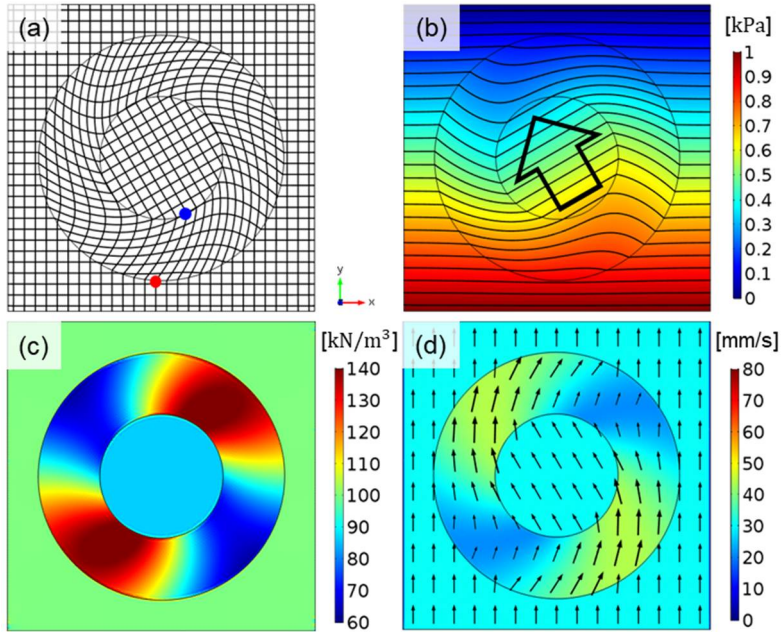


**Figure 2.5.3.** Simulation results of the 30° rheological rotator: (a) transformed coordinate system, (b) pressure fields, (c) pressure gradient fields, and (c) velocity fields.

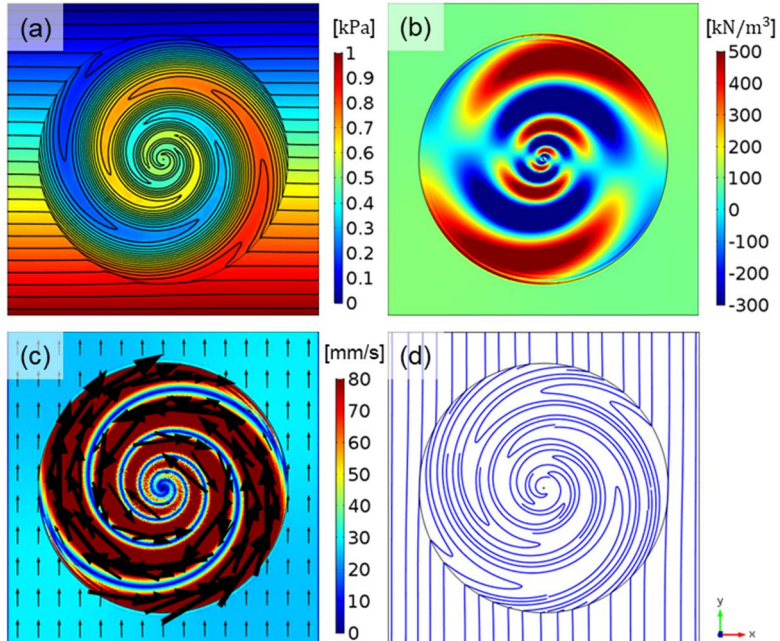


**Figure 2.5.4.** Simulation results of the 1800° rheological rotator as an artificial tornado: (a) transformed coordinate system, (b) pressure fields, (c) pressure gradient fields, and (c) velocity fields.

## 2.5.4. Metamaterial design

### 2.5.4.1. Prototype design

Metamaterials based on transformation physics have always been designed by using effective unit cells. Unlike unit cell designs in the metamaterials cloak and concentrator, unit cells for the metamaterial rotators have been designed through a mathematical method [41,56]. The overall unit cell design process is to find the effective material properties for the principal axis of a unit cell and then calculate the angle of the unit cell to tilt. The metamaterial rotator is composed of a homogeneous layer that does not need to change the viscosity according to radial position. Therefore, only a single unit cell was designed and mapped on the entire layer of the rotator. For convenience of design, the rotating shell was divided into five layers and each unit cell has a hexahedron shape with a dimension of 400 by 400 by 50  $\mu\text{m}^3$ .

The principal axes of the unit cells are  $r$  and  $\theta$  axes before tilted, however these are changed to  $u$  and  $v$  axes after tilted (**Fig. 2.5.5(b)**). Two viscosity components for the principal axes are named  $\mu_u$  and  $\mu_v$ . An ancillary angle was defined as  $\tau$  and the tilting angle of the unit cell was set to  $\tau/2$ . Then, the transformed viscosity tensor defined in **Eqn. 2.5.8** can be expressed as

$$\begin{aligned} \tilde{\boldsymbol{\mu}}' &= \begin{bmatrix} 1+t^2 & t \\ t & 1 \end{bmatrix} \boldsymbol{\mu} \\ &= \begin{bmatrix} \cos\frac{\tau}{2} & -\sin\frac{\tau}{2} \\ t\sin\frac{\tau}{2} & \cos\frac{\tau}{2} \end{bmatrix} \begin{bmatrix} \cos\theta & -\sin\theta \\ \sin\theta & \cos\theta \end{bmatrix} \begin{bmatrix} \mu_u & 0 \\ 0 & \mu_v \end{bmatrix} \begin{bmatrix} \cos\theta & \sin\theta \\ -\sin\theta & \cos\theta \end{bmatrix} \begin{bmatrix} \cos\frac{\tau}{2} & \sin\frac{\tau}{2} \\ -\sin\frac{\tau}{2} & \cos\frac{\tau}{2} \end{bmatrix} \boldsymbol{\mu} \quad (2.5.13) \end{aligned}$$

By calculation, **Eqn. 2.5.13** can be simplified to

$$\tilde{\boldsymbol{\mu}}' = \begin{bmatrix} \mu_u \cos^2\frac{\tau}{2} + \mu_v \sin^2\frac{\tau}{2} & (\mu_u - \mu_v) \cos\frac{\tau}{2} \sin\frac{\tau}{2} \\ (\mu_u - \mu_v) \cos\frac{\tau}{2} \sin\frac{\tau}{2} & \mu_u \sin^2\frac{\tau}{2} + \mu_v \cos^2\frac{\tau}{2} \end{bmatrix} \boldsymbol{\mu} \quad (2.5.14)$$

Then, the principal values of  $\tilde{\boldsymbol{\mu}}'$  were calculated from the Eigenvalues of the matrix from

the relationship of  $|\tilde{\boldsymbol{\mu}}' - \lambda \tilde{\mathbf{I}}| = 0$ .

$$\tilde{\boldsymbol{\mu}}' = \begin{bmatrix} \mu_u & 0 \\ 0 & \mu_v \end{bmatrix} = \begin{bmatrix} 1 + \frac{1}{2}t^2 + \frac{1}{2}t\sqrt{t^2 + 4} & 0 \\ 0 & 1 + \frac{1}{2}t^2 - \frac{1}{2}t\sqrt{t^2 + 4} \end{bmatrix} \mu \quad (2.5.15)$$

From **Eqn. 2.5.15**, the four sets of the viscosity components in the principal axes for the 180°, 90°, 30°, and 1800° rotators were obtained as

$$\tilde{\boldsymbol{\mu}}' = \begin{bmatrix} 22.5 & 0 \\ 0 & 0.04 \end{bmatrix} \mu \text{ for the } 180^\circ \text{ rotator} \quad (2.5.16)$$

$$\tilde{\boldsymbol{\mu}}' = \begin{bmatrix} 7.01 & 0 \\ 0 & 0.14 \end{bmatrix} \mu \text{ for the } 90^\circ \text{ rotator} \quad (2.5.17)$$

$$\tilde{\boldsymbol{\mu}}' = \begin{bmatrix} 2.10 & 0 \\ 0 & 0.48 \end{bmatrix} \mu \text{ for the } 30^\circ \text{ rotator} \quad (2.5.18)$$

$$\tilde{\boldsymbol{\mu}}' = \begin{bmatrix} 29.95 & 0 \\ 0 & 0.03 \end{bmatrix} \mu \text{ for the } 1800^\circ \text{ rotator} \quad (2.5.19)$$

To make  $\mu_v$  1.2 greater than 1 for achievable experimental conditions, the scale factors of 30, 8.57, 2.5, and 40 should be multiplied by  $\tilde{\boldsymbol{\mu}}'$  of **Eqns. 2.5.16-19**. The scaled viscosity tensors were obtained as

$$\tilde{\boldsymbol{\mu}}' = \begin{bmatrix} 675 & 0 \\ 0 & 1.2 \end{bmatrix} \mu \text{ for the } 180^\circ \text{ rotator} \quad (2.5.20)$$

$$\tilde{\boldsymbol{\mu}}' = \begin{bmatrix} 60.1 & 0 \\ 0 & 1.2 \end{bmatrix} \mu \text{ for the } 90^\circ \text{ rotator} \quad (2.5.21)$$

$$\tilde{\boldsymbol{\mu}}' = \begin{bmatrix} 5.25 & 0 \\ 0 & 1.2 \end{bmatrix} \mu \text{ for the } 30^\circ \text{ rotator} \quad (2.5.22)$$

$$\tilde{\boldsymbol{\mu}}' = \begin{bmatrix} 1198 & 0 \\ 0 & 1.2 \end{bmatrix} \mu \text{ for the } 1800^\circ \text{ rotator} \quad (2.5.23)$$

To figure out the tilt angles of the micropillar placed in each unit cell, the ancillary angle ( $\tau$ ) was defined as follows from the relationship of **Eqns. 2.5.13-14**.

$$\tau = \cos^{-1}\left(\frac{t}{\sqrt{t^2 + 4}}\right) = \sin^{-1}\left(\frac{2}{\sqrt{t^2 + 4}}\right) \quad (2.5.24)$$

The ancillary angles for **Eqns. 2.5.20-23** were calculated as 23.82°, 41.38°, 69.19°, and 20.71°, orderly. These angles indicate that the unit cells should be tilted by 11.91°, 20.69°, 34.60°, and 10.36°, orderly, for the designed spatial distortion.

Among them, the 30° rotator was chosen as a subject of experimental realization for the following reasons. First, the radial viscosity terms for the other rotators are relatively large, making it difficult to control the unit cell design precisely. Furthermore, too small rotation angles cause the gap between micropillars in the unit cells to be too narrow, excessively increasing the impedance of the rotator. As a result, the fluid cannot flow into the rotator and rotate following coordinates, but flow only out of the rotator.

The basic unit cell was modeled based on the concept of the effective viscosity unit cell demonstrated in Section 2.3.4.2. This unit cell consists of a 400 by 400 μm<sup>2</sup> hexahedron block with a micropillar of 349 μm length, 50 μm width, and 50 μm height. The radial and azimuthal effective viscosities of the basic unit cell are calculated to be about 5.5 mPa·s and 1.2 mPa·s, which are very similar to **Eqn. 2.5.22**. According to other metamaterial designs reported previously, it was expected that the desired 30° metamaterial rotator could be produced by mapping this basic unit cell with the 34.6° tilted micropillar (**Figs. 2.5.5(a-b)**). The background area was impedance-matched by arranging 130 μm cylinders (**Fig. 2.5.5(c)**).

A three-dimensional model of the prototype rotator was drawn by using CATIA 5.18, a commercial CAD (computer-aided design) program. The layers from 1 to 5 (from inside to outside) of the metamaterial rotator are composed of 35, 41, 47, 54, and 60 unit cells, orderly. The isotropic unit cells containing a 130 μm cylinder were mapped to 50 by 50 in the background region for impedance matching. After introducing the designed pillar-arrayed model into the hexahedron block, the pillar-arrays were removed by operating Boolean function and the resultant empty space indicates the solid domain situated in the fluid domain.

Numerical simulation was performed to confirm that the “prototype” rheological metamaterial rotator can function properly as intended (**Fig. 2.5.6**). Simulation conditions

are the same as in the continuous media simulation described in Section 2.5.3.1. The simulation results are compared with the results from the continuous media case (**Fig. 2.5.6**). First, the impedance at the interface between the spaces was perfectly matched so that the inside and outside of the rotator were not distorted, and hence the streamlines outside the rotator maintain a straight shape. Also, the direction of the fields inside the rotator ( $r' < a$ ) were changed by about  $20^\circ$ . However, unfortunately, the prototype rotator did not achieve the desired rotation performance that has to rotate by  $30^\circ$ .

The lack of rotational performance of the prototype metamaterial rotator is presumed to be caused by unit cell characteristics for effective viscosity. In the design of the metamaterial rotators for optics or thermodynamics in the previous studies, the effective material properties of a unit cell are determined by the complex characteristics of the materials constituting the unit cell. On the other hand, the effective viscosity of a unit cell is largely affected by the environmental conditions such as boundary conditions and unit cell size rather than the characteristics of the composite material itself. Therefore, since only the internal micropillar rotated instead of the rotation of the whole unit cell, the desired rotational effect could not be obtained by using the conventional method. To solve this problem, an additional process should be attempted to advance the prototype metamaterial rotator.

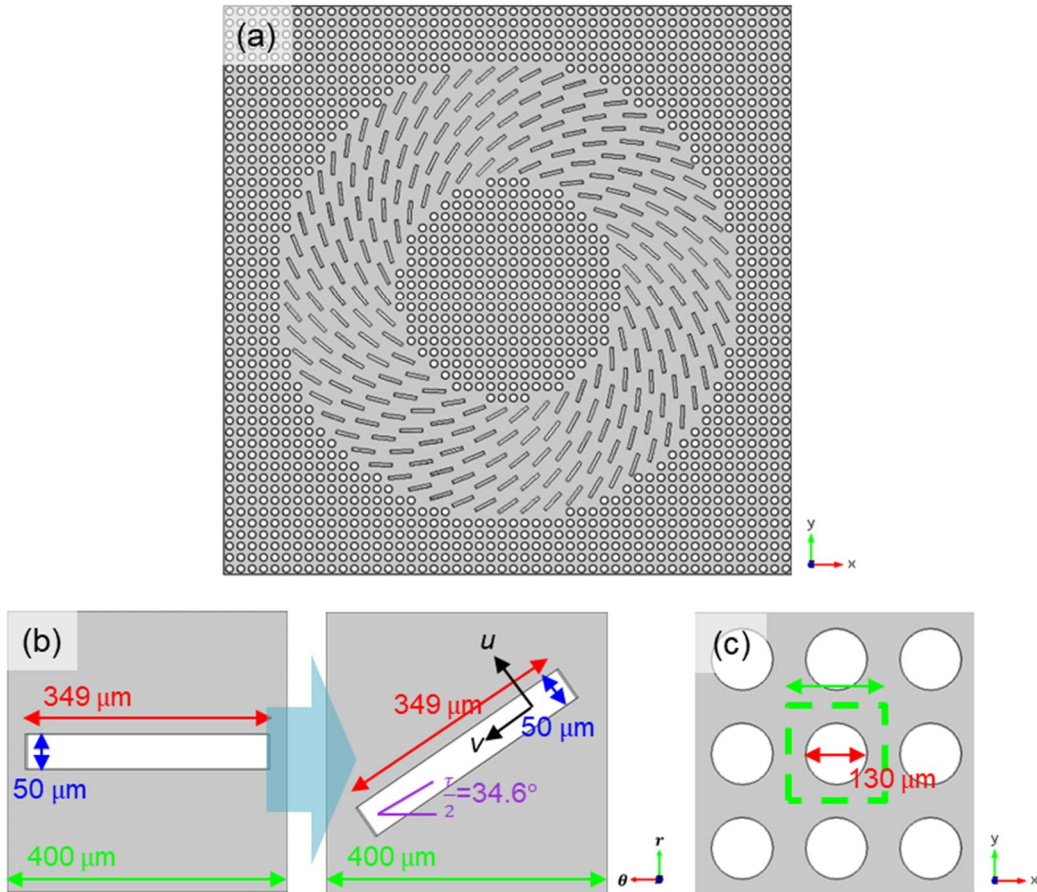


**Figure 2.5.5.** Design of the prototype rheological metamaterial rotator. (a) Total configuration. Configuration of the unit cells mapped on (b) the rotating shell (left: before tilting and right: after tilting) and (c) the background region.

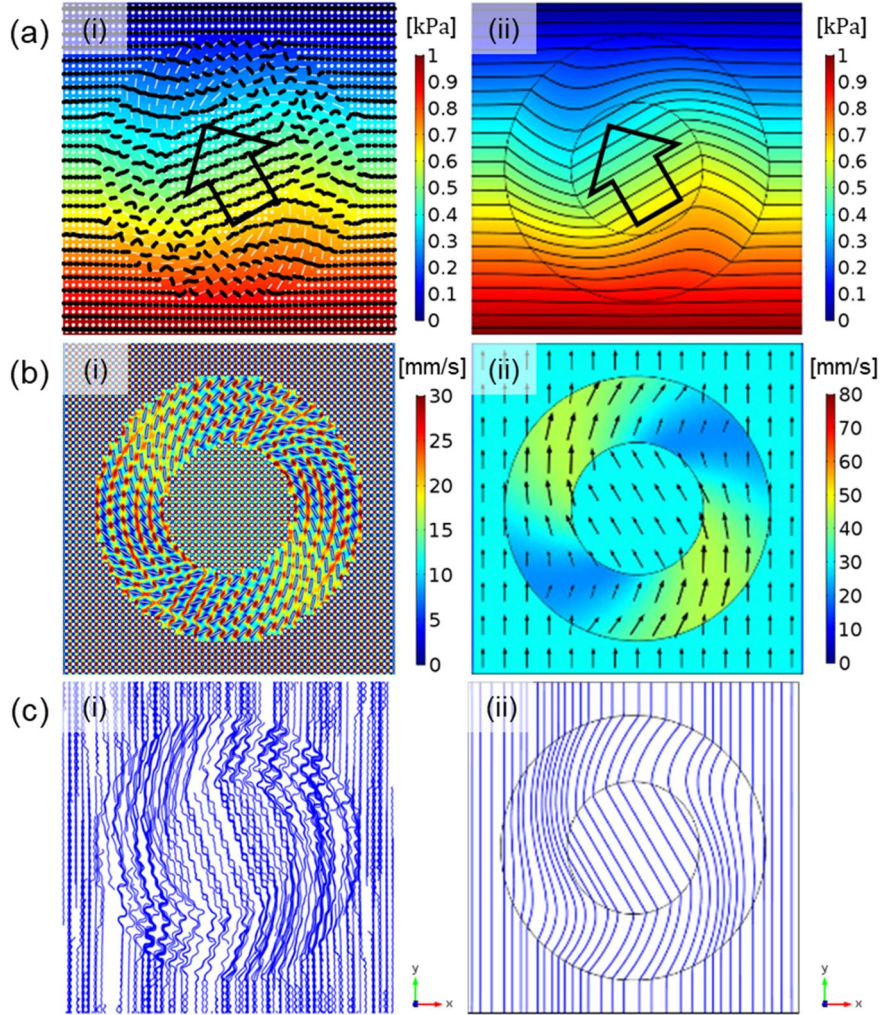


**Figure 2.5.6.** Simulation results of (a) pressure fields, (b) velocity fields, and (c) flow streamlines for (i) the prototype rheological metamaterial rotator and (ii) the ideal rotator of the continuous media.



### 2.5.4.2. Unit cell modeling

A strategy was built to address the problem raised in Section 2.5.4.1. Instead of using the mathematical method that has been used in previous studies, a unit cell was designed directly by a numerical method similar to Section 2.3.4.2 and Section 2.4.4.2. Therefore, the unit cell implementing the transformed viscosity tensor of **Eqn. 2.5.11** was directly designed. Effective viscosity was controlled by regarding superficial velocity of the unit cell through inserting a micropillar. COMSOL Multiphysics was used to simulate the velocity field and calculate the effective viscosity of the unit cells. Boundary conditions defined in Sections 2.3.4.2 and 2.4.4.2 were applied to the unit cell in the simulation.

Definition of the effective viscosity unit cell for the rotator was not sufficient with **Eqn. 2.3.22** alone because there are off-diagonal terms in the transformed viscosity tensor. However, there is no previous research on the effective unit cell modeling especially for the off-diagonal terms. Hence, the off-diagonal terms should be defined as **Eqn. 2.5.25** and used for the design of the rheological metamaterial rotator.

$$\mu_{eff,ij} = \left( \frac{\langle \tilde{\mathbf{u}}_{0,i} \rangle_S + \langle \tilde{\mathbf{u}}_{0,j} \rangle_S}{\langle \tilde{\mathbf{u}}_{pillar,i} \rangle_S + \langle \tilde{\mathbf{u}}_{pillar,j} \rangle_S} \right) \mu \quad (2.5.25)$$

, where  $\langle \tilde{\mathbf{u}}_{0,i} \rangle_S$  and  $\langle \tilde{\mathbf{u}}_{pillar,i} \rangle_S$  are the superficial velocity values in  $i$ -axis without or with the micropillar,  $\langle \tilde{\mathbf{u}}_{0,j} \rangle_S$  and  $\langle \tilde{\mathbf{u}}_{pillar,j} \rangle_S$  are the superficial velocity values in  $j$ -axis without or with the micropillar, and  $\mu$  is the intrinsic fluid viscosity.

Numerical analysis was carried out until the target viscosity tensor was obtained by gradually increasing the micropillar length from 349  $\mu\text{m}$ . When the micropillar length reached 500  $\mu\text{m}$ , the effective viscosity of the unit cell almost agreed with the ideal value of the transformed viscosity tensor in **Eqn. 2.5.11** as follows.

$$\widetilde{\boldsymbol{\mu}}_{30^\circ} = \begin{bmatrix} 2.43 & 1.47 \\ 1.10 & 1.59 \end{bmatrix} \mu \quad (2.5.26)$$

The geometric information and velocity fields of the unit cell are shown in **Fig. 2.5.7**.

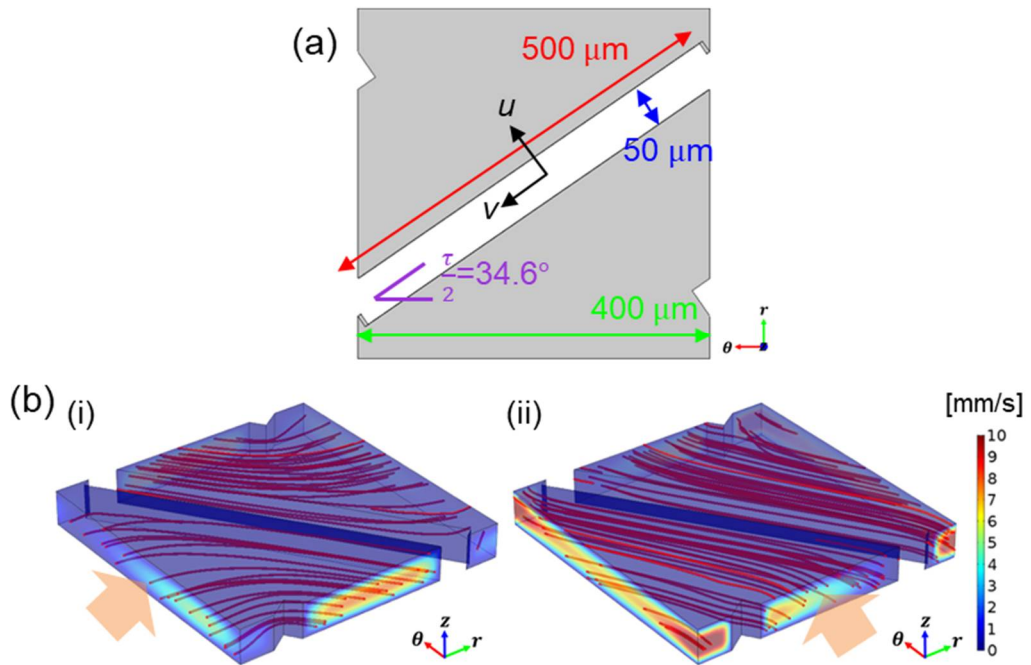


**Figure 2.5.7.** Design and numerical simulation results for effective viscosity unit cell for the direct-type rheological metamaterial rotor. (a) Configuration of the unit cell. (b) The simulated velocity fields for (i) radial and (ii) azimuthal direction.

### 2.5.4.3. Designed metamaterial rotator

A direct-type rheological metamaterial rotator was designed by mapping the unit cells that implement the unique viscosity terms of **Eqn. 2.5.26 (Fig. 2.5.8)**. The number and arrangement of the unit cells are the same as those of the prototype metamaterial rotators, and only the length of the micropillars in the unit cells was changed from 349  $\mu\text{m}$  to 500  $\mu\text{m}$ . The direct-type rotator was modeled by using CATIA 5.18 in the same way as used in Section 2.5.4.2. The designed metamaterial rotator was subjected to numerical analysis by using COMSOL Multiphysics with the simulation conditions and the material property described in Section 2.5.4.2. Free tetrahedral meshes consists of 742938 domain elements, 358736 boundary elements, 53200 edge elements

The simulation results of pressure fields, velocity fields, and flow streamlines for the designed metamaterial rotator are shown in **Fig. 2.5.9**. All simulation results agree with the results of the continuous media case. The angle of the pressure contour in the central area was successfully tilted by  $30^\circ$  as designed, while the background pressure fields was not affected at all (**Fig. 2.5.9(a)**). The unperturbed pressure contours and straight streamlines indicate that the rotator only distorts the space in the annular shell region. The impedance at the interface was perfectly matched and hence the gap between the pressure contours in the central region was neither widened nor narrowed. Also, it could be confirmed from the velocity field and streamlines that the flow direction was accurately changed by  $30^\circ$  (**Fig. 2.5.11(b)**).

Magnified images of the velocity field in the center area with or without the designed rotator clearly show how many degrees the flow direction changed (**Fig. 2.5.10**). The flow direction can be confirmed by the velocity field distribution in the dashed rectangle indicating the unit cell. By measuring the tilted angle, it was estimated that the fluid direction inside the rotator changed to the angle of  $-30^\circ$  relative to  $+y$  axis. Through the numerical analysis results (**Figs. 2.5.9-10**), it was figured out that that the direct numerical method is more accurate for designing the effective viscosity unit cell than the existing mathematical method, in order to yield the rheological metamaterial rotator.

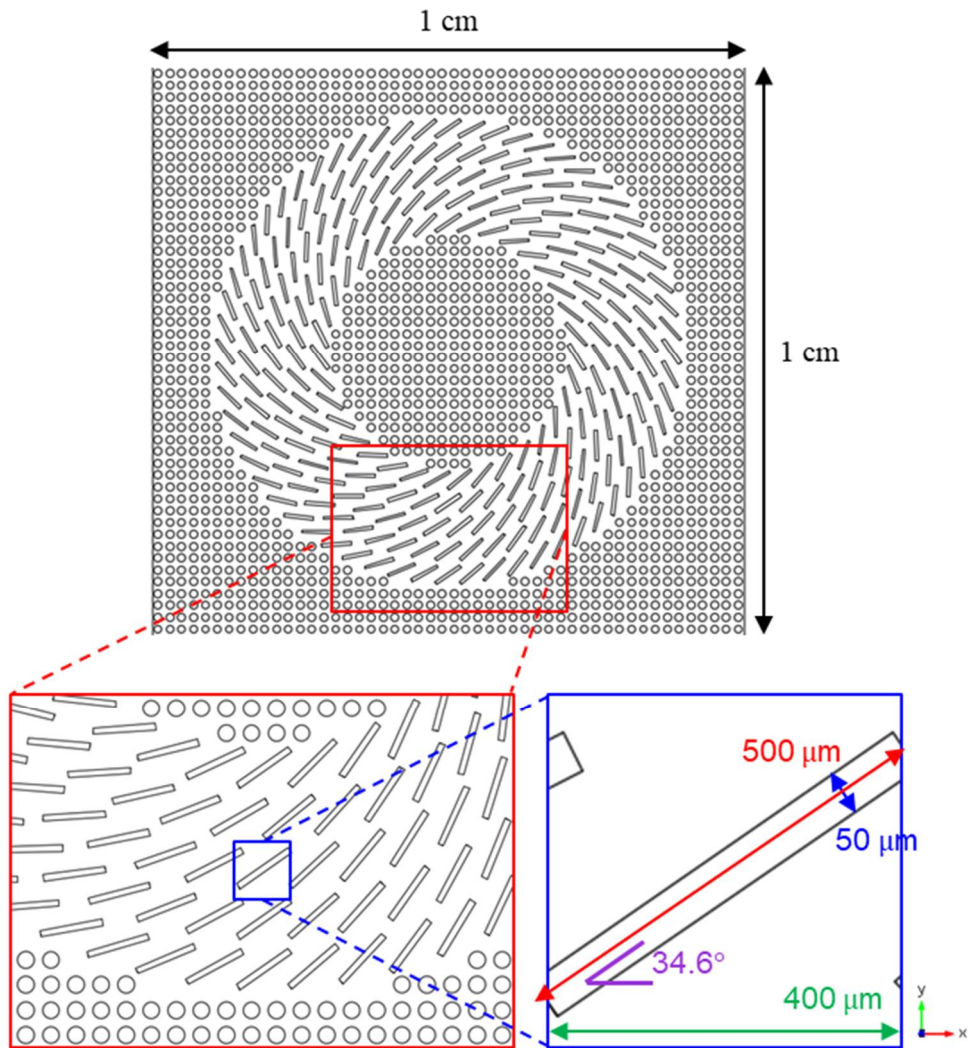


**Figure 2.5.8.** Design of the direct-type rheological metamaterial rotator with configuration and magnified views.

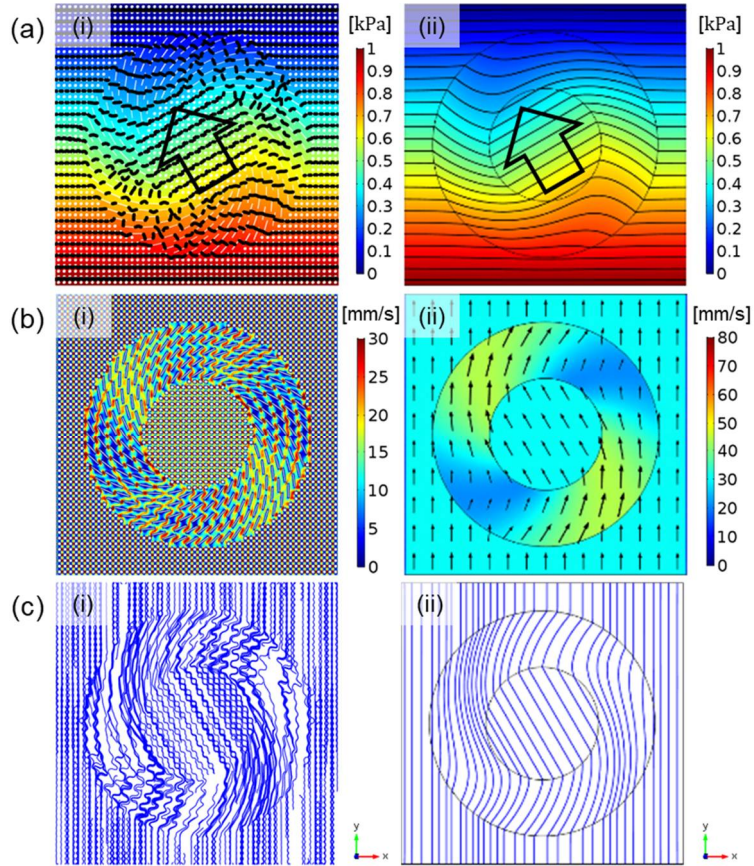


**Figure 2.5.9.** Simulation results of (a) pressure fields, (b) velocity fields, and (c) flow streamlines for (i) the direct-type rheological metamaterial rotator and (ii) the ideal rotator of the continuous media.

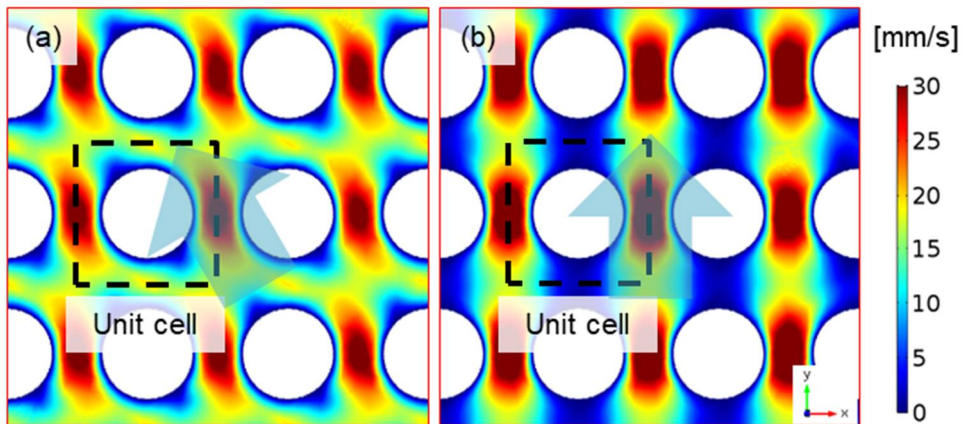


**Figure 2.5.10.** Magnified images of the simulated velocity fields in the central region: (a) with the rotator and (b) without the rotator. Dashed squares indicate the unit cell.

## 2.5.5. Experimental realization

### 2.5.5.1. Fabrication method

The direct-type rheological metamaterial rotator was drawn by using a commercial CAD program, AutoCAD 2017 (**Fig. 2.5.11**). The metamaterial rotator was placed in a microfluidic channel for performance verification through experiments, such as in the cases of the metamaterial cloak and concentrator. The configuration of the microchannel is identical to that of the metamaterial cloak and concentrator. The right drawing in **Fig 2.4.13** is the designed metamaterial rotator and the left one is the concentrator demonstrated in Section 2.4. The microchannel containing the rotator was placed in a 4-inch circle indicating a silicon (Si) wafer and the two reservoirs of 2 mm diameter were created to inject fluid into the microchannel.

The fabrication details of the microfluidic device are described in Section 2.4.5.1. The patterned chromium mask, the patterned Si master, and the fabricated microchannel, which were used in the fabrication process, are shown in **Figs. 2.5.12(a-c)**. The microdevice of the rheological metamaterial rotator was fabricated and its microstructure is shown in **Fig. 2.5.13** with the drawing. Not only was the overall shape replicated well from the Si master, but also the shape of the microstructure perfectly matched the drawing.

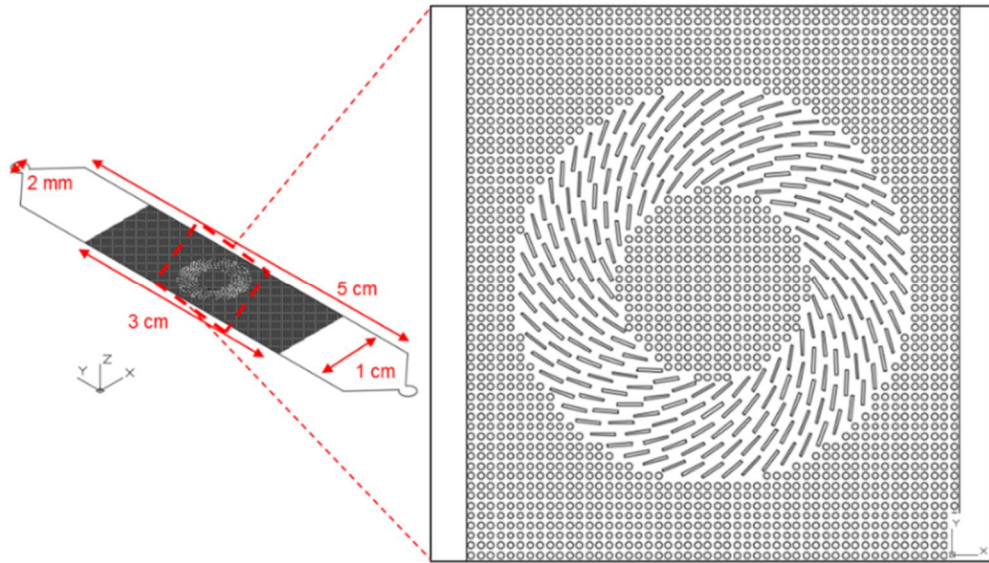


**Figure 2.5.11.** A microscale view and configuration of the rheological metamaterial rotator.

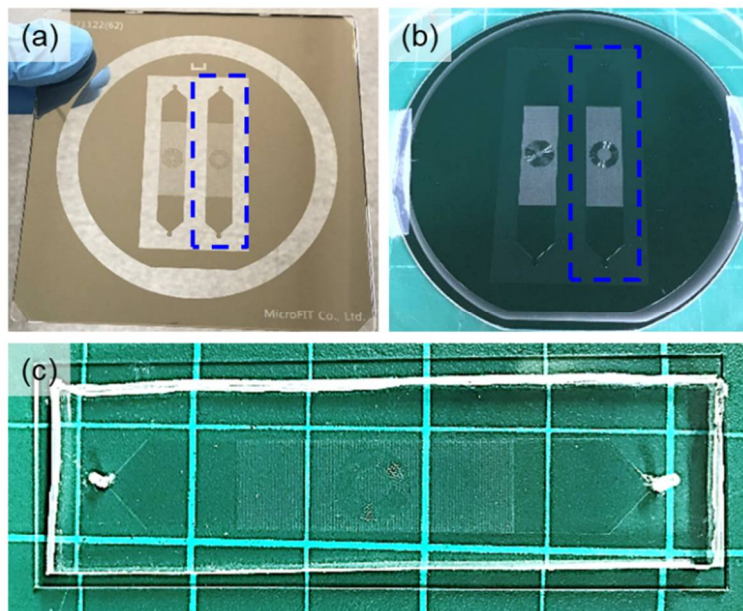


**Figure 2.5.12.** Fabrication details of the rheological metamaterial rotator. (a) The Cr mask patterned with the designed drawing, (b) the fabricated silicon master, and (c) the manufactured microfluidic device. The figures in the blue dashed rectangle are the rotators and the others are the metamaterial concentrators discussed in Section 2.4.

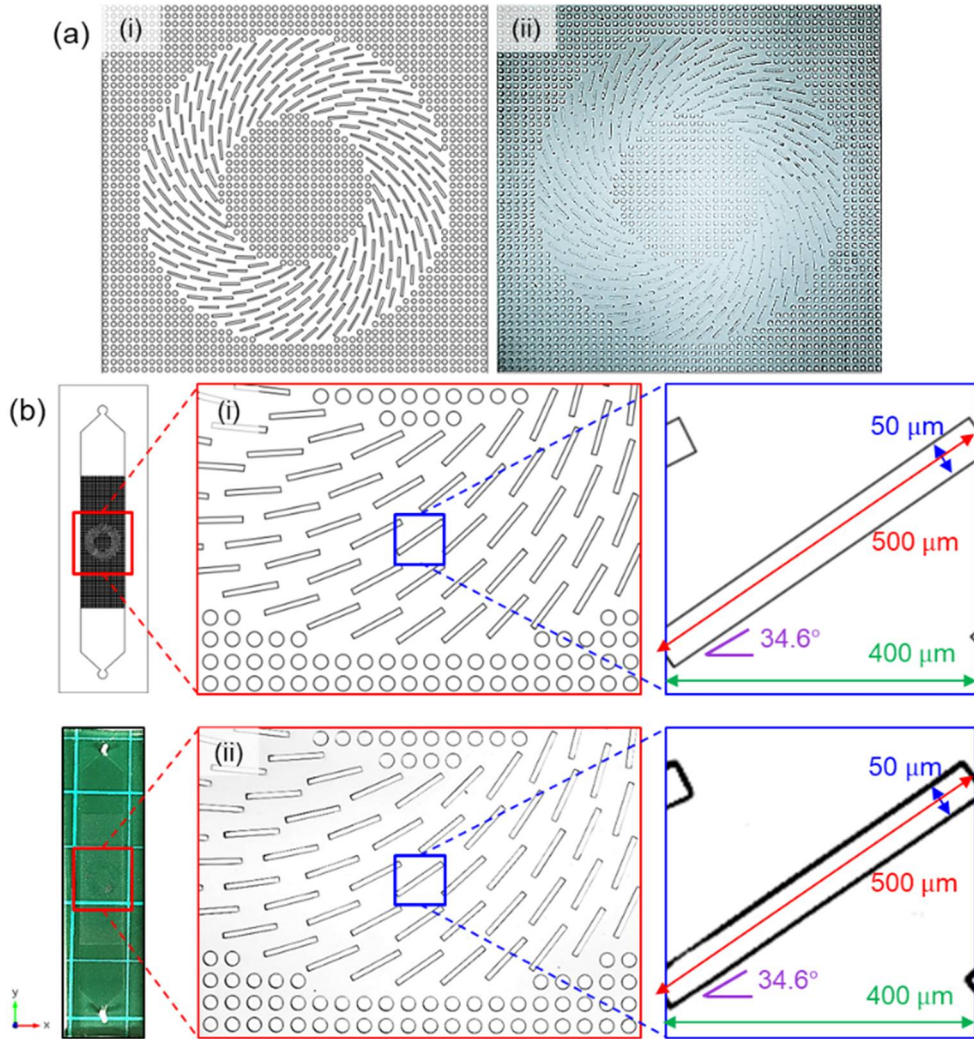


**Figure 2.5.13.** Comparison of microstructure of the rheological metamaterial rotator; (a) the designed drawing and (b) the fabricated device. Detailed configuration of (a) the designed rheological metamaterial rotator and (b) the fabricated rheological metamaterial rotator at microscale.



### 2.5.5.2. Experimental method

The method for experimental realization is the same as that of the rheological metamaterial cloak and concentrator. The detail experimental method is provided in Section 2.3.5.2 and **Fig. 2.3.24**.

### 2.5.5.3. Experimental results

The rotational fluid flow by the fabricated rheological metamaterial rotator was found in the fabricated microfluidic device. **Figure 2.5.14** shows the captured flow streamlines for three discrete parts of the metamaterial rotator, which are entrance, left-side, and central regions. The simulated streamlines and microstructures for each region were simultaneously displayed with the captured streamlines and their patterns were compared with each other.

The experimentally captured streamlines are in good agreement with the simulated streamlines in the entire region of the metamaterial rotator. The streamlines at the entrance region (**Fig. 2.5.14(a)**) indicate that the fluid flow is successfully guided in the rotating shell as designed. The fluid flow entering the rotator reaches the inner central region after being rotated exactly 30 degrees. The straight shape of streamlines in the background area means a perfect impedance match. The streamlines at the left-side region (**Fig. 2.5.14(b)**) are also perfectly consistent with the simulation results. The streamlines at the central region (**Fig. 2.5.14(c)**) covered by the metamaterial rotator were tilted by 30 degrees, confirming that the coordinate space system was successfully distorted as designed.

The important point is that the flow rate in the central space tilted at 30 degrees is equal to the flow rate in the non-tilted background space. This means that the fluid flow is not forcibly controlled by external forces or fields, but is precisely controlled by the spatial design. Due to the limitations of the design and experimental methods, only the 30° rotator could be experimentally materialized. However, if the effective viscosity control technique of space achieves more progress, it is obvious that a variety of rheological rotators can be developed that can rotate at larger angles as theoretically proven.

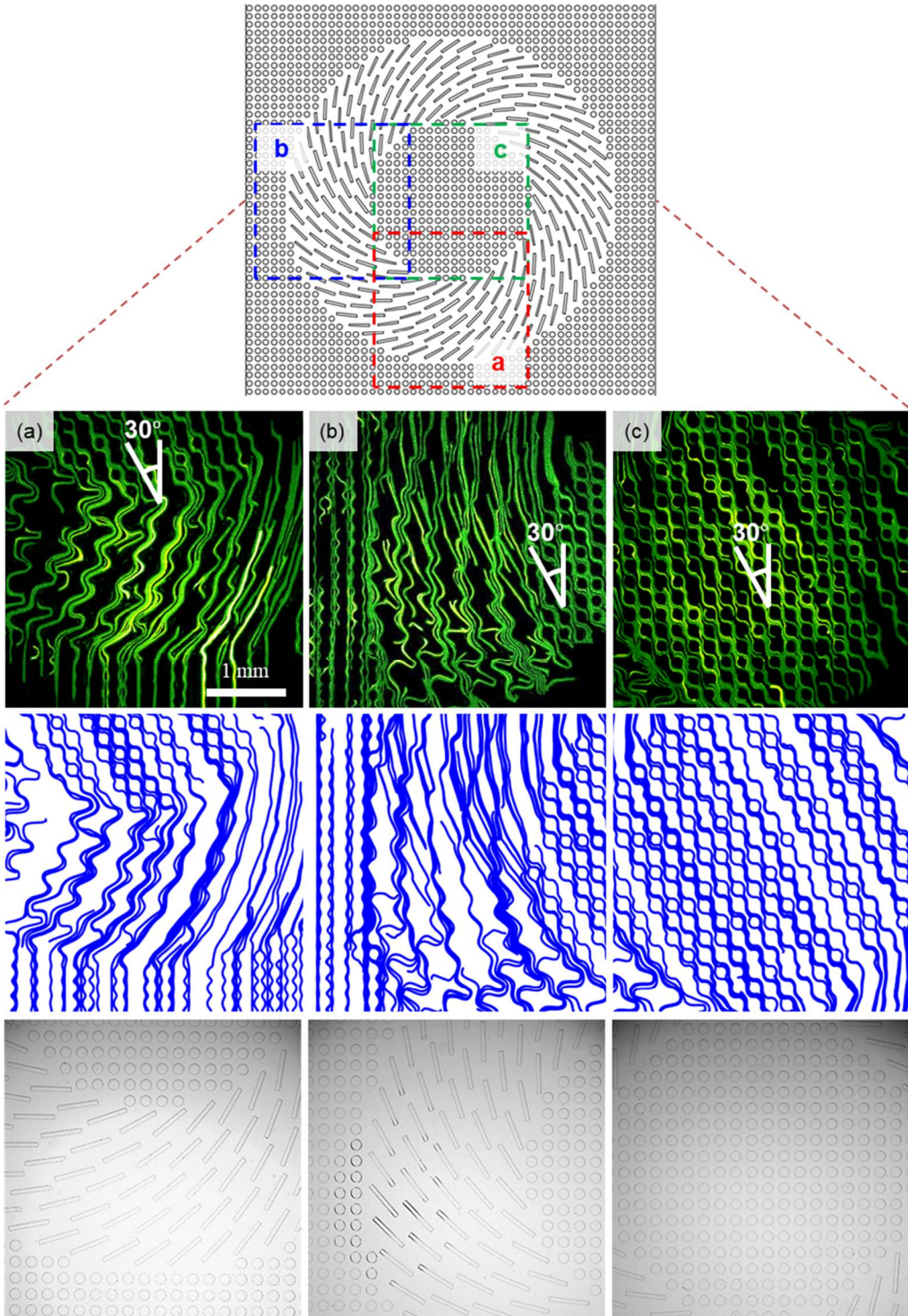


**Figure 2.5.14.** Flow streamlines of the rheological metamaterial rotator at (a) the entrance region, (b) left-side region, and (c) central region: observed streamlines (top), simulated streamlines (middle), and microstructure during the experiment (bottom).

### **2.5.6. Conclusions**

In the present section, the rheological rotator was proposed throughout a full development process from mathematics, numerical calculation, metamaterial design to experimental characterization. The rotating shell with the precisely twisted fluidic space was proposed as a mathematically defined Jacobian transformation matrix in a tensor form. Transformation rheology yielded the four transformed viscosity tensors, which rotate the coordinate spaces by  $180^\circ$ ,  $180^\circ$ ,  $90^\circ$ , and  $30^\circ$ . The fluidic rotating behaviors were confirmed by numerical analysis with the transformed viscosity tensors. The rheological metamaterial rotator was designed by mapping the effective viscosity unit cells that were directly calculated and designed. The designed metamaterial rotator was theoretically simulated and fabricated as a microfluidic device. The perfectly matched flow streamlines between the simulation and experimental results manifest that the designed rotator can guide fluid flow successfully. The capability to control the flow direction as desired will provide a new perspective on various fields of fluid dynamics. In particular, applications of the rheological metamaterial rotator to technologies for operating of aircrafts, shipping, or automobiles are able to bring out a significant progress in fuel efficiency and navigation safety.

## 2.6. Summary

The research goal of this chapter is to apply the metamaterial concept based on transformation optics to fluid mechanics, deriving transformation rheology. It was succeeded in presenting the overall process from mathematical modeling to experimental implementation of cloaks, concentrators, and rotators, which are the most important and frequently handled metamaterials. In Section 2.2, a mathematical proof process was described for the development of transformation rheology as a fundamental step. Transformation rheology suggested a way to calculate transformed viscosity tensors and to develop rheological metamaterials. The simulation and experimental results of the cloak, concentrator, and rotator showed that the desired metamaterials were successfully fabricated in a real material and worked properly. In Section 2.3, the rheological metamaterial cloak was developed. The strategy of applying an invisibility cloak to rheology was able to achieve the effect of dramatically minimizing drag acting on the obstacle. The rheological metamaterial concentrator was proposed in Section 2.4. The space-concentrating strategy succeeded in aggregating fluid energy several times to a specific site. Thirdly, the rheological metamaterial rotator was introduced in Section 2.5. The technique by the rheological rotator, which can lead to the desired flow direction different from the surrounding fluid, can be applied in various ways in industry and academia involved in fluid dynamics, including energy harvesting and drag reduction.

# Chapter 3.

## Shape Memory Polymeric Metasurfaces

### 3.1. Overview

In this chapter, the nanostructured metasurfaces made of a shape memory polymer (SMP) are introduced, which achieve a sustainable and improved energy transfer by nanoscale impedance matching.

Modulation of thermomechanics nature is a critical issue for an optimized use of shape memory polymers (SMPs). In Section 3.2, a strategic approach was proposed to control the transition temperature of SMPs, especially based on acrylic chemicals. Five SMPs were chemically designed and synthesized; three shape memory polyacrylates (SMACs) as a basic SMP and two shape memory copolyacrylates (SMCPAs) to modify transition temperature by changing the composition of monomers. Chemical structure and composition of the synthesized SMPAs and SMCPAs were analyzed. Thermomechanical properties and shape memory performance of the SMPs were examined. Numerical simulation was performed to model the shape memory behavior of the synthesized SMPs. Optical transparency of the samples was identified. It is envisaged that the smart materials proposed in this section can help develop a new type of shape-memory devices in biomedical and aerospace engineering applications.

Antireflection (AR) nanostructures mimicking moth eye, the most famous metasurface, have been developed for optical devices to achieve high transmittance of light energy. However, mechanical vulnerability has always been pointed out as a drawback of the nanostructures. In Section 3.3, a unique AR strategy is proposed, which is to infuse shape recovery ability into nanopattern arrays for the high sustainability of the AR nanostructure. The SMCPA (S-MMA/BMA) developed in Section 3.1 was used, where the transition temperature was modulated close to body temperature for facile shape recovery. Nanoscale shape recoverability of the patterns was explored at body temperature. Light

transmittance was analyzed experimentally according to the shape state of the AR nanopattern, and the shape recovery function restored the damaged antireflection performance. The underlying mechanism of the sustainable AR based on nanopattern was suggested by calculating theoretical transmittance. Omnidirectional antireflectivity by the nanopattern was examined by measuring oblique incident transmittances with their sustainability. The nanomechanical property and the sustainable self-cleaning effect induced by the smart nanostructures were also confirmed experimentally. The approach proposed in this study is expected to provide new insights into biomimetic optics.

Low electric energy loss is a very important problem to minimize the decay of transferred energy intensity due to impedance mismatch. This issue has been dealt with by adding an impedance matching layer at the interface between two media. In Section 3.4, a metasurface strategy was proposed to improve the charge transfer from human body to a biometric device by using an impedance matching nanostructure. Nanocomposite pattern arrays were fabricated with the SMCPA (S-MMA/BMA) developed in Section 3.1 and carbon nanotubes (CNTs). The shape recovery ability of the nanocomposite patterns could enhance durability and sustainability of the structure. It was found that the composite nanopatterns improve the current transfer by two times compared with the non-patterned composite sample. The underlying mechanism of the enhanced charge transport was understood by carrying out numerical simulation. It is anticipated that this study can provide a new pathway for developing advanced biometric devices with high sensibility of biological information.

## 3.2. Shape memory polymer synthesis

### 3.2.1. Introduction

Smart materials such as shape memory polymers (SMPs) [65,66,168], self-healing polymers [169–171], piezoelectric materials [172], and photovoltaics [173,174] have attracted great attention for a myriad of applications in academic and industrial areas due to their fascinating unique features. In particular, SMPs have the ability to recover their permanent original shape by applying external stimuli, *e.g.*, thermal heating above transition temperature [65]. Unlike shape memory metals or ceramics, SMPs have revealed high biocompatibility and low cytotoxicity. For this reason, they have been designed and fabricated for biomedical applications, such as surgical, ophthalmic, and cardiovascular applications [105,107,110].

SMPs are basically composed of fixing and switching segments, where are related with the shape memorization and the reverse change of phase, respectively. When SMPs are heated above the transition temperature, the switching segments (*e.g.*, semi-crystalline domains [71,175–177] or amorphous domains [178–181]) are melted or un-entangled. This molecular phenomenon leads to a dramatic drop in the modulus of SMPs. At elevated temperature, SMPs become deformable materials with low modulus and their shapes can be programmed into a temporary shape as intended. When polymeric chains of SMPs are re-entangled by cooling below transition temperature, the decreased modulus is returned to an original state, and then the temporarily programmed shape is locked. Once the deformed SMPs are heated above the transition temperature, their chains start moving. Then, entropic elasticity induced by micro Brownian motion of switching segments entails the shape recovery to the permanent shape of SMPs [65,182].

Various types of SMPs with different mechanisms have been reported; chemically crosslinked amorphous SMPs [69,183,184], physically crosslinked semi-crystalline SMPs [185–187], and liquid crystalline SMPs [64,188,189]. Among them, the chemically crosslinked amorphous SMPs based on acrylic polymers have a lot of possibilities for applications in optical devices due to their high transmittance, high chemical resistance, and low cost.

Transition temperatures of SMP need to be manipulated for optimized use under certain circumstances. However, it is not easy to develop new chemicals to tune the transition temperature. Thermomechanical properties of SMPs are mainly determined by chemical composition. Hence, several researches have been attempted to modulate the transition temperature of SMPs by changing the content and molecular weight of crosslinkers [70,107,190–193]. Similarly, the transition temperature can be adjusted relatively easily based on multi-copolymerization by blending different kinds of monomers. The simple blending of different monomers has not yet been applied to the acrylic SMPs. In addition, the spectroscopic analysis of chemical structures of the acrylic SMPs has hardly been conducted, even if it is helpful to understand underlying chemistry behind chemico-physical properties.

In this section, a facile and effective strategy of tailoring the transition temperature of SMPs was proposed. Acrylic SMPs were formulated and fabricated with use of combination of different monomers; Methyl methacrylate (MMA), n-Butyl methacrylate (BMA), and b-Butyl acrylate (BA). A blending process of different monomers enables the transition temperature modulation of the synthesized copolymers. A chemical reaction procedure was designed and the resulting chemical structures were analyzed using XPS (X-ray photoelectron spectroscopy) and FTIR (Fourier-transform infrared spectroscopy). In addition, a dynamic mechanical thermal analysis (DMTA) was carried out to investigate thermomechanical behavior of the tri-copolymers. Numerical simulation confirmed the shape memory behavior of the synthesized materials by using a hyperelastic model [194–198]. The potential for optical applications was evaluated by UV-vis spectroscopy analysis.



## 3.2.2. Experimental

### 3.2.2.1. Materials for SMP synthesis

Methyl methacrylate (MMA), n-Butyl methacrylate (BMA), and n-Butyl acrylate (BA) (Daejung Chemicals, Republic of Korea) were selected as monomers for the precursors of SMP synthesis. Poly-(ethylene glycol) dimethacrylate (PEGDMA,  $M_n \approx 525$ , Sigma Aldrich, United States) was used as a crosslinking agent. The volume ratio of the monomers and the crosslinker was 1:2. A photo initiator (0.02 wt %), Phenylbis (2, 4, 6-trimethylbenzoyl) phosphine oxide (BAPOs, Sigma Aldrich, United States), was employed due to its high absorptivity in a UV (ultraviolet) light range and high solubility in acrylate chemicals.

### 3.2.2.2 Fabrication method of SMP specimen

Five combinations of monomers were designed for the SMP synthesis; MMA, BMA, BA, MMA/BMA (1:1), and BA/BMA (1:1). The five SMP samples are named as S-MMA, S-BMA, S-BA, S-MMA/BMA, and S-BA/BMA, where “S” refers to “shape memory”. S-MMA, S-BMA, and S-BA are in the group of SMPA (shape memory polyacrylate) and S-MMA/BMA and S-BA/BMA are in the group of SMCPA (shape memory copolyacrylate). The precursors composed of the monomers, the crosslinker, and the photo initiator were prepared through vigorous vortex mixing for 30 minutes. A mold for the fabrication of SMPs was made of two slide glasses with a 1 mm gap. The precursors were injected into the gap and UV light ( $\lambda \approx 365$  nm) was irradiated over the mold for 30 minutes. A post-heating process was fulfilled in an oven at 100°C for 30 minutes. After then, the SMP samples were detached from the mold and rinsed with ethanol. Schematic illustration of the fabrication process is shown in **Fig. 3.2.1**.

### 3.2.2.3. Characterizations

Fourier transform infrared spectroscopy (FTIR) was employed to characterize chemical composition of the SMPs. The spectral data of the samples were acquired using an attenuated total Reflectance-Fourier transform infrared (ATR-FTIR) mode. All data were obtained at resolution of 4  $\text{cm}^{-1}$  in the mid infrared region from 4000 to 650  $\text{cm}^{-1}$  with 64 scans using a Varian 660 FTIR spectrometer. The data were normalized for comparison

between the SMP samples. The Varian Resolutions Pro software was employed to analyze the data.

X-ray photoelectron spectroscopy (XPS) analysis was conducted by using an AXIS-His electron spectrophotometer (Kratos Ltd., United Kingdom) with a monochromatic Mg Ka X-ray source ( $h\nu = 1253.6$  eV) of 450 W power. The SMP samples were prepared by coating a film on the Al substrate placed on the XPS sample holder. The samples were scanned under a high vacuum pressure of  $5 \times 10^{-10}$  torr at room temperature. A survey spectrum was recorded over a binding energy range from 0 to 1500 eV by using a pass energy of 300 eV. Detailed analysis of the C1s region for the samples was carried out over a binding energy range from 280 to 300 eV by using a pass energy of 150 eV. The corresponding data was analyzed by using the CasaXPS program for deconvolution of the C1s spectra, background subtraction, fitting, peak integration, and quantification of chemical elements. Since C is a dominant element in the spectra, the charging effect induced by the C 1s peak of hydrocarbons was considered for the results. Details on this methodology is explained in the reference [199]. The curve fitting of spectrum peaks was carried out by combining the Gaussian with the Lorentzian peak shapes.

Thermomechanical properties of the SMP samples were characterized by running a dynamic mechanical thermal analysis machine (DMTA machine, TA Q800 DMA, United States). The samples were cut into a dimension of  $1 \times 5.3 \times 40$  mm<sup>3</sup> and held in the clamp. Storage and loss moduli of the samples were measured in the single frequency tensile loading mode at 1 Hz. The conditions of 0.2% strain, 5°C/min thermal heating rate, 125 % force track, and 0.001 N preloading were applied while heating of the samples.

Transmittance of the samples was measured by using a UV-vis spectrophotometer (Cary 100, Agilent Technologies, United States). The used optical configuration and monochromator were double beam and the Czerny-Turner type, respectively. The wavelength range of light was from 380 nm to 900 nm.

Transient shape recovery ratio ( $R_r$ ) was evaluated by measuring the change of angle during the shape recovery [93,200]. The tests were conducted at 80°C, 40°C, and 0°C. In the shape programming step, the SMP samples were heated up to 20°C above  $T_g$ , bended, and cooled down to 20°C below  $T_g$ . The initial angle ( $\theta_i$ ) and the recovered angle ( $\theta_r$ )

were examined at 80°C, 40°C, and 0°C. The shape recovery ratio was calculated by following definition.

$$R_r = \frac{\theta_i - \theta(t)}{\theta_i - \theta_r} \times 100 \quad (3.2.1)$$

where  $\theta_i, \theta(t)$ , and  $\theta_r$  are the initial angle, the deformed angle at time  $t$ , and the recovered angle.

Cyclic stress-strain-temperature (SST) curves of S-MMA/BMA and S-BA/BMA were obtained by using the TA Q800 DMA with a 3-point bending mode clamp. The samples were bended by 2 mm deflection ( $\varepsilon=3\%$ ) at 40°C for S-MMA/BMA and 0°C for S-BA/BMA, respectively. The cooling step was conducted at 0°C for S-MMA/BMA and -40°C for S-BA/BMA, while maintaining the applied deformation strain. After the unloading step, the heating step was applied at 40°C for S-MMA/BMA and 0°C for S-BA/BMA, for shape-recovery of the original permanent shape.

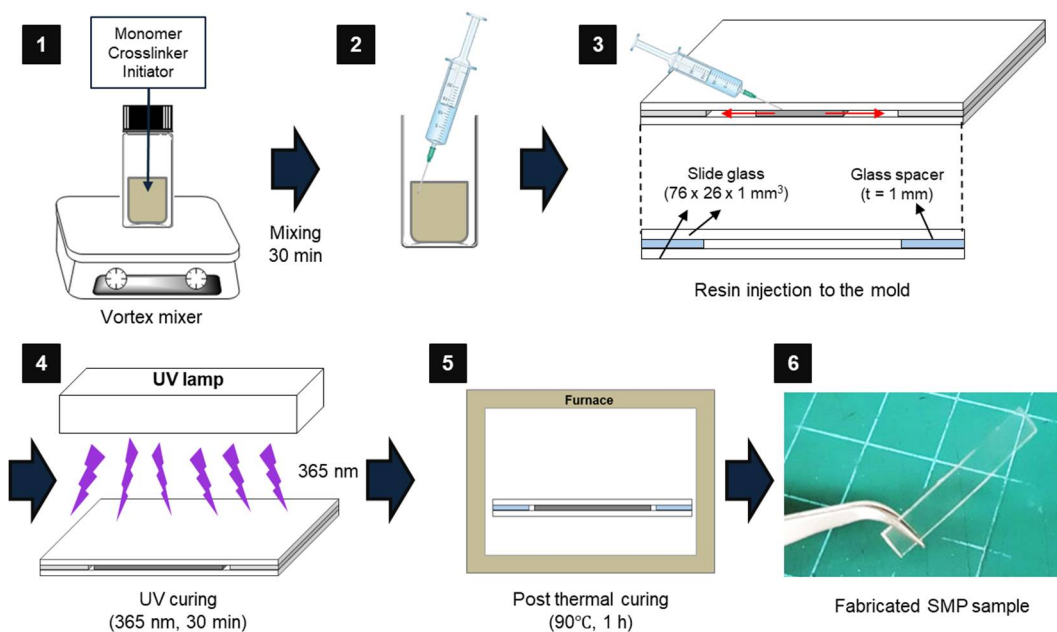


**Figure 3.2.1.** Fabrication scheme of the SMP samples.

### 3.2.3. Numerical analysis

Numerical analysis for modeling shape memory behavior of the samples was studied by using ABAQUS/CAE, which is based on a finite element method (FEM) code, with user subroutines UMAT and SDVINI. Neo-Hookean model, the hyperelastic model, was used in the simulation by assuming the existence of strain energy as a form of Helmholtz potential for deformation of the material. Also, an isothermal, compressible, and hyperelastic material was assumed. In the simulation, the material properties were modeled as continuously changed dependent on the applied temperature condition. In the hyperelastic model, non-linear material properties are defined and modeled by using stored strain energy function ( $\psi$ ). The stored strain energy function consists of a glassy phase part ( $\alpha$ ) and a rubbery phase part ( $1 - \alpha$ ). The constitutive equations are expressed as

$$\psi_t = (1 - \alpha)\psi_r + \int_{t_i}^t \psi_g d\tau \quad (3.2.2)$$

$$\psi_r = C_{10}(\bar{I}_{\kappa_r} - 3) + \frac{1}{D_1}(J_{\kappa_r} - 1)^2 \quad (3.2.3)$$

$$\psi_g = C_{20}(\bar{I}_{\kappa_{g(t)}} - 3) + \frac{1}{D_2}(J_{\kappa_{g(t)}} - 1)^2 \quad (3.2.4)$$

, where  $\psi_t$  is the total stored strain energy function,  $\psi_r$  is the stored strain energy function for the rubbery region,  $\psi_g$  is the stored strain energy function for the glassy region,  $\bar{I}_{\kappa_r}$  and  $\bar{I}_{\kappa_{g(t)}}$  are the first invariant of the isochoric part of the right Cauchy-Green deformation tensors,  $J_{\kappa_r}$  and  $J_{\kappa_{g(t)}}$  are the Jacobian matrices for each region at time  $t$ . The subscripts “r” and “g” refer to the rubbery and glassy phases, respectively.  $C_{10}(= \mu_r/2)$  and  $C_{20}(= \mu_g/2)$  are the material input parameters which are related to shear modulus ( $\mu$ ). Similarly,  $D_1(= 2/K_r)$  and  $D_2(= 2/K_g)$  are the material input parameters related to bulk modulus ( $K$ ). These parameters are continuously updated while running the simulation according to the changes of phase content and deformation gradients at the current state.

The temperature-dependent glass content function ( $\alpha$ ) was defined as a linearized temperature variation like

$$\alpha = \frac{T_{rub} - T}{T_{gla} - T_{rub}} \quad (3.2.5)$$

, where  $T$  is the current temperature,  $T_{gla}$  is the temperature at the fully glassy state and  $T_{rub}$  is the temperature at the fully rubbery state. The four simulation steps of loading, cooling, unloading, and heating were modeled and coded in ABAQUS/CAE program, in the same way as the experimental shape memory test using the DMTA machine.

The defined non-linear material behaviors were programmed in the user subroutine code UMAT. A stiffness tensor matrix ( $\mathbb{C}$ ) should be mathematically derived to be built and used in a finite element method (FEM) program. The process to derive the tangent stiffness matrix of glass shape memory polymers from the stored energy function ( $\psi$ ) is briefly suggested below based on the Barot's dissertation [197]. A more detailed description of the term definition and modeling is provided in this reference, beyond the scope of this dissertation. The ABAQUS program requires the stiffness matrix defined as the following relationship.

$$\mathbb{C} = \frac{1}{J} \frac{\partial \boldsymbol{\tau}^J}{\partial \mathbf{D}} \quad (3.2.6)$$

, where  $\boldsymbol{\tau}^J$  is the Jaumann rate of Kirchoff stress defined as

$$\begin{aligned} \boldsymbol{\tau}^J &= \dot{\boldsymbol{\tau}} - \mathbf{W}\boldsymbol{\tau} - \boldsymbol{\tau}\mathbf{W}^T \\ &= \dot{j}\boldsymbol{\sigma} + j\dot{\boldsymbol{\sigma}} - j\mathbf{W}\boldsymbol{\sigma} - j\boldsymbol{\sigma}\mathbf{W}^T \\ &= \dot{j}\boldsymbol{\sigma} + j\boldsymbol{\sigma}^J \end{aligned} \quad (3.2.7)$$

And  $\mathbf{D}$  is the symmetric part of the spatial gradient of velocity. Therefore, the stiffness matrix can be transformed by putting **Eqn. 3.2.7** into **Eqn. 3.2.6** as

$$\mathbb{C} = \boldsymbol{\sigma} \otimes \mathbf{I} + \frac{\partial \boldsymbol{\sigma}^J}{\partial \mathbf{D}} \quad (3.2.8)$$

To calculate the stiffness matrix, the Cauchy stress tensor ( $\boldsymbol{\sigma}$ ) and the Jawman rate of Cauchy stress ( $\boldsymbol{\sigma}^J$ ) should be obtained first. The Cauchy stress tensor ( $\boldsymbol{\sigma}$ ) for hyperelastic materials is defined as

$$\boldsymbol{\sigma} = \frac{2}{J} \mathbf{F} \frac{\partial \psi}{\partial \mathbf{C}} \mathbf{F}^T \quad (3.2.9)$$

, where  $\mathbf{F}$  is the deformation gradient with respect to reference configuration. The stored energy function ( $\psi$ ) for the glassy phase at each time increment (used in **Eqn. 3.2.9**) can be written as

$$\begin{aligned} \psi = (1 - \alpha) & \left\{ C_{10} (\overline{I}_{\kappa_r} - 3) + \frac{1}{D_1} (J_{\kappa_r} - 1)^2 \right\} \\ & + \int_{t_i}^{\tau} \left\{ C_{10} (\overline{I}_{\kappa_r} - 3) + \frac{1}{D_1} (J_{\kappa_{g(t)}} - 1)^2 \right\} \frac{d\alpha}{d\tau} d\tau \end{aligned} \quad (3.2.10)$$

The derivative of stored energy function with  $\mathbf{C}$  (the right Cauchy stretch tensor) on the right-hand-side of **Eqn. 3.2.9** is derived as

$$\begin{aligned} \frac{\partial \psi}{\partial \mathbf{C}} = (1 - \alpha) & \left\{ C_{10} (\det \mathbf{C}_{\kappa_r})^{-\frac{1}{3}} \left( \mathbf{I} - \frac{1}{3} \text{tr} \mathbf{C}_{\kappa_r} \mathbf{C}_{\kappa_r}^{-T} \right) + \frac{1}{D_1} (J_{\kappa_r}) (J_{\kappa_r} - 1) \mathbf{C}_{\kappa_r}^{-T} \right\} \\ + (\alpha) & \left\{ C_{20} (\det \mathbf{C}_{\kappa_{g(t)}})^{-\frac{1}{3}} \left( \mathbf{I} + \frac{1}{3} \text{tr} \mathbf{C}_{\kappa_{g(t)}} \mathbf{C}_{\kappa_{g(t)}}^{-T} \right) + \frac{1}{D_1} (J_{\kappa_{g(t)}}) (J_{\kappa_{g(t)}} - 1) \mathbf{C}_{\kappa_{g(t)}}^{-T} \right\} \end{aligned} \quad (3.2.11)$$

, where  $\mathbf{I}$  is the identity tensor. From **Eqns. 3.2.9** and **3.2.11**, the Cauchy stress tensor ( $\boldsymbol{\sigma}$ ) can be calculated by the following relationship, where  $\overline{\mathbf{B}}$  is the isochoric part of the deformation component for each phase.

$$\begin{aligned} \boldsymbol{\sigma} = (1 - \alpha) & \left\{ \frac{2C_{10}}{J_r} \left[ \overline{\mathbf{B}}_{\kappa_r} - \frac{1}{3} \overline{\mathbf{B}}_{\kappa_r} \mathbf{I} \right] + \frac{1}{D_1} (J_{\kappa_r} - 1) \mathbf{I} \right\} \\ + (\alpha) & \left\{ \frac{2C_{20}}{J_g} \left[ \overline{\mathbf{B}}_{\kappa_{g(t)}} - \frac{1}{3} \overline{\mathbf{B}}_{\kappa_{g(t)}} \mathbf{I} \right] + \frac{2}{D_2} (J_{\kappa_{g(t)}} - 1) \mathbf{I} \right\} \end{aligned} \quad (3.2.12)$$

The material derivative of the Cauchy stress tensor ( $\dot{\boldsymbol{\sigma}}$ ) is defined as

$$\begin{aligned}
\dot{\boldsymbol{\sigma}} = & (1 - \alpha) \left\{ \frac{2C_{10}}{J_{\kappa_r}} \left[ \mathbf{L}\bar{\mathbf{B}}_{\kappa_r} + \bar{\mathbf{B}}_{\kappa_r}\mathbf{L}^T - \frac{2}{3} \text{tr}D\bar{\mathbf{B}}_{\kappa_r} - \frac{2}{3} \bar{\mathbf{B}}_{\kappa_r} \cdot \mathbf{DI} + \frac{2}{9} \text{tr}D \text{tr}\bar{\mathbf{B}}_{\kappa_r}\mathbf{I} \right] \right. \\
& \left. - \frac{1}{J_{\kappa_r}} \left[ \bar{\mathbf{B}}_{\kappa_r} - \frac{1}{3} \text{tr}\bar{\mathbf{B}}_{\kappa_r}\mathbf{I} \right] + \frac{2}{D_1} J_{\kappa_r} \text{tr}D\mathbf{I} \right\} \\
& + (\alpha) \left\{ \frac{2C_{20}}{J_{\kappa_{g(t)}}} \left[ \mathbf{L}\bar{\mathbf{B}}_{\kappa_{g(t)}} + \bar{\mathbf{B}}_{\kappa_{g(t)}}\mathbf{L}^T - \frac{2}{3} \text{tr}D\bar{\mathbf{B}}_{\kappa_{g(t)}} - \frac{2}{3} \bar{\mathbf{B}}_{\kappa_{g(t)}} \cdot \mathbf{DI} \right] \right. \\
& \left. + \frac{2}{9} \text{tr}D \text{tr}\bar{\mathbf{B}}_{\kappa_{g(t)}}\mathbf{I} \right] - \frac{1}{J_{\kappa_{g(t)}}} \left[ \bar{\mathbf{B}}_{\kappa_{g(t)}} - \frac{1}{3} \text{tr}\bar{\mathbf{B}}_{\kappa_{g(t)}}\mathbf{I} \right] \\
& \left. + \frac{2}{D_2} J_{\kappa_{g(t)}} \text{tr}D\mathbf{I} \right\} \tag{3.2.13}
\end{aligned}$$

, where  $\mathbf{L}$  is the spatial gradient of velocity ( $\partial v / \partial x$ ). Therefore, the Jaumann rate of the Cauchy stress tensor ( $\boldsymbol{\sigma}^J$ ) is obtained by the following relationship.

$$\begin{aligned}
\boldsymbol{\sigma}^J = & (1 - \alpha) \left\{ \frac{2C_{10}}{J_{\kappa_r}} \left[ D\bar{\mathbf{B}}_{\kappa_r} + \bar{\mathbf{B}}_{\kappa_r}D^T - \frac{2}{3} \text{tr}D\bar{\mathbf{B}}_{\kappa_r} - \frac{2}{3} \bar{\mathbf{B}}_{\kappa_r} \cdot \mathbf{DI} + \frac{2}{9} \text{tr}D \text{tr}\bar{\mathbf{B}}_{\kappa_r}\mathbf{I} \right] \right. \\
& \left. + \frac{2}{D_1} (2J_{\kappa_r} - 1) \text{tr}D\mathbf{I} \right\} \\
& + (\alpha) \left\{ \frac{2C_{20}}{J_{\kappa_{g(t)}}} \left[ D\bar{\mathbf{B}}_{\kappa_{g(t)}} + \bar{\mathbf{B}}_{\kappa_{g(t)}}D^T - \frac{2}{3} \text{tr}D\bar{\mathbf{B}}_{\kappa_{g(t)}} - \frac{2}{3} \bar{\mathbf{B}}_{\kappa_{g(t)}} \cdot \mathbf{DI} \right] \right. \\
& \left. + \frac{2}{9} \text{tr}D \text{tr}\bar{\mathbf{B}}_{\kappa_{g(t)}}\mathbf{I} \right] + \frac{2}{D_2} (2J_{\kappa_{g(t)}} - 1) \text{tr}D\mathbf{I} \left\} - \boldsymbol{\sigma} \text{tr}D \tag{3.2.14}
\end{aligned}$$

By using **Eqns. 3.2.12** and **3.2.14**, the stiffness matrix ( $\mathbb{C}$ ) is derived by the Kirchhoff stress-Newman strain rate relationship as an essential input in the ABAQUS/CAE program.

$$\mathbb{C}_{IJ} = \frac{1}{2} (\mathbb{C}_{ijkl} + \mathbb{C}_{ijlk}) \tag{3.2.15}$$

$$\begin{aligned}
\mathbb{C}_{ijkl} = & \left\{ (1 - \alpha) \left\{ \left( \frac{2\mathbf{C}_{10}}{J_{\kappa_a}} \right) (\delta_{ik} \bar{\mathbf{B}}_{a_{ij}} + \bar{\mathbf{B}}_{a_{ik}} \delta_{jl}) + \left( -\frac{4}{3} \frac{\mathbf{C}_{10}}{J_{\kappa_a}} \right) (\delta_{kl} \bar{\mathbf{B}}_{a_{ij}} + \bar{\mathbf{B}}_{a_{kl}} \delta_{ij}) \right. \right. \\
& + \left. \left( \frac{4}{9} \frac{\mathbf{C}_{10}}{J_{\kappa_a}} \right) (\text{tr} \bar{\mathbf{B}}_a) \delta_{kl} \delta_{ij} + \left( \frac{2}{D_1} \right) (2J_{\kappa_a} - 1) \delta_{kl} \delta_{ij} \right\} \\
& + (\alpha) \left\{ \left( \frac{2\mathbf{C}_{20}}{J_{\kappa_{g(t)}}} \right) (\delta_{ik} \bar{\mathbf{B}}_{g_{ij}} + \bar{\mathbf{B}}_{g_{ik}} \delta_{jl}) + \left( -\frac{4}{3} \frac{\mathbf{C}_{20}}{J_{\kappa_{g(t)}}} \right) (\delta_{kl} \bar{\mathbf{B}}_{g_{ij}} + \bar{\mathbf{B}}_{g_{kl}} \delta_{ij}) \right. \\
& \left. \left. + \left( \frac{4}{9} \frac{\mathbf{C}_{20}}{J_{\kappa_{g(t)}}} \right) (\text{tr} \bar{\mathbf{B}}_g) \delta_{kl} \delta_{ij} + \left( \frac{2}{D_2} \right) (2J_{\kappa_{g(t)}} - 1) \delta_{kl} \delta_{ij} \right\} \right\} \quad (3.2.16)
\end{aligned}$$

, where  $\delta_{ij}$  is Kronecker delta. The stiffness matrix was used in the ABAQUS/CAE program as a linearized weak formulation of principle of virtual work (P.V.W.).

$$D_{\Delta \mathbf{u}} \delta W_{int} = 2 \int_{\Omega_0} (\mathbb{C} \mathbf{F}^T \text{Grad} \Delta \mathbf{u} \cdot \mathbf{F}^T \text{Grad} \delta \mathbf{u}) dV + \int_{\Omega_0} (\text{Grad} \Delta \mathbf{u} \mathbf{S} \cdot \text{Grad} \delta \mathbf{u}) dV \quad (3.2.17)$$

At the end of every time increment, the UMAT code is invoked for each nodal point of meshes, and updates stresses and solution-dependent state variables with the SDIVINI subroutine.

The input material parameters for the simulation were obtained by performing isothermal tensile tests at some temperature points [49]. The obtained material parameters are listed in **Table 3.2.1**.

A geometry for the simulation was constructed based on the real measurement specimen,  $1 \times 5.3 \times 40 \text{ mm}^3$  (**Fig. 3.2.2(a)**). The C3D8IH elements with 8-node linear brick, hybrid, linear pressure, incompatible modes were used when generating meshes. A loading boundary condition was applied at the specimen center by using an analytical rigid plate with a reference point. A constrained boundary condition was set at the two side pins to prevent detaching after the unloading step (**Fig. 3.2.2(b)**). As a simulation result, the von Mises stress contour at the end of each step was calculated and visualized.



**Table 3.2.1.** Material parameters of the SMCPAs employed in the simulation.

	S-MMA/BMA	S-BA/BMA
$T_r$ (°C)	60	10
$T_g$ (°C)	-20	-60
$C_{10}$ (MPa)	6	6
$C_{20}$ (MPa)	370	398
$D_1$ (1/MPa)	0.06	0.05
$D_2$ (1/MPa)	0.001	0.0008
$\nu$	0.35	0.35

\* $T_r$ : Temperature on fully rubbery phase.

\*\* $T_g$ : Temperature on fully glassy phase.

\*\*\* $\nu$ : Poisson ratio.

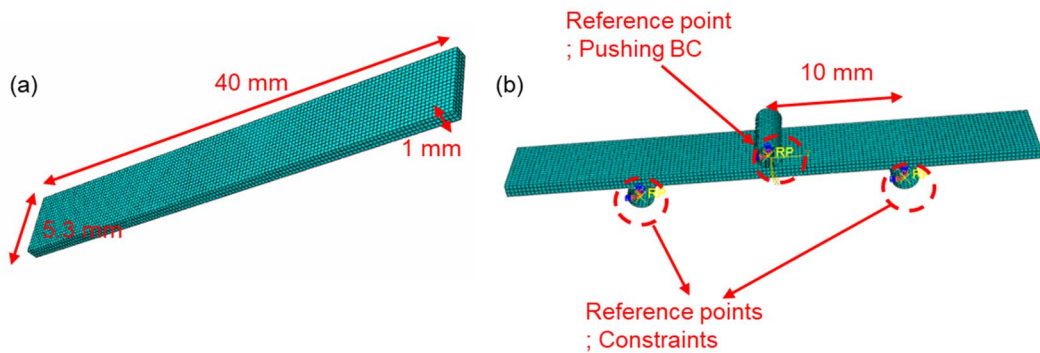


**Figure 3.2.2.** Constructed geometry for the shape memory simulation. (a) The modeled specimen. (b) The applied boundary conditions.

### 3.2.4. Results and discussion

#### 3.2.4.1. Synthesis and chemical structure of SMPs

A free radical vinyl polymerization method was employed for the synthesis of the SMPs. The sequential synthetic process is demonstrated in **Figs. 3.2.3(a-c)**. The polymeric chains of the SMPs are formed by adding successive building blocks and breaking double bonds of vinyl chemicals. Free radicals are generated by photolysis of the photo initiator, BAPOs, when UV light is irradiated to the precursors of SMPs (**Fig. 3.2.3(a)**). When the P-C bonds of BAPOs are cleaved by the UV irradiation, two free radicals are produced and then stabilized by bonding with carbon atoms. The chain extension mechanism is explained in **Fig. 3.2.3(b)**. **Figure 3.2.3(c)** shows the chemical crosslinking reaction between the pre-polymer chains and the crosslinker. The propagation of polymeric chains continues until there are no more chemicals to react with.

In these polymeric network structures, the crosslinking points between the pre-polymeric chains and PEGDMA act as a shape fixing point to memorize the permanent shape of SMPs. Otherwise, the long chain segments lead to the state transformation from a glassy state to a rubbery state at above the glass transition temperature and vice versa. This switchable property is a key feature of SMPs. The synthesized final chemical structure is shown in **Fig. 3.2.3(d)**. In the structure, the various monomers were denoted with  $R_1$  and  $R_2$  that indicate a methyl or a butyl group and  $R_1'$  and  $R_2'$  that represent a hydrogen or a methyl group (**Table 3.2.2**).

A schematic figure for the SMPs is illustrated in **Fig. 3.2.3(e)**. For the group of SMAC, "A" and "B" signify the same kind of monomers. In the meanwhile, the SMCPAs are composed of three kinds of acrylic chemicals, A, B, and C. Since two monomers were simply mingled without additional treatments, the SMCPAs do not have regular configuration such as periodic or alternating copolymers. Nevertheless, thermomechanical properties of the SMCPAs could be tuned by a rule of mixture due to changes in the overall composition.

The ATR-FTIR analysis was carried out to confirm the chemical structure of the SMPs. **Figure 3.2.4(a)** shows that the resulting characteristic peaks of the SMPs were observed at 2960, 2870, 1720, 1140, and 1100  $\text{cm}^{-1}$  indicating  $\text{CH}_3$  vibration,  $\text{CH}_2$  vibration, carbonyl

vibration, C-O vibration of acrylate, and C-O vibration of the crosslinker, respectively [201,202]. The CH<sub>2</sub> peak of S-MMA at 2870 cm<sup>-1</sup> is lower than that of the others, which suggests that the others have much larger amount of the CH<sub>2</sub> moiety than S-MMA in the chemical structure. This result can be supported from the monomer peaks at 2960 and 2870 cm<sup>-1</sup> (**Fig. 3.2.4(b)**). The sharp carbonyl peak of S-MMA at 1720 cm<sup>-1</sup> means that the amount of the acrylate moiety decreases with increasing the amount of the CH<sub>2</sub> moiety in the SMPs. The decreasing area of the ester peaks of acrylates at 1140 cm<sup>-1</sup> in S-BMA and S-BA can be explained by the reduced fraction of the ester moiety with an increase in the amount of the CH<sub>2</sub> moiety. The ester peaks at 1100 cm<sup>-1</sup> originate from the crosslinker peak as shown in **Fig. 3.2.4(b)**. It is verified by the ATR-FTIR analysis that the SMPs were synthesized successfully as designed.

The XPS analysis was carried out to further elucidate the chemical composition and the ratio of methyl and butyl moieties in the SMPs. The XPS data of C1s spectra are presented in **Fig. 3.2.6**. All XPS spectra reveal that the two main components are C and O. A high resolution scan of C1s spectra was performed for more detailed information of the SMPs. The deconvolution of the C1s scan for the five components (C1, C2, C3, C4, and C5) was conducted. The C1 (284.5 eV) peak was associated with a single carbon atom and hydrogen atoms. S-BMA has the highest ratio of C1 peak because of its bulky structure of butyl moiety. On the other hand, S-BA shows the second highest ratio of C1 peak. The C2 (285.30 eV) peak corresponds to the carbon associated with other CO<sub>2</sub> moiety. The C3 (286.1 – 286.2 eV) peak is allocated to the hydrocarbons bound to one oxygen. The C4 (286.6 – 287.4 eV) peak is related to the carbon atom bound to two oxygen atoms. The C5 (288.6 – 289.3 eV) peak corresponds to the carbon atom connected with one carbonyl oxygen and other non-carbonyl oxygen atoms. The chemical structures shown in **Fig. 3.2.5** were confirmed by the peaks from C1 to C5 (**Table. 3.2.3**). It was found that the measured results were consistent with the results in the literature [203–205].

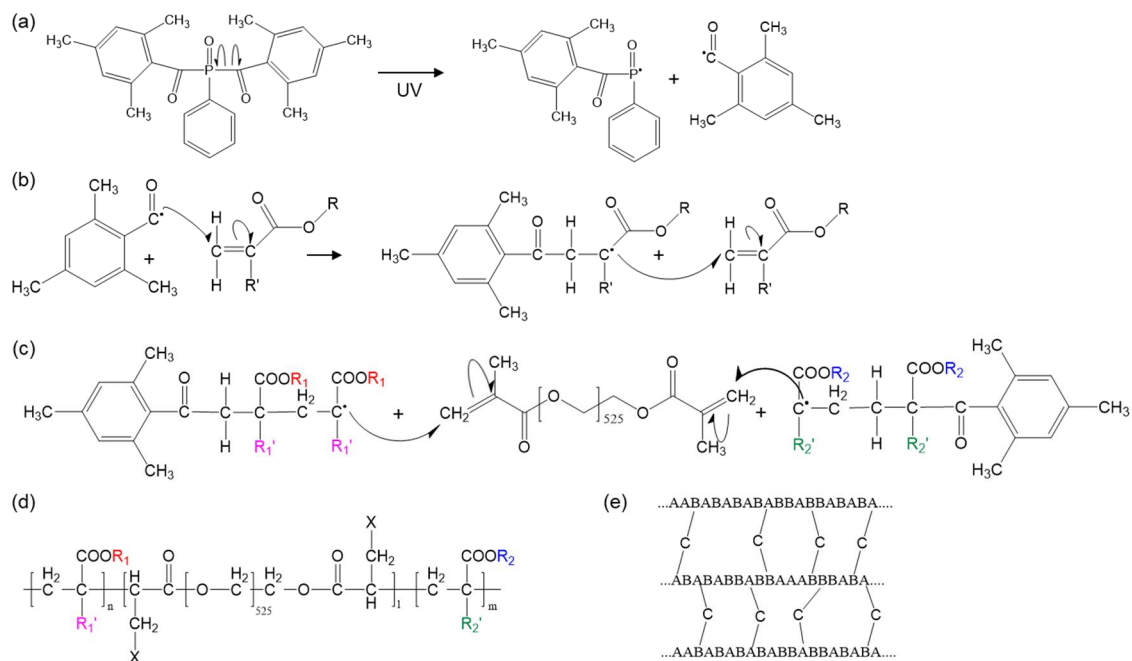


**Figure 3.2.3.** Chemical reaction scheme for the SMPs synthesis. (a) Reaction initiated by UV light irradiation. (b) Generation of pre-polymer chains by free radical electrons. (c) Crosslinking reaction of the pre-polymer chains and the crosslinker. (d) Suggested chemical structure of SMPs. (e) Schematic illustration of shape memory copolymers with monomers (“A” and “B”) and a crosslinker (“C”).

**Table 3.2.2.** Polymeric chain composition of the SMP samples.

	R1	R2	R1'	R2'
S-MMA	Methyl	Methyl	Methyl	Methyl
S-BMA	Butyl	Butyl	Methyl	Methyl
S-BA	Butyl	Butyl	Hydrogen	Hydrogen
S-MMA/BMA	Methyl	Butyl	Methyl	Methyl
S-BA/BMA	Butyl	Butyl	Hydrogen	Methyl

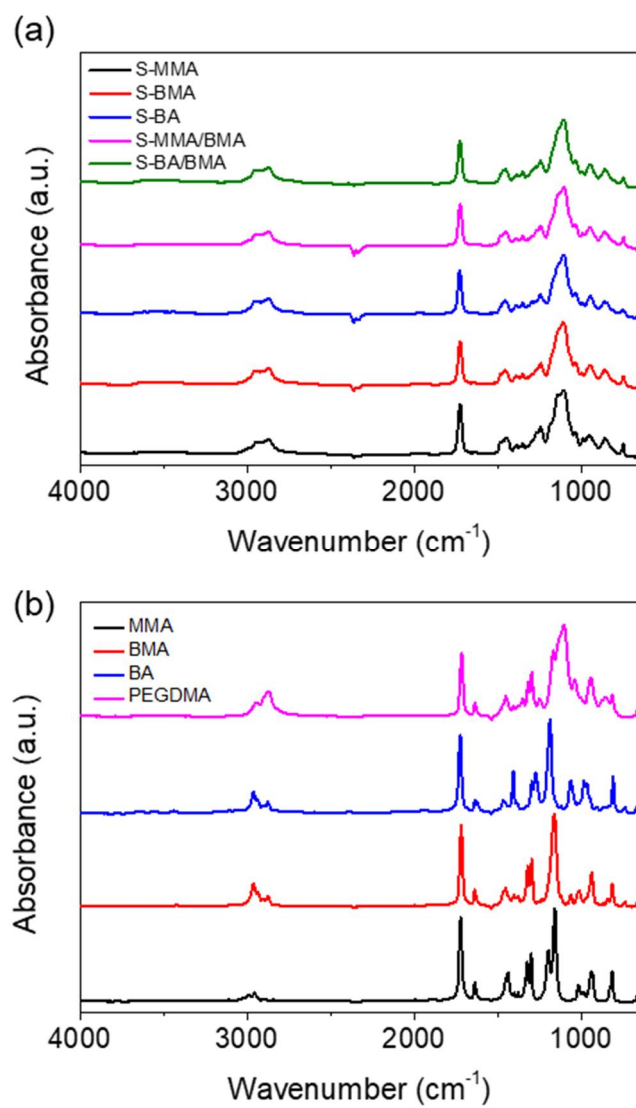


**Figure 3.2.4.** ATR-FTIR spectra of (a) the basic chemicals and (b) the synthesized SMPs.

**Table 3.2.3.** XPS peak information of the SMP samples.

#	Name	Position (At%)	Position (At%)	Position (At%)	Position (At%)	Position (At%)
C1	C-C, C-H	284.50 (37.39)	284.50 (45.97)	284.50 (40.11)	284.50 (35.36)	284.50 (39.52)
C2	$\underline{C}H_2-$ $CO_2-$	285.30 (18.74)	285.30 (11.46)	285.30 (18.81)	285.30 (19.75)	285.30 (16.60)
C3	C-O	286.24 (23.52)	286.17 (20.79)	286.06 (12.37)	286.10 (27.71)	286.10 (16.20)
C4	O-C-O	286.95 (16.50)	287.36 (16.38)	286.64 (24.98)	286.90 (7.67)	286.97 (20.16)
C5	O=C-O	288.93 (3.85)	289.34 (5.40)	289.01 (3.73)	288.61 (9.51)	288.71 (7.51)

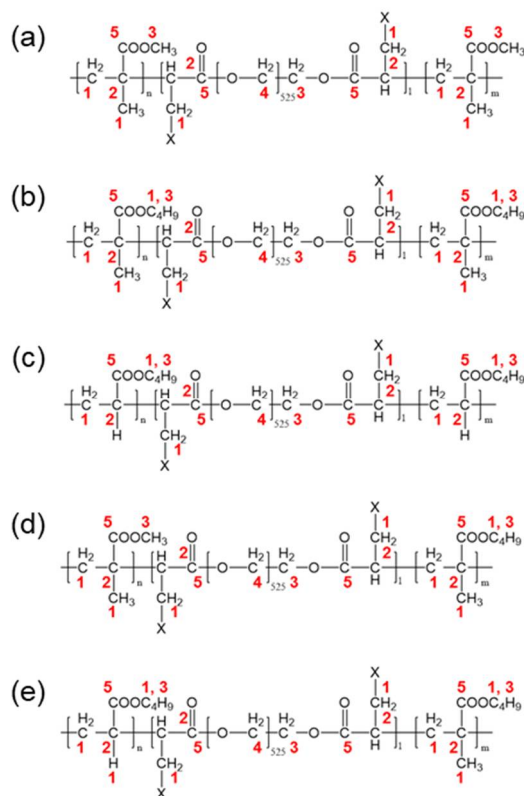


**Figure 3.2.5.** Chemical formula of the SMPs; (a) S-MMA, (b) S-BMA, (c) S-BA, (d) S-MMA/BMA, and (e) S-BA/BMA.

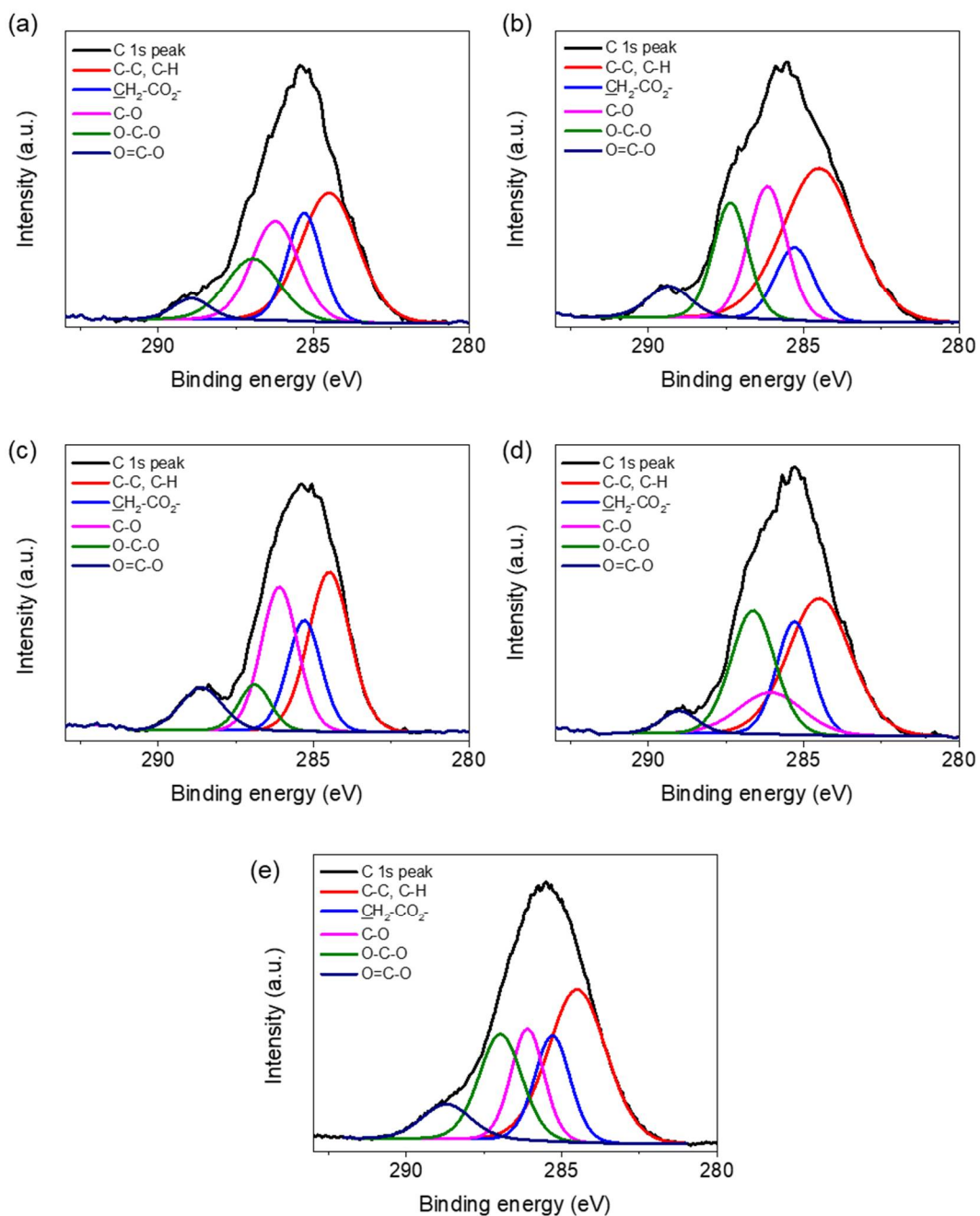


**Figure 3.2.6.** XPS spectra of the SMPs: (a) S-MMA, (b) S-BMA, (c) S-BA, (d) S-MMA/BMA, and (e) S-BA/BMA.

### 3.2.4.2 Thermomechanical properties of SMPs

Thermomechanical features of all samples were investigated by the DMTA tests (**Fig. 3.2.7**). At temperature above the transition temperature of SMPs, the micro-Brownian motion of polymeric chains induces rubbery behavior of polymeric chains. However, this motion is frozen at temperature below the transition temperature, and the materials become glassy. Storage moduli of the SMPs are presented as a function of temperature in **Fig. 3.2.7(a)**. It was verified from the comparison between S-MMA and S-BMA that the storage modulus is highly dependent on the size of side moiety of monomers, such as methyl and butyl groups. S-MMA is transformed from a glassy state to a rubbery state at a relatively higher temperature than that of S-BMA, which is explained by the longer side chain of S-BMA and the resulting higher chain flexibility. Because the methyl group on  $\alpha$ -carbon position of the acrylate group has a bulky structure, this feature does not let the polymer have larger flexibility [206]. Therefore, S-BA has the transition temperature lower than that of S-BMA. It is found that the transition temperatures of the SMCPAs are determined by a simple rule of mixture based on the blended two monomers [207].

Tangent delta curves were evaluated by calculating the ratio of the loss modulus to the storage modulus (**Fig. 3.2.7(b)** and **Table 3.2.4**). Generally, a transition temperature region of amorphous SMPs is relatively broader than that of semi-crystalline SMPs, around 30°C. Glass transition temperature ( $T_g$ ) is defined as the temperature at the center of the transition region, which is the same as temperature at a peak value of a tangent delta graph.

The permanent shape can be recovered by the micro Brownian motion at a temperature slightly higher than transition onset temperature ( $T_{onset}$ ). **Figure 3.2.7(c)** shows the variation of  $T_g$ ,  $T_{onset}$ , and rubbery modulus ( $E_r$ ). It was verified that the synthesized SMPs shows higher  $T_g$  and  $T_{onset}$  values in the order of S-MMA, S-MMA/BMA, S-BMA, S-BA/BMA, and S-BA as chemically designed.  $E_r$  is an elastic modulus in the rubbery state after sufficient heating over  $T_g$ . Generally, there is a large difference between the rubbery and glassy moduli of SMPs in a constrained condition [70]. All the samples showed a big drop in modulus larger than 3000 MPa in the cooling step, which is sufficient enough for achieving a high shape recovery ratio.



**Table 3.2.4.** Thermomechanical properties of the fabricated SMPs.

	$E_r$ (MPa)	$T_g$ (°C)	$T_{onset}$ (°C)
S-MMA	60.7	68.8	52.6
S-BMA	52.0	24.1	0.3
S-BA	39.2	3.9	-14.7
S-MMA/BMA	53.6	48.3	26.1
S-BA/BMA	45.8	12.4	-5

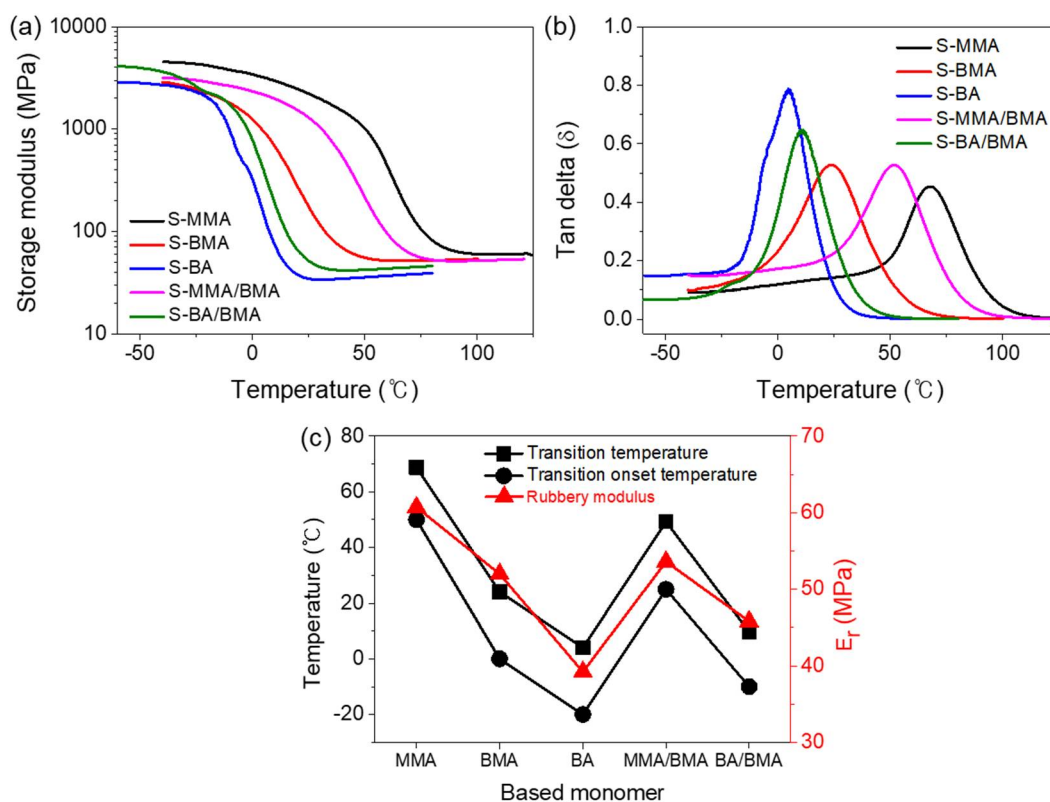


**Figure 3.2.7.** DMTA results of the SMPs. (a) Storage modulus as a function of temperature. (b) Tangent delta as a function of temperature. (c) Transition temperature, transition onset temperature, and rubbery modulus of the SMPs.

### 3.2.4.3 Shape recovery behavior of SMPs

Time-dependent shape recovery behavior of the SMPs was investigated by carrying out the transient shape recovery test. Three discrete recovery temperatures were selected for the test as 80, 40, and 0 °C. **Figure 3.2.8(a)** shows the transient shape recovery of S-MMA/BMA measured at 40 °C in the aqueous condition. The shape recovery ratios were characterized as a function of time by measuring the angle change of the sample upon heating and plotted in **Figs. 3.2.8(b-d)**. It was identified from **Fig. 3.2.8(b)** that all samples can recover the original shape when the applied thermal energy is large enough to release stored strain energy. The S-MMA and S-MMA/BMA samples recovered the original shape perfectly within 7 seconds and 3 seconds, respectively. However, shorter time was enough for the shape recovery of the other samples.

S-MMA did not display any shape recovery behavior at 40 °C due to its high  $T_g$  (68.8 °C), however, S-MMA/BMA could recover from the deformed geometry as shown in **Fig. 3.2.8(c)**. It was shown by the comparison between the recovery ratios at 40 °C and 80 °C that S-BMA and S-BA/BMA have shorter recovery time with respect to temperature. The samples can be classified into two groups from the shape recovery test at 40 °C: the first group which can recover to the original shape around body temperature and the other group which cannot do that. The shape recovery capability at body temperature is a desirable function for biomedical applications. On the other hand, S-BMA and S-BA cannot be employed to the biomedical applications due to their seriously low mechanical property at this temperature. Consequently, S-MMA/BMA is the best candidate for biomedical applications among all samples.

S-MMA and S-MMA/BMA did not show shape recovery behavior at 0 °C (**Fig. 3.2.8(d)**). The shape recovery time of S-BMA and S-BA/BMA at 0 °C was estimated seven times and three times higher than that at 40 °C. Since S-BA/BMA has sufficiently high shape recovery ratio and high mechanical properties with short recovery time, it can be the best smart material for aerospace applications.

For the quantitative analysis of shape recovery performance, cyclic stress-strain-temperature (SST) curves for the two SMCPAs (S-MMA/BMA and S-BA/BMA) were obtained by using the 3-point bending machine. As shown in **Figs. 3.2.9(a-b)**, the S-MMA/BMA sample was heated to 40 °C and then bended with a deflection of 2

mm ( $\epsilon = 3\%$ ). The deformed shape was frozen at 0°C during the cooling step by generating glassy regions in the sample. Since the stored strain energy of rubbery phase was very small, the deformed shape was maintained even after the unloading step. When temperature was elevated to 40°C, the original shape was recovered with a recovery ratio over 90%. S-BA/BMA was also characterized experimentally by using the similar procedure. Heating temperature was changed from 40°C to 0°C, and cooling temperature was altered from 0°C to -40°C. The results are shown in **Figs. 3.2.9(a)** and **(c)**. In this case, the original shape was fully recovered at 0°C.

The shape memory–recovery behavior can be explained by the two-fold molecular mechanism. The first mechanism is the release of stored elastic energy due to reduced stiffness of the SMCPAs in the heating process. The second mechanism is based on the driving force exerted by the crosslinking points to recover the original permanent shape. Both S-MMA/BMA and S-BA/BMA were almost completely recovered to their original shapes within 20 minutes. The time required for full shape recovery was much longer than that required in aqueous condition (see **Fig. 3.2.8**), since heating the samples takes longer time in a convection heating chamber than in water.

To model the shape memory behavior of S-MMA/BMA and S-BA/BMA theoretically, numerical analysis was carried out using ABAQUS/CAE with the subroutines UMAT and SDVINI. When SMPs are deformed, the strain energy is accumulated in the bended region. Thereafter, it is stored during glass transition and the stiffness is increased in the cooling process. The following heating process causes the shape recovery through transition from glassy phase to rubbery phase.

A constitutive model for glassy shape memory polymers was proposed by Khanolkar *et al.* and employed in this study [198]. The simulated SST curves are shown in **Figs. 3.2.9(a-c)**. The numerical simulation results are in good agreement with the experimental data. The measured and simulated curves have different shapes during the cooling step. It was caused by the assumption that phase transition is linearly proportional to the glassy state fraction ( $\alpha$ ). The change of  $\alpha$  was simply defined as  $\alpha = (T_{rub} - T)/(T_{gla} - T_{rub})$ , where  $T$  is the current temperature,  $T_{gla}$  is the temperature for fully glassy state and  $T_{rub}$  is the temperature for fully rubbery state.

**Figure 3.2.10** shows the von Mises stress contours formed in the specimens as a result

of the numerical simulation. The stress applied in the loading step fades out in the next cooling step since the newly generated glassy region is in a stress-free state. After unloading, the stress in the specimen disappears, but the sample cannot recover its original shape in contrast to general elastic materials. The deformed sample is recovered upon heating. From the numerical structural analysis, the underlying mechanism of the shape memory behavior was understood and the position where the strain energy accumulates were verified theoretically.

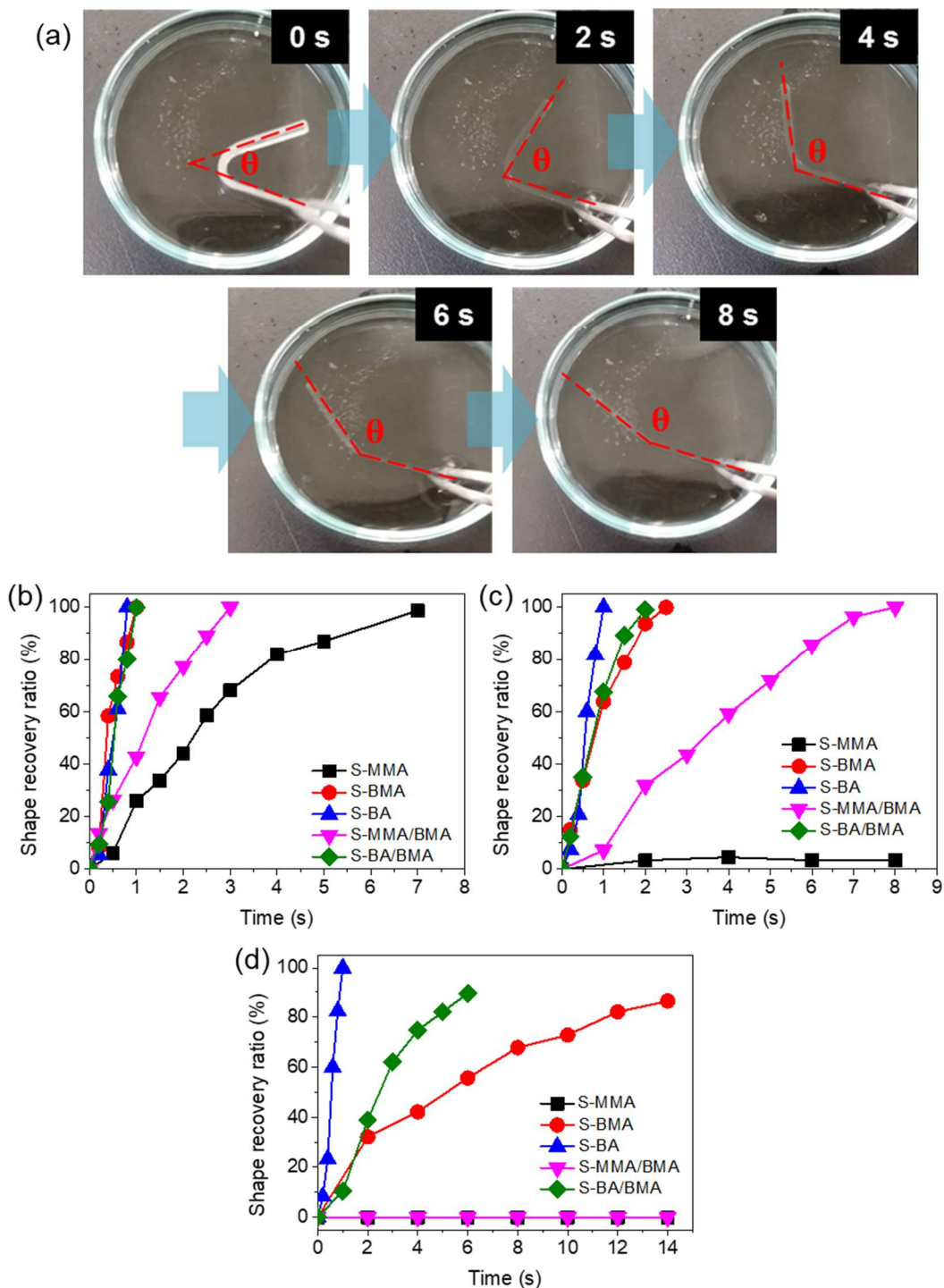


**Figure 3.2.8.** Transient shape recovery tests. (a) Snap shots of the shape recovery process of S-MMA/BMA taken at 40°C and shape recovery ratios measured at (b) 80°C, (c) 40°C, and (d) 0°C.

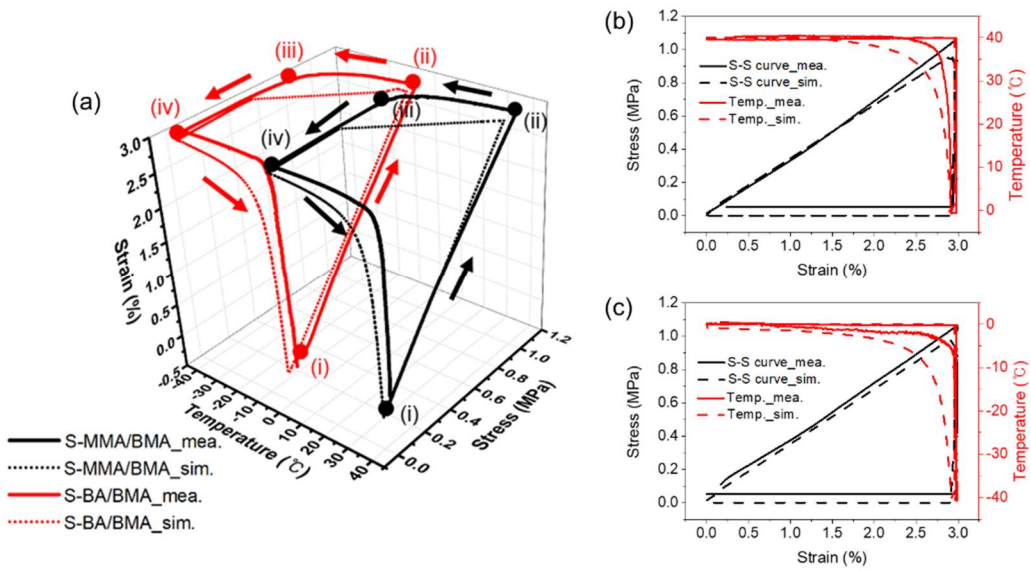


**Figure 3.2.9.** Cyclic shape memory tests of the SMCPAs. (a) The measured and simulated SST curves of S-MMA/BMA and S-BA/BMA. 2D plot of the SST curves for (b) S-MMA/BMA and (c) S-BA/BMA.

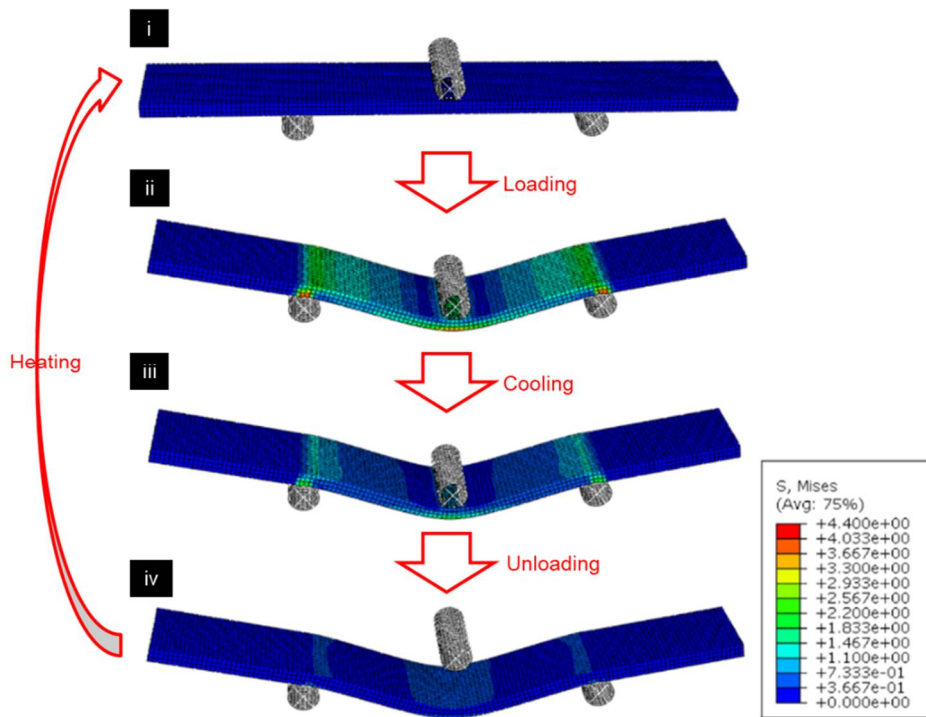


**Figure 3.2.10.** Numerical simulation results of S-MMA/BMA.

### 3.2.4.4 Optical property of SMPs

**Figure 3.2.11** shows the light transmittance of the SMPs measured by using the UV-vis spectrophotometer. Since the synthesized SMPs have a very low level of crystallinity due to the bulky moiety of acrylate chemicals, the transmittance of the samples was measured to be about 90% in the wavelength range from 430 nm to 800 nm. In the wavelength range from 380 to 430 nm, the samples revealed a decay of transmittance as shown in the inset figure. It was presumed that the decay was induced by the immiscibility of monomers (S-MMA/BMA and S-BA/BMA) and the bulkier moiety of monomers (S-MMA, S-BMA, and S-BA) [208]. The butyl moiety of the acrylate group of S-BMA and S-BA could cause the scattering of light in the lower wavelength range. And the reaction inhibitor and unreacted photo initiator remained in the samples could also provoke the light absorption in this wavelength range.

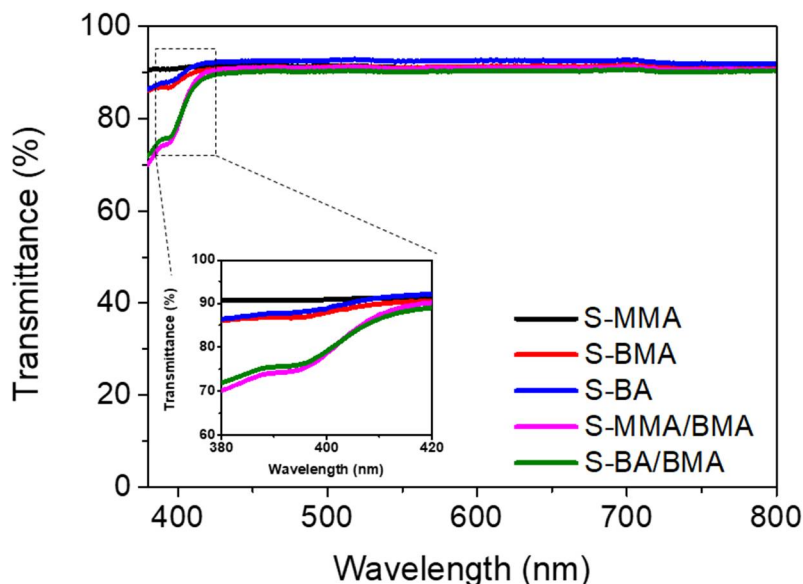


**Figure 3.2.11.** Light transmittance of the SMPs with respect to wavelength.

### **3.2.5. Conclusions**

In this section, optically transparent shape memory copolymers were synthesized and fabricated by using a tri-copolymerization method for thermomechanical modulation. The chemical formula of the SMPs was suggested based on the sequential reaction scheme and confirmed by the spectroscopic experiments. The characteristics of SMPs were identified by XPS, FTIR, DMTA, shape recovery tests, and the optical tests. The numerical simulation results coincided with the experimental results and confirmed the underlying nature of shape recovery mechanism. All the samples were optically transparent due to their low crystallinities. S-MMA/BMA and S-BA/BMA provided useful thermomechanical properties compared with the other SMP samples. Consequently, these copolymer materials showed great potential as smart materials for medical and aerospace applications. This design strategy can be applied to other specific circumstances for accomplishment of optimized shape recovery performance.



## 3.3. Antireflective SMP nanopattern

### 3.3.1. Introduction

Highly transparent materials have been studied intensively for optical devices in order to satisfy the performance required for photoelectronic applications such as solar cell systems [209,210], photodetectors [211], and optical lenses [212]. Especially, antireflection (AR) treatments for transparent films have attracted a great deal of attention to minimize the reflected light energy.

Several AR techniques have been developed; a homogeneous layer method, an inhomogeneous layer method [213,214], and a bio-inspired nanopatterning method [215,216]. Among them, the nanopatterning method is the best strategic approach since it does not face a de-bonding problem between coating layers and owns omnidirectional features even at broadband wavelengths [217]. The main mechanism of the nanopatterning method is optical impedance matching which reduces a difference of the optical impedance (*i.e.*, refractive index) between two different media. The AR nanostructures can produce a gradually changing refractive index (gradient-index, GRIN) layer, as a metasurface, at the interface between distinguishing media due to their subwavelength structures [218]. The GRIN layer can blur the interface having abrupt refractive index change. This phenomenon leads to the reduction of light reflection and the increase of transmitted light [219].

However, the nanopatterns are deformed easily and even damaged by external forces since they have poor mechanical properties [220]. This drawback deteriorates the AR characteristics of nanostructures and limits industrial applications to many electronic gadgets such as touch panels for mobile electronic devices. Employing a shape memory polymer (SMP) is a feasible solution to overcome this problem [221]. SMPs belong to the categories of smart materials which can recover its original shape by an external trigger [182]. A temporary shape is programmed in a shape deforming process over the transition temperature region and maintained after cooling to lower than the transition temperature. After SMPs are deformed by a force, applying external heat above the transition temperature allows the programmed feature to be restored to its original shape. Then the permanent shape is restored due to the release of elastic entropy by the micro-Brownian

motion of polymeric chains. By using this function, SMPs have been researched for many applications, such as anticounterfeiting [114,222], 4D printing [223], smart actuators [224], biomedical applications [110,225], and photonic crystals [226,227].

However, nanostructures made of SMP have rarely been employed in optical applications, where optical transparency, short recovery time, and good processability are required. The SMP nanopatterns can be restored to their original shape after certain deformation. Actually, even if nanopatterns consist of a general flexible polymer, such nanopatterns may break or become permanently deformed when subjected to stresses greater than the elastic limit. Although the SMP nanopatterns are easily deformed under high stresses, they can return to the original shape at relatively high temperature without permanent deformation, which are advantageous for sustainable antireflection.

On the other hand, commercially available transparent SMPs, *e.g.*, polynorbornene and shape memory epoxy are relatively expensive and don't have appropriate thermomechanics for tailoring their transition temperature close to human body temperature.

In this section, a strategy for sustainable AR is proposed by constructing the nanopattern arrays with shape recovery ability in the vicinity of body temperature. Shape memory copolyacrylate (SMCPA) proposed in Section 3.2 (S-MMA/BMA) was used as a constituent material of the nanopatterns [228]. The SMCPA nanopattern arrays were produced by using a replica molding method. Shape memory-recovery behavior and corresponding sustainable antireflection effect of the samples were confirmed experimentally and the underpinning mechanism was suggested theoretically. Angular transmittance of the samples was measured to examine omnidirectional antireflectivity. Nanoindentation and wettability test were conducted, which contribute to the antireflection performance.

### 3.3.2. Experimental

#### 3.3.2.1. Precursor materials of SMCPA

A precursor material composed of monomers, a crosslinker, and a photo initiator were prepared by mixed together using a vortex-mixer. Two monomers, methyl methacrylate (MMA, Daejung Chemicals, Republic of Korea) and butyl methacrylate (BMA, Daejung Chemicals, Republic of Korea), were combined with a 1:1 (2 ml: 2 ml) volumetric ratio. The crosslinking agent, polyethyleneglycol dimethacrylate (PEGDMA, Mw=525, Sigma Aldrich, United States), forms crosslinking points between pre-polymeric chains. The photo initiator, Phenylbis(2, 4, 6-trimethylbenzoyl) phosphine oxide (BAPOs), was also purchased from Sigma Aldrich. A volume ratio of the total monomers and the crosslinker was about 1:2 (4 ml: 8 ml) and the amount of the crosslinker was 0.2 wt% (0.018 g) of the total weight of the precursor material. The synthesized SMP was denoted as SMCPA (shape memory copolyacrylate).

#### 3.3.2.2. Fabrication of SMCPA nanopattern

A replica molding method was employed to construct nanopattern arrays on a sample surface. A silicon (Si) master (shown in **Fig. 3.3.1(a)** and the reference [229]) with nanoholes of 230 nm depth, 200 nm diameter, and 200 nm spacing (see **Fig. 3.3.6(a)**) was prepared by using an e-beam lithography method. The Si master needs to be cleaned by rinsing in the solution of hydrogen peroxide and sulfuric acid ( $H_2O_2:H_2SO_4=3:1$ ) to remove polymeric residue before the patterning process. After the cleaning step, a monolayer was coated on the surface of the Si master by depositing trichloro(1H,1H,2H,2H-perfluoro-octyl)silane (Sigma Aldrich, United States) for 5 hours at room temperature, for easy separation between the fabricated sample and the master. A mold for engineering nanopatterns was made of the Si master, a glass slide, and two glass spacers (thickness of the spacers=1 mm). Schematic illustration and optical photograph of the mold is shown in **Figs. 3.3.1(b-c)**. The prepared photo-curable precursor solution was injected into the mold gap by using a syringe pump. Thereafter, UV light (wavelength at 365 nm) was irradiated over the transparent side of the mold, followed by a post-thermal curing step.

#### 3.3.2.3. Characterizations of SMCPA nanopattern

The fabricated nanopatterns on the samples were observed by using a field emission scanning electron microscope (FE-SEM, JSM-6390LV, JEOL, Japan). Four types of samples were investigated; the samples with no pattern (bare), original (Ori.), deformed (Def.), and recovered (Rec.) patterns. An atomic force microscopy (AFM, Park NX10, United States) was used to examine a height profile and three-dimensional (3-D) morphology. A non-contact mode at a 300 kHz resonant frequency was applied with a 20 nm set point. The same samples were used for the FE-SEM and AFM observation.

Transmittance of the samples was measured by using a UV-vis spectrophotometer (Cary 100, Agilent Technologies, United States) in the wavelength range from 400 nm to 900 nm. A double beam was used as an optics configuration and the Czerny-Turner monochromator was employed. Angular transmittance of the samples was measured by placing the samples as tilted while running the machine.

Nanoscale mechanical property was investigated by running a Hysitron Tribolab nanoindenter (Hysitron TI-0039, Inc., United States). A total of 100 tests for the nanopatterned samples were performed by using a Berkovich tip with a three-sided pyramid (angle: 142.3°, radius: 100 nm). The applied maximum load was 500  $\mu\text{N}$  and the load was held for 2 seconds before unloading. Force-displacement graphs were obtained during the cyclic loading-unloading step. The stiffness and dissipated energy during the indentation tests were evaluated from the slope in the unloading step and the integrated area of the curves, respectively.

Wettability of the sample surfaces was measured by using a contact angle goniometer (Attension® Theta Lite, Biolin Scientific, Sweden). Static contact angle (CA) and contact angle hysteresis (CAH) of a water droplet on the sample surfaces were determined. For the CA measurement, the samples were positioned on a horizontal sample stage, and a water droplet was placed onto the surface. CA was evaluated by averaging the angles of both contacted sides. CAH was analyzed after tilting the sample stage up to 30°, and the subsequent steps were the same as those for the CA measurement. The CAH values were quantified by calculating the difference between the advancing angles and receding angles.

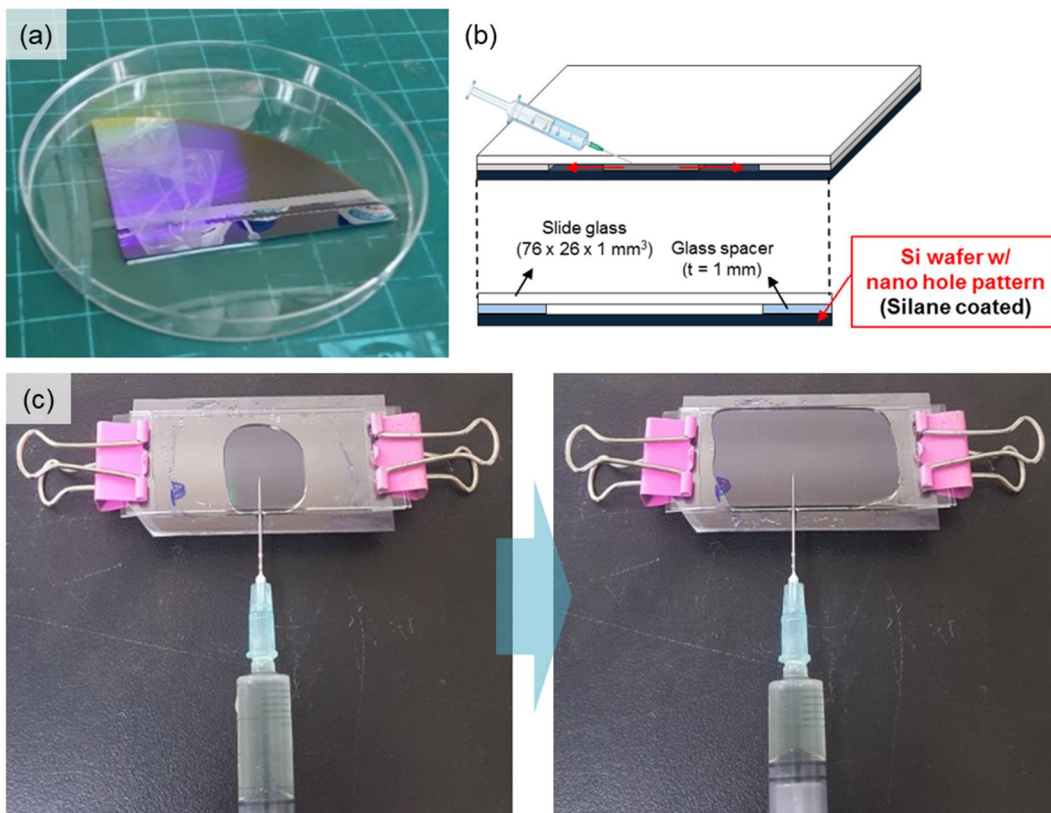


**Figure 3.3.1.** Experimental set up for the nanopatterning process. (a) Optical photograph of the fabricated Si wafer. (b) Schematic illustration of the used mold. (c) Optical photographs of injecting the SMCPA resin into the mold.

### 3.3.3. Numerical analysis

#### 3.3.3.1. Modeling SMCPA nanopatterns

The same modeling methodology described in Section 3.2.3 was used to simulate the shape memory-recovery behavior of SMCPA nanopatterns. The nanopattern geometry to be used in the simulation was drawn in 3-D, which resembles the real topology, *i.e.*, a 200 nm height, a 200 nm spacing, and a 200 nm diameter (**Fig. 3.3.2(a)**). The 4 steps used in the simulation consist of loading, cooling, unloading, and heating steps. In the loading step, temperature was set to 40°C ( $\alpha=0.125$ ), and the Encastre boundary condition was imposed on the ground plate (**Fig. 3.3.2(b)**). In the deforming step, the nanopatterns were compressed to 70 nm by using an analytical rigid plate as the same feature observed in the SEM image. The followed cooling step increased the glass content up to 0.625. At the unloading step, the plate was removed from the nanopatterns, and the applied heating recovered the deformed geometry.

#### 3.3.3.2. EMT analysis for theoretical transmittance

An effective medium theory (EMT) method was employed to provide a theoretical mechanism for sustainable antireflection by comparing transmittances depending on a shape of the nanopatterns. The unit cells shown in **Figs. 3.3.3(a-b)** were obtained from the shape memory simulation results and used for this analysis. After splitting the nanopatterned layer into 20 layers, a volume fraction of air and the substrate was calculated at each layer. The effective refractive index ( $n_e$ ) of each layer is defined as,

$$n_e = (V_f(n_c)^{2/3} + (1 - V_f))^{3/2} \quad (3.3.1)$$

, where  $V_f$  is the volume fraction of nanopatterns at each layer and  $n_c$  is the refractive index of SMCPA. The refractive indices of SMCPA were semi-empirically determined from the measured transmittance data by calculating Fresnel equation (**Table 3.3.1**). The experimental refractive indices of SMCPA were expected to be about 1.4 at 550 nm since the refractive index of PEGDMA is 1.466, 1.411 for MMA, and 1.422 for BMA. The inversely calculated refractive indices were overestimated due to the immiscibility between the material phases. Moreover, the surface roughness contributes to this disagreement.

Theoretical transmittance for normal incident light was obtained by using a multilayer Fresnel equation coded in MATLAB.

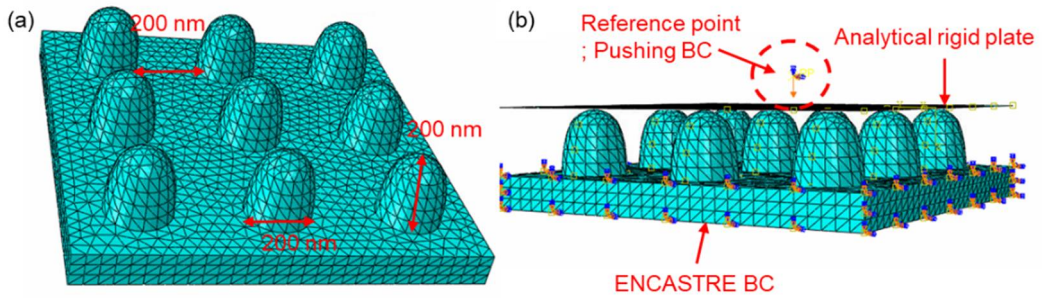


**Figure 3.3.2.** Constructed nanopattern geometry for the shape memory simulation. (a) The 3 by 3 modeled nanopattern array and its configuration. (b) The applied boundary conditions to the nanopattern geometry.

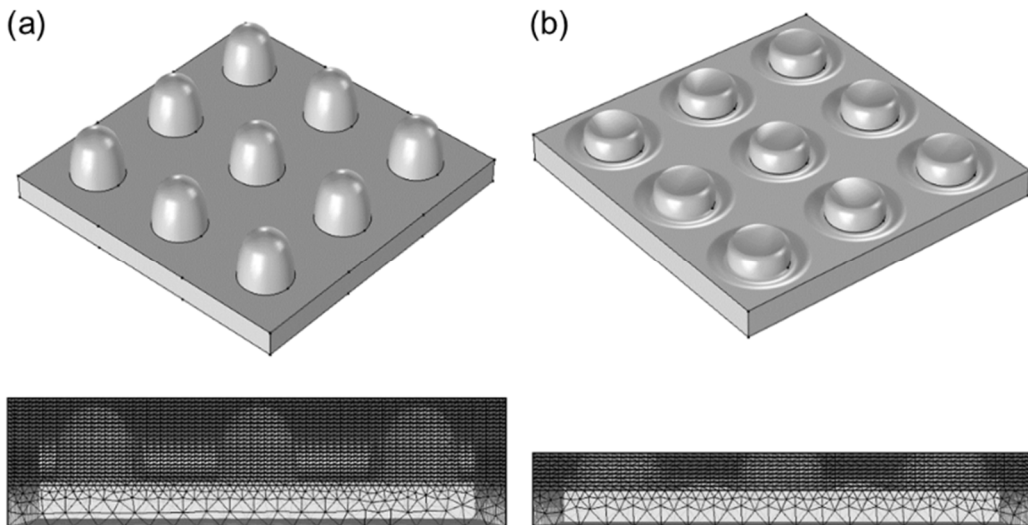


**Figure 3.3.3.** Unit cells constructed for the EMT analysis; (a) the original nanopatterned surface and (b) the deformed nanopattern surface.

**Table 3.3.1.** Calculated effective refractive indices of SMCPA.

Wavelength (nm)	Refractive index
900	2.193189
850	2.219151
800	2.181369
750	2.260984
700	2.243690
650	2.251259
600	2.302070
550	2.383295
500	2.347006
450	2.392323
400	2.601424
350	2.959534



### 3.3.4. Results and discussion

#### 3.3.4.1. Preparation of SMCPA nanopattern

SMCPA (Shape memory copolyacrylate), the transparent acrylic shape memory copolymer, was synthesized by using a free radical vinyl polymerization method which is initiated by UV light irradiation. The formula of the synthesized chemical is presented in **Fig. 3.3.4(a)**. The SMCPA was strategically designed to have a proper transition temperature ( $T_{tr}$ ) region for facile shape recovery which is able to be triggered by gentle heating at body temperature. The ability to recover shape at body temperature is significant in that it can repair the deformed features by touching the nanopattern with a finger or the like.

Coexistence of MMA and BMA in the polymeric chains can modulate chain mobility, facilitating the adjustment of thermomechanics of the SMCPA. UV light irradiation generates free radical electrons by cleaving the covalent bonds of the initiator and this reaction then propagates along pre-polymer chains. Simultaneously, a chemical crosslinking reaction occurs to construct 3-D networks that consist of MMA (A), BMA (B), and PEGDMA (C) as shown in **Fig. 3.3.4(b)**. The synthesis procedure is illustrated in **Fig. 3.2.3** in detail. The expected chemical formula and composition of the SMCPA are in good agreement with the measured spectroscopic data of X-ray spectroscopy (XPS) and Fourier transform infrared spectroscopy (FTIR) (shown in **Figs. 3.2.3** and **3.2.5**).

Dynamic mechanical analysis (DMA) was carried out to investigate the thermomechanics and shape recovery behaviors of the SMCPA. From the DMA curves shown in **Fig. 3.3.4(c)**, the specific  $T_{tr}$  and the transition onset temperature of the SMCPA were verified as 48°C and 26°C, respectively. This result implies that body temperature (37°C) can initiate shape recovery of the SMCPA owing to the broad transition temperature range of amorphous SMPs. In a copolymer system,  $T_{tr}$  is approximately governed by a simple rule of mixture [207]. In this sense, the SMCPA was designed to have an intermediate  $T_{tr}$  between MMA-based SMP and BMA-based SMP (**Fig. 3.2.6**). **Figure 3.2.3(d)** shows the cyclic stress-strain-temperature (SST) curve. After the SMCPA specimen was deformed at 40°C, the following cooling immobilized the polymeric chains while retaining the changed shape. Gentle heating at 40°C restored the permanent original shape with a shape recovery ratio of almost 100%. The simulation result obtained from

ABAQUS/CAE (dashed line in **Fig. 3.3.4(d)**) also agrees well with the empirical result.

Sufficient transmittance (about 85%) is achieved in the visible range of wavelength since the SMCPA is composed of amorphous acrylic chemicals with low crystallinity (**Fig. 3.3.4(e)**). Synthesizing such a transparent SMP is a prerequisite for preparation of the basic material employed in this study. The relatively low transparency compared to general acrylic polymers originates from the crystallinity of the crosslinker, but it is an inevitable characteristic for imposing the shape memory ability.

The SMCPA samples with nanopattern arrays were fabricated by employing a replica molding method (**Fig. 3.3.5**). The silicon wafer master contains square-arrayed nanoholes of 240 nm depth, 200 nm diameter, and 200 nm spacing (**Fig. 3.3.6(a)**). Since the precursor material has low viscosity compared to other photo-curable resins ( $\sim 6$  mPa·s, **Fig. 3.3.4(f)**), defects were hardly observed on the overall surface of the nanopatterned SMCPA (**Fig. 3.3.6(b)**). The low viscosity of the precursor is an advantageous property for achieving high processability in nanoscale patterning since the capillary force-driven wetting is a main mechanism of filling nanoholes. After injecting the precursor into the mold, UV light irradiation was performed to initiate the free radical polymerization as shown in **Fig. 3.3.5(ii)**. A height of the nanopattern arrayed on the SMCPA samples was found to be 200 nm (**Fig. 3.3.7(a)**). The 30 nm difference between the hole depth and the pattern height is due to the air trapped in the nanoholes. The pattern transcription ratio, which is defined as the ratio of hole depth to the pattern height, was calculated as 87%.

In general, nanoimprinting processes require high compression pressure or assistant vacuum to completely fill the nanoholes on a replication master when using a common prepolymer resin that is UV curable. However, the precursor resin used in this study had low viscosity at the time of injection because the monomers were injected into the nanoholes and synthesized afterwards. The monomers with low viscosity were polymerized in the nanohole without an external force, and did not cause wrinkling of the prepolymer chains which would exist in the prepolymer resin by the external pressure. Accordingly, it is expected that residual stresses in the nanopatterns would be drastically reduced and as a result, robust nanopatterns could be manufactured. For AR applications, one of the most critical factors is a gradually changing slope of patterns in the normal direction in order to implement impedance matching along the direction of light rays [230]. Therefore, the

master with inverse lens-shaped holes was employed to achieve the impedance matching behavior as that in the previous study [231].

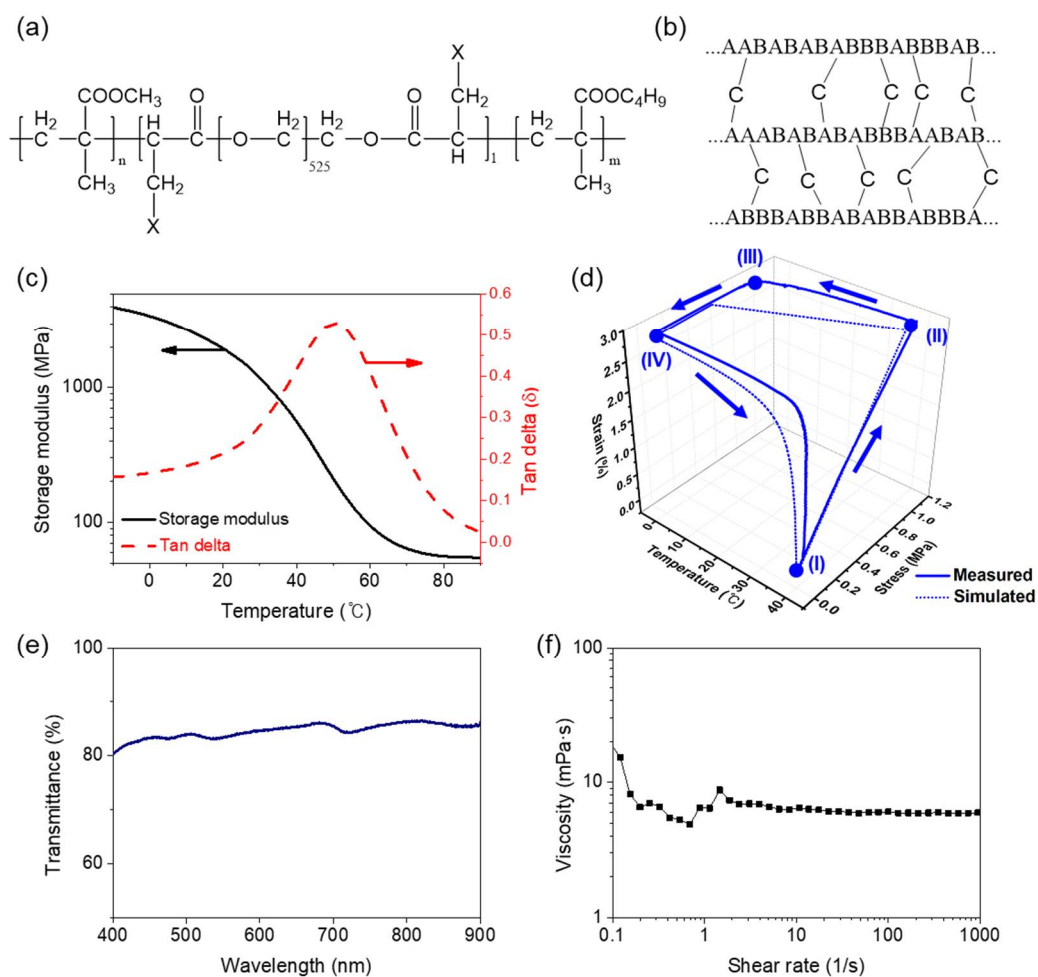


**Figure 3.3.4.** Characteristics of the synthesized SMCPA: (a) chemical formula, (b) schematic representation of polymer chain networks, (c) thermomechanical behaviors, (d) measured and simulated cyclic SST curves, (e) measured optical transmittance, and (f) viscosity of the SMCPA resin.

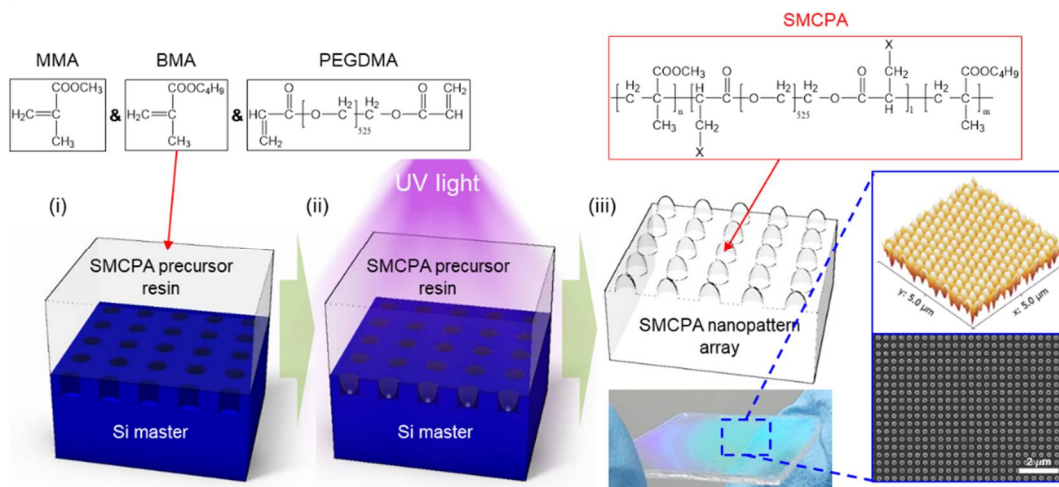


**Figure 3.3.5.** Replica molding method for SMCPA nanopattern array: (i) injection of the precursor resin into the mold, (ii) the polymerization process by irradiating UV light, and (iii) the nanopattern array of SMCPA.

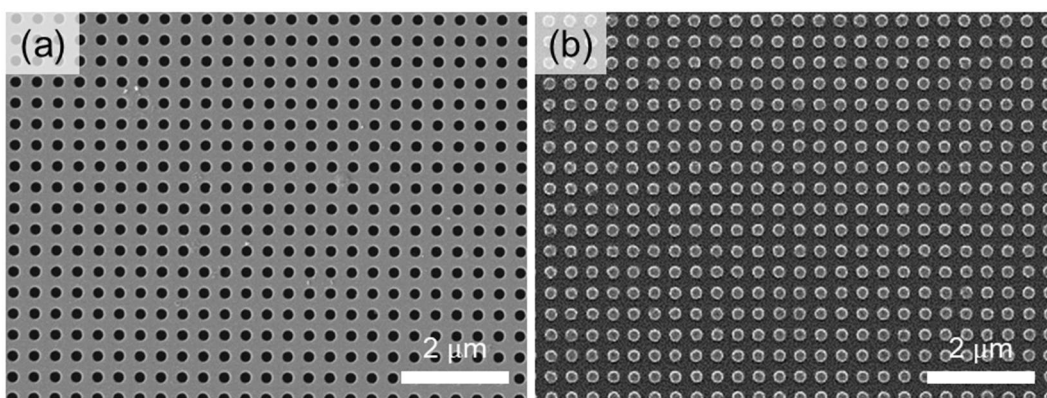


**Figure 3.3.6.** SEM images of (a) the Si master and (b) the SMCPA nanopattern array on the sample surface.

### 3.3.4.2. Nanoscale shape memory effect

Nanoscale shape recovery of the patterns on the sample surface was examined by carrying out shape memory cycle experiments and observing the following changes in topology. In the shape-programming step, the sample surface was compressed with a pressure of 30 MPa at 40°C, followed by cooling to 0°C in the fixing step. After that, the nanopatterns were deformed as shown in **Fig. 3.3.7(b)**. The lowered height of the nanopattern was about 70 nm, representing 65% compressive strain. This deformation of nanopatterns could be a potential obstacle for maintaining the AR function. The deformed nanopatterns were recovered to their original shape by gentle heating at 40°C. Topology of the recovered nanopatterns was verified from the SEM and AFM images as shown in **Fig. 3.3.7(c)**. The images display almost the same topology as those of the original pattern, implying a shape recovery ratio over 90%.

The experimental results were validated by numerical simulation based on the real geometry and material properties. Shape memory-recovery mechanism of the SMCPA was demonstrated by using a Hyperelastic model [194,196] which employs the concept of the stored strain energy function. In this model, the absence of plastic deformation is assumed and viscoelastic behavior is not considered. The applied strain energy is transformed into an entropy term, a Helmholtz potential.

The simulation results are shown in **Fig. 3.3.8**. In the loading step (I → II), the applied pressure caused the nanopatterns to deform up to 65% strain (130 nm displacement), and the applied strain energy was stored in the form of Helmholtz free energy. In the cooling step (II → III), the material was stiffened by generating stress-free glassy regions in it and therefore some fractions of the generated stress disappeared. Most applied stress was eliminated after the unloading step (III → IV). However, the deformed shape was maintained since the stored elastic strain energy cannot overcome the reinforced threshold for deformation. In the following heating step (IV → I), the generated glass region disappeared and the stored elastic energy was released without mechanical hindrance. In this step, the shape recovery ratio reached 100% since the nanopatterns were not constrained. From the simulation, von-Mises stress distribution in the nanopatterns could be visualized and analyzed and the shape memory mechanism of the nanopattern arrays could be understood at each step.

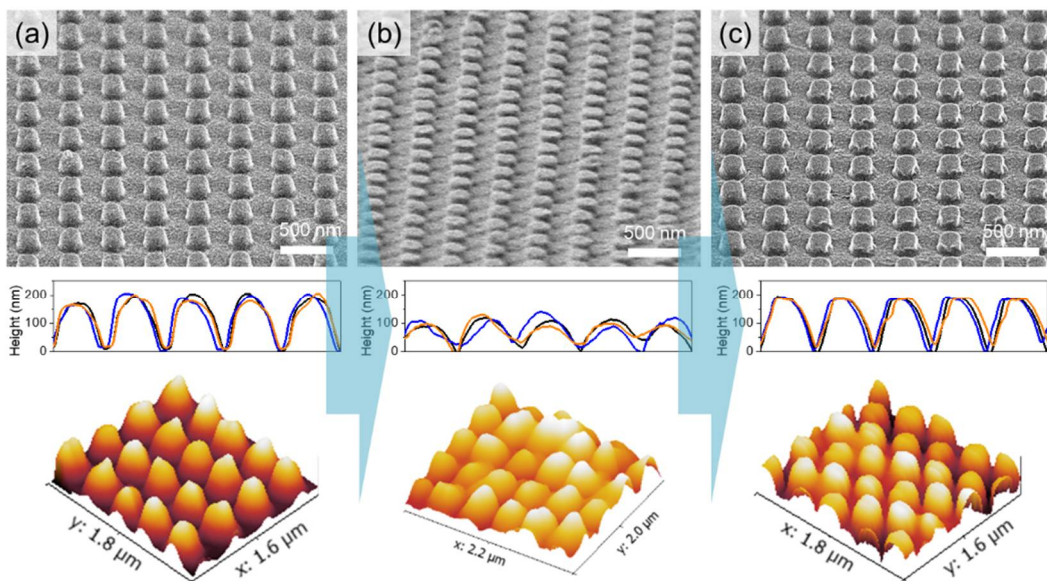


**Figure 3.3.7.** Shape memory-recovery behavior of the SMCPA nanopatterns. SEM and AFM images of the nanopattern arrays: (a) original ( $45^\circ$  tilted), (b) deformed ( $80^\circ$  tilted), and (c) recovered ( $45^\circ$  tilted) surface.

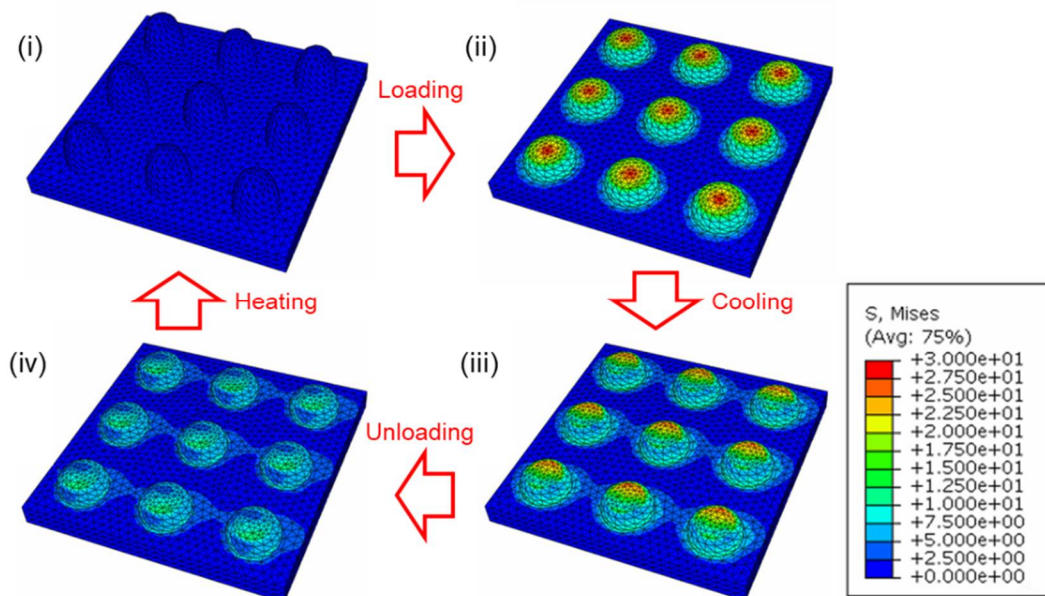


**Figure 3.3.8.** Numerical simulation results of the SMCPA nanopatterns: (i) original nanopatterns, (ii) deformed patterns at  $40^\circ\text{C}$ , (iii) deformed patterns after cooling to  $0^\circ\text{C}$ , and (iv) deformed patterns after unloading. The original shape of the nanopatterns is recovered (i) after heating up to  $40^\circ\text{C}$  again.

### 3.3.4.3. Sustainable antireflection

Enhancement of optical transparency by the nanopatterns was identified as shown in **Figs. 3.3.9-10**. **Figure 3.3.9** shows the difference in the surface reflectance between the bare sample and the nanopatterned sample under two light conditions. It was clearly found that the nanopatterns reduce the gloss of the surface by delivering light energy to the inner medium with less loss. Transmittance of each case was measured by using the UV spectrometer (see **Fig. 3.3.10(a)**). The transmittance of the bare sample was measured to be about 85% in the visible light range. The optical impedance mismatching at the interface between two separate domains diminishes the propagation of optical energy. In other words, when the incident light is projected from air to the bare surface of SMCPA, the light energy cannot be totally transmitted due to the abrupt change of refractive indices. For this reason, 15% of the total light energy was reflected from the surface of the bare sample.

Embedding the nanopattern arrays on the SMCPA surface enhanced the transmittance up to 95% in the wavelength range over 600 nm, which was about 10% higher than that of the non-patterned sample. It is noteworthy that 67% of the reflected component is reduced. Interestingly, despite the low aspect ratio (1:1) of the pattern, the bullet-shaped nanopattern with a gradual decrease in radius with respect to height leads to a significantly improved transmittance because it brings out the optical impedance matching feature. Decay of the transmittance at wavelengths below 600 nm is attributed to the light scattering arising from the nanoscale topology. This phenomenon occurs when light passes through a rough interface which has a topological wavelength larger than light wavelength, *i.e.*, wide spacing of patterns [219]. Therefore, the nanopattern arrays need to have a topological wavelength much lower than that of the incident light to operate as a more efficient GRIN (gradient-index) layered metasurface.

The nanopatterns can be deformed when the patterns encounter some compressive or shear forces. This weakens or completely deprives the performance of the nanopatterns. In this respect, high dimensional stability is essential to maintain the nanopattern-driven functions and enhance durability. The reduced gap between the deformed patterns caused a slightly higher transmittance than original patterns at wavelengths below 400 nm. However, the deformed sample revealed 5% lower transmittance than the original patterned sample in the wavelength range over 600 nm (**Fig. 3.3.10(a)**). Also, the reflection of light

was increased at the interface of air and the top surface of the impedance matching layer. As a result, the deformed sample showed the worse AR performance.

The use of SMP as a constituent of the nanopatterns became a plausible solution to overcome this drawback. In the previous section, the nanoscale shape recovery was identified in the numerical and experimental analyses. After shape-recovery of the deformed nanopatterns on the sample, the transmittance was restored close to that of the original sample. The cyclic transmittance tests were performed to examine sustainable AR effects based on shape memory function (**Fig. 3.3.10(b)**). The transmittance for the original sample was denoted to Ori., and D1-5 and R1-5 mean the transmittances of the samples that were deformed and recovered according to the number of repetitions of the experiment. Transparency of the samples decreased slightly as the experiment was repeated, since the recovery rate of the pattern is not completely 100% but over 90%. However, sustainability of the patterns could be confirmed sufficiently.

Theoretical transmittance of the samples was investigated by using effective medium theory (EMT) to further elucidate the significance of sustainable nanopatterns in maintaining AR performance from a nanotopological perspective [232,233]. The profile of volume fractions of the nanostructures ( $V_f$ ) were shown in **Fig. 3.3.10(c)** as a function of the pattern height.

The  $V_f$  for the bare sample is suddenly increased from 0% to 100% at 0 nm height since there is no pattern on the surface. Therefore, the effective refractive index ( $n_e$ ) abruptly changes from 1 (the refractive index of air) to 2.38 (the refractive index of SMCPA at 550 nm), which induces large mismatching of optical impedance (**Fig. 3.3.10(d)**). The large impedance mismatching provokes great amount of light reflection on the interface between two domains. Unlike this, the original and recovered samples have the gradually increasing  $V_f$  from the top to the bottom of the nanopatterns. This structural feature serves as a nanoscale GRIN layer that mitigates a sharp change in refractive index and reduces reflection.

Theoretical transmittance in the normal incident direction was calculated by using a multi-layer Fresnel equation with the calculated effective refractive index ( $n_e$ ) profile (**Table 3.3.1**) and the results are plotted in **Fig. 3.3.10(a)**. The measured and calculated graphs have a similar tendency in the wavelength region over 600 nm. However, the



simulation could not successfully predict empirical behaviors in the wavelength region below 600 nm because the light scattering by the nanotopology was not considered in the calculation. Nevertheless, the EMT analysis can explain the underlying mechanism of AR nanostructures and emphasize the significance of the recoverability of nanopatterns as a desirable feature for maintaining high AR performance.

Transmittances at various angles, which are vertical incidence ( $\theta=0^\circ$ ),  $20^\circ$ , and  $60^\circ$ , were measured to examine omnidirectional antireflectivity of the samples. In general, the transmittance of a material is decreased when the incident angle is increased [221]. The transmittance at 700 nm, as a representative, of the bare sample was changed from 85% ( $0^\circ$ ), 78% ( $20^\circ$ ) to 55% ( $60^\circ$ ) by tilting the sample (**Fig. 3.3.11(a)**). Meanwhile, the oblique transmittances of the nanopatterned sample were not significantly affected according to incident angles as shown in **Fig. 3.3.11(b)**. The transmittance at 700 nm of the nanopatterned sample was only varied from 95% ( $0^\circ$ ), 93% ( $20^\circ$ ) to 92% ( $60^\circ$ ).

Omnidirectional antireflectivity is a well-known nanoeffect due to its subwavelength nanostructure [234]. The oblique incident light to the nanopatterns can be bent to vertical direction and this feature enables the omnidirectionality [235]. The bending effect must be weakened after the nanopatterns were deformed (**Fig. 3.3.11(c)**). The transmittance at 700 nm of the deformed sample was decreased from 90% ( $0^\circ$ ), 83% ( $20^\circ$ ) to 66% ( $60^\circ$ ). When the nanopatterns were in the original state, only 3% in transmittance was reduced by tilting  $60^\circ$ . However, the transmittance was reduced by 23% after the nanopatterns were deformed. The undermined nanoeffect could be restored by recovering the nanopatterns as shown in **Fig. 3.3.11(d)**, 94% at  $0^\circ$ , 92% at  $20^\circ$  and 91% at  $60^\circ$ . Therefore, it could be confirmed that the shape recovery function of the nanopattern is a very essential element for the omnidirectional antireflection.



**Figure 3.3.9.** Optical photograph for comparison of surface reflectance between the bare and the nanopatterned surface under (i) solar light and (ii) fluorescent light.

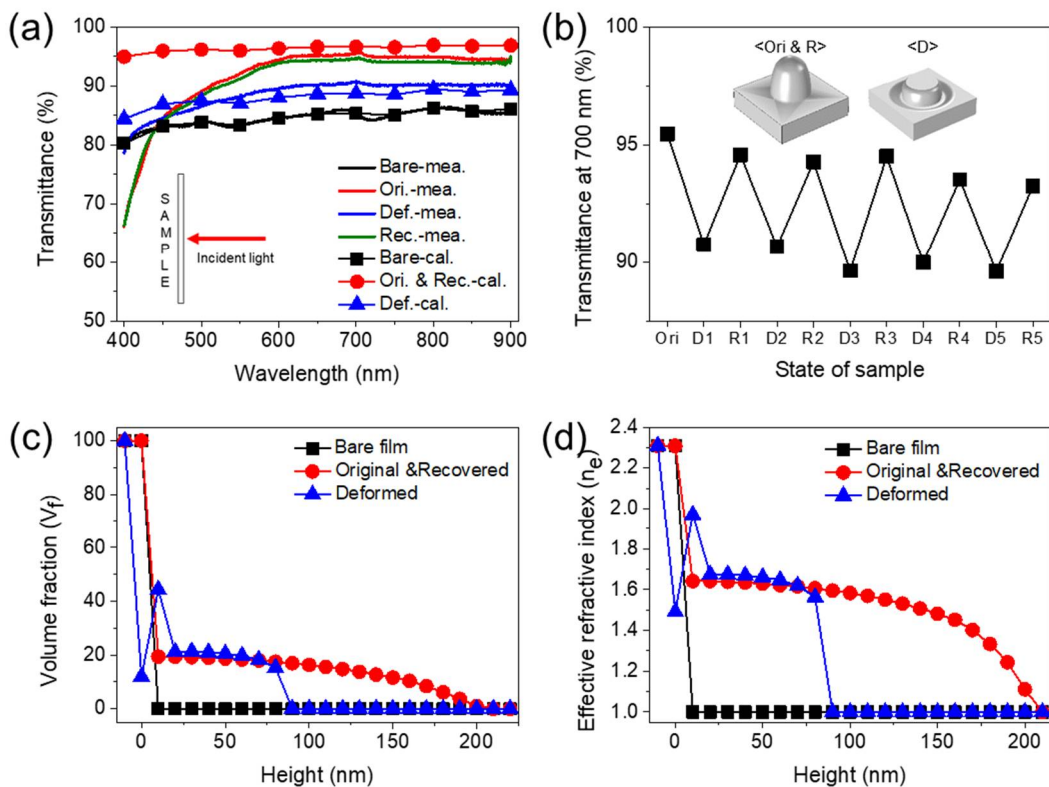


**Figure 3.3.10.** Sustainable antireflection by the SMCPA nanopatterns. (a) Measured (Mea.) and calculated (Cal.) transmittances for each sample. (b) Results of cyclic transmittance tests. (c) Nanopattern volume fraction and (d) calculated effective refractive indices depending on the height-profile.

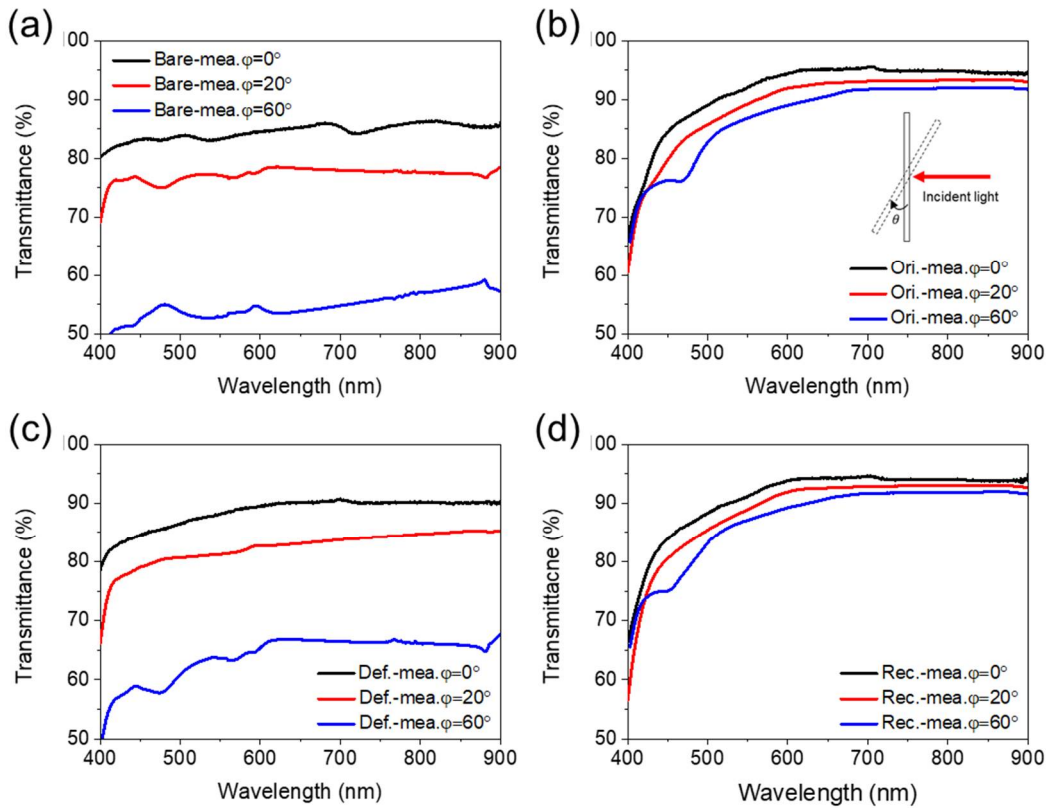


**Figure 3.3.11.** Omnidirectional antireflection by the SMCPA nanopatterns: angular transmittances of (a) the bare, (b) the original patterned, (c) the deformed, and (d) the recovered samples.

#### 3.3.4.4. Mechanical energy dissipation

Nanoindentation on the samples was carried out to investigate the mechanical energy dissipation of the nanopatterns. The force-displacement results shown in **Fig. 3.3.12(a)** reveal a remarkable distinction between the two curves. When applying a force of up to 500  $\mu\text{N}$ , the nanopatterned region was compressed more easily and absorbed more mechanical energy than the ground surface region. The dissipated energy and stiffness were quantified from the results (**Fig. 3.3.12(b)**). The stiffness was estimated from the slope of the curves in the unloading step and the dissipated energy was calculated by integrating the area below the curves. Compared with the ground surface region, the amount of dissipation

energy for the nanopatterned region was increased by two times from 111.03 pJ to 205.92 pJ.

A nanoscale tip with a 100 nm radius was used for pressing the regions in the indentation test. Flexibility of the patterned region induced the decreased stiffness, which stems not from the bulk material property but from the nanoscale structure. Also, the flexibility led to an increase in the energy dissipation, allowing the patterns to act as a shock resistant layer. That is, the nanopattern arrays are compressed before the ground surface undergoes deformation under compression. This phenomenon could be theoretically verified in the numerical simulation results presented above. When compression was applied, the resulting deformation was identified mostly in the nanopatterned region rather than the ground surface region (**Fig. 3.3.8**). This nanomechanical property can help protect the devices when an external force is applied on the surface.

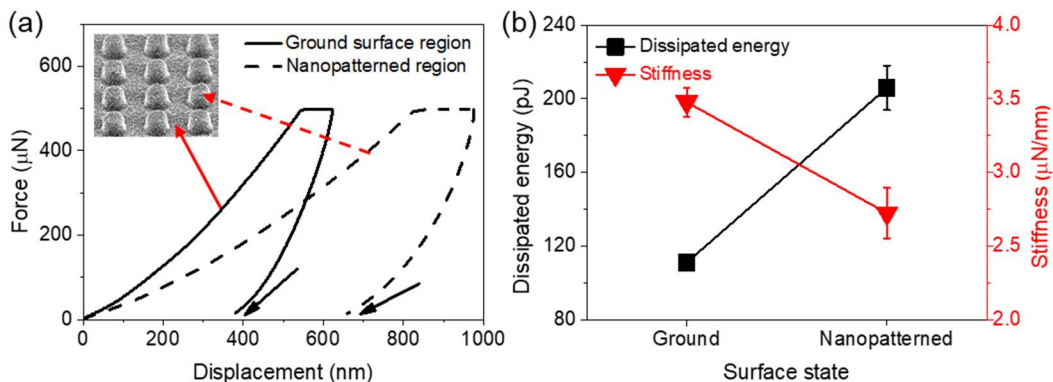


**Figure 3.3.12.** Nanoindentation results for the SMCPA nanopatterns: (a) force-displacement graph and (b) dissipated energy and stiffness for the ground surface and the nanopatterned region.

### 3.3.4.5. Restorable self-cleaning

A hydrophobic function helps prevent fog or remove dust on the surface, which is called a self-cleaning effect or an antifogging effect. Therefore, this is one of the additional functions to consider when creating AR nanostructures [236]. However, the self-cleaning function induced by nanopatterns can also be damaged by external shocks. This section explains that shape memory effect can solve the mechanical weakness that adversely affects the maintenance of hydrophobicity.

Wettability of the samples was analyzed by using a contact angle (CA) goniometer to confirm the antifogging effect of the nanopattern arrays (**Figs. 3.3.13(a-d)**). Generally, the nanopatterned surface has a low surface energy due to trapped air in Cassie-Baxter state [237]. Therefore, the CA of the nanopatterned surface ( $113.0^\circ$ ) is larger than that of the bare surface ( $65.6^\circ$ ). The nanopatterned surface cannot satisfy the condition of superhydrophobicity (greater than  $150^\circ$ ) because of hydrophilicity of the SMCPA itself. Although the nanopatterned surface does not have a sufficiently high CA, the CA is increased significantly compared to that of the bare sample. This change can improve the antifogging performance of the samples. After deformation of the patterns, the CA was decreased to  $78.8^\circ$  due to the smaller air pockets between the nanopatterns. Accordingly, the shape recovery could return the CA from  $65.6^\circ$  to  $112.6^\circ$ .

A contact angle hysteresis (CAH) was also analyzed by tilting the sample stage up to  $30^\circ$  to provide in-depth explanation regarding the self-cleaning effect of the nanopatterned surface (**Figs. 3.3.13(e-g)**). The CA on the tilted surface is related to the performance of self-cleaning to automatically remove dust from the surface. On the deformed surface, the water droplet was widespread, thus yielding a very small difference between the ascending angle and the descending angle (CAH= $1.1^\circ$ ). This means that it is difficult for the water droplet to remove dusts naturally. However, the water droplet has a relatively large difference between the angles at both sides on the original and recovered surfaces (CAH= $23.5^\circ$  and  $21.4^\circ$ , respectively). This enables the self-cleaning of the surfaces by eliminating attached contaminants. The recovered CA and CAH show that the shape memory function of the nanopatterns can lead to the restoration of hydrophobicity and this presents a new strategy for sustainable self-cleaning function.

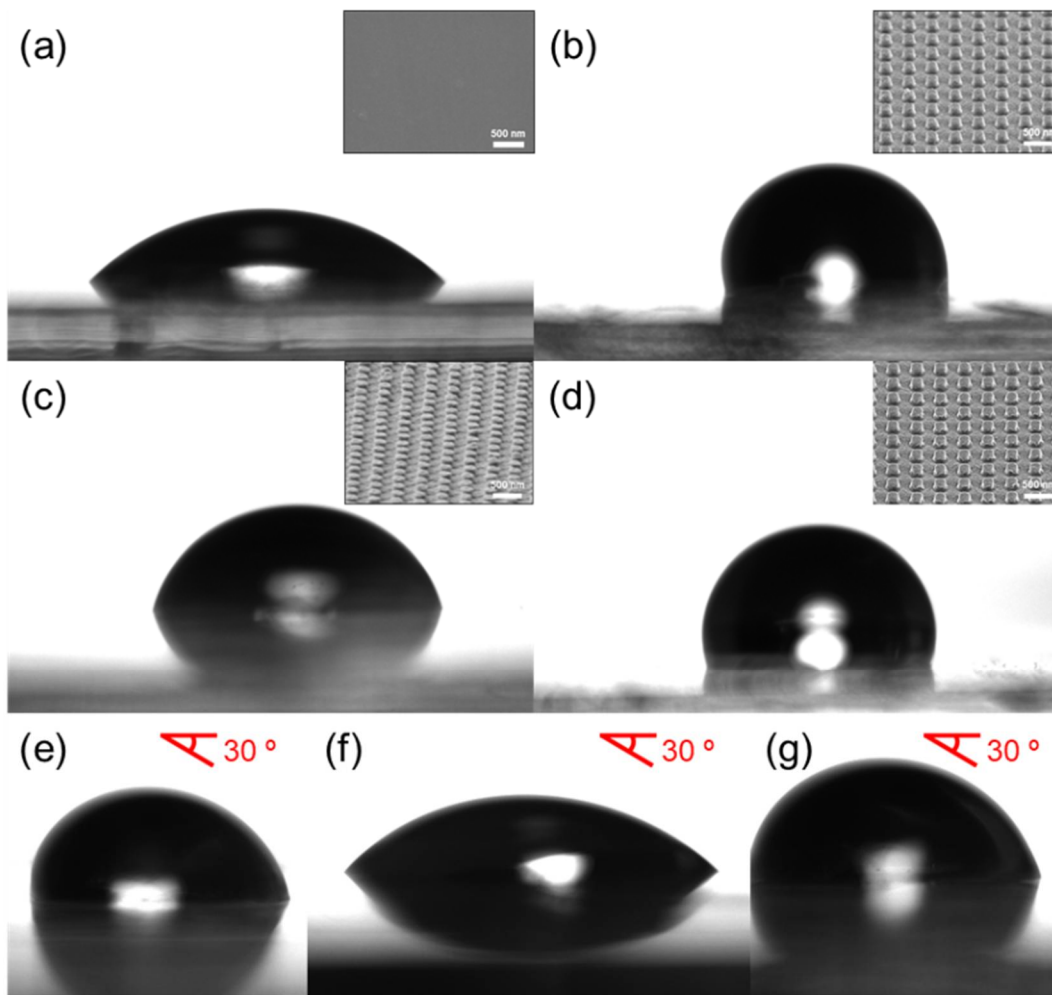


**Figure 3.3.13.** Recoverable hydrophobicity by the SMCPA nanopatterns: results of the CA analysis for the (a) bare, (b) original, (c) deformed, and (d) recovered surfaces. A water droplet on the 30° tilted samples: the (e) original, (f) deformed, and (g) recovered surfaces.

### **3.3.5. Conclusions**

In this section, the metasurface made of shape memory polymeric nanopattern arrays was explored for sustainable antireflection (AR). The nanopatterns were synthesized by using nanoscale in-mold polymerization with the designed acrylic chemical, SMCPA. The shape memory-recovery test on the nanopatterns confirmed the sustainability of the nanopattern arrays at body temperature. The measured transmittance of the samples showed that the reduced transmittance after damaged is restored to its original level after restoring the deformed shape of the patterns. The EMT analysis provides a rationale for the geometric dependent AR performance of the nanopatterns. The shape recoverable nanopatterns also imparted robust omnidirectional antireflectivity to the material. The mechanical energy dissipation of the nanopatterns was evaluated from the nanoindentation test. The surface hydrophobicity could also be recovered by shape recovery and this can induce the sustainable antifogging and self-cleaning effects helping antireflection. Overall, this research is expected to pave a way for developing advanced optical devices based on metasurface concept and smart biomimetic nanotechnology.

## 3.4. Biometric SMP nanopattern

### 3.4.1. Introduction

Biometric systems [238], which are capable of uniquely identifying or evaluating a person, have emerged with a rise of smart electronic devices. As one of the biometric systems, a personal identification system has been developed for encrypting personal information using finger prints [239], hand geometry [240], or other biological templates. Furthermore, the biometric system is also utilized for gathering anthropometric information for *in-vitro* diagnosis, such as electrocardiogram [241], ultrasonography [242], electric impedance tomography (EIT) [243], and body mass index (BMI) [244]. A prerequisite for improving the accuracy of biometric devices is to improve signal quality by reducing energy loss at the interface between the two media, *i.e.*, human body and a touch pad. In general, an impedance matching gel is used under wet condition as an intermediate medium at the interface [245].

Developing highly conductive materials is essential to advance the sensing efficiency of touch pads in biometric systems [246,247]. Polymeric nanocomposites have been researched to develop not only electrically conductive but also mechanically robust materials [248,249]. Among them, carbon nanotube (CNT) embedded composites are one of the most widely studied materials for substituting metals, due to the high strength and exceptional electron mobility of CNTs [250–252]. Indeed, CNTs possess unique physico-chemical properties such as super-hydrophobicity [237] and indirect heating for a remote control of shape memory polymer (SMP) composites [253,254].

Nanopattern array [255,256] is a functional nanostructure for metasurfaces to increase energy transfer due to gradual change in impedance at the interface between discrete media. In the moth eye nanostructure, optical impedance matching, *i.e.*, refractive index matching, is a key mechanism to enhance light transmittance by directing the ray in the vertical direction of the pattern [219,257,258]. The nanopattern/air coexisting region at the interface between air and the substrate acts as a role of a gradient-index (GRIN) layer [235].

“Impedance matching” means a strategic way to reduce the loss induced by the impedance difference of two different connection stages [259,260]. An new idea was



contrived that a nanopatterned metasurface, as a two-dimensional metamaterial, can also serve as an electrical impedance matching layer between two different media by directing and focusing the electrical current flow toward the patterns. This impedance matching strategy has advantages over the gel-based method since it is a dry-state method. However, surface nanopatterns must have poor structural stability by repetitive direct contact.

On the other hand, shape memory polymer (SMP) [261,262] is a smart material that can memorize and recover its original permanent shape. So far, SMPs have been applied for various purposes, *e.g.*, to impart a switchable function to microstructures [114,115] or to be used for adhesion in a dry state [120,122]. Recently, SMPs have been applied to enhance the sustainability of nanostructures for overcoming the mechanical drawback of nanopatterns [221,257]. SMPs have also been studied in a myriad of biological applications due to their fascinating functionality and biocompatibility [110,262,263].

In this study, a novel nanostructure was developed, which is made of SMP/CNTs nanocomposites for an advanced biometric sensing system. The amount of delivered energy was increased due to the synergistic nanoeffects; CNT-induced effect and nanopattern-induced effect. SMCPA (S-MMA/BMA developed in Section 3.2), which can be triggered at body temperature, was employed as a SMP matrix for retaining the nanoeffects. After blending CNTs with the SMCPA resin, a replica molding method was used to fabricate the nanocomposite pattern arrays. CNTs embedded in the patterns were identified by using an X-ray photoelectron spectroscope (XPS) and a focused ion beam (FIB). Shape memory behavior at nanoscale was verified experimentally and numerically. The intensity of electric current transmitted from human skin to a biometric sensor was measured by using a lab-made touch sensor circuit and a nanoelectronic phenomenon was simulated and analyzed numerically.

## 3.4.2. Experimental

### 3.4.2.1. Precursor materials of SMCPA/CNTs

Shape memory copolyacrylate (SMCPA) was synthesized by using a free radical polymerization method. The precursor consists of two monomers (methyl methacrylate (MMA, Daejung Chemicals, Republic of Korea) and butyl methacrylate (BMA, Daejung Chemicals, Republic of Korea)), a crosslinker (polyethylene glycol dimethacrylate (PEGDMA, Mw=525, Sigma Aldrich, USA)), and a thermal initiator (2,2-Azobis(isobutyronitrile) (AIBN, Daejung Chemicals, Republic of Korea)). Unlike the previous synthesis method (Sections 3.2.2 and 3.3.2), the thermal initiator (AIBN) should be used in this case because dispersed CNTs interfere with polymer polymerization using ultraviolet light. The volume ratio of the mixed co-monomer (MMA:BMA=1:1) to the crosslinker was 1:2. 0.2 wt% AIBN was added to the precursor. 1 wt% multiwall carbon nanotubes (MWCNT, CM-95, Hanwha chem., Republic of Korea) with 10 to 15 nm in diameter and 2  $\mu\text{m}$  in length were incorporated with the precursor. The mixture was rigorously vortex-mixed for 30 minutes, and then ultrasonic waves were applied to the mixture for well-dispersion of CNTs.

### 3.4.2.2. Fabrication of nanocomposite pattern arrays

A silicon (Si) master with nanohole patterns of 230 nm in depth, 200 nm in diameter, and 200 nm distance between the nanoholes was fabricated by using a e-beam lithography (**Fig. 3.3.6**). A replica molding method was employed to fabricate the samples with the nanocomposite pattern arrays on the surface. Trichloro(1*H*,1*H*,2*H*,2*H*-perfluoro-octyl)-silane (Sigma Aldrich, United States) was deposited on the surface of the Si master for easy separation. A mold for manufacturing the samples was built by using 1 mm spacers and a slide glass. After filling the mold with the precursor resin, the mold was placed in a hot oven for polymerization. Residual monomers and crosslinkers were cleaned by rinsing the samples with isopropyl alcohol (IPA, Daejung Chemicals, Republic of Korea), and then the samples were completely dried.

### 3.4.2.3. Characterizations

Nanocomposite patterns arrayed on the sample surfaces were observed by using a field

emission scanning electron microscope (FE-SEM, JSM-6390LV, JEOL, Japan) and an atomic force microscope (AFM, Park NX10, United States). A cross-section of the nanocomposite patterns was prepared and observed by using a dual beam focused ion beam (DB-FIB, Helios NanoLab™, FEI, Netherlands) system. To avoid collapse of the patterns, a Pt protection layer was deposited on the surface of the samples before splitting the nanocomposite patterns. Electrical conductivities of the specimens were evaluated by using a 2-point-probe method with a digital multi-meter (HiTESTER 3454-11, Hioki E.E. Corporation, Japan). Electric current passing through the samples was measured by using a lab-made touch sensor circuit (**Fig. 3.4.1**). The touch circuit is made of a 12-channel self-calibration capacitive touch sensor (TSM12M, Touch-On corp., Republic of Korea) and a digital multi-meter (Fluke 27/FM Military Digital Multimeter, Fluke corp., United States).

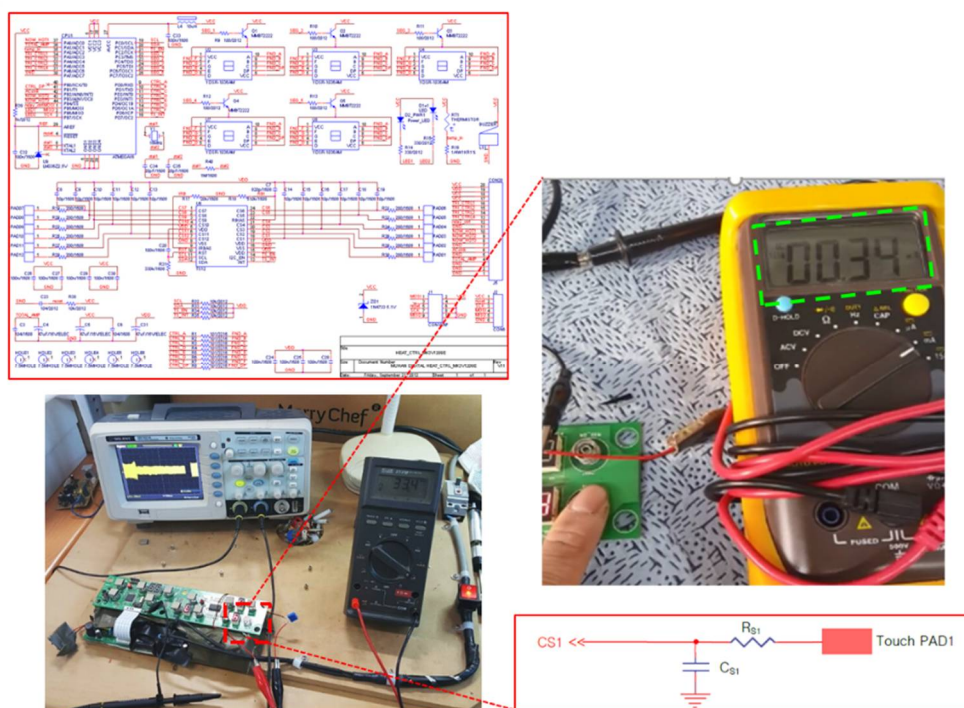


**Figure 3.4.1.** Lab-made touch sensor circuit. The enlarged figure shows the measured electric current when touching the sample with the SMPAC/CNT nanocomposite pattern array.

### 3.4.3. Numerical analysis

#### 3.4.3.1. Modeling shape memory behavior of SMP/CNT nanopattern

The same modeling methodology described in Section 3.3.3 was used to simulate the SMCPA/CNT nanocomposite patterns. However, the different material properties were used as listed in **Table 3.4.1**.

#### 3.4.3.2. Nanoelectronic simulation

Numerical simulation for the nanoelectronic phenomenon was carried out by employing a commercial FEM (finite element method) program, COMSOL Multiphysics. Unit cells were built to mimic the actual topology of the surface of the samples (**Fig. 3.4.2**). The electrical conductivities of each domain,  $\sigma_{smp}$  and  $\sigma_{skin}$ , were brought from the measured data of the bulk materials and applied in the simulation. Directionality of CNTs embedded in the nanopatterns was not considered in the simulation. It was assumed that a lipid layer completely fills the gap between the nanopatterns and the electrical conductivity of the lipid layer was same as to the measured conductivity of the finger skin (**Fig. 3.4.13**).

Electric potential boundary conditions were applied through the unit cells in z-direction. The applied potential conditions were set so that the simulation result of CB is equal to the measured value, and only the geometrical effect by the nanopatterns was investigated. Periodic boundary conditions were applied on the lateral surfaces of the unit cells in x,y-directions. Electrical fields ( $\mathbf{E}$ ) in each unit cell were calculated by solving the current conservation equations below.

$$\nabla \cdot \mathbf{J} = 0 \quad (3.4.1)$$

$$\mathbf{J} = \sigma \mathbf{E} \quad (3.4.2)$$

$$\mathbf{E} = -\nabla V \quad (3.4.3)$$

, where  $\mathbf{E}$  is the electrical field,  $V$  is the applied electric potential,  $\mathbf{J}$  is the electric current field, and  $\sigma$  is the electrical conductivity. The magnitude of current density fields ( $J_{nor}$ ) and calculated current values ( $I_{cal}$ ) was calculated and compared each other.

**Table 3.4.1.** Material parameters of SMCPA/CNT employed in the shape memory effect simulation.

SMCPA/CNT	
$T_r$ (°C)	60
$T_g$ (°C)	-20
$C_{10}$ (MPa)	6
$C_{20}$ (MPa)	405
$D_1$ (1/MPa)	0.03
$D_2$ (1/MPa)	0.001
$\nu$	0.35

\* $T_r$ : Temperature on fully rubbery phase.

\*\* $T_g$ : Temperature on fully glassy phase.

\*\*\* $\nu$ : Poisson ratio.

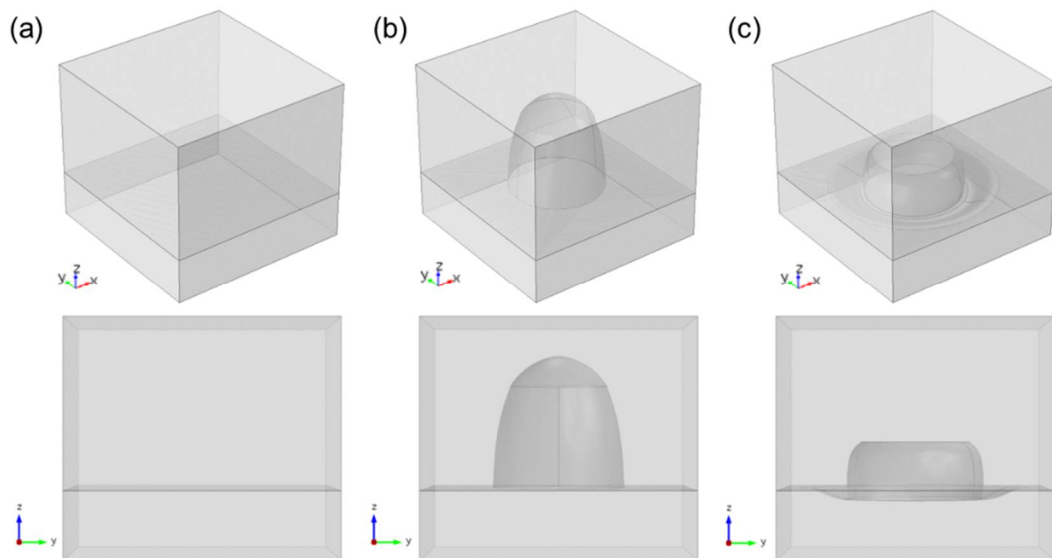


**Figure 3.4.2.** Employed unit cells for the nanoelectronic simulation. (a-c) A 3-D view and (d-f) a yz plane view of the unit cells for the CB, CP, and deformed CP unit cells, orderly.

### 3.4.4. Results and discussion

#### 3.4.4.1. Preparation of materials

A replica molding method was employed to inversely copy the geometry of the prepared silicon master for constructing SMCPA/CNT nanocomposite pattern arrays. **Figure 3.4.3** illustrates a scheme of the fabrication process. The SMCPA material [228,257] was designed to grant the shape recovery capability at body temperature and synthesized using the two monomers (methyl methacrylate (MMA) and butyl methacrylate (BMA)) and the crosslinker (polyethylene glycol dimethacrylate (PEGDMA,  $M_w=525$ ). The SMCPA/CNT composite resin was prepared by incorporating 1 wt% CNTs into the SMCPA resin. 1 wt% of CNTs is sufficient to form an interconnected network of CNTs in the SMCPA matrix for fast electric charge transfer [264]. The composite resin was injected into the nanoholes arrayed on the silicon master before polymerization (**Fig. 3.4.3**). The viscosity of the composite resin was measured by using a rheometer and it was compared with that of the pure SMCPA resin (**Fig. 3.4.4**). Despite high viscosity of the composite resin, the high production rate of the nanopatterns was achieved due to the shear thinning behavior and surface tension of the resin [265,266].

After filling the nanoholes, the composite resin was polymerized by thermal irradiation based on the two chemical reactions, *i.e.*, chain elongation reaction and crosslinking reaction, simultaneously (**Fig. 3.4.3(ii)**). A scheme for the synthesis is portrayed in **Fig. 3.4.7**. Free radicals are generated on AIBN (2,2-Azobis(isobutyronitrile), the thermal initiator) by thermal decomposition of the N-C bonds of AIBN. The generated radicals react with alpha-carbons of adjacent monomers and crosslinkers. As a result, polymer chains are lengthened and 3-D shape memory networks are formed. The fabricated samples were coded as IB (Intrinsic bare SMCPA sample), IP (Intrinsic patterned SMCPA sample), CB (CNT-embedded bare SMCPA/CNT sample), and CP (CNT-embedded patterned SMCPA/CNT sample), depending on the presence and absence of CNTs and patterns.

It is of great importance to verify the existence of CNTs placed in the nanocomposite patterns which mainly contribute to the nanoscale impedance matching. For this, XPS analysis of the nanocomposite patterns was performed for indirect confirmation of the

existence of CNTs in the pattern. The results show a discrepancy in the chemical binding energy between the IP and CP samples (**Fig. 3.4.5(a)** and **Table 3.4.2**). The X-ray of the XPS instrument penetrates only a shallow depth beneath the sample surface [267] because a subwavelength structure (SWS) of nanopatterns scatters the X-ray. Since the X-ray cannot reach the bottom-ground area, it is possible to examine the carbon binding energy of the pattern alone. The graph of the CP sample shows a 10% higher content of C-C and C-H bonding peaks than the peaks of the IP sample. The difference in chemical binding energy proves the presence of CNTs in the nanocomposite patterns. In addition, a dual beam focused ion beam (DB-FIB) system was used to directly observe the presence of CNTs in the nanocomposite pattern (**Fig. 3.4.5(b)**). Several CNTs were found in the pattern cross-section of the CP sample, whereas the pattern on the IP sample surface did not own any particles on the cross-section.

Mechanical properties of the samples were examined by using a universal testing machine (UTM) at macroscale and a nanoindenter at nanoscale (**Figs. 3.4.6(a-b)**). It was found from the tensile test results that the elastic modulus of the CP sample was increased by 168% compared to that of the IP sample and the tensile strength was also doubled. Difference in the mechanical properties between the patterned and non-patterned specimens were not readily figured out in the UTM experiments since they have the same material composition. Therefore, the nanoindentation test was harnessed for nanoscale mechanical analysis. It was verified that inclusion of CNTs enhances the stiffness of the nanopatterns by 9 times (*i.e.*, from 359.8 to 3254.4 N/m) as well as the stiffness of the bottom-ground region by 7 times (*i.e.*, from 515.4 to 3782.1 N/m). The nanoindentation results indicate that the nanocomposite patterns can withstand greater damages than the intrinsic patterns.

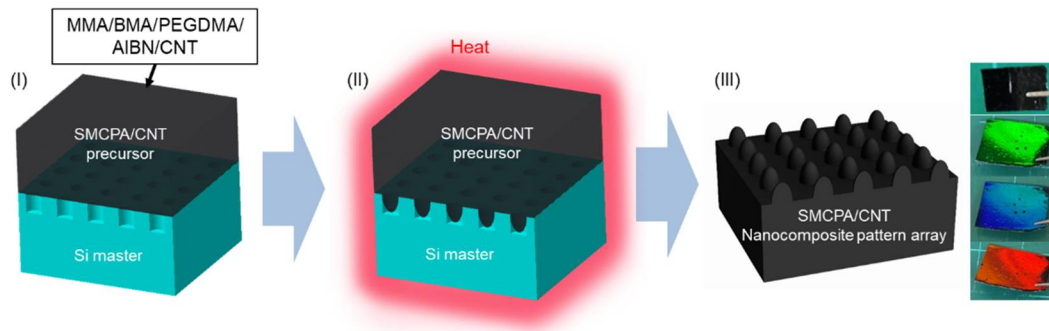


**Figure 3.4.3.** Schematic illustration of the fabrication process for SMCPA/CNT nanocomposite pattern arrays: (i) injection of the resin mixture into the mold, (ii) polymerization by thermal heating, and (iii) demolding of the samples with nanocomposite pattern array.

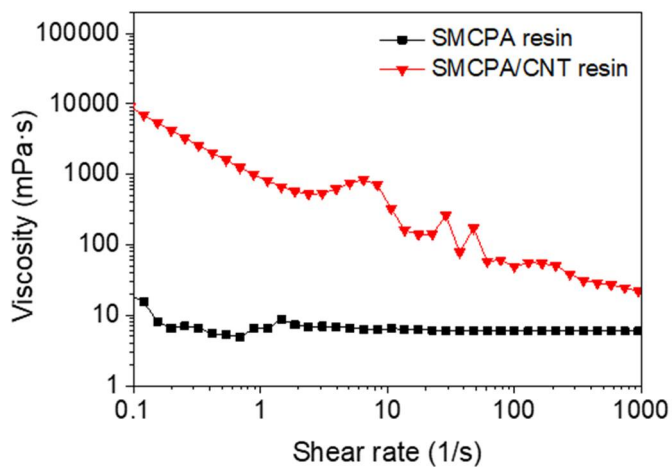


**Figure 3.4.4.** Measured viscosity of the SMCPA resin and the SMCPA/CNT resin.



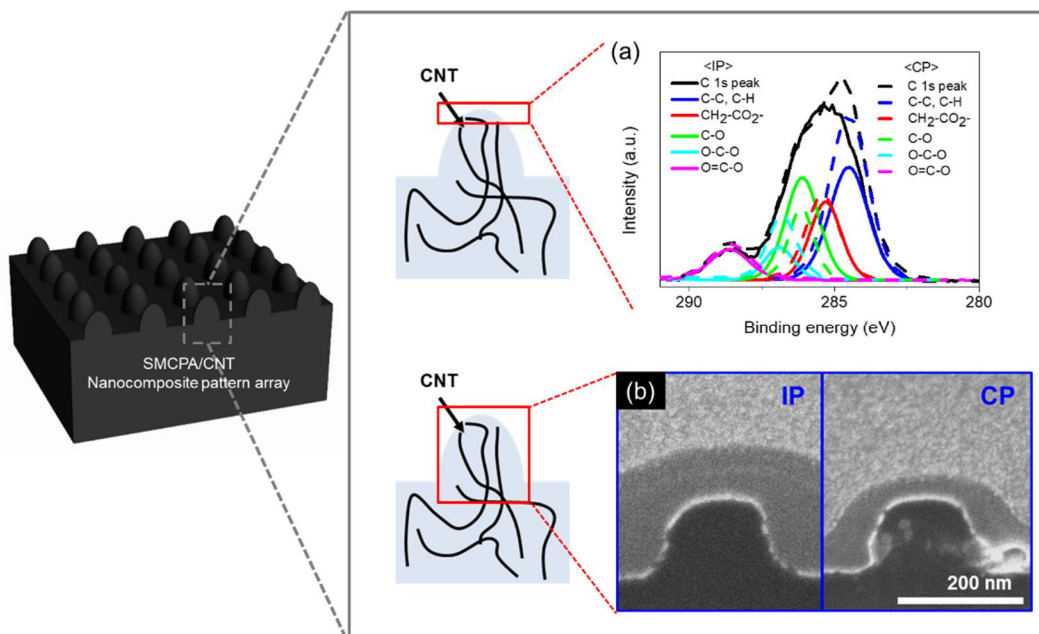


**Figure 3.4.5.** Confirmation of presence of CNTs embedded in the nanocomposite pattern with use of (a) XPS (X-ray photoelectron spectroscopy) data and (b) DB-FIB (dual beam focused ion beam microscope).

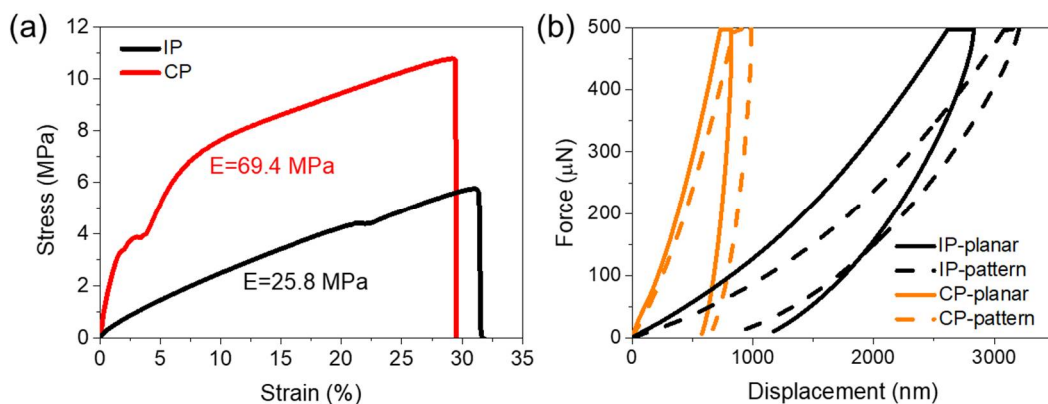


**Figure 3.4.6.** Measured mechanical properties of the samples. (a) Young's moduli of the specimens and (b) force-displacement curves, which are macroscopic and nanoscopic mechanical properties, respectively.

**Table 3.4.2.** XPS peak information of the patterned samples, IP and CP.

#	Name	IP	CP
		Position (At%)	Position (At%)
C1	C-C, C-H	284.5 (35.4)	284.5 (45.7)
C2	$\underline{\text{C}}\text{H}_2\text{-CO}_2^-$	285.3 (19.8)	285.4 (20.1)
C3	C-O	286.1 (27.7)	286.1 (12.3)
C4	O-C-O	286.9 (7.7)	286.8 (12.8)
C5	O=C-O	288.6 (9.5)	288.6 (9.1)

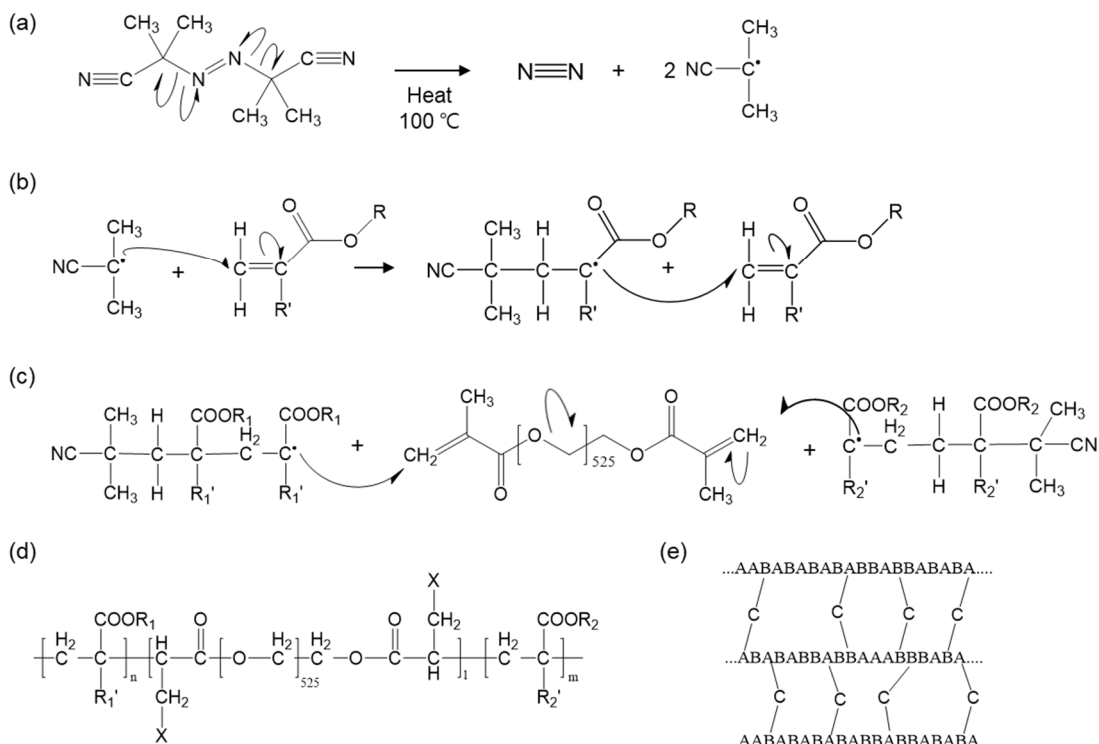


**Figure 3.4.7.** Synthetic scheme of SMCPA. (a) Excitation of AIBN by heating. Free radical vinyl polymerization for (b) extending monomer chains and (c) chain crosslinking. (d) A chemical structure and (e) a schematic structure of the synthesized SMCPA.

### 3.4.4.2. Topological characterizations

Nanotopology of the CP sample was observed by using a scanning electron microscope (SEM) and an atomic force microscope (AFM). Dimensions of the nanopatterns are 200 nm in height, 200 nm in diameter at the bottom surface, and 200 nm for distance between peaks of the pattern (**Figs. 3.4.8-9(a)**). The transcription ratio of the nanocomposite pattern was evaluated as about 90% due to the trapped air in the holes. The gradually changing geometry of the nanocomposite patterns makes it possible to construct an impedance matching system at nanoscale [219,257].

Shape memory-recovery behavior of the nanocomposite patterns was examined by conducting a cyclic shape memory test at nanoscale. A pressure of about 30 MPa for compressive deformation was first applied to the sample surface with the patterns at 40°C, followed by cooling. The height of the deformed patterns was confirmed to be about 55 nm (**Fig. 3.4.8(b)**). It has been proved in the previous reports that the nanoscale impedance matching effect must be attenuated when the nanopatterns are compressed or deformed [221,257]. Deformed nanopatterns cannot provide sufficient nano-functionality because of their low height and flat top surface. Detail explanations about the underlying mechanism are discussed in Section 3.4.4.5.

For this reason, the SMCPA, which is capable of recovering from body temperature, was used as a constituent material of the nanocomposite patterns for sustainable biometric systems. As a result, the deformed patterns could recover their permanent geometry by heating at body temperature. **Figure 3.4.8(c)** shows the fully recovered shape of the nanocomposite patterns. The wide image of the nanocomposite pattern array was shown in **Fig. 3.4.9(a)**. The embedded CNTs have a diameter of 15 to 20 nm, and a length of about 20  $\mu\text{m}$  with a high aspect ratio of about 2000:1 (**Fig. 3.4.9(b)**). The CNTs in the SMCPA matrix were dispersed well as shown in **Fig. 3.4.9(c)**.

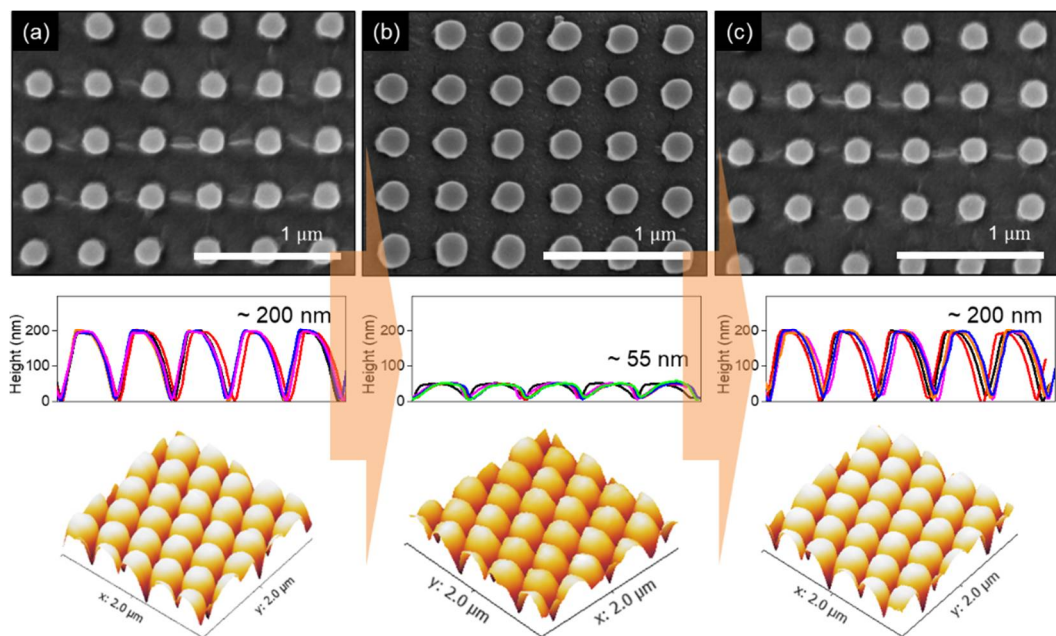


**Figure 3.4.8.** Shape memory-recovery behavior of the SMCPA/CNT nanocomposite patterns arrayed on the CP sample surface. SEM and AFM images of the sample surface on (a) the original, (b) deformed, and (c) recovered states.

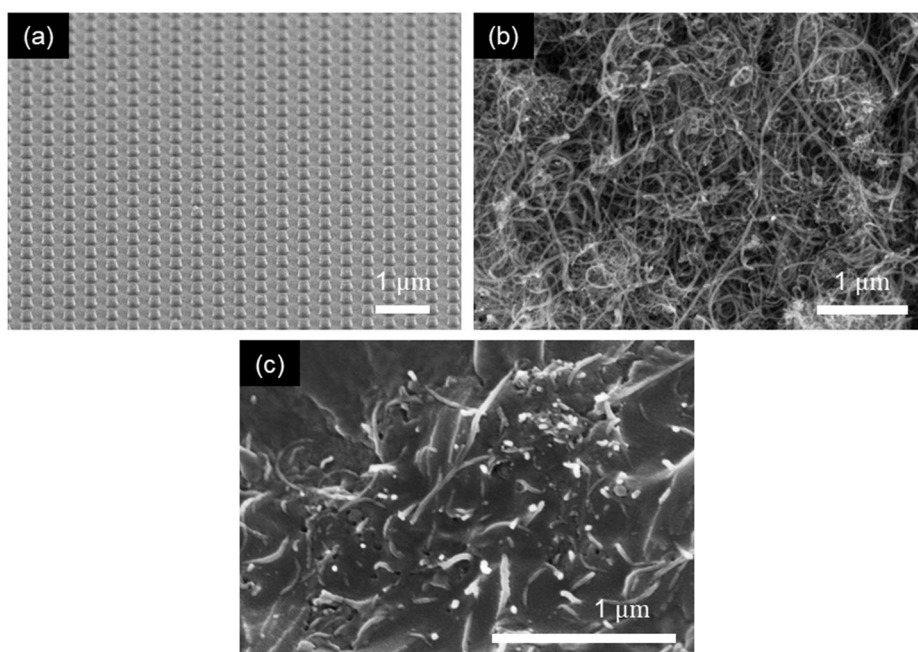


**Figure 3.4.9.** Topological observation of the CP sample by using SEM. (a) Side view of the nanocomposite pattern array at a relatively low magnification. Morphology of the (b) employed CNTs and (c) embedded CNTs in the matrix.

### 3.4.4.3. Thermomechanics analysis

Thermomechanical characteristics of the samples were investigated by running a dynamic mechanical thermal analysis (DMTA) machine. **Figure 3.4.10(a)** shows the thermomechanical properties of the IP and CP samples at the temperature range from -20 to 100°C. Embedding CNTs increased the storage modulus ( $E'$ ) by 2 times. When compared with the modulus drop of the IP sample (*i.e.*, around 2000 MPa), a relatively large reduction in modulus was found in the graph of the CP sample (*i.e.*, around 4250 MPa) and it could reinforce the capability for shape memory and recovery [253]. Glass transition temperature ( $T_g$ ) of the CP sample was lowered from 46°C (IP) to 40°C (CP). Addition of CNTs increases thermal conductivity of materials, leading to rapid heat transfer across specimens [268]. The SMCPA/CNT composites are suitable materials for developing bio-based instruments due to their appropriate mechanical and thermodynamic properties, such as high modulus drops and shape recovery capability at body temperature.

Cyclic shape memory experiments were conducted to obtain stress-strain-temperature (SST) curves by using the DMTA machine (see the solid line in **Fig. 3.4.10(b)**). The IP and CP specimens were subjected to this experiment. Details of the test method are presented in Section 3.2.2. The specimen was deformed to 3% compressive strain at 40°C (i→ii) and cooled to 0°C (ii→iii). Stored strain energy maintained the deformed shape even after the applied stress was removed (iii→iv). Gentle heating triggered the shape restoration with over 90% shape recovery ratio. Remote shape recovery was also possible by irradiating the microwave in just 1 second, due to the joule heating phenomenon by CNTs.

Theoretical shape memory behavior was demonstrated by performing numerical simulation with a hyperelastic neo-Hookean model, which uses entropic elastic energy [194]. By applying thermomechanical material parameters, the theoretical SST curve was obtained as the dot line in **Fig. 3.4.10(b)**. Inconsistency between the two curves in the cooling and heating steps originates from the assumption that phase transition is linearly proportional to the glassy state fraction ( $\alpha$ ) according to the temperature change [228]. Also, some errors could be caused by the fact that the neo-Hookean model cannot take into account viscoelastic properties of materials. However, the numerical modeling works quite well with little error in our cases.

A similar simulation was carried out at nanoscale by using the unit cells constructed

based on the real topology of the nanocomposite pattern arrays on the CP sample surface. **Figure 3.4.11** displays von Mises stress contours during the shape memory-recovery cycle of the simulation. The nanopatterns were compressed up to 55 nm at 40°C in the loading step (i→ii), where the deformation energy was saved as an entropy, the Helmholtz potential. The cooling step (ii→iii) generated glassy regions in the pattern. The following unloading step did not trigger the shape recovery since the stored elastic entropy at high temperature could not overcome the increased stiffness. The deformed patterns restored their original shape by changing the material from glassy to rubbery states. From the simulation, the stress distribution in the nanocomposite pattern could be visualized numerically and the shape memory behavior at nanoscale was explained theoretically.

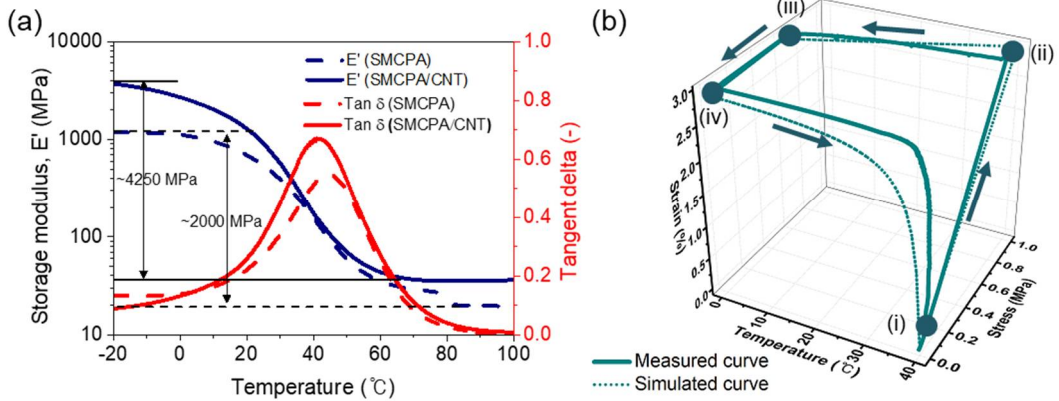


**Figure 3.4.10.** Shape memory behavior of the samples. (a) Thermomechanics of the IP and CP samples. (b) Characterized SST curves of the CP sample.

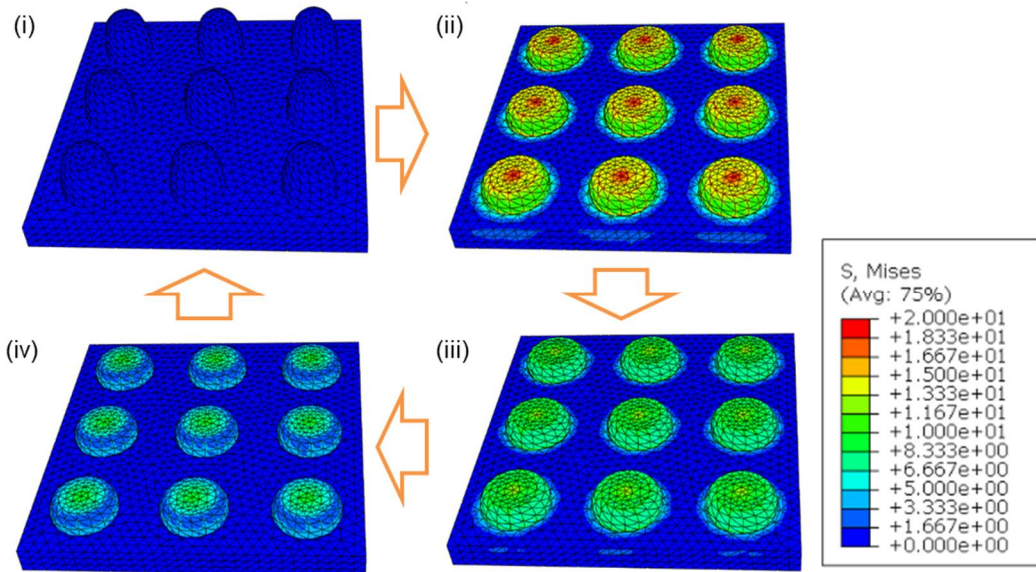


**Figure 3.4.11.** Numerical simulation results of the SMCPA/CNT nanocomposite patterns; (i) the initial state, (ii) the deformed state after heating up to 40°C, (iii) the cooled state by 0°C, (iv) the unloaded state, and (iv→i) the recovery of a shape of the patterns.

#### 3.4.4.4. Enhanced current transfer

A lab-made touch sensor circuit was employed to examine the current transfer performance in a biometric system. Schematic illustration of the circuit is shown in **Fig. 3.4.12(a)** and the relevant configuration is provided in Section 3.4.2. While supplying a voltage to the circuit in contact with a finger, the returning current from body was measured.

Before measuring the return current, electrical conductivities of the samples were measured by using a 2-point-probe method. The electrical conductivity is an inverse value of electrical resistance, *i.e.*, electrical impedance. **Figure 3.4.13** shows that addition of 1 wt% CNTs into the SMCPA matrix results in an increase of 8 orders of magnitude in the conductivity;  $1.06 \times 10^{-10}$  S/m for IB,  $2.16 \times 10^{-11}$  S/m for IP,  $2.5 \times 10^{-3}$  S/m for CB, and  $1.0 \times 10^{-3}$  S/m for CP. This trend accords with the electrical conductivity of polymer/CNT composites reported in the literature when a percolated network of CNTs is successfully formed [267,269]. The patterned samples (IP and CP) exhibit a relatively lower electrical conductivity than that of the bare samples (IB and CB). When measuring electrical conductivity of the patterned samples, the measuring tip of the multimeter contacted only the top of the patterns. Therefore, the contact area of the measuring tip on the nanopatterned surfaces was much smaller than that of the bare sample. This resulted in a decrease in the measured current flow between the device and the sample as discussed in the reference [267].

On the other hand, a different phenomenon was found in the biometric experiment since a lipid layer of skin filled the gaps between the patterns. The lipid layer before and after touching the pad was identified by using an alpha-step profiler as shown in the right-hand side of **Fig. 3.4.12(a)**. This lipid layer over the nanopattern can serve as an electrical impedance matching layer for high electrical current transmission. The current flow can be directed to the normal direction of the patterns, avoiding loss at the interface between the two media.

**Figure 3.4.12(b)** shows the experimental results for biometric sensing. Since the IB and IP samples are not conductive, they cannot be used as a constituent material of the sensing pad. For the CB sample embedded with CNTs, the current value was measured as  $169.3 (\pm 39.3) \mu\text{A}$ . Furthermore, the current of the CP sample with nanocomposite pattern arrays was estimated as  $336.4 (\pm 30.3) \mu\text{A}$ , which is about twice as high as that of the CB



sample.

Several mechanisms can be speculated to understand these experimental results based on nano-effects. The first mechanism is the enlarged specific surface area of the nanoscale patterns. This feature can significantly reduce the interfacial contact resistance between the two media. The second mechanism is orientation of CNTs in the patterns. Although the orientation of CNTs cannot be observed clearly, the FIB test confirms the presence of CNTs within the nanopatterns. The shear stress developed by the resin flow into the nanoholes during the filling step could align the CNTs unidirectionally in the patterns [267]. The third mechanism is the impedance matching phenomenon that causes the current to drift toward the patterns. It is deduced that this operation enabled efficient transmission of the current to the biometric device.

All potential mechanisms could not be proved experimentally in this study. Furthermore, it is not clear which one is the major mechanism among them. The nanoscale phenomena, *e.g.*, moth eye effect, have been reported mainly in the theoretical perspective. It has failed to provide an experimental basis about the nanoeffect. Therefore, numerical analysis on nanoelectronic modeling was performed and the results are discussed in Section 3.4.4.5 to present a plausible rationale of the results obtained by the experiments.

The hypothesis about the nano-effect driving function was supported by the current measurement according to the shape change of the nanopattern (**Fig. 3.4.12(c)**). After deformation of the pattern, the current value was reduced to 67% of the original value of CP, *i.e.*,  $227.1 (\pm 36.9) \mu\text{A}$ . The deformation of the nanopatterns greatly reduced the interfacial area between the finger and the sample. In addition, directionality of the composite patterns was weakened as the height decreased to about 55 nm, resulting in a decrease in the focusing ability of the patterns. The degree of CNT alignment in the nanocomposite patterns also decreased due to the lowered pattern height. The degraded current sensing capability could be recovered to the original level ( $323.6 (\pm 28.7) \mu\text{A}$ ) after gentle heating at body temperature.

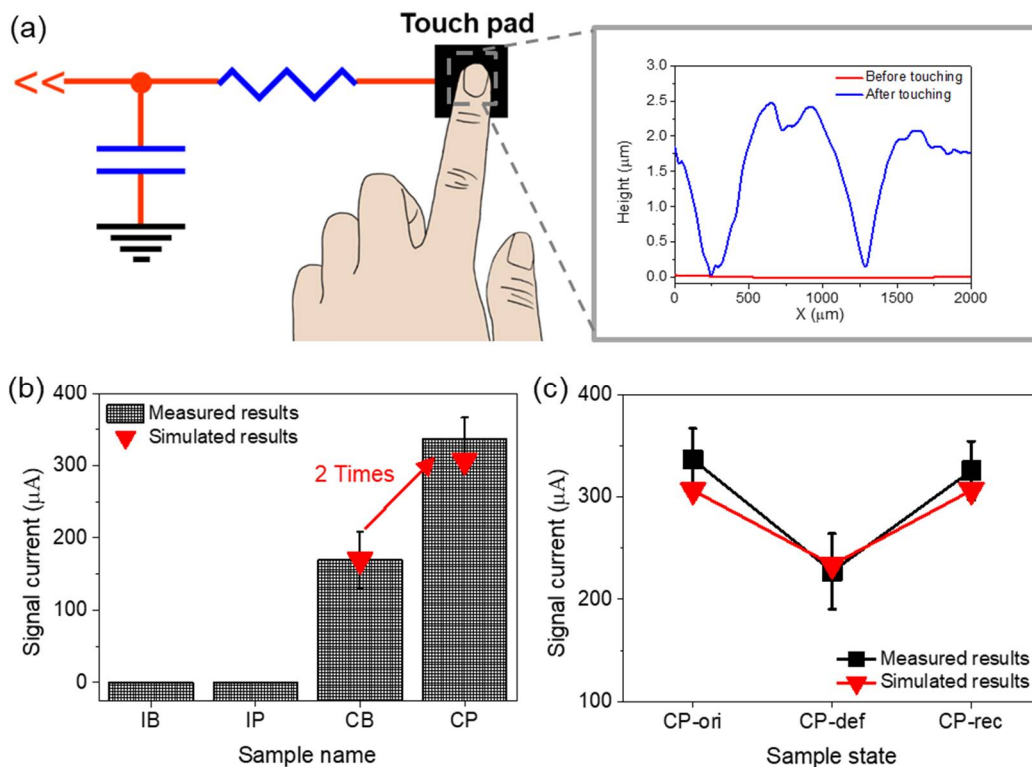


**Figure 3.4.12.** Experimental results of biometric sensing. (a) Schematics of the circuit employed to measure electric signal current passing through the touch pad. The right-hand side figure shows alpha-step profiles before and after touching. (b) Measured and simulated signal current for the IB, IP, CB, and CP samples. (c) Measured signal current according to the shape change of the nanopatterns.

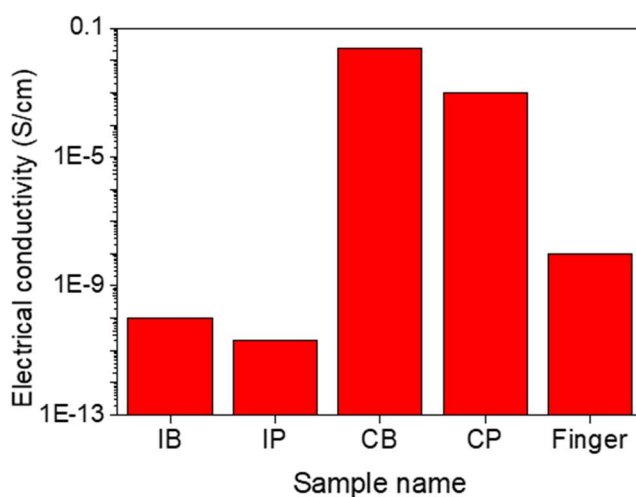


**Figure 3.4.13.** Measured electrical conductivities of the samples and a finger.

### 3.4.4.5. Nanoelectronic modeling

Numerical analysis was performed to verify that the improved current transfer was induced by the nanopatterned structure (**Fig. 3.4.14**). It was assumed in the simulation that the impedance matching arises only from the nanopattern array. Three-dimensional unit cells were created to model the interface between the finger and the touch sensor pad (**Fig. 3.4.2**).

The current conservation equation was solved with boundary conditions on the unit cells. **Figure 3.4.14(a)** shows the normalized current density ( $J_{nor}$ , A/m<sup>2</sup>) and the current density field ( $\vec{J}$ ), which are represented with color contours and white arrows, respectively. In the CB unit cell (**Fig. 3.4.14(a), (i)**), both  $J_{nor}$  and  $\vec{J}$  are not distorted at the interface between the two domains. However, the current density field vectors focus on the nanopattern (**Fig. 3.4.14(a), (ii)**). **Figure 3.4.14(c)** shows the electric charge density ( $\rho_q$ , C/m<sup>3</sup>) fields formed in the unit cells. It was found that an enormous amount of electric charge is accumulated nearby the top of the nanopattern in the CP unit cell. This nanoelectronic phenomenon allows electric current to pass relatively easily through the interface between the two media. The current concentration is an important mechanism that permits more current to be delivered with low loss.

A volume fraction of the nanopattern is sufficiently small in the entire CP domain. Thus, the improved current transfer is estimated to be due to the nanopattern effect rather than the increased amount of a conductive material. When looking at the deformed CP unit cell (**Fig. 3.4.14(a), (iii)**), the current field vector is directed toward the pattern.

The theoretical current transfer efficiency was quantitatively analyzed from the simulation results by calculating the current passing through the unit cell ( $I_{cal}$ ). The current value through the unit cell was calculated by integrating the normalized current density ( $J_{nor}$ , A/m<sup>2</sup>) over the bottom surface of each unit cell (**Fig. 3.4.14(b)**).  $I_{cal}$  of the CP unit cell was calculated as 306.3  $\mu$ A. This value is in good agreement with the measured value of 323.6  $\mu$ A. Also, the other  $I_{cal}$  values also matches with measured results; 169.6  $\mu$ A for the CB unit cell and 233.6  $\mu$ A for the deformed CP unit cell. Although the orientation of CNTs and the interfacial resistance were not considered in modeling, the simulation results successfully demonstrate that the nanoeffects of both CNTs and the nanopattern can provoke synergetic contribution to the enhancement of the current transfer for high-quality biometric information sensing.

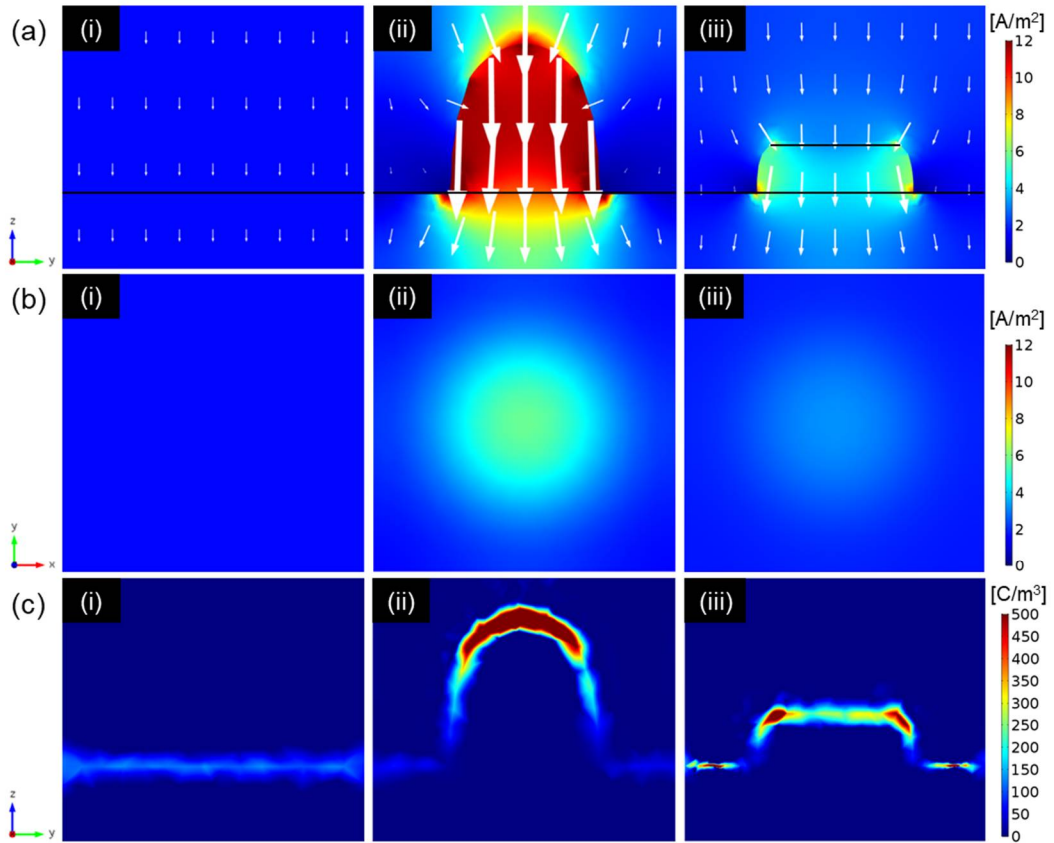


**Figure 3.4.14.** Numerical simulation results of the impedance matching nanostructure. The normalized current density fields in (a) yz cut-plane and (b) at bottom. (c) The charge density fields in yz cut-plane; (i) the CB, (ii) original CP, and (iii) deformed CP unit cells.

### **3.4.5. Conclusions**

In this section, the metasurface arrayed with CNT embedded nanocomposite patterns was produced to develop the advanced biometric sensing system by using the synergetic nanoeffect. The presence of CNTs in the nanopattern was confirmed experimentally by using the XPS analysis and the FIB machine. The embedded CNTs contributed to the enhancement of the mechanical strength of the patterns. The CNT embedded nanocomposite patterns were engineered by using the SMCPA as a smart material, which can recover the original shape at body temperature. This performance could improve the sustainability of nanopatterns and their nanoeffects. The magnitude of the transferred current was increased twice due to the nanocomposite patterns on the touch pad surface. The electrical impedance matching at nanoscale, the metasurface property developed in this study, was understood through the theoretical modeling based on nanoelectronics. The metasurface developed in this study is expected to inspire the nanocomposite field and can be applied to various advanced biometric devices requiring high transfer efficiency of electric energy.

### 3.5. Summary

In this chapter, the nano-architected shape memory polymeric metasurfaces were proposed from synthesis of basic materials, numerical modeling, fabrication, to experimental characterization. The synthetic strategy for shape memory copolyacrylate (SMCPA) capable of adjusting the transition temperature to operating temperature was developed in Section 3.2. Among the synthesized SMPs, S-MMA/BMA which can recovery the original shape at body temperature was applied to two nanotechnological applications. In Section 3.3, the antireflective metasurface composed of SMPAC nanopatterns were engineered and various experiments and theoretical studies were performed to examine the sustainability of the nanofunctions. In Section 3.4, nanoscale impedance matching was materialized by producing the biometric metasurface consisted of SMCPA/CNT nanocomposite patterns arrayed on the sample surface. The applicability to advanced biometric devices was confirmed experimentally and theoretically. As a follow-up study, it is expected that the synthesis of optimized SMPs will further increase the application range of SMP in other environments. In addition to the antireflection and biometrics, it is anticipated to be applied to a variety of nanotechnologies, particularly for bioengineering applications.

# Chapter 4.

## Polymeric Poroacoustic Meta-absorbers

### 4.1. Overview

The polymeric poroacoustic meta-absorbers are proposed in this chapter, which implement extraordinary sound absorption performance beyond the density limitation by modulating microcellular structures. Under a general sense, the performance of sound absorbing materials is determined by the thickness and density of the material. Satisfactory sound absorption with a low mass density foam is one of the biggest goal of researchers engaged in NVH (noise, vibration, and harness) technology.

In Section 4.2, the polyurethane (PU) foam with optimum cell size was designed, fabricated, and analyzed, which reveals the superior sound absorbing performance at low frequencies. The optimum cell size of PU foams was predicted by multiscale poroacoustics simulation. The PU foam with the optimum cell size was fabricated by using an ultrasonic foaming method to adjust the microcellular structure. Mechanical activation of the reaction resin was used only to manipulate the internal structure of the PU foam without any further treatment. It was found from the measured and simulated sound absorption coefficients that the modulation of cell diameter can adjust the major operating frequency of the sound absorbing foams regardless of macroscopic parameters, as a poroacoustic meta-property. The cell size optimization strategy is expected to break the stereotypes of existing industrial sound absorbing materials and pave the way for the development of advanced sound absorbing materials.

The purpose of Section 4.3 is to render a poroacoustic meta-absorber that exhibits satisfactory sound absorbing performance to alleviate the limitations of mass density. The relationship between cell openness of the PU foam and sound absorption behavior was demonstrated both theoretically and experimentally. By controlling the rheological properties of the resin in the foaming reaction, the cell openness of the PU foam could be

experimentally manipulated to a desired range. The fabricated PU foam with the best cell openness showed outstanding sound absorption performance among samples and the performance was even better than that of the foam with double mass density. The cell openness control technology will pave a more efficient and economical way to manufacture low mass density sound absorbing foams.

In Section 4.4, novel syntactic hybrid foams (SHFs), showing superior sound absorption with low density, are suggested by designing hollow microbeads embedded open cell PU foam. Numerical simulation was carried out to predict sound absorbing performance by employing periodic unit cells representing microstructures of a bare foam (BF) and SHFs. It was found from the simulation that the sound damping performance of SHFs was improved significantly by a detoured sound propagating path provoked by the embedded microbeads. The predicted sound absorption performance of the SHFs was even superior to that of the bare foam with double density. Furthermore, heat transfer and structural analysis showed that the SHFs can provide high thermal insulation and mechanical robustness. It is anticipated that the designed hybrid microstructure is utilized to develop next generation sound absorbing materials with outstanding sound absorption, thermal insulation, and mechanical stiffness.



## 4.2. PU foam with optimum cell size

### 4.2.1. Introduction

There are many issues to improve the driving conditions for better quality of life. Among them, noise pollution is a critical problem in daily life [270–273]. In order to solve this problem, many sound proof materials and systems have been developed over a long period of time. There are two kinds of sound proof materials; sound absorption materials and sound insulation materials. The insulation material is a massive material having high surface density [126–128] and reflects the incident sound waves resulting high transmission loss. Unlike the insulation material, the sound absorption material is a lightweight material with porosity higher than 90% [274].

The absorption material has two major sound damping functions; “visco-inertial and thermal damping” in a fluid domain (air) and “viscoelastic damping” in a solid domain (*i.e.*, a polymeric part) [275,276]. For the visco-inertial and thermal damping, acoustic waves propagating in a porous media are mainly dissipated by viscous friction on the interconnected pores and thermal heat exchange at the solid-fluid boundary [277–279]. Theoretical models reflect these mechanisms with complex effective bulk density ( $\rho(\omega)$ ) and effective bulk modulus ( $K(\omega)$ ). In the aspect of the viscoelastic damping, transferred acoustic waves from the air to the solid are attenuated by molecular friction in the vibration mode [280,281]. According to these mechanisms, energy of offensive noise transforms into heat loss.

Porous polymeric foams are widely used for sound absorption of buildings, automobiles, and aircrafts [282,283]. A polyurethane (PU) foam is the most frequently employed material in industrial areas because of its light weight, low cost, and good processability. In the manufacturing process of the PU foam, the reactant A (consisting of polyol, blowing agent, catalyst, surfactant, *etc.*) and reactant B (consisting of isocyanate) are mixed at high speed and then injected into a mold having a certain shape [284–286]. Two chemical reactions occur simultaneously in the foaming process; a gelling reaction and a blowing reaction. From the gelling reaction, the hydroxyl (-OH) group in the polyol and the isocyanate (-NCO) group in the isocyanate cause a covalent chemical bond reaction

to link the polymeric chains with a urethane group. The blowing reactions are classified into chemical and physical blowing reactions. In the former reaction, the chemical foaming agent (*e.g.*, water) reacts with the isocyanate functional group, generating carbon dioxide gases in the reaction resin. The carbon dioxide gases yield nuclei when they contain sufficient energy. The resulting nuclei grow into micro-sized bubbles. In the process of physical blowing, the physical blowing agents dissolved in the polyol (*e.g.*, hydrofluorocarbons, cyclopentane) act as a nucleus after forming clusters by triggering phase changes of the dissolved gas under heating or pressure drop processes.

Damping of low frequency noise has received considerable attention in many industrial sectors because conventional sound absorbers do not perform well at low frequencies [287–291]. Moreover, there are only two solutions for improving low frequency sound absorption, which have limitations for industrial applications; an increase of foam mass density [292,293] or a change of foam thickness [294]. So, microstructure manipulation is considered as the best strategy to improve or optimize acoustic damping characteristics without changing other material properties.

Several strategies for the manipulation of microcellular structure of PU foams have been reported. Composite foams with nanoparticles is one of the strategies to promote heterogeneous nucleation [292,295]. If nanoparticles are suspended in a polymeric matrix during a foaming reaction, the critical energy required for bubble formation is reduced at the particle surface due to the low surface tension [296]. The other methodology is an ultrasonic foaming method [297]. The effect of ultrasonic waves on the reaction resin of polymeric foams have been investigated for irradiation period, timing, and magnitude of the waves [298–302].

Theoretical modeling has been performed to predict and investigate sound absorption performance of porous materials [275,303,304]. Recently, multiscale poroacoustics modeling based on a finite element method [305–307] was reported to consider not only macroscopic parameters but also microstructural features. For microscale simulation, a periodic unit cell (PUC) is constructed by considering a real geometry of samples. Poroacoustics parameters for macroscale simulation (*e.g.*, flow resistivity) are obtained by solving two flow problems for PUC. Sound absorption coefficient is calculated by an analytical or numerical method with such theoretical models as diphasic models (*e.g.*,

Biot's theory [280]) and motionless skeleton models (*e.g.*, Johnson-Champoux-Allard model [278,279]).

In this section, the PU foam with optimized cell size is demonstrated with theoretical design and experimental fabrication of that. The optimum cell diameter of the PU foam with  $80 \text{ kg/m}^3$  density and 2 cm thickness was predicted from the simulation result. Cell size modulation of the PU foam was conducted by using the ultrasonic foaming method while controlling the magnitude of the irradiated waves. A B&K impedance tube was used to empirically measure sound absorption coefficients of the samples and additional analyses for noise damping evaluators were performed to assess the sound absorption performance in a multifaceted way.

## **4.2.2. Experimental**

### **4.2.2.1. Materials**

NIXOL SA-120 (denoted to Reactant A, KPX Chemical, Republic of Korea) is composed of polyether polyol (~94 wt%), water (~2.3 wt%), surfactants, and catalysts. SUPRASEC® 2527 (Reactant B, Huntsman Holland BV, Netherlands) is an isocyanate-based compound composed of diphenylmethane 4,4'-diisocyanate (MDI, ~50 wt%) and isocyanic acid (~20 wt%), and other additives. AKO-HM207K (Akochem, Republic of Korea) was used as a releasing agent of PU foams for easy separation from a mold.

### **4.2.2.2. PU foaming method**

A 5:2 ratio of NIXOL SA-120 and SUPRASEC® 2527 was mixed at a high speed of about 3000 rpm for 5 seconds by using a digital overhead stirrer HS-100D (WiseStir®, Germany). After the high speed blending, ultrasonic waves were irradiated for 7 seconds at 20 kHz frequency. Ultrasonication power varied from 0%, 37% to 75% of the maximum output of 750 W and each sample was labeled 80-1, 80-2 and 80-3. The ultrasonicated resin mixture was inserted into the pre-heated mold (at 50°C) of 15 x 15 x 2 cm<sup>3</sup>. After pouring the mixture, the mold was sealed with a weighted cover to produce samples with identical and precise dimensions. The fabrication of PU foams was completed after curing the mixture in the mold for 15 minutes.

### **4.2.2.3. Characterizations**

Microstructures of cells and interconnecting pores were observed by using a field emission scanning electron microscope (FE-SEM, JEOL, Japan). The fabricated PU foams were lyophilized to maintain the microcellular structure by using liquid nitrogen and then cut into specimens. Each cell diameter was estimated by averaging the long and short axes lengths of the cells, and the total average cell diameter of each sample was evaluated as the average diameter of all cells found in the FE-SEM images. Diameters of the interconnecting pores and the total average value of interconnecting pores were also calculated by using the same method. Cell number density, defined as the number of cells per mm<sup>2</sup>, was estimated by dividing the number of cells in the captured SEM images by the total area of image.

Normal incidence absorption coefficient of the samples was measured by using a B&K two-microphone standing wave tube type 4206 (29 mm diameter) shown in **Fig. 4.2.1(a)** according to ASTM E1050 [308]. The sound pressure at two microphones is measured and reflection coefficient ( $R$ ) is calculated by employing the transfer equation which governs the sound pressure ratio between the two microphones. Finally, the absorption coefficient ( $\alpha$ ) is obtained by the equation of  $\alpha = 1 - |R|^2$ .

Flow resistivity is one of the parameters for evaluating the acoustic performance such as sound absorption coefficient and transmission loss. Flow resistance is defined as the ratio of the air pressure differential to the steady state air velocity. The flow resistivity is calculated as the flow resistance per unit material thickness,  $R_f = (p_2 - p_1)S/vh$ , where  $v$  is the volumetric airflow rate passing through the material in  $\text{m}^3/\text{s}$ ,  $S$  is the cross sectional area of the material, and  $h$  is the thickness of the material. The flow resistivity has the unit of  $\text{N}\cdot\text{m}^4\cdot\text{s}$  or MKS Rayls/m. The flow resistivity of porous materials was measured by using the equipment shown in **Fig. 4.2.1(b)** according to ISO 9053.

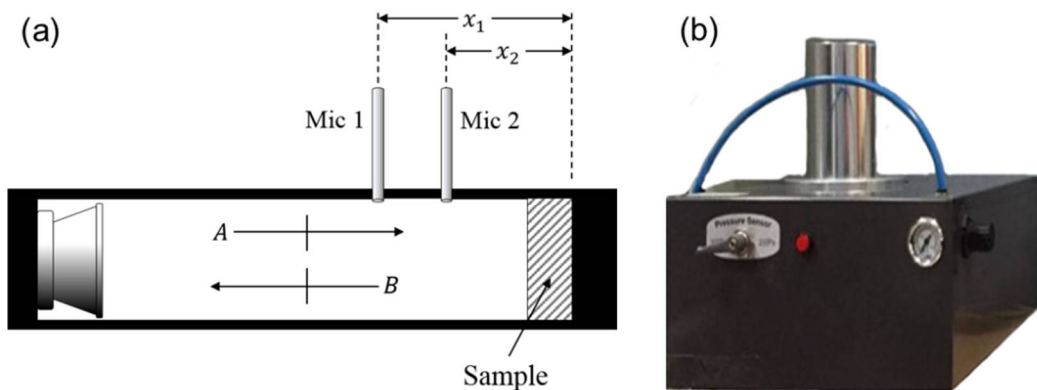


**Figure 4.2.1.** Acoustic characteristics measurement instruments. (a) A schematic figure of the B&K impedance tube for measuring sound absorption coefficient. (b) A photo of the device for flow resistivity measurement.

### 4.2.3. Numerical analysis

#### 4.2.3.1. Unit cell modeling method

Unit cells were constructed by using a CATIA program (computer aided three-dimensional interactive application ver. 5.18, Dassault Systèmes, France) by mimicking an actual microstructure of the foam with average cell diameter, average diameter of interconnecting pores, and mass density (**Fig. 4.2.2**). Tetrakaidecahedron has been known as the most suitable structure for resembling the microgeometry of polymeric foams [309–311]. In recent papers, a method for structural modeling of a high density foam has been developed and used in this study to create solid walls with a hole in the center of each face to consider the narrow interconnection pores [275,312].

The diameter of the tetrakaidecahedron ( $D$ ) was defined as the perpendicular distance between the opposite sides of squares and set to be the average cell diameter of each sample. The length of ligaments ( $L$ ) was automatically calculated as  $D = 2\sqrt{2}L$ . The average interconnecting pore diameter ( $I$ ) was used as the diameter of the hole on each face having an approximately 1/7 size of the average cell diameter. The porosity was fixed to be 92% coinciding with the mass density of the foam,  $80 \text{ kg/m}^3$ , and it was properly adjusted by manipulating the diameter of balls ( $R$ ), diameter of ligaments ( $r$ ), and thickness of solid walls ( $t$ ). 15 tetrakaidecahedron were combined to construct a cluster representing a porous structure of the unit cells (**Fig. 4.2.2(a)**). After imparting a periodic hexahedron, periodic unit cells (PUCs) were built by subtracting the combined structure from the hexahedron by using Boolean operation in the CATIA program (**Fig. 4.2.2(b)**).

All PUCs with various cell diameters (100, 200, 400, 600, 800, 1000, and 1200  $\mu\text{m}$ ) were constructed by executing Scaling operation which changes the size of PUCs with the same aspect ratio. The constructed PUCs were used for the simulation with periodic boundary conditions on the lateral faces. Free tetrahedron meshes of 264867 domain elements, 61286 boundary elements, and 9004 edge elements were put into each PUC (**Fig. 4.2.2(c)**). In order to reflect the mass density of the fabricated foam in the PUC, the volume fraction of empty space was set to be 0.92 corresponding to an  $80 \text{ kg/m}^3$  foam.

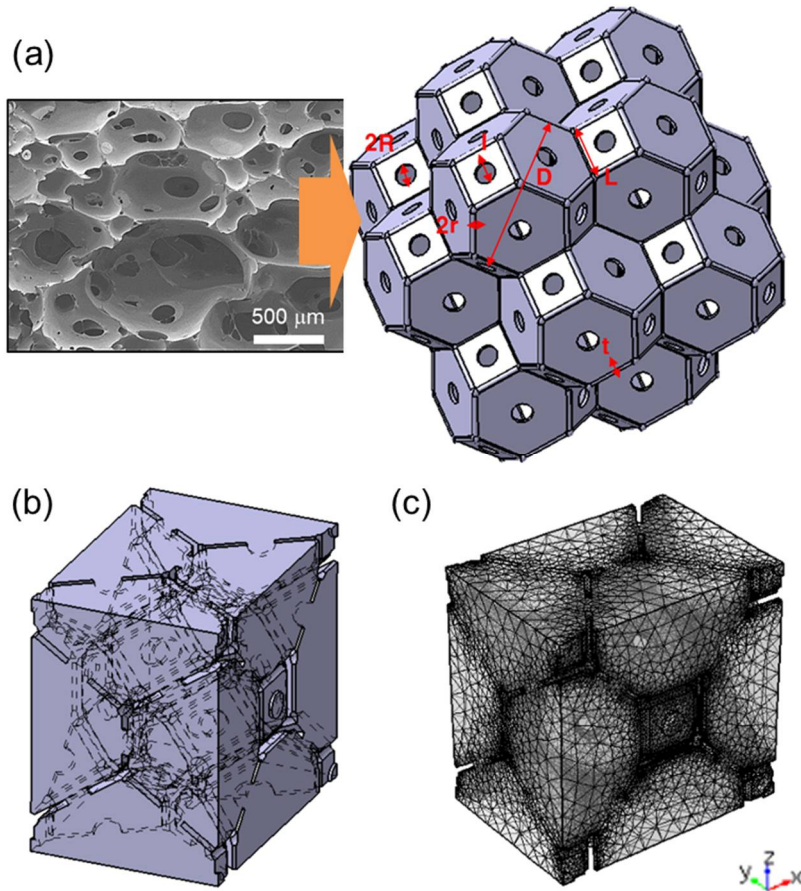


**Figure 4.2.2.** Construction process for periodic unit cells (PUCs). (a) A cluster of combined tetrakaidecahedron mimicking the real topology of a fabricated PU foam. (b) Constructed PUC. (c) Free tetrahedron meshes generated in fluid domain of the PUC.

#### 4.2.3.2. Multiscale poroacoustics simulation method

Numerical simulation for predicting sound absorption performance was carried out by using a multiscale poroacoustics simulation method which consists of a microscale flow analysis and a macroscale acoustical analysis [275,304,306]. The purpose of this simulation is to understand the effect of PU foam cell size on sound absorption performance. A commercial finite element program, COMSOL Multiphysics, was employed in this study.

In the microscale analysis, poroacoustics parameters for Johnson-Champoux-Allard (JCA) model were calculated by solving two flow problems in the constructed periodic unit cells (PUCs). In this analysis, the viscoelastic damping due to deformation and vibration of the PU solid frame was ignored since the JCA model is a semi-empirical equivalent fluid model assuming rigid frame acoustics. The calculated parameters, *i.e.*, flow resistivity ( $R_f$ ), tortuosity ( $\tau_\infty$ ), and characteristic lengths ( $L_v$  and  $L_{th}$ ), represent the specific geometric feature of microcellular structure of each sample.

After generating free tetrahedral meshes in PUCs (**Fig. 4.2.2(c)**), Stokes' equation is used with boundary conditions for solving a viscous flow problem as [275,313,314]

$$\mu \nabla^2 \mathbf{v} - \nabla p = \mathbf{g} \text{ in } \Omega_f \quad (4.2.1)$$

$$\nabla \cdot \mathbf{v} = 0 \text{ in } \Omega_f \quad (4.2.2)$$

$$\mathbf{v} = 0 \text{ on } \Omega_{sf} \quad (4.2.3)$$

, where  $\mu$  is the viscosity of air,  $p$  is the pressure,  $\mathbf{v}$  is the velocity field,  $\Omega_f$  is the fluid domain,  $\mathbf{g}$  is the constant vector field of pressure gradient throughout the fluid domain, and  $\Omega_{sf}$  is the boundary of the solid-fluid domain. The velocity vector field is obtained from the solution of **Eqns. 4.2.1-3**. The permeability field ( $\mathbf{k}_0$ ) is calculated by the definition as  $\mathbf{k}_0 = -\mu \mathbf{v} / |\mathbf{g}|$ , where  $\mathbf{g}$  is the pressure gradient which is constant throughout the whole fluid domain of PUC. Flow resistivity of PUC is defined as  $R_f = \mu / (\langle \mathbf{k}_0 \rangle_f \cdot \epsilon_p)$  where  $\epsilon_p$  is the porosity.  $\langle \mathbf{k}_0 \rangle_f \cdot \epsilon_p$  is the permeability of a porous medium, which is calculated as the product of  $\epsilon_p$  and the averaged value of permeability field ( $k_0$ ) of PUC considering the whole fluid domain.

In the multiscale poroacoustics modeling, the inertial flow problem has been replaced



by an electrical conduction problem given by the Laplace equation due to its theoretical similarity between the two equations. The inertial flow behaves like incompressible-inviscid ideal flow of electric conduction governed by Laplace problem. Equations of the electrical conduction (Laplace problem) with boundary conditions are defined as

$$\mathbf{E} = -\nabla\varphi + \mathbf{e} \text{ in } \Omega_f \quad (4.2.4)$$

$$\nabla \cdot \mathbf{E} = 0 \text{ in } \Omega_f \quad (4.2.5)$$

$$\mathbf{E} \cdot \mathbf{n} = 0 \text{ on } \Omega_{sf} \quad (4.2.6)$$

, where  $\mathbf{E}$  is the scaled electric field,  $\mathbf{e}$  is the unit vector field, and  $\nabla\varphi$  is the fluctuating part with the scalar field  $\varphi$ . The scaled electric field is obtained from the solution of **Eqns. 4.2.4-6**. The scaled electric field obtained from the solution of **Eqns. 4.2.4-6** was utilized to evaluate tortuosity factor ( $\tau_\infty$ ) and viscous characteristic length (VCL), defined as  $\tau_\infty = \langle \mathbf{E}^2 \rangle_f / \langle \mathbf{E} \rangle_f^2$  and  $\text{VCL} = L_v = 2 \int_{\Omega_f} \mathbf{E}^2 d\Omega_f / \int_{\Omega_{sf}} \mathbf{E}^2 d\Omega_{sf}$  [304]. Porosity ( $\epsilon_p$ ) and thermal characteristic length (TCL) were calculated from the volume ratio of the solid/fluid domain and the relationship of  $\text{TCL} = L_{th} = 2 \int_{\Omega_f} d\Omega_f / \int_{\Omega_{sf}} d\Omega_{sf}$ .

By using the calculated poroacoustics parameters above, two frequency-dependent complex values, effective bulk density ( $\rho(\omega)$ ) and effective bulk modulus ( $K(\omega)$ ), were calculated from the JCA model equations as shown below.

$$\rho(\omega) = \frac{\tau_\infty \rho_f}{\epsilon_p} \left( 1 + \frac{R_f \epsilon_p}{i\omega \rho_f \tau_\infty} \sqrt{1 + \frac{4i\omega \tau_\infty^2 \mu \rho_f}{R_f^2 L_v^2 \epsilon_p^2}} \right) \quad (4.2.7)$$

$$K(\omega) = \frac{\gamma_f P_A}{\epsilon_p} \left[ \gamma_f - (\gamma_f - 1) \left( 1 + \frac{8\mu}{i\omega L_{th}^2 Pr \rho_f} \sqrt{1 + \frac{i\omega \rho_f Pr L_{th}^2}{16\mu}} \right)^{-1} \right]^{-1} \quad (4.2.8)$$

, where  $\rho_f$  is the density of air,  $\omega$  is the angular frequency,  $\gamma_f$  is the heat capacity ratio for air,  $P_A$  is the ambient pressure,  $Pr$  is the Prandtl number, and  $\mu$  is the viscosity of air.

Sound pressure fields affected by various sound absorbers with different

microstructures were numerically simulated by solving simple Helmholtz equation (S.H.E.) with the calculated complex values ( $\rho(\omega)$  and  $K(\omega)$ ) from **Eqns. 4.2.7-8**. A 2-D tube geometry was employed for the numerical simulation, which has the same dimension of the B&K impedance tube [315] used for measuring sound absorption coefficients (**Fig. 4.2.3**).

It was assumed that the air in the tube has linear elastic fluid properties. A perfectly matched layer (PML) was introduced at the top of the tube to theoretically implement an infinitely large air domain assuming no reflection from the top. Sound hard boundary conditions were applied to the bottom and the lateral surfaces of the tube. A foam domain was placed at the bottom of the tube with 20 mm thickness and 29 mm width, the same as the typical sample dimension [315,316]. The normal incident background pressure field under a plane wave condition was given in the tube as  $p_{inc} = \exp(-i(kx))$ , where  $p_{inc}$  is the pressure of incident wave and  $k$  is the wavenumber. The scattered pressure field ( $p_s$ ) by the introduced foam domain was obtained and the total pressure field ( $p_t$ ) was calculated from the definition of  $p_t = p_{inc} + p_s$ . The theoretical sound absorption coefficient ( $\alpha$ ) was calculated by  $\alpha = 1 - R^2$ , where  $R = p_s/p_{inc}$ , at the interface boundary between the air domain and the foam domain.

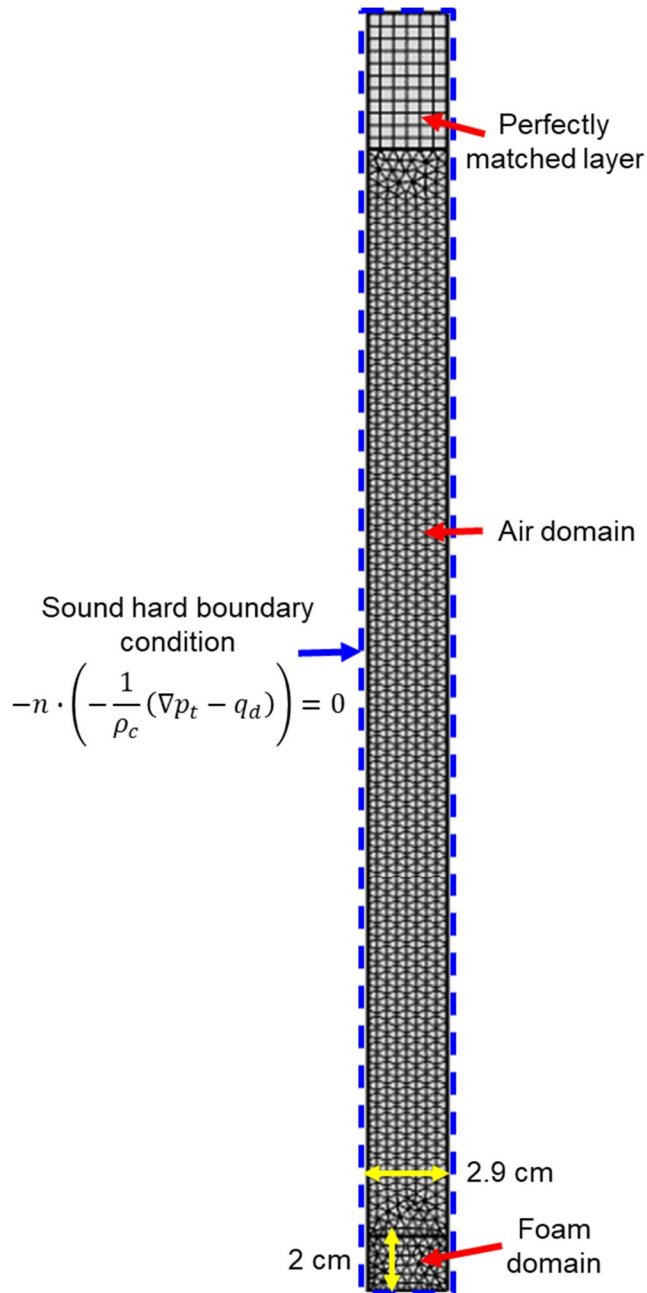


**Figure 4.2.3.** B&K impedance tube geometry used in the macroscale analysis.

## 4.2.4. Results and discussion

### 4.2.4.1. Theoretical analysis of optimum cell size

Multiscale poroacoustics modeling was employed to predict theoretical optimum cell size and understand the cell size effect for sound absorption performance. For each PUC, two transport problems were solved and the poroacoustics parameters were obtained as listed in **Table 4.2.1**. In the viscous flow problem, solid domains were assigned to the empty space of the PUCs and the remained region was set as the fluid domain. A uniform pressure gradient in z-direction, no-slip boundary conditions, and periodic boundary conditions were applied to the PUCs. As a simulation result, the scaled velocity field, in other words, the static viscous permeability field, was calculated by dividing the velocity profile by the pressure gradient and visualized with streamlines (**Fig. 4.2.4(a)**). The flow resistivity ( $R_f$ ) for each PUC was calculated from the simulation result of the viscous flow problem.

The scaled potential fields were calculated and visualized in **Fig. 4.2.4(b)** as a solution of the inertial flow problem. Viscous characteristic length (VCL,  $L_v$ ) and tortuosity ( $\tau_\infty$ ) were calculated by the equations as mentioned in the numerical method section. The VCL is a weighted hydraulic diameter related to energy damping of air flow in a complex porous medium. The energy damping is caused by viscous friction due to relatively narrower pathways than surrounding structures. Therefore, the tortuosity reflects the complexity of the path of sound propagation in the PUC. The tortuosity was calculated to be the same 1.94 for all PUCs because it depends only on the shape of the domain.

Effective bulk density ( $\rho(\omega)$ ) and effective bulk modulus ( $K(\omega)$ ) of each PUC were calculated by using the five poroacoustics parameters ( $\rho_f$ ,  $L_{th}$ ,  $L_v$ ,  $\tau_\infty$ , and  $\epsilon_p$ ) for the JCA model (**Eqns. 4.2.7-8**). The background and scattered pressure fields for acoustic waves from 0 to 6400 Hz were simulated and the representative results of 400  $\mu\text{m}$  PUC at 1000, 2000, and 4000 Hz are shown in **Figs. 4.2.5(a-c)**. From the simulation results, it was observed that the sound waves affected by the porous layer containing the 400  $\mu\text{m}$  PUC have a very low pressure field amplitude, especially at 2000 Hz, which is relatively lower than the sound pressure of the background pressure field.

Sound damping performance depending on cell diameter was confirmed by comparing the sound absorption coefficient curves (**Fig. 4.2.6**). All curves have a distinctly different

shape with respect to changes in cell size. Root mean square (RMS) values of sound absorption curves were evaluated for the quantitative comparison and plotted as a function of cell diameter (**Figs. 4.2.6(b-f)**).

Among them, the RMS value from 0 to 2000 Hz ( $\alpha_{\text{rms},2000}$ ) is the most significant parameter since it contains most of the low frequency noises generated by automobiles (**Fig. 4.2.6(b)**). From the curve, 400  $\mu\text{m}$  cell diameter was determined as the best cell diameter with a RMS value of 0.66. The reason why low frequency sound absorption performance drops in the PUC smaller than 400  $\mu\text{m}$  is that the surface impedance is excessively increased. The increased flow resistivity due to the very small microcellular structure hinders penetration of sound waves into the foam, which leads to an increase in the surface impedance. At the surface of the foam, most incident sound waves are reflected back to the original media rather than being transmitted internally. On the other hand, cell structures larger than 400  $\mu\text{m}$  cannot sufficiently attenuate acoustic energy because the flow resistance is not sufficiently high under the same tortuosity. Therefore, for noises in the frequency range from 0 to 2000 Hz, it is expected that the best performance of sound absorption will be achieved when the average cell diameter of the PU foam is controlled to about 400  $\mu\text{m}$ .

The RMS analysis in different frequency ranges was carried out to examine the cell size effect more extensively, as shown in **Figs. 4.2.6(c-f)**;  $\alpha_{\text{rms},1000}$  (from 0 to 1000 Hz),  $\alpha_{\text{rms},5000-6000}$  (from 5000 to 6000 Hz), and  $\alpha_{\text{rms},6400}$  (from 0 to 6400 Hz). It could be found in **Fig. 4.2.6(c)** that the optimum cell size is not always 400  $\mu\text{m}$ . The  $\alpha_{\text{rms},1000}$  values indicate that 200  $\mu\text{m}$  is the best cell size for the lower frequency range below 1000 Hz. Generally, the peak of sound absorption curves shifts to the lower frequency range as  $R_f$  and  $\tau_\infty$  increase [317]. For this reason, sound absorbing materials with smaller cell sizes can lead to higher sound absorption performance at lower frequencies. Meanwhile, **Figs. 4.2.6(d-f)** show that 400  $\mu\text{m}$  is the best cell size for  $\alpha_{\text{rms},5000-6000}$  and  $\alpha_{\text{rms},6400}$ , which represent the sound absorption performance in the high frequency range and the entire frequency range, respectively. Consequently, it could be figured out that the cell size inducing properly high  $R_f$  enables optimal sound absorbing performance except for in some cases.

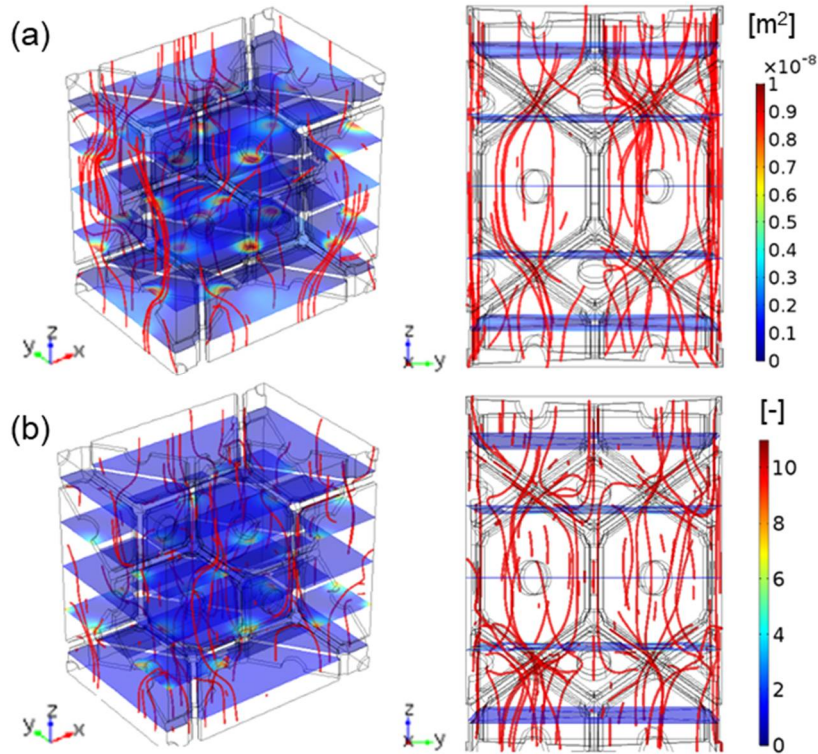


**Figure 4.2.4.** Simulation results for microscale flow analyses. (a) A scaled velocity field with streamlines as a solution of the viscous flow problem. (b) A scaled electric field with streamlines as a solution of the inertial flow problem.

**Table 4.2.1.** Calculated poroacoustics parameters for JCA model.

	80-1	80-2	80-3
Porosity, $\epsilon_p$ (-)	0.92	0.92	0.92
Flow resistivity, $R_f$ ( $N \cdot m^4 \cdot s$ )	6998	10467	16514
Tortuosity, $\tau_\infty$ (-)	1.94	1.94	1.94
Viscous characteristic length, $L_v$ ( $\mu m$ )	65	49	39
Thermal characteristic length, $L_{th}$ ( $\mu m$ )	219	169	135

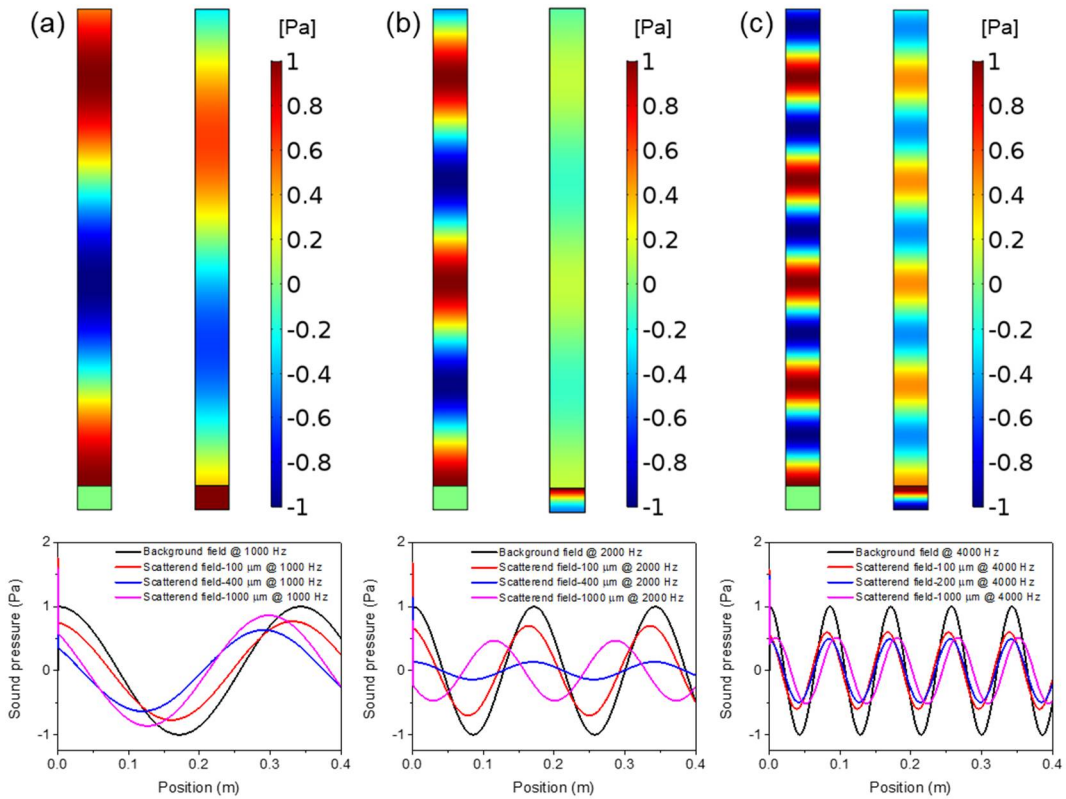


**Figure 4.2.5.** Simulated acoustic pressure fields for 400  $\mu\text{m}$  PUC, which are the results of macroscopic acoustic modeling (left: background sound field, right: scattered sound field): at (a) 1000, (b) 2000, and (c) 4000 Hz. The graphs below indicate sound pressure profiles in the tube for each case.

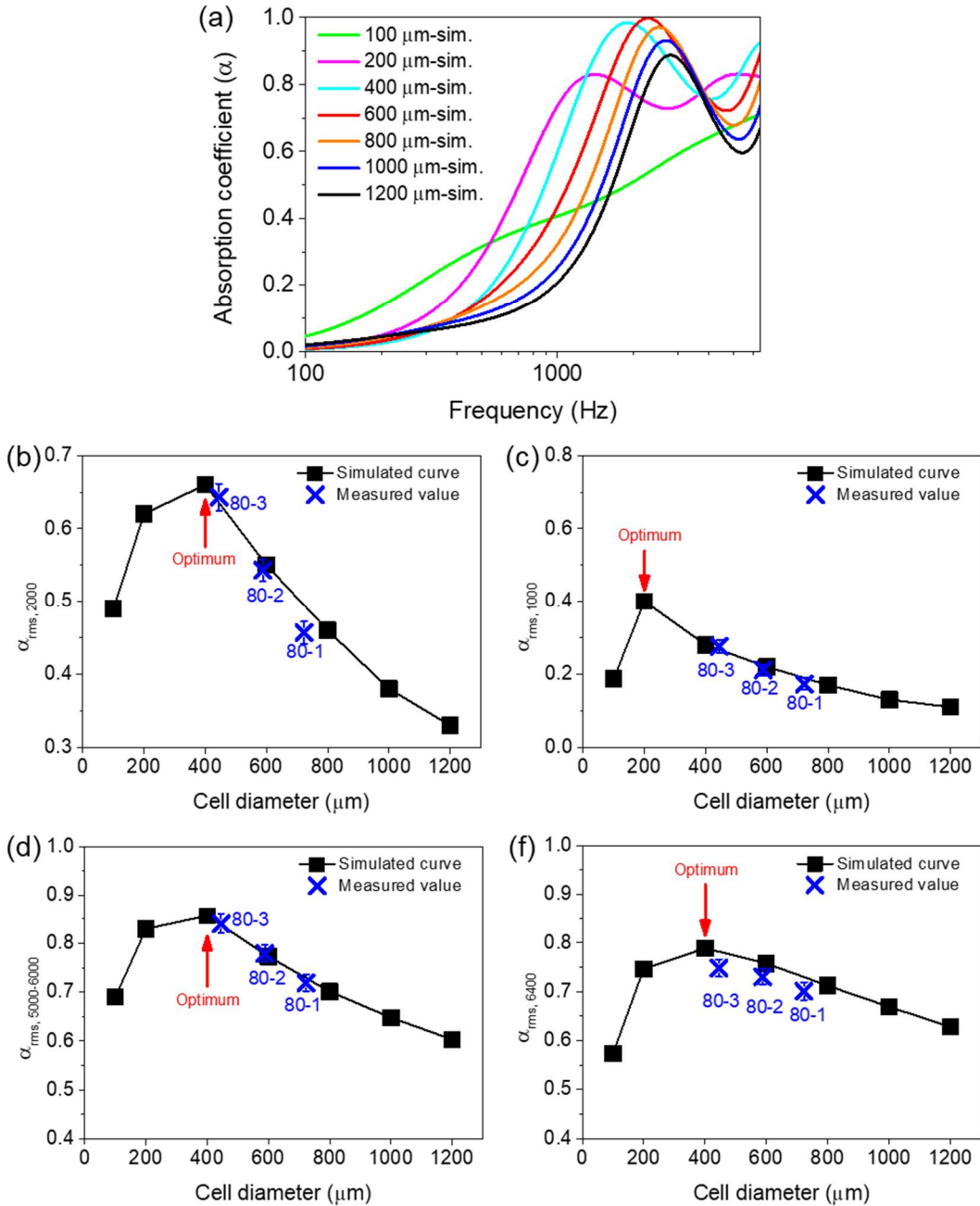


**Figure 4.2.6.** Theoretical sound absorption performance of PU foams according to cell size. (a) Sound absorption coefficient curves of the PUCs with various cell sizes. Root mean square values of sound absorption coefficient curves in the frequency range (b) from 0 to 2000 Hz ( $\alpha_{\text{rms},2000}$ ), (c) from 0 to 1000 Hz ( $\alpha_{\text{rms},1000}$ ), (d) from 5000 to 6000 Hz ( $\alpha_{\text{rms},5000-6000}$ ), and (e) from 0 to 6400 Hz ( $\alpha_{\text{rms},6400}$ ).



#### 4.2.4.2. Cell structure modulation

Cellular structure of PU foams was modulated to achieve the optimal cell size distribution using the ultrasonic foaming method. Based on the simulation results, the target average cell size was evaluated as 400  $\mu\text{m}$ .

In the cluster nucleation theory, the equation of the nucleation rate is defined as  $J_n = C(N)\exp(-\Delta F_n^*/kT)$ , where  $J_n$  is the nucleation rate,  $C(N)$  is the number of gas molecules in polymeric resin,  $\Delta F_n^*$  is the critical free energy needed to form critical clusters,  $k$  is the Boltzmann constant, and  $T$  is the absolute temperature. In the equation above,  $\Delta F_n^*$  is defined as  $\Delta F_n^* = f_L^5(kT)^3/486v_m^2(P_s - P_0)$ , where  $P_0$  is the environmental pressure,  $f_L$  is the lost degree of freedom in the process of dissolution,  $v_m$  is the equilibrium molecular volume of a gas when it loses all of the translation kinetic energy, and  $P_s$  is the constant saturation pressure. Therefore,  $\Delta F_n^*$  is inversely proportional to the magnitude of the negative environmental pressure ( $-P_0$ ). Ultrasonic waves from an ultrasonication tip induce the negative pressure in the polymeric resin by a cavitation effect. It reduces the critical energy required for bubble nucleation, and then the nucleation rate is increased. This phenomenon leads to smaller and more uniform cell size distribution of PU foams by nucleating more clusters. In addition, the ultrasonic processing promotes more nucleation by helping the two resins to disperse well.

Irradiation time, period, and power are the most important processing conditions in the ultrasonic foaming method. It has been known that ultrasonic irradiation should be applied only at the bubble nucleation stage in order to reduce the cell size by increasing the nucleation rate [297]. If the irradiation is maintained until the end of the cell growth state, the cell walls cannot be stabilized due to excessive vibration and the resulting bubbles collapse [298]. Therefore, in the experiment, ultrasonic waves were excited in the resin mixture only until a cream phase before the foam raises.

High ultrasonic power can induce higher nucleation rates in the resin because the amplitude of the waves is determined by the power of the ultrasonic generator. The proportionate relationship between the ultrasonic power and the nucleation rate was already proven in the previous work [318]. It was verified that 4 times higher magnitude of negative pressure is achieved by increasing the ultrasonic power from 10% to 20%. Schematic illustration in **Fig. 4.2.7** shows the underlying mechanism of the ultrasonic foaming method.

In this study, the three foams of 80-1, 80-2, and 80-3 with different cell size distributions were fabricated by applying ultrasonic waves of 0%, 37%, and 75% of the total output.

Internal microstructure of each sample was observed by using a field emission scanning electron microscope (FE-SEM) as shown in **Fig. 4.2.8(a)**. The average cell diameter of the samples became smaller as the output of the ultrasonic wave increases. The average cell diameter of the 80-1 sample was evaluated as 723  $\mu\text{m}$  (standard deviation,  $\pm 159 \mu\text{m}$ ), that of the 80-2 sample was 588  $\mu\text{m}$  ( $\pm 108 \mu\text{m}$ ), and that of the sample was 445  $\mu\text{m}$  ( $\pm 86 \mu\text{m}$ ). The average interconnecting pore diameters of the samples were 102  $\mu\text{m}$ , 91  $\mu\text{m}$ , and 69  $\mu\text{m}$ , respectively (**Figs. 4.2.8(b-d)**). Because the amount of foaming agent (water) added to Reactant A is the same, the total volume of cells inside the fabricated foams is the same for all samples. This is why increasing the rate of nucleation makes each cell smaller and leads to homogeneous cell distribution.

The cell diameter of 80-3 (445  $\mu\text{m}$ ) is similar to the optimal value of the simulation results, and it is significant that ultrasonic excitation alone can reduce the cell size to 60% of the conventional size (723  $\mu\text{m}$ ) without any further treatment. Because the average cell diameter of the ultrasonicated foams (80-2 and 80-3) decreased, a smaller interconnecting area was created at the interface between adjacent cells. The cell number density was inversely proportional to the average cell diameter, so the higher values of the cell number density were calculated in the ultrasonicated foams (**Fig. 4.2.8(d)**). Compared to 80-1, the average cell diameter of the 80-3 sample decreased by 38%, the average pore diameter decreased by 32%, and the cell number density doubled from 3.75 to 7.81 (**Table 4.2.2**).

Actually, the cell size of the fabricated foam had to be made smaller than 445  $\mu\text{m}$  to clearly demonstrate the optimal cell size. In the foaming process using a physical blowing agent, a very high nucleation rate can be achieved with the excitation of the ultrasonic waves. Ultrasonic excitation can be performed for a sufficient time in the nucleation period in the resin because the physical blowing agent is pre-incorporated into a polyol resin at high saturation pressure. Thus, in the previous study, the much smaller cell diameter of the foam ( $\sim 50 \mu\text{m}$ ) could be obtained by using the ultrasonic foaming method. In the meanwhile, in the chemical blowing method, carbon dioxide gases are not saturated in the resin beforehand, but rather are generated in the reaction of the chemical blowing agent with isocyanates. Therefore, the blowing gas is not sufficiently saturated in the resin

mixture at the start of ultrasonic excitation. For this reason, it is difficult to obtain a cell size of 400  $\mu\text{m}$  or less in the processing of open cell PU foams.

Three PUCs were constructed by reflecting the microcellular structure information of the three samples (80-1, 80-2, and 80-3) prepared from the experiment. The poroacoustics parameters of the PUCs were calculated by the multiscale simulation and the complex values were calculated (**Fig. 4.2.9**). The normalized flow resistivity ( $R_f$ ) is defined as the ratio of  $R_f$  in the non-treated foam (80-1) to that in the ultrasonicated foams (80-2 and 3) (**Fig. 4.2.9(a)**). The normalized  $R_f$  increased more than two times as the cell size was reduced by increasing the output of the ultrasonic wave for both measured and simulated values. The reason why the measured values are much higher than the simulated values is due to the skin layer of the sample surface causing friction and the simulation error. The tortuosity ( $\tau_\infty$ ) of the PUCs was the same but TCL and VCL showed lower values at 80-3 with much smaller cell size and interconnecting pore size (**Fig. 4.2.9(b)**).

These changes in the poroacoustics parameters induce a variation of the frequency-dependent complex values. The normalized complex variables by air properties are plotted in **Figs. 4.2.10(a-c)**. The effective bulk density ( $\rho(\omega)$ ) is the specific air density in a porous medium corrected by the poroacoustics parameters.  $\rho(\omega)$  is proportional to  $R_f$  and inversely proportional to VCL (see **Eqn. 4.2.7**). Therefore, the PUC of 80-3 revealed the maximum value among the samples. Meanwhile, the effective bulk modulus ( $K(\omega)$ ) is the specific air modulus affected by the complicated microstructure of the foam. Since  $K(\omega)$  is inversely proportional to the increase of TCL, it was decreased by the ultrasonication. From the two complex variables, complex phase speed ( $c_c$ ) in a porous medium was calculated by the definition of  $c_c = \sqrt{K(\omega)/\rho(\omega)}$ . The complex phase speed of sound in the foam with small microcellular structure has a lower value in all frequency ranges (**Fig. 4.2.10(c)**).

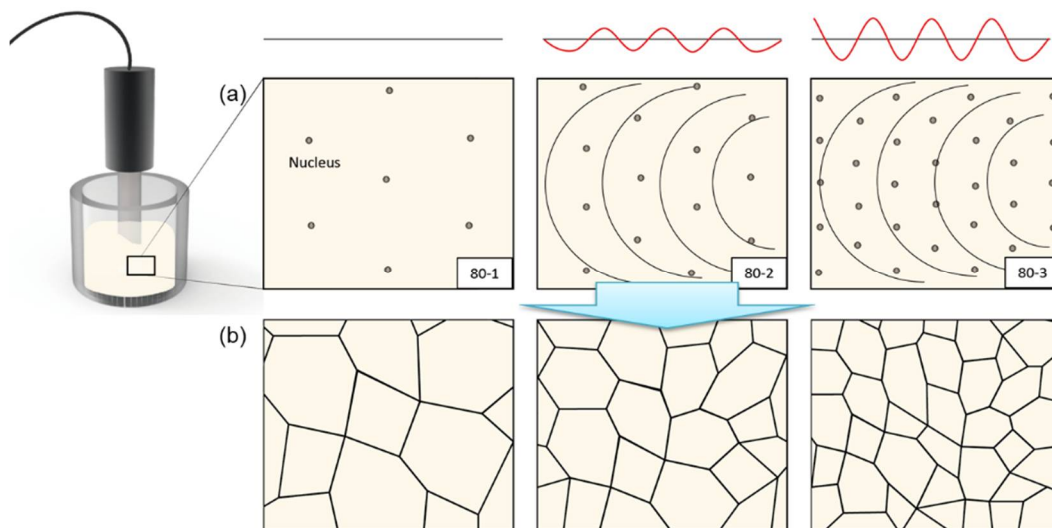


**Figure 4.2.7.** Schematic illustration of the ultrasonic PU foaming method. (a) The state diagram of the reaction resin in the ultrasonic wave excitation (gray dots: generated nuclei, black curves: wave front of ultrasonic waves, and red standing wave mode shape: the amplitude of waves). (b) Microcellular structures foamed after each ultrasonic state.

**Table 4.2.2.** Microcellular structure information of the fabricated samples.

	80-1	80-2	80-3
Average cell diameter ( $\mu\text{m}$ )	723 ( $\pm 159$ )	588 ( $\pm 108$ )	445 ( $\pm 86$ )
Average diameter of interconnecting pore ( $\mu\text{m}$ )	102 ( $\pm 79$ )	91 ( $\pm 66$ )	69 ( $\pm 54$ )
Cell number density ( $\#/\text{mm}^2$ )	3.75	5.63	7.81

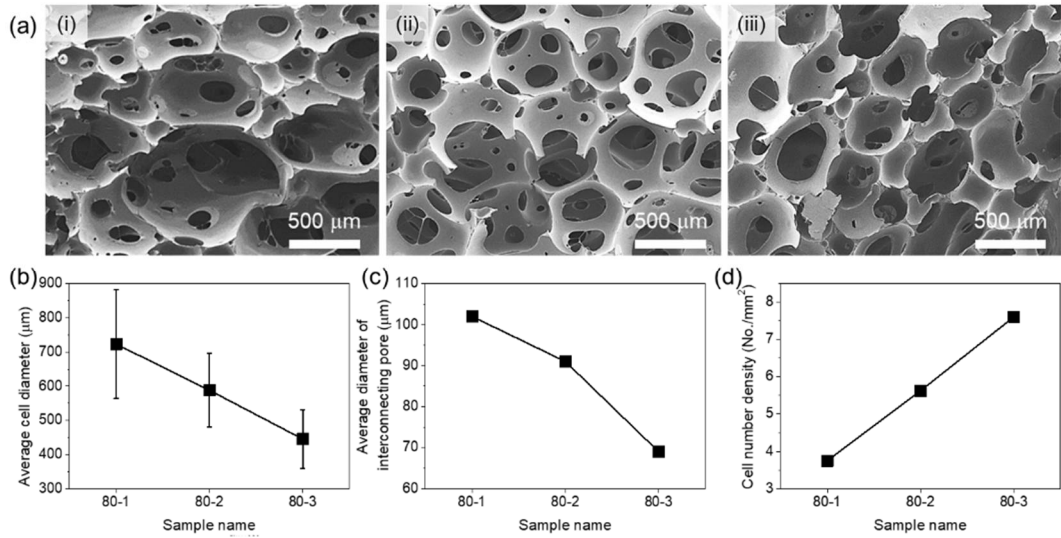


**Figure 4.2.8.** Observation and analysis of microcellular structure of the fabricated PU foams. (a) Observed SEM images of (i) 80-1, (ii) 80-2, and (iii) 80-3. Analyzed (d) average cell diameter, (e) average diameter of interconnecting pores, and (f) cell number density of the samples.

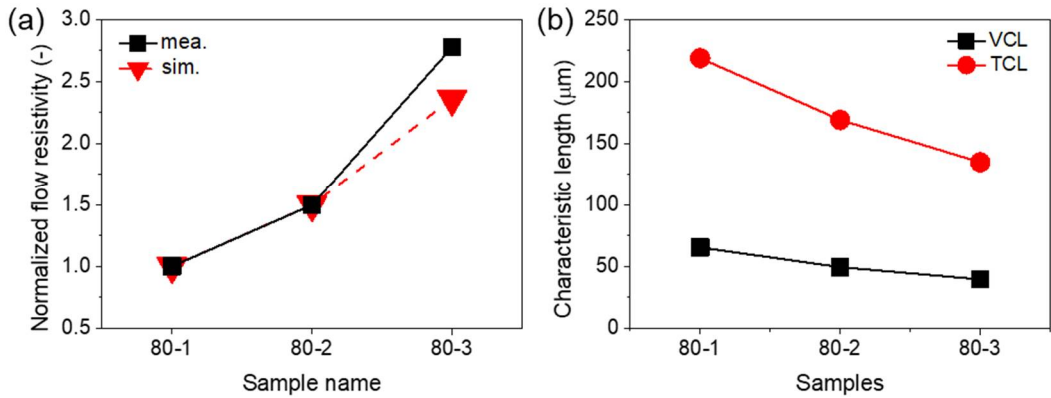


**Figure 4.2.9.** Measured and simulated poroacoustics parameters of the PUCs representing the fabricated PU foam samples: (a) flow resistivity and (b) characteristic lengths.

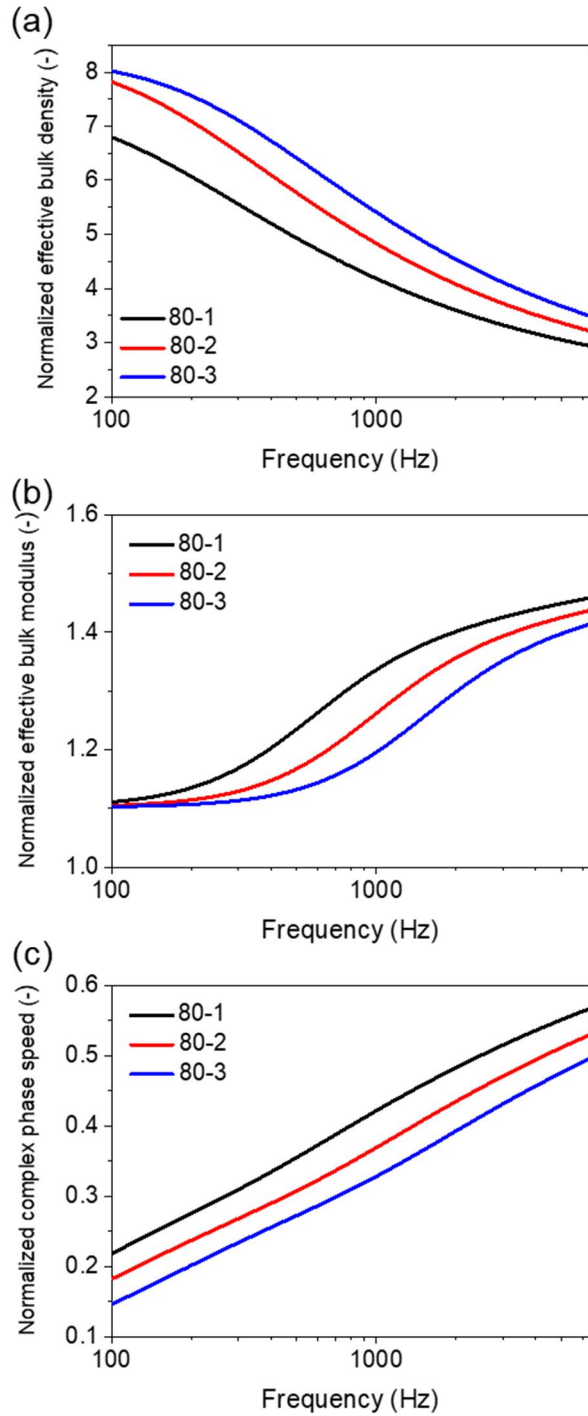


**Figure 4.2.10.** Simulated normalized complex variables of the PU foam samples: (a) effective bulk density, (b) effective bulk modulus, and (c) complex phase speed.

#### 4.2.4.3. Sound absorption performance

Sound absorption coefficients of the fabricated PU foams were experimentally characterized by using a B&K impedance tube. The measured and simulated sound absorption coefficients were plotted in **Fig. 4.2.11(a)** and the two curves show very similar trends. All fabricated foams are the same materials composed of same chemicals from a macroscopic point of view since all samples have the same mass density and dimensions. However, the sound absorption coefficient curves were differently characterized for each sample.

The only difference between the samples is the internal microcellular structure, *i.e.*, the cell size, changed by the mechanical excitation to the reaction resin. By decreasing cell size of the foams (80-1, 80-2 to 80-3), the maximum peak of the curve shifted from 2544 to 1920 Hz (**Fig. 4.2.11(b)**). The decrease of the sound speed inside the foam due to the smaller cell diameter is presumed to be the dominant factor for the peak shift. This peak shift indicates that low frequency range noise can be easily attenuated on the ultrasonic foamed foams. A relatively large difference between the experimental and numerical results was found in the high frequency region. This difference might stem from the experimental trial error and the theoretical assumption of the rigid frame ignoring the damping effect on the solid frame.

Various acoustic damping evaluators, *i.e.*, root mean square (RMS), noise reduction coefficient (NRC), and 1/3 octave band spectrogram, were analyzed (**Figs. 4.2.11(c-e)**). The RMS value from 0 to 2000 Hz ( $\alpha_{\text{rms},2000}$ ) (**Fig. 4.2.11(c)**) shows an ascending slope with respect to the reduction of cell size. On the contrary, there was no significant improvement in the residual range from 2000 to 6400 Hz ( $\alpha_{\text{rms},2000-6400}$ ) (**Fig. 4.2.11(d)**). It is worth noting that the fabricated 80-3 foam is close to the optimum sound absorber in the perspective of  $\alpha_{\text{rms},2000}$  (**Fig. 4.2.6(b)**). NRC is an evaluation factor for the overall frequency noise reduction performance of materials calculated by averaging the sound absorption coefficients at 128, 256, 512, 1024, 2048 and 4096 Hz. In **Fig. 4.2.11(e)**, the ultrasonicated foam samples have the NRC values greater than that of 80-1 even though these have a similar sound absorption ability in high frequency ranges.

Sensitivity analysis was performed to elucidate which poroacoustic parameters improved the sound absorption performance, by changing only one poroacoustic parameter

while keeping the other poroacoustic parameters fixed (**Fig. 4.2.12**). As shown in **Fig. 4.2.12(a)**, the change in the curves mainly originates from flow resistivity ( $R_f$ ) rather than other poroacoustics parameters as reported in several studies. The  $R_f$  of the samples were measured to compare with the simulated  $R_f$ . Both normalized values reveal the same ascending trend from 80-1 to 80-3 (**Fig. 4.2.9(a)**). A relatively high  $R_f$  was measured on the ultrasonicated foams because the cell diameter reduction leads to a narrower and more complex sound propagation path.

High effective bulk density and low effective bulk modulus achieved in the foam with high  $R_f$  make the sound speed slower. Moreover, other researchers proved that the slow sound speed can induce the high sound damping efficiency for low frequency noise [287,288]. Phenomenologically, in the experiment, the low frequency sound energy could be dissipated better in the foams with small cell diameters.

Octave band spectrogram is often used for analyzing acoustical data. It is characterized by dividing measured frequencies into one octave band range. One octave range is a frequency range where the highest frequency is two times higher than the lowest frequency. Although there are several octave bands, 1/3 octave band spectrogram is most commonly used because the frequency range of each band matches the human audible frequency range. The 1/3 octave band spectrograms were obtained from the measured and simulated sound absorption coefficient curves and plotted in **Fig. 4.2.13(a)**. Each band was numbered from #1 to #25 and their central frequencies were listed in **Table 4.2.4**. The bands of the ultrasonicated foams show higher values in most bands from # 1 to # 22 than in the non-treated foam, but not in # 23-25.



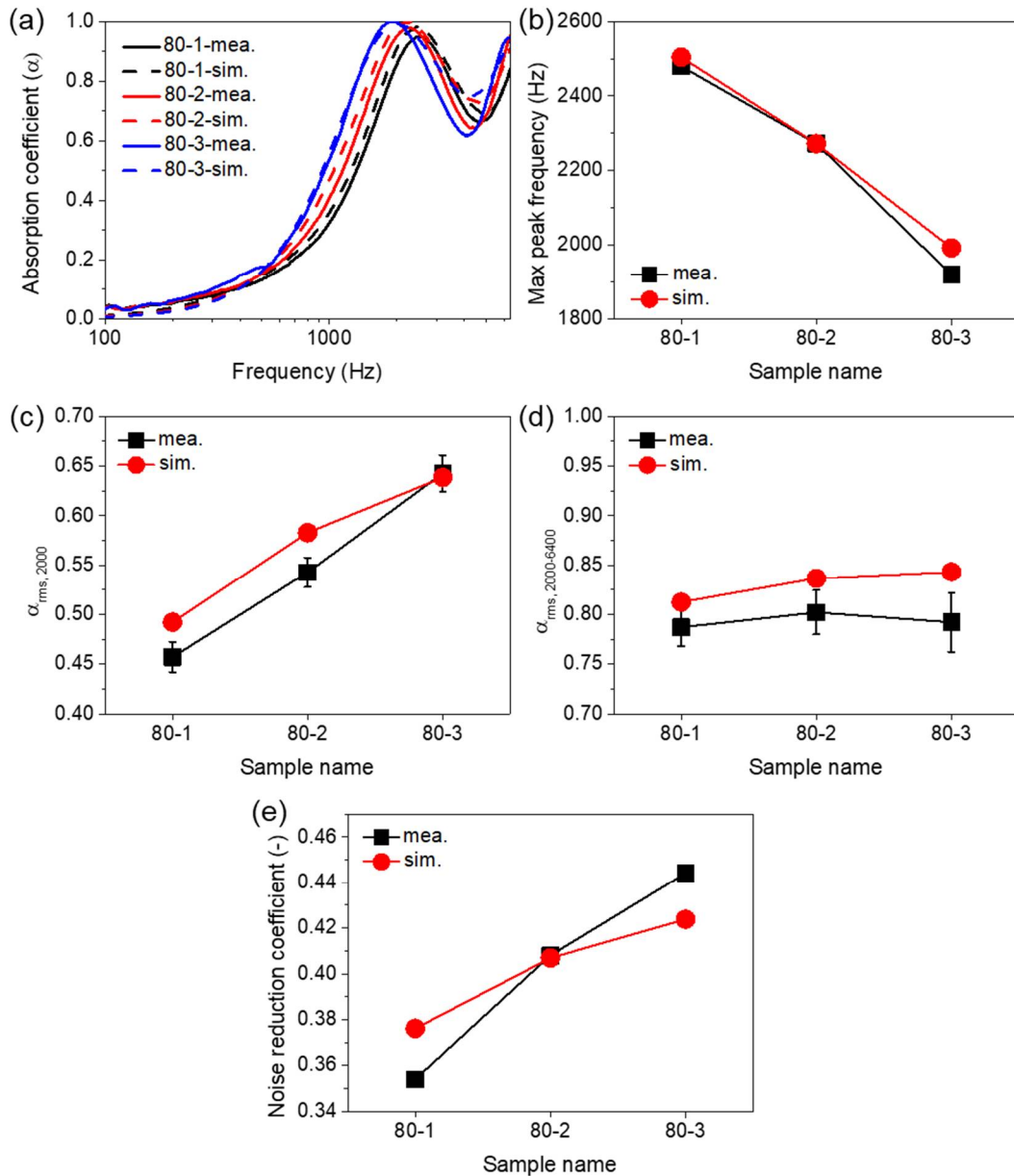


**Figure 4.2.11.** Sound absorption performance of the fabricated PU foams. (a) Measured (solid lines) and simulated (dash lines) sound absorption coefficients from 0 to 6400 Hz. (b) A tendency of max peak shift. Root mean square values (c) from 0 to 2000 Hz and (d) from 2000 to 6400 Hz. (e) Noise reduction coefficient curves.

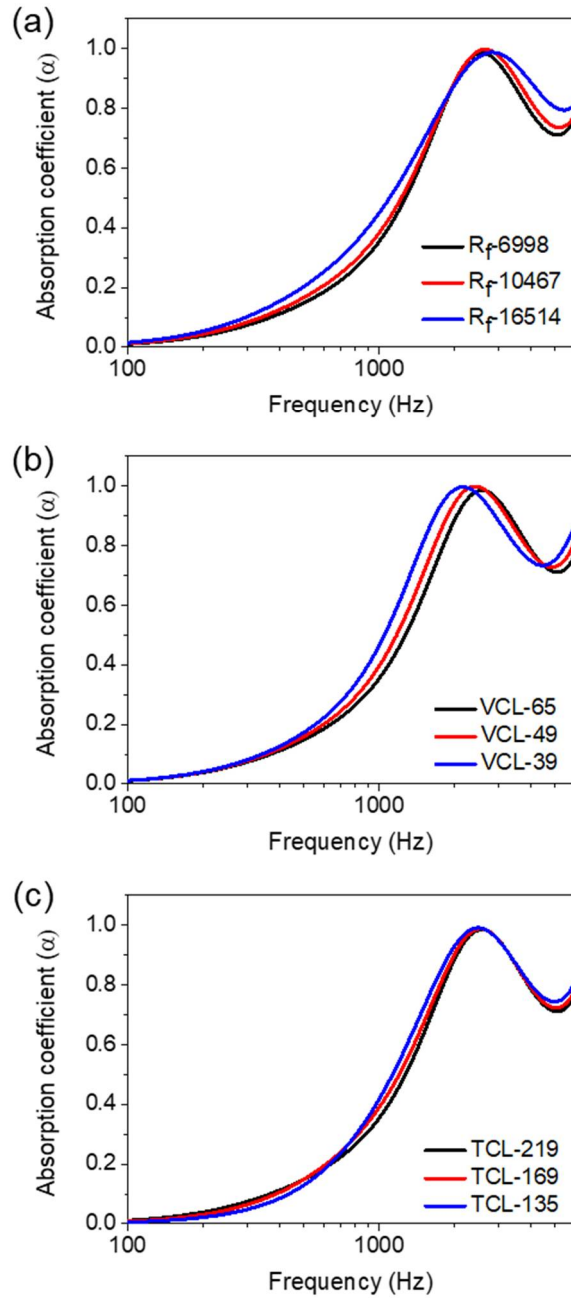


**Figure 4.2.12.** Sensitivity analysis for (a) flow resistivity, (b) viscous characteristic length (VCL), and (c) thermal characteristic length (TCL).

**Table 4.2.3.** Acoustic damping evaluators of the PUCs for the samples.

	80-1	80-2	80-3
Frequency at max peak (Hz)	2544	2272	1920
$\alpha_{\text{rms},2000}$ (-)	0.457	0.543	0.643
$\alpha_{\text{rms},2000-6400}$ (-)	0.777	0.802	0.791
Noise reduction coefficient (-)	0.354	0.408	0.444

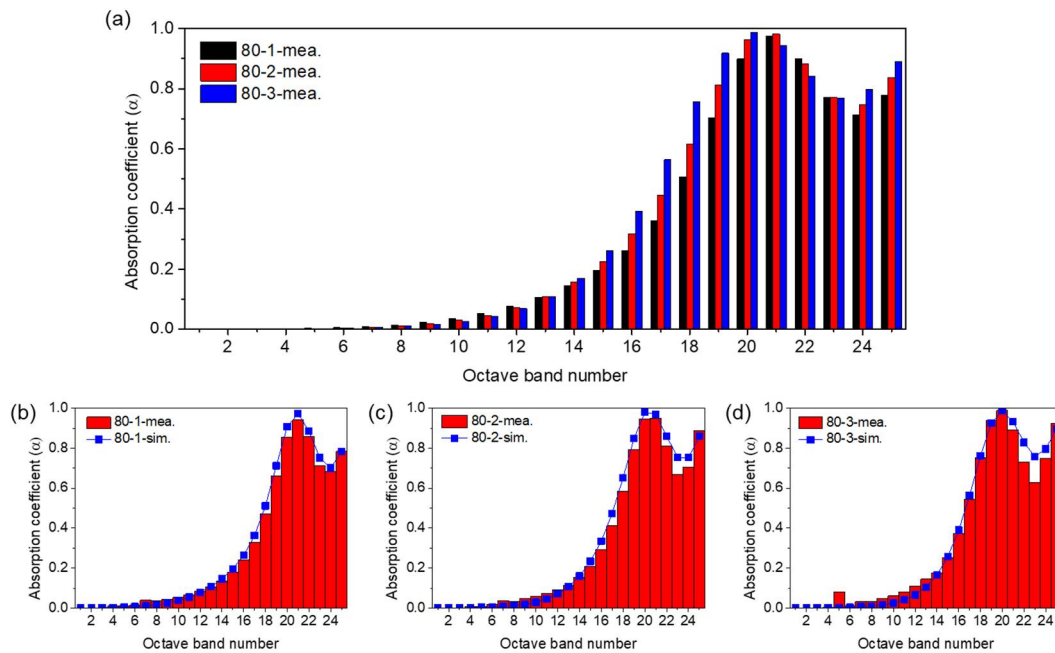


**Figure 4.2.13.** 1/3 octave band spectrograms. (a) 1/3 octave bands from #1 band to #25 band. (b-d) Comparisons between the measured and simulated values of bands for each sample.

**Table 4.2.4.** Band numbers of 1/3 octave band spectrogram.

Band number (#)	Center frequency of band (Hz)
1	25
2	31.5
3	40
4	50
5	63
6	80
7	100
8	125
9	160
10	200
11	250
12	315
13	400
14	500
15	630
16	800
17	1000
18	1250
19	1600
20	2000
21	2500
22	3150
23	4000
24	5000
25	6300

#### **4.2.5. Conclusions**

In this section, the strategy for the poroacoustic meta-absorber was demonstrated by designing and manufacturing the sound absorbing PU foam with optimized cell size. The optimum cell diameter for low frequency sound absorption of the PU foam with  $80 \text{ kg/m}^3$  density and 2 cm thickness was theoretically predicted to be  $400 \text{ }\mu\text{m}$  by performing the multiscale poroacoustics modeling. The PU foam with the optimal cell size was fabricated by using the ultrasonic foaming method which applies the mechanical excitation to the reaction resin. The ultrasonication makes the internal microcellular structure of the foam about 40% smaller than the not-irradiated foam. The experimental measurement showed that the enhanced noise damping at low frequency was achieved by structural modulation of the PU foam. Using this strategy, a low density foam in a small space is sufficient to control noise at low frequencies, thus achieving fuel savings in transportation. In addition, it is expected that the sound attenuation efficiency can be drastically improved by installing the customized sound absorption foams according to the main noise frequency.

## 4.3. Openness-modulated PU foam

### 4.3.1. Introduction

A myriad of porous materials, *e.g.*, microcellular foams [274,315], fibrous bundles [319,320], and granular spheres [317], have been studied for various purposes, such as sound absorption, thermal insulation, and electromagnetic shielding. Sound absorption of the porous material is one of the most significant applications since noise pollution is considered to be a critical problem in daily life [321,322]. Microcellular polymeric foams with porosity higher than 90% are mostly installed in the required locations to eliminate annoying noises. For the polymeric foams, the visco-inertial and thermal damping dominates the overall sound absorption behavior rather than the viscoelastic frame damping (see Section 4.2.1). Accordingly, tuning the microcellular structure of foams is a crucial issue in order to facilitate the advanced sound absorption performance.

Polyurethane (PU) foams are fabricated in general by employing a reaction injection molding (RIM) process [284]. PU foams have such advantages as low costs, good processability, and light weight when compared with other sound absorbers. In the fabrication of PU foams, Reactant A (polyols, foaming agent, catalyst, surfactants and *etc.*) and Reactant B (isocyanates) are blended at high speed and then the mixed resin is injected into a mold of a desired shape. Two chemical reactions, chemical blowing reaction and gelling reaction, occur simultaneously. The reaction balance between them is governed by a chemical composition and processing conditions [323].

Noise control in low frequency ranges has received considerable attention due to difficulties in achieving sufficient performance [289–291]. The use of either massive or thick foams is a solution to the problem, but it has limitations for industrial applications due to some adverse effects [292,293]. Therefore, microstructure manipulation is the best strategy to improve the acoustic damping properties circumventing the adverse effects. As one of the structural parameters of microcellular foams, cell size has been manipulated by incorporating nucleating agents or applying mechanical excitation in the previous studies and Section 4.2 [284,296,324,325].

Cell openness is another structural parameter of microcellular foams. Porous materials are classified into three types of foams depending on the degree of cell opening; open cell foams, closed cell foams, and semi-open cell foams. The semi-open cell foams with appropriate cell openness bring out satisfactory sound absorption performance due to their complex inner geometry which enables a complex sound path in the foam [326,327]. Hence, controlling the cell openness is an important issue in engineering sound absorbing materials.

It has been reported that cell opening of the foam occurs by the following mechanisms; spontaneous film rupture [328], urea precipitation [329,330], surfactant phase separation [331], and viscosity rise of foam matrix. Two strategies have been used to employ these mechanisms for controlling cell opening; surface rheology control and bulk rheology control. For the surface rheology control, surface tension of the resin is adjusted by adding a silicon surfactant [332–334]. Accordingly, the fraction of cell windows is affected by changing a drainage rate. For the bulk rheology control, cell openness is regulated by balancing the gelling reaction and the blowing reaction changing reaction kinetics with catalysts [323].

In recent studies, a novel type cell opener has been developed based on reactive cell opening mechanism [335–338]. When bulky molecules having a high cloud point are contained in the PU resin as a reactive cell opener, the blowing reaction is delayed since hydroxyl groups of the cell opener occupy isocyanate groups of Reactant B. It results in a reduction of the increase rate of molecular weight and then induces low viscosity during the foaming reaction. Accordingly, the incorporation of the reactive cell opener can be utilized to fabricate openness-controlled semi-open cell PU foams.

Many theoretical results have been reported to model sound absorption performance of porous materials [339,340]. Among them, multiscale poroacoustics modeling using a numerical method was developed recently to investigate the effects of microcellular geometry [312,314]. Periodic unit cells (PUCs) are built by considering microcellular geometry of the porous material to obtain microscale flow properties. Poroacoustic parameters are estimated by solving two flow problems by using PUCs. These parameters are used for modeling of a macroscale acoustic behavior and theoretical sound absorption coefficient ( $\alpha$ ) is obtained by solving a poroacoustics model.

The objective of the present work is to study the effects of cell openness on sound

absorption. The best cell openness for low frequency sound damping of the PU foam with 40 kg/m<sup>3</sup> density and 2 cm thickness was estimated at 15% from the simulation results. The PU foam with the best cell openness was tailored by infusing the reactive cell opener in the reaction resin to adjust rheological behaviors. Microscale topologies of the fabricated samples were observed and sound absorption coefficients were measured by using a B&K impedance tube. Additional analyses were performed to evaluate the sound absorption performance of the cell openness-controlled PU foams.



## 4.3.2. Experimental

### 4.3.2.1. Materials

A polyol mixture (NIXOL SA-120 and NIXOL RNF-180, KPX Chemical, Republic of Korea) and 4,4'-diphenylmethane diisocyanate (MDI, MCNS, Republic of Korea) were used as Reactant A and Reactant B, respectively. Poly (ethylene glycol) 2000 (PEG 2000, Daejung Chemicals, Republic of Korea), which has a molecular weight of 2000, was selected as a reactive cell opening agent. To diversify the cell openness of the PU foam, the cell opener of various weight fractions of 0, 3, and 6 wt% was contained in the Reactant A. AKO-HM207K (Akochem., Republic of Korea) was used as a mold releasing agent of PU foams for easy detachment from the mold.

### 4.3.2.2. PU foaming method

The polyol mixture (NIXOL SA-120: NIXOL RNF-180 = 3:1) and the cell opener (PEG 2000) were mixed rigorously by using a digital regulator (WiseStir® model HS-100D, Germany). The Reactant A with the cell opener and the Reactant B were mingled at a ratio of 1:1 and poured into the prepared mold (15 x 15 x 2 cm<sup>3</sup>, the same mold used in Section 4.2). The fabricated foams were detached from the mold after 0.5 hour. The samples were labeled as P0, P3, and P6, respectively, named after the weight fraction of the incorporated cell opener.

### 4.3.2.3. Characterizations

Microstructure of the PU foams was observed by using a field emission scanning electron microscope (MERLIN Compact FE-SEM, ZEISS, Germany). After freeze-drying of the foam with liquid nitrogen, the SEM specimens were prepared by cutting the frozen foams. Cell diameter and openness of the samples were determined from the taken SEM images based on porosimetry calculation by using Image-Pro Plus 6.0 software. Each cell diameter was defined by averaging the length of long and short axes of a single microcell. The total average cell diameter of the sample was determined by averaging diameter of all cells found in the taken SEM images. Cell openness ( $p$ ) was defined as  $p = S_{open}/S_{tot}$ , where  $S_{open}$  is the area of the open cell walls and  $S_{tot}$  is the total area of the cell [341].

Normal incidence absorption coefficient was measured by using a B&K two-microphone standing wave tube type 4206 in the same manner as in Section 4.2.2. Tortuosity ( $\tau_\infty$ ) was measured by using a lab-made electrokinetic set up. The measuring set up was built by following the work elsewhere [342]. By comparing electrical resistance of the pure conductive fluid ( $\Omega_f$ ) with the resistance of the fluid-saturated foam ( $\Omega_m$ ),  $\tau_\infty$  was evaluated as  $\tau_\infty = \varepsilon \cdot (\Omega_m/\Omega_f)$  where  $\varepsilon$  is the porosity.

### 4.3.3. Numerical analysis

#### 4.3.3.1. Unit cell modeling method

Periodic unit cells (PUCs) were built by using CATIA (Computer Aided Three-dimensional Interactive Application, Dassault Systèmes, France) and MATLAB (Matrix laboratory, MathWorks, United States) programs for microscale flow analysis (**Figs. 4.3.1(a)**). A cluster composed of tetrakaidecahedron cells is regarded as the most appropriate structure for foam modeling [309,310]. The PUCs were constructed by using the cluster by reflecting the microstructural information extracted from the captured SEM images of the fabricated samples. Cell openness of the PUCs was modulated by eliminating cell walls which were selected by a mathematical code for random number generation built in MATLAB (**Figs. 4.3.1(a), (i→ii)**). After implanting the hexahedron in the cluster (**Figs. 4.3.1(a), (ii→iii)**), the PUCs were generated by executing a Boolean operation (**Figs. 4.3.1(a), (iii→iv)**). The mass density of all PUCs was fixed at  $40 \text{ kg/m}^3$  which is identical to the fabricated samples. Cell diameter of all PUCs was set as  $500 \text{ }\mu\text{m}$  reflecting the SEM images of the samples.

Four PUCs with the cell openness of 15%, 25%, 50%, and 100% were constructed (**Figs. 4.3.1(b-e)**). The cell openness for each PUC was defined as the area ratio of the opened cell windows to the total cell windows, similar to that used for experimental evaluation [341]. The semi-open PUCs, *i.e.*, the 15%, 25%, and 50% cell openness PUCs, were modeled by eliminating cell walls of the center cell. Only the center cell walls were removed to apply periodic flow conditions on the lateral faces of the PUCs. The PUC with

15% openness was constructed by opening 2 rectangles and 2 hexagons of the center cell. 3 rectangles and 4 hexagons were removed for the 25% openness PUC, and 6 rectangles and 8 hexagons were eliminated for the 50% openness PUC by employing the same execution. The PUC with 100% openness was built by clearing all cell walls to represent the structure of a fully open cell foam.

#### 4.3.3.2. Multiscale poroacoustics simulation method

The same numerical simulation described in Section 4.2.3 was conducted by using the multiscale poroacoustics method. The purpose of this simulation is to determine how the cell openness of PU foams affects the sound absorption performance.

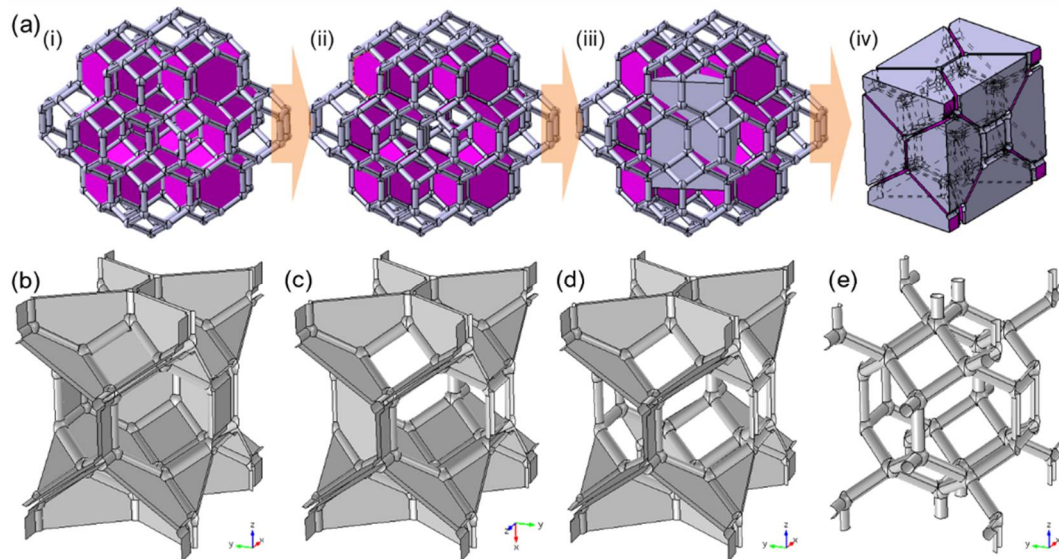


**Figure 4.3.1.** Modeling of PUCs with various cell openness. (a) Production process of PUCs: (i) a cluster consisted of 15 tetrakaidecahedron, (ii) elimination of selected cell walls, (c) imparting the hexahedron into the cluster, and (d) Boolean operation generating PUC. Constructed PUCs having (b) 15%, (c) 25%, (d) 50%, and (e) 100% cell openness.

## 4.3.4. Results and discussion

### 4.3.4.1. Theoretical study on cell openness

Multiscale poroacoustics simulation was carried out by using the periodic unit cells (PUCs) to examine the influence of cell openness to sound absorption. The four PUCs having 15%, 25%, 50%, and 100% cell openness were manufactured in Section 4.3.3.1. The microscale flow analysis was conducted in two steps using the respective PUCs to calculate the poroacoustics parameters. In the viscous flow analysis, pressure boundary conditions were applied on the surfaces of the PUC in z-direction. At the same time, periodic boundary conditions were applied on the lateral surfaces. No-slip boundary conditions were assumed on the solid-air interface. Permeability fields ( $\mathbf{k}_0$ ) were obtained by solving Stokes' flow equation and calculated by scaling the obtained velocity fields (**Figs. 4.3.2(a-d), (i)**). In the inertial flow analysis, electric fields were obtained by solving the current conservation equation while applying a potential boundary condition on the surfaces of the PUC in z-direction with periodic boundary conditions. Likewise, the scaled dimensionless electric fields ( $\mathbf{E}$ ) were obtained by normalizing electric fields (**Figs. 4.3.2(a-d), (ii)**).

The calculated permeability fields are formed by the fluid flow only through the open cell windows. It means that flow resistivity ( $R_f$ ) is increased as the openness of PUCs decreases from 100% to 15% inducing narrow air paths (**Table 4.3.1**). In general,  $R_f$  has been known as a dominant factor determining sound absorption behaviors of 80 kg/m<sup>3</sup> density PU foams due to their small interconnecting pores [315,317,326]. However, the impact of  $R_f$  is relatively small compared to the case in Section 4.2 because the PUCs employed in the present work have both large cell diameter (500  $\mu\text{m}$ ) and low mass density (40 kg/m<sup>3</sup>).

In the meanwhile, the scaled electric fields ( $\mathbf{E}$ ) are also generated along the opened cell window path similar to the permeability fields. Therefore, the low openness implies more complex pathways in the PUCs, leading to higher tortuosity factors; 1.02 (100% open PUC), 1.4 (50% open PUC), 2.0 (25% open PUC), and 3.7 (15% open PUC) (**Table 4.3.1**). Due to weak impact of the flow resistivity, the tortuosity factor ( $\tau_\infty$ ) governs the sound absorption performance of the PU foam in the case of low density PU foams.

The pressure acoustics simulation was conducted at macroscale to explore sound

propagation behavior affected by the foams with various cell openness. The representative simulation results at 1000, 2000, 4000, and 6400 Hz frequencies were shown with the background and scattered pressure fields (**Fig. 4.3.3**). The difference in intensity of each scattered pressure field indicates that the sound attenuation efficiency depends on the degree of cell openness of the foam. Intuitively, it was found that the 15% openness PUC derives the best performance especially in the low frequency ranges at 1000 and 2000 Hz.

Frequency-dependent complex variables, effective bulk density ( $\rho(\omega)$ ) and effective bulk modulus ( $K(\omega)$ ), were evaluated by using the JCA model (**Fig. 4.3.4**). As the cell openness decreases,  $\tau_\infty$  is increased and two characteristic lengths, VCL and TCL, are decreased (**Table 4.3.1**). An increase of  $\rho(\omega)$  for the low openness PUCs mainly stems from both the increase of  $\tau_\infty$  and the decrease of VCL (**Fig. 4.3.4(a)**). Meanwhile,  $K(\omega)$  is proportional to the value of TCL (**Fig. 4.3.4(b)**). The increasing rate of  $\rho(\omega)$  is much higher than the decreasing rate of  $K(\omega)$ . It makes the low openness PUCs entail slower complex phase speed ( $c_c$ ) as shown in **Fig. 4.3.4(c)**. Characteristic impedance ( $Z_c$ ), which means a resistance of acoustic flow in the medium and defined as  $Z_c = [K(\omega)\rho(\omega)]^{1/2}$ , was calculated and compared each other (**Fig. 4.3.4(d)**). Obviously, the trend of the  $Z_c$  value shows the opposite behavior to the  $c_c$  graph, indicating high resistance to sound wave propagation. From this phenomenon, it can be noticed that a foam with low cell openness behaves like a massive foam with high density in the propagation of sound waves, even if modeled at the same mass density.

Theoretical sound absorption coefficients were calculated by using the complex variables and shown in **Fig. 4.3.8(a)**. The peaks of the curves not only shift to low frequency range but also reveal the higher values, according to the decrease of cell openness (**Fig. 4.3.8(e)**). Actually, the PUCs having 15% and 25% cell openness could be modeled in many ways since there are many cases of how to remove cell walls. Moreover, in the two cases, the calculated sound absorption coefficients may depend on the applied direction of sound propagation.

In order to avoid the randomness and asymmetry of the PUCs, many types of PUCs were constructed and corresponding multiscale poroacoustics simulations were performed (**Fig. 4.3.5**). The calculated absorption coefficient curves show very similar performance for the PUCs modeled as having the same openness. The exact sound propagation path

through each PUC was different from each other, but the tortuosity as a main governing factor was not varied significantly among them. The PUC modeling method can be validated from the simulation results.

In the comparative analysis with the experimental results, only representative graphs in each case are shown in **Fig. 4.3.8(a)**. More discussion about sound absorbing performance is explained in Section 4.3.4.3 with the measured results. From the simulation results, it could be understood that the fabrication of a PU foam having 15% openness is the best way to accomplish improved sound absorbing performance under conditions of 40 kg/m<sup>3</sup> mass density and 500 μm cell diameter.

**Table 4.3.1.** Calculated poroacoustics parameters for JCA model.

Openness	15%	25%	50%	100%
Porosity, $\epsilon_p$	0.96	0.96	0.96	0.96
Flow resistivity, $R_f$ (N·m <sup>4</sup> ·s)	4620	3100	2738	2326
Tortuosity, $\tau_\infty$	3.7	2.0	1.4	1.02
Viscous characteristic length, $L_v$ (μm)	80	138	159	301
Thermal characteristic length, $L_{th}$ (μm)	165	174	231	516

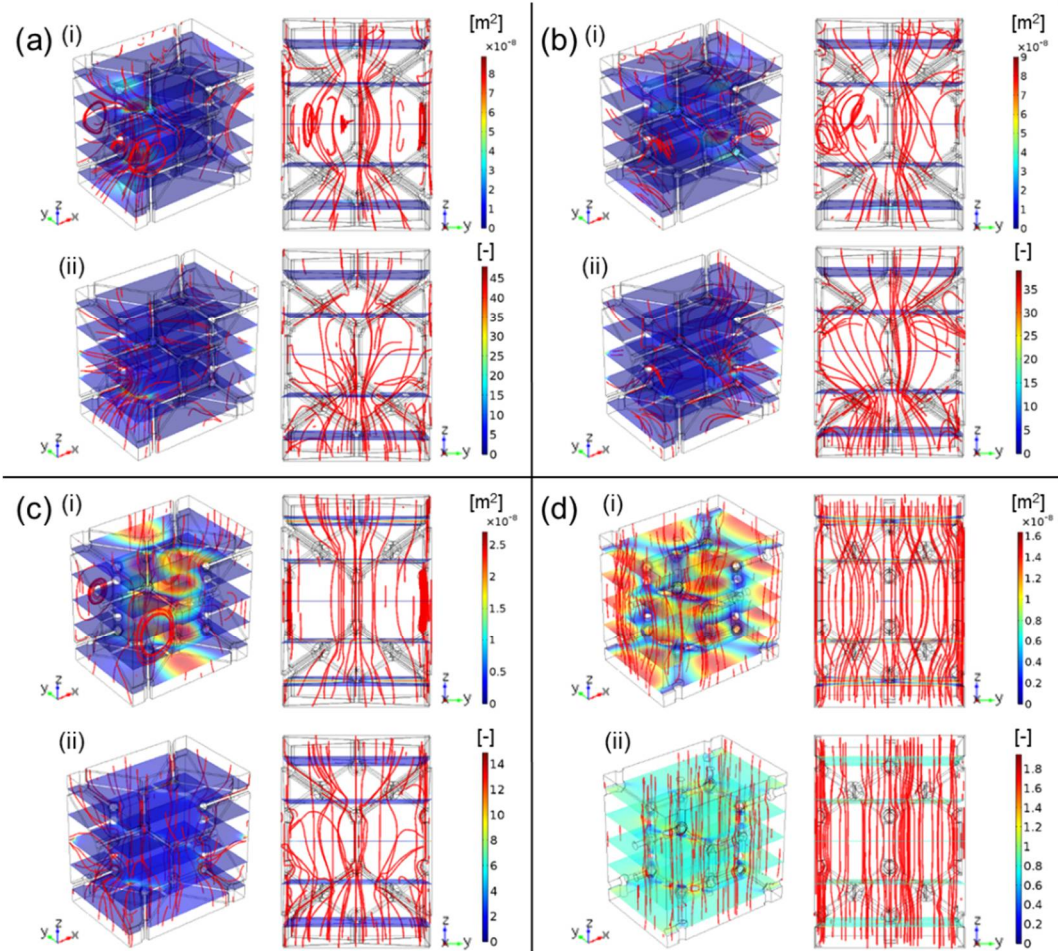


**Figure 4.3.2.** Microscale numerical simulation results using PUCs with (a) 15%, (b) 25%, (c) 50%, and (d) 100% cell openness. (i) and (ii) show the solutions of the viscous flow problem and inertial flow problems.

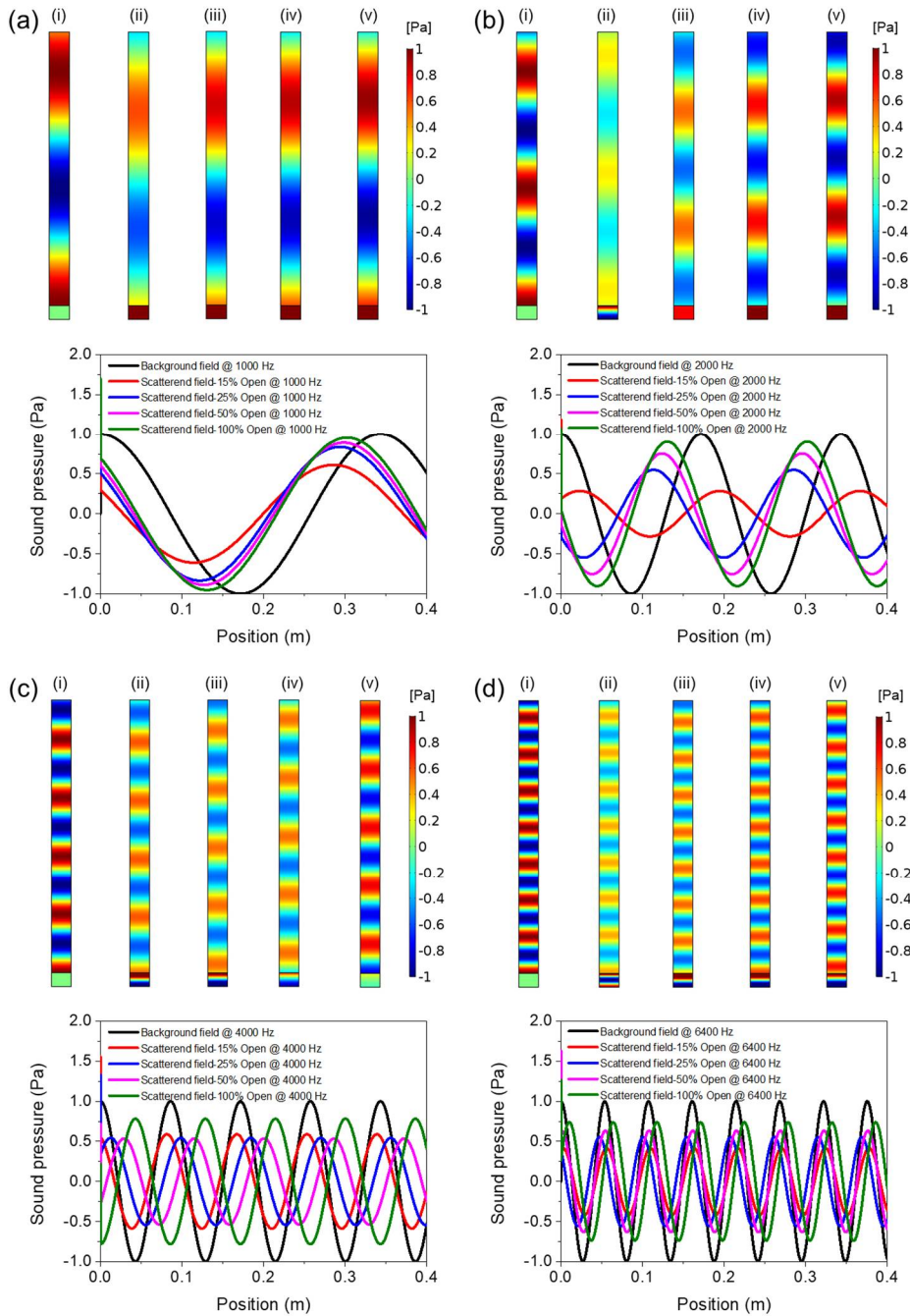


**Figure 4.3.3.** Macroscale pressure acoustics simulation results at (a) 1000 Hz, (b) 2000 Hz, (c) 4000 Hz, and (d) 6000 Hz. (i) means the background pressure field, and (ii-v) mean the scattered pressure fields for 15%, 25%, 50%, and 100% openness PUCs, respectively. The graphs below reveal the profiles of sound pressure field in the tube for each PUC case at each frequency.



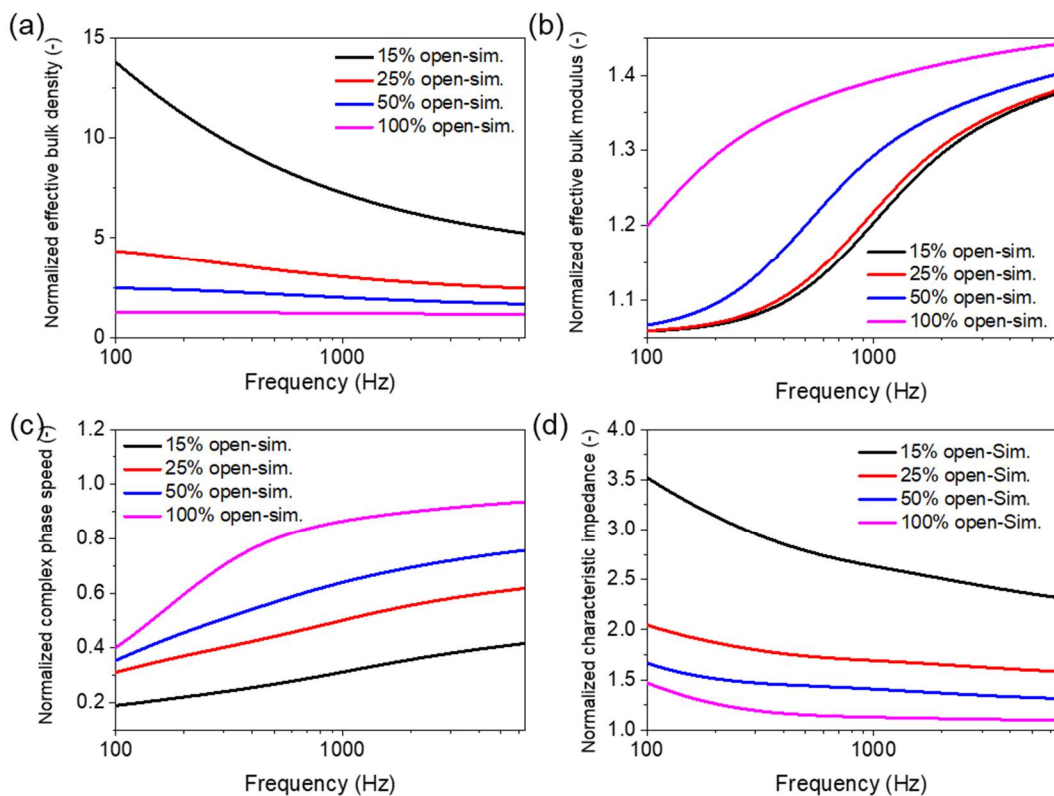


**Figure 4.3.4.** Theoretical complex variables as a function of frequency: (a) effective bulk density, (b) effective bulk modulus, (c) complex phase speed, and (d) characteristic impedance curves normalized with the reference air properties.

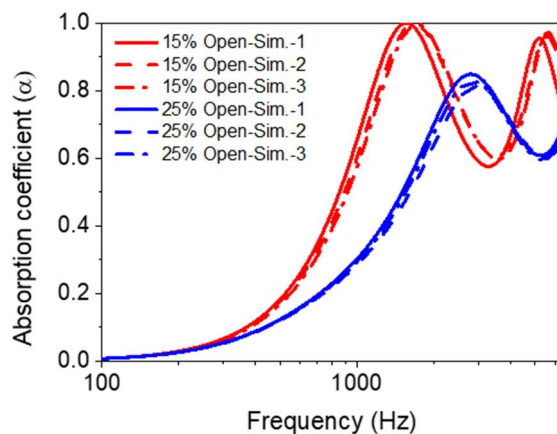


**Figure 4.3.5.** Simulated sound absorption coefficient curves for the various PUCs modeled for 15% and 25% cell openness.

#### 4.3.4.2. Cell openness control

The reactive cell opener, PEG 2000, was added to the polyol mixture to tailor the foam with the optimum cell openness evaluated in the theoretical analysis. During the foaming reaction, the incorporated PEG 2000 reacts with the isocyanate functional groups (-NCO) of the MDI molecules. This reaction slows down the elongation of polymeric chains and it results in the low molecular weight PU chains. Then the rate of the blowing reaction becomes relatively faster than that of the gelling reaction. As the balance between the two reactions is adjusted, the low molecular weight reduces viscosity of the resin in the foaming reaction. Therefore, the thickness of cell walls becomes thinner and the elastic property of the wall is also deteriorated. Consequently, closed cell walls in the PU foam are collapsed easily by a pressure of the generated CO<sub>2</sub> gas, yielding higher cell openness of the foam.

The underlying mechanism of the reactive cell opening is schematically illustrated in **Fig. 4.3.6(a)**. Without PEG 2000, most of the cell windows are closed with cell walls. However, with PEG 2000, the cell walls cannot be stabilized enough because the cell opening is hastened before the cellular structure is formed completely. Different amounts of the cell opener, 0 wt%, 3 wt%, and 6 wt% PEG 2000, were added to Reactant A to fabricate foams with distinct cell openness. The prepared samples were coded as P0, P3, and P6 by following the weight fraction of the cell opener.

Microstructure of the fabricated samples was observed by using the SEM (**Figs. 4.3.6(b-d)**). **Figure 4.3.6(b)** shows a fully-closed cell structure of the P0 sample with few defects. The defects are scars generated while preparing the specimen. For the P0 sample having 0% cell openness, sound waves hardly propagate in the porous medium due to the absence of open pores and the waves cannot even penetrate into the inner domain. Hence, the closed cell foam acts as a poor sound absorber. As shown in **Figs. 4.3.6(c-d)**, it was found that closed cell walls were opened by embedding PEG 2000 in the resin. The cell openness of the P3 and P6 samples is estimated at about 15% and about 22%, respectively.

All fabricated samples have similar cell size distribution in the vicinity of 500  $\mu\text{m}$  (**Fig. 4.3.7**). The specific dimension of cells for each sample was estimated at  $507 \pm 130$   $\mu\text{m}$  (P0),  $478 \pm 93$   $\mu\text{m}$  (P3), and  $515 \pm 128$   $\mu\text{m}$  (P6). A small difference in cell size between the samples indicates that the rheological change of the resin did not significantly affect the rate of cell nucleation but only the reaction balance.

In fact, if the cell openness could be controlled in a wider range, the optimized cell openness would be experimentally demonstrated more clearly. However, when a larger amount of the cell opener (more than 6 wt%) was added to the resin, the cell structure cannot be formed but destroyed since the cell opening moment would be advanced excessively. Therefore, cell openness higher than 22% could not be experimentally feasible for the PU composition employed in this study. On the other hand, a foam having less than 15% openness could not be obtained because it was difficult to induce a substantial effect when less than 3% of the cell opener was included in the resin. Therefore, the PU foams with 0% (P0), 15% (P3), and 22% (P6) cell openness were fabricated and their sound absorption performance was evaluated and compared with the simulation results.

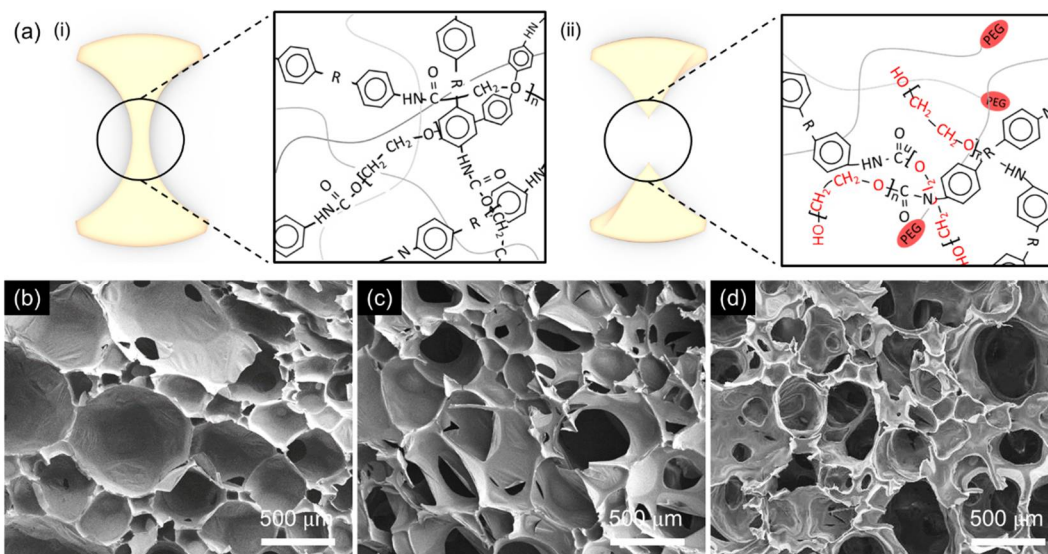


**Figure 4.3.6.** Schematic illustration of reactive cell opening mechanism and SEM images of the fabricated PU foams. (a) Chemical formulas of (i) a closed cell PU foam and (ii) a semi-open cell PU foam during the foaming reaction. (b-d) SEM images of the fabricated samples; P0 (0% openness), P3 (15% openness), and P6 (22% openness).

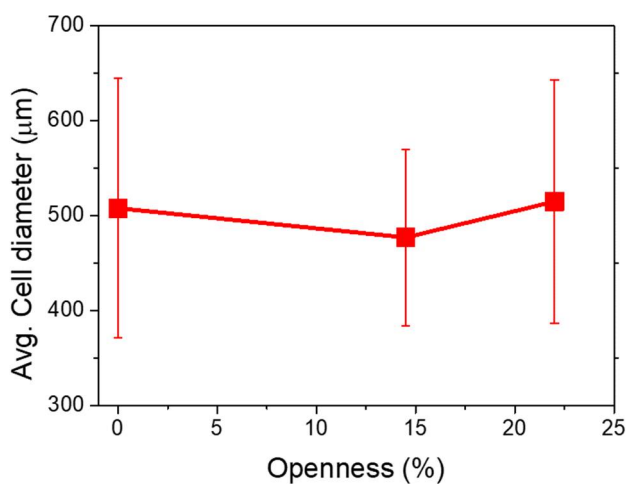


**Figure 4.3.7.** Cell size distribution of the fabricated PU foam samples.

#### 4.3.4.3. Sound absorption performance

Sound absorption coefficients of all specimens were characterized experimentally by using the B&K impedance tube. Both empirical and numerical results are shown in **Fig. 4.3.8(a)**. Simulation of the P0 sample could not be performed because only the visco-inertial and thermal damping was considered in the numerical modeling.

As expected from the SEM image, the P0 sample exhibited poor sound absorbing performance due to the absence of the path of propagating acoustic waves. Except for the area near the maximum peak value, all values of the sound absorption coefficient of the P0 sample were measured to be 0.2 or less. On the other hand, the P6 sample having 22% cell openness dissipated much more sound energy than the P0 sample. The measured curve of P6 lies between the simulation curves for the PUCs with 15% and 25% openness. Furthermore, the measured curve of the P3 sample with 15% openness was located in the lower frequency region than that of the P6 sample case.

The measured peaks frequency of each sample are found at 1792 Hz and 1352 Hz for the P6 and P3 samples, respectively. The sound absorption coefficient at the maximum peak is also increased from 0.84 (P6) to 0.92 (P3) (**Fig. 4.3.8(e)**). The simulation result given by using the 15% openness PUC coincides well with the experimental data of the P3 sample. It is clear that the difference in cell openness between the two samples is a major contributor to improvement of the sound absorption behavior at low frequencies since the cell sizes of the two samples are approximately the same.

Two evaluating parameters, a root mean square (RMS) and a noise reduction coefficient (NRC), were calculated for both measured and simulated curves to quantitatively analyze noise attenuation performance. RMS was calculated over the major noise frequency range of automobiles, from 0 to 2000 Hz, and the value was denoted to  $\alpha_{rms,2000}$  (**Fig. 4.3.8(c)**). The P3 sample shows the highest  $\alpha_{rms,2000}$  value among the samples, which means that the P3 sample can effectively remove most of noises from the automobiles. NRC is a standard value for evaluating noise reduction performance over the entire frequency range and it is calculated by averaging sound absorption coefficients at 128, 256, 512, 1024, 2048, and 4096 Hz. The P3 sample was also estimated as the best sound absorber according to the NRC curves (**Fig. 4.3.8(d)**) even though the impact is less than for  $\alpha_{rms,2000}$ . This empirical trend matches well with that of the simulation results.

1/3 Octave band spectrogram is a generally used to evaluate subjective responses to noise damping performance. **Figure 4.3.9(a)** shows the octave bands of simulation results for the case of each cell openness. Except for few bands, most bands of the 15% openness PUC scores much higher values than other cases. The simulation results show the same trends with the measured data as shown in **Fig. 4.3.9(b)**.

The assertion for numerical simulation, that the tortuosity dominates the change in sound absorption behavior, was supported by the empirical relationship between  $\tau_\infty$  and sound absorption coefficients of the samples. It was found by comparing the measured  $\tau_\infty$  values with simulation results (see **Fig. 4.3.8(b)**) that the changing trend of the measured results is consistent with the change in the simulated values. Because the P3 sample contains more closed cells, the P3 sample possesses a more complex cellular structure for sound wave propagation and has a higher  $\tau_\infty$  value than the P6 sample. A suitable high content of closed cells in a PU foam can distort the sound wave propagation path and thereby lead to improved sound absorption performance.

To support the causality suggested above, sensitivity analysis was carried out by varying  $\tau_\infty$ , characteristic lengths (VCL and TCL, simultaneously), and  $R_f$ , while maintaining the other poroacoustics parameters. The parameters of the 100% openness PUC were used as the default parameters (**Fig. 4.3.10**). The increase of  $\tau_\infty$  shifts the curves to low frequency ranges, and the decrease of both characteristic lengths induces the higher value of sound absorption coefficients in all frequency region. As expected in the previous section,  $R_f$  does not significantly affect the absorption coefficients due to low density of the foam. Therefore, the enhanced sound damping of the foam with 15% openness (P3) at low frequency originates from the narrow and complex sound propagating path in the foam.

The measured sound absorption performance of the P3 sample and the 80 kg/m<sup>3</sup> density PU foam developed in Section 4.2 [315] were compared with each other to emphasize the significance of this study. The performance of the P3 sample is comparable with that of the 80 kg/m<sup>3</sup> foam (**Fig. 4.3.11(a)**). The maximum peak frequency of the P3 sample is even lower than that of the 80 kg/m<sup>3</sup> foam. It can be seen from the RMS and NRC values that the P3 sample has the best sound absorption performance as shown in **Figs. 4.3.11(b-c)**.

Generally, higher density foams show better performance on low frequency noise damping due to their complex microcellular geometry which originates from the small interconnecting pores connecting adjacent cells. This microstructural feature provokes high flow resistivity and high tortuosity, resulting in slow sound speed in the foam. However, low density PU foams cannot contain narrow interconnecting pores but consist of thin struts or cell walls with large pores. These foams cannot achieve sufficient performance in sound absorption due to excessively high or low cell openness. However, the optimized semi-open cell foams having the best cell openness (15%) enable outstanding sound absorption performance while overcoming the limitation of mass density.

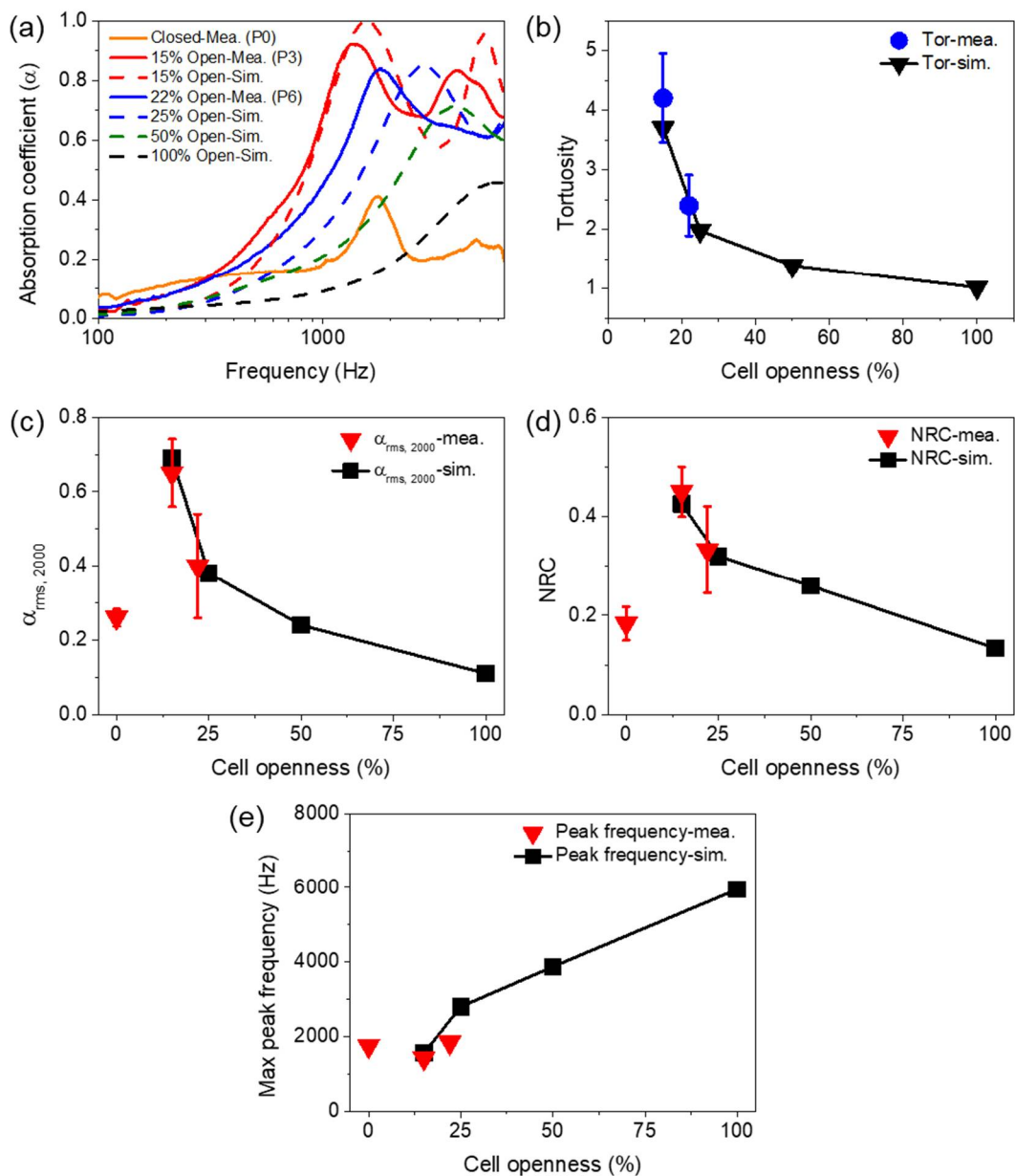


**Figure 4.3.8.** Sound absorption performance of the fabricated PU foams: (a) sound absorption coefficient curves, (b) measured and simulated tortuosity as a function of cell openness, (c) RMS values from 0 to 2000 Hz, (d) NRC values, and (e) shift of maximum peak frequency dependent on cell openness.



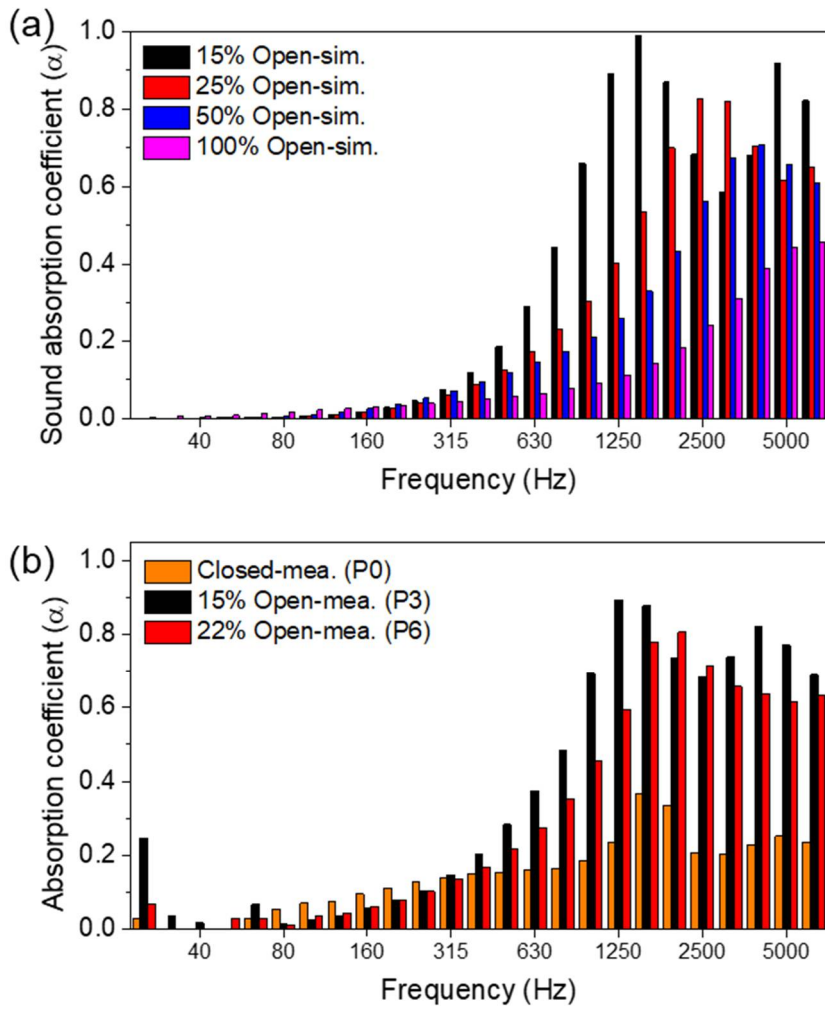
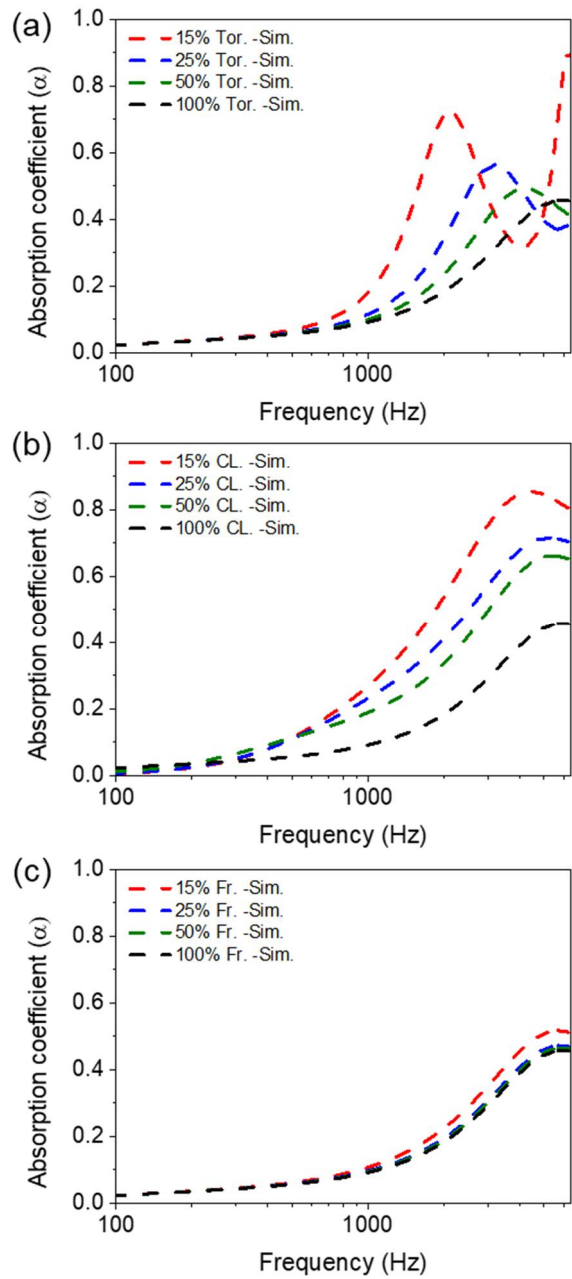
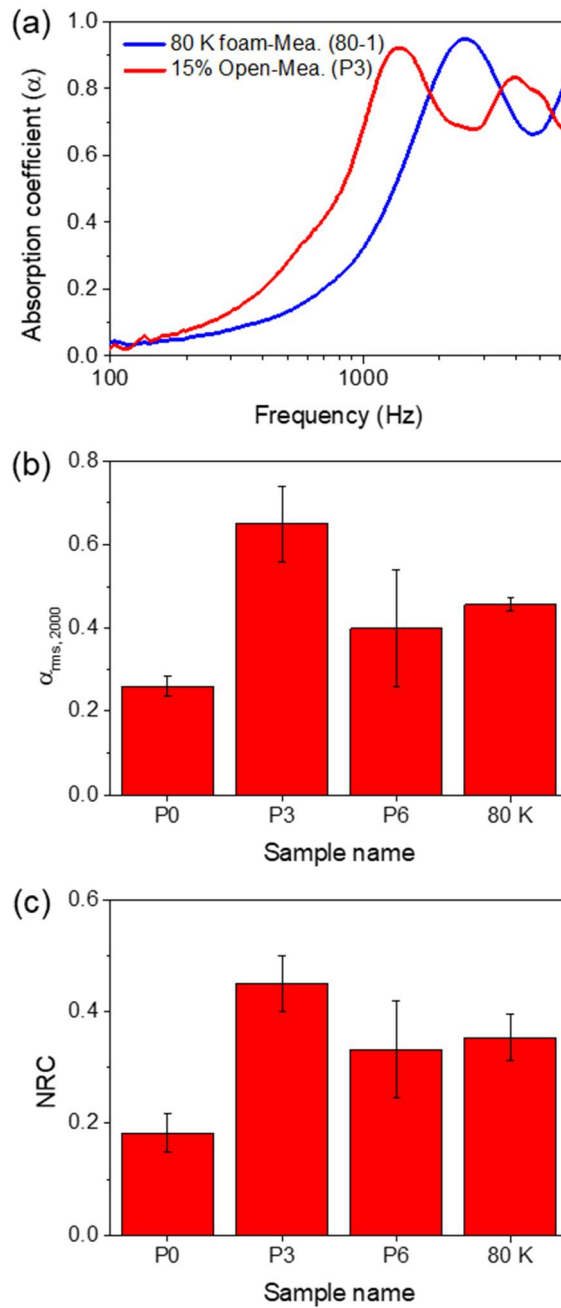


Figure 4.3.9. 1/3 octave bands for (a) the simulation results and (b) the measurement results.



**Figure 4.3.10.** Sensitivity analysis for (a) tortuosity (Tor.), (b) characteristic lengths (CL.), and (c) flow resistivity (Fr.).



**Figure 4.3.11.** Comparison of sound absorption performance between the P3 sample and the 80 kg/m<sup>3</sup> sample developed in Section 4.2: (a) sound absorption coefficient curves, (b) RMS values from 0 to 2000 Hz, and (c) NRC values.

### 4.3.5. Conclusions

In this section, the cell-openness modulated poroacoustic meta-absorber was theoretically investigated and experimentally implemented. The optimum openess for PU foams was predicted as 15% when that cell diameter is 500  $\mu\text{m}$  and mass density is 40  $\text{kg}/\text{m}^3$ . The results of numerical studies prove the importance of cell openness and its influence on tortuosity. Materialization of the foam samples was accomplished by using the reactive cell opening method which incorporates PEG 2000 into the polyol mixture. The measured sound absorption coefficients, RMS, and NRC values are in good agreement with the simulation results, and these values indicate that the foam with 15% cell openness (P3) is the best among other samples. Moreover, the P3 sample of 40  $\text{kg}/\text{m}^3$  showed even better sound absorbing performance than the 80  $\text{kg}/\text{m}^3$  density foam, breaking the existing stereotype. It is worth noting that this work opens a pathway to mitigation of minimum mass density criteria for damping of low frequency noises. For industrial applications, the engineered material in this study can be applied to transportation vehicles for more economical noise damping by accomplishing lightweight body.

## 4.4. Hybrid microstructured PU foam

### 4.4.1. Introduction

Polyurethane (PU) foams with a porous microstructure are widely utilized for sound absorption [315,316] and thermal insulation [286,343]. Energy fields passing through the porous structure are dissipated or blocked effectively due to its complex structural characteristics. Among them, the sound absorption capability has improved our quality of life by eliminating troublesome noises. Sound waves propagating through the foam are mainly eliminated by the visco-inertial and thermal damping rather than the viscoelastic damping, because the volume fraction of a solid part in the foam is much smaller than that of the air [275,276]. The visco-inertial and thermal damping diminishes acoustic pressure magnitude by viscous friction and thermal exchange on solid-air interfaces [277–279]. Therefore, manipulating and optimizing microcellular structures can induce the improved sound absorption of foams without increasing density or foam thickness as discussed in Sections 4.2 and 4.3 [131,326,344,345].

Microcellular structures of sound absorbing foams have been optimized to achieve more advanced performance [132,304,315,341,346,347]. There are two significant structural parameters that affect sound absorbing behavior of the microcellular foam; cell size and cell openness. In Section 4.2, optimized cell size was predicted by carrying out multiscale poroacoustics simulation, and the PU foam having the optimized cell size was fabricated by using an ultrasonic foaming method [315]. Also, in Section 4.3, a theoretical study on optimized cell openness was attempted with the same simulation method as above, yielding the best semi-open cell PU foam with superior performance to the double density foam [316]. In addition, various studies have been carried out on the microcellular structure theoretically or experimentally [341,348].

Meanwhile, fabrication of composite foams is another strategy to improve sound absorbing performance [292,295,349]. The previous researches about composite foams have provided a meaningful pathway to improve sound absorbing performance of polymeric foams. However, the nanocomposites manufacturing strategy has focused on the damping property of the material itself without considering the main mechanism of sound

absorption of foams. Therefore, this strategy cannot provide an effective way to reduce density of foams or to significantly improve the sound absorption performance of existing foams.

Generally, sound absorbing foams have a relatively high density of about  $80 \text{ kg/m}^3$  since they require a certain compressive stiffness and a complex microcellular structure. Hence, low density open cell PU foams cannot be used as a sound absorber because of poor sound absorbing performance and mechanical vulnerability. The cell openness control discussed in Section 4.3 can achieve good sound absorption of a low density ( $40 \text{ kg/m}^3$ ) foam. However, it is very difficult to precisely control the cell openness with chemical additives, and this method may possibly deteriorate other material properties. In addition, conventional sound absorbing PU foams have failed to achieve good performance in thermal insulation since the thermal energy flows facilely through open cell media [343,350]. The easy heat flow occurred because the open cell structure allows the convection heat transfer through the open walls.

The present work proposes a conceptual design of the unique hybrid microstructures with low density, superior sound absorption, and multifunction. The proposed structures consist of polystyrene hollow microbeads ( $40 \text{ kg/m}^3$  density) and microstructure of an open cell PU foam ( $40 \text{ kg/m}^3$  density). The materials with hybrid microstructures are named as syntactic hybrid foams (SHFs). Periodic unit cells (PUCs) were constructed based on the design of ideal porous structures for a bare foam (BF) and SHFs. Multiscale poroacoustics simulation was carried out, and sound absorption coefficient curves were obtained theoretically for different periodic unit cells (PUCs) and compared each other. Mechanical and thermal insulation properties of PUCs were also investigated numerically, and effective material properties were evaluated.

#### 4.4.2. Design of syntactic hybrid foams

A syntactic foam is a composite material fabricated by embedding hollow particles into polymer [351–353] or metal [354,355] matrices to achieve low density and high specific stiffness, simultaneously. By using the concept of the syntactic foam, the hybrid microstructures were designed by stacking spherical microbeads in the microcellular matrix of an open cell polyurethane (PU) foam.

The strength of this microstructure design strategy is attributed to the ability to implement more complex microcellular structures without increasing density. The embedded particles (*i.e.*, closed cell PS (polystyrene) microbeads) can create closed cell regions in the open cell matrix, generating more complex microstructures. The difference from conventional syntactic foams is the scale of incorporated particles and the state of the matrix. Two ideal conditions were assumed; the PS microbeads do not affect the shape of the microcellular structure of the PU foam and are precisely stacked following lattice points of typical crystal structures. In other words, the PS beads can obstruct the open space of the PU foam and act as closed cells by just occupying the space. Therefore, the composite foams have a synergistic hybrid microstructure composed of both open and closed cells, as well as the hybrid material composition of PS and PU. A conceptual illustration is shown in **Fig. 4.4.1(a)** and these composite materials were named as syntactic hybrid foams (SHFs).

Periodic unit cells (PUCs) representing each hybrid foam microstructure were designed and constructed by using a CAD (computer-aided design) program. A tetrakaidecahedron cluster, as used in Sections 4.2 and 4.3, was employed as a basic structure since this polyhedron is an widely used geometry when mimicking an ideal microcellular structure of a PU foam in numerical analysis [278,309]. The diameter of microcells of the PU foam was set as 600  $\mu\text{m}$ , and the density was fixed to 40  $\text{kg}/\text{m}^3$  yielding the porosity of 0.96. After imparting a hexahedron that has sliced planes making periodic surfaces of the unit cell, Boolean operation was executed to generate the hexahedron unit cell containing the tetrakaidecahedron geometry. The hexahedron unit cell was scaled in y-direction to yield a cubic-shape unit cell. This anisotropic scaling process was essential to place the spheres into the crystal lattices, precisely. Then, PUC of BF (a

bare foam) was obtained and its specific dimension is  $848.264 \times 848.264 \times 848.264 \mu\text{m}^3$  (**Fig. 4.4.1(b), (i)**).

PUCs of three syntactic hybrid foams (SHFs) were constructed by combining BF with the PS beads. The PS bead is a hollow concentric sphere. The shell thickness was  $5 \mu\text{m}$  to fix the density of the PS beads to  $40 \text{ kg/m}^3$ . The PS beads were located at lattice points resembling those of the cubic unit cells. Each SHF was denoted to SC (simple-cubic)-SHF, BCC (body-centered-cubic)-SHF, and FCC (face-centered-cubic)-SHF. The radius of the PS beads for each SHF PUC was different to satisfy the packing geometry;  $420 \mu\text{m}$  for SC-SHF,  $365 \mu\text{m}$  for BCC-SHF, and  $290 \mu\text{m}$  for FCC-SHF. The different sizes of the beads can affect the performance of the SHFs. However, the bead size should be varied in order to implement the close packing structure properly. All constructed PUCs of the SHFs are shown in **Fig. 4.4.1(b)**. Overall density was not changed even after embedding the microbeads since they have the exactly same density with the BF PUC.

The constructed PUCs were used in three FEM (finite element method) numerical simulations; multiscale poroacoustics simulation, structural simulation, and heat transfer simulation. In the poroacoustics simulation, the fluid (air) domain was only considered due to the rigid frame conditions assumed in the JCA model. Meanwhile, only solid structures (PU and PS) were regarded in the structural analysis under the assumption that the modulus of gas domain is negligible. In the heat transfer analysis, both solid (PU and PS) and fluid domains (air and butane gas) were solved with the material properties (**Table 4.4.1**).



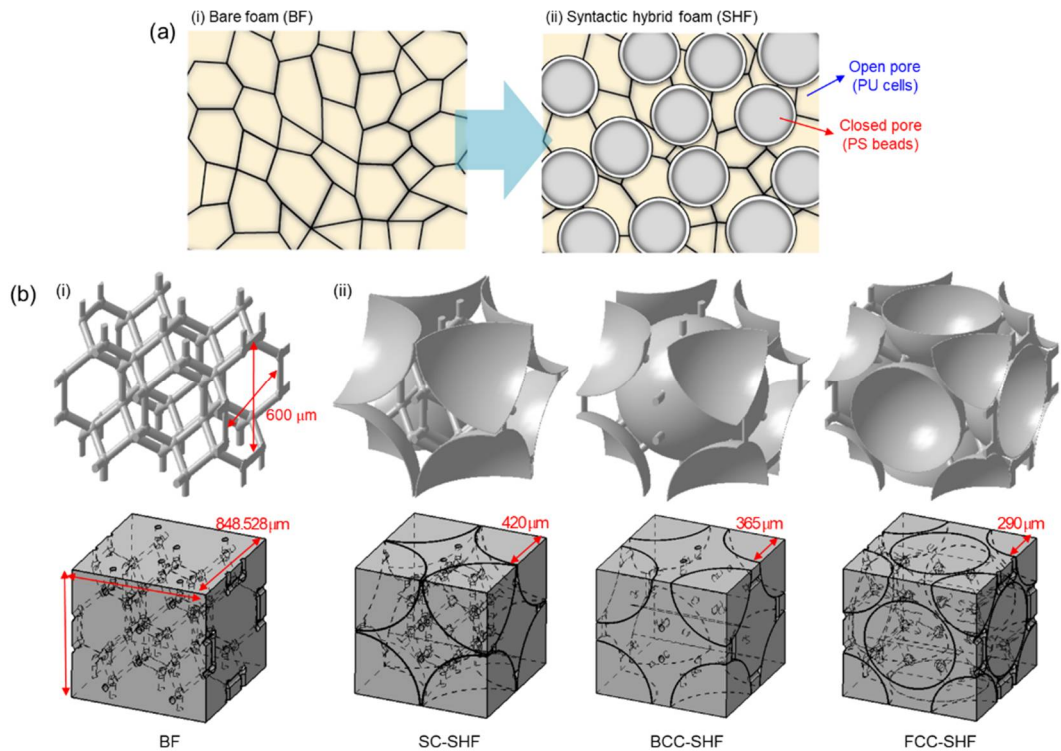


**Figure 4.4.1.** Design strategy for syntactic hybrid foams (SHFs). (a) Schematic illustration of microcellular structures of (i) an open cell bare foam (BF) and (ii) a syntactic hybrid foam (SHF) with PS microbeads. (b) Constructed PUCs showing solid frames (upper) and fluidic domains (lower); (i) PUC of BF, (ii) PUCs of SHFs for SC-SHF, BCC-SHF, and FCC-SHF.

**Table 4.4.1.** Material properties employed in the simulations.

	Polyurethane	Polystyrene	Air	Butane
Density ( $\text{kg}/\text{m}^3$ )	1200	1050	1.2	2.5
Elastic modulus (MPa)	360	3000	-	-
Poisson's ratio (-)	0.34	0.34	-	-
Thermal conductivity ( $\text{mW}/\text{m}\cdot\text{K}$ )	240	100	24	15
Specific heat ( $\text{J}/\text{kg}\cdot\text{K}$ )	1760	1200	1000	1580
Specific heat ratio (-)	-	-	1.4	1.1
Emissivity (-)	0.8	0.8	-	-

### 4.4.3. Numerical analysis

#### 4.4.3.1. Multiscale poroacoustics simulation

The same numerical simulation described in Section 4.2.3 was conducted by using the multiscale poroacoustics method. The purpose of this simulation is to analyze theoretically how the hybrid microstructures affect the improvement of sound absorption performance.

#### 4.4.3.2. Heat transfer simulation

Fourier's heat conduction equation was employed as a governing equation for modeling conductive heat transfer as

$$\nabla \cdot (k\nabla T) = Q \quad (4.4.1)$$

, where  $k$  is the thermal conductivity of each material,  $T$  is the temperature, and  $Q$  is the external heat source. The heat conduction equation (**Eqn. 4.4.1**) was solved by using a finite element method code assuming steady state and no heat accumulation. Hot (393 K) and cold (293 K as room temperature) temperature boundary conditions were applied in  $z$ -direction of PUCs. Convective heat transfer could be neglected in the simulation because the cell sizes of PUCs are smaller than 1.5 mm [356]. Radiation heat transfer was considered in the simulation as a boundary condition by defining radiation heat flux ( $\mathbf{q}_{rad}$ ) at the surface of the solid frame as

$$-\mathbf{n} \cdot \mathbf{q}_{rad} = \varepsilon\sigma(T_{amp}^4 - T^4) \quad (4.4.2)$$

, where  $\varepsilon$  is the emissivity,  $\sigma$  is the Stefan-Boltzmann constant,  $T_{amp}$  is the ambient temperature, and  $\mathbf{n}$  is the normal vector to the solid surface. All employed material properties are listed in **Table 4.4.1**.

Effective thermal conductivity ( $k_{eff}$ ) of each PUC was evaluated by processing the heat flux data obtained from the simulation results. Heat flux magnitude of each domain in PUC ( $q_i$ , W/m<sup>2</sup>) was obtained in each propagating direction ( $i=x$ ,  $y$ , and  $z$ ). From a microscale perspective, it can be assumed that the whole unit cell owns the uniform isothermal property [357,358]. Therefore, the overall heat flux of PUC in each direction ( $\langle q_i \rangle$ ) was calculated by averaging heat flux values in entire domains. From the overall heat

flux of PUCs, the average thermal conductivity of each PUC ( $k_{eff,i}$ ) in the x, y, and z direction was evaluated as

$$k_{eff,i} = \frac{\langle q_i \rangle}{\partial T / \partial x_i} \quad (4.4.3)$$

, where  $i = x, y,$  and  $z$ . The thermal conductivities in each of the three axial directions are calculated differently since all PUCs have anisotropy. Consequently, the effective thermal conductivity ( $k_{eff}$ ) was determined as the magnitude of the  $k_{eff,i}$  matrix.

#### 4.4.3.3. Structural analysis simulation

Structural stress analysis was performed using a finite element method to confirm the mechanical improvement of the SHFs. Fixed boundary conditions were used at the bottom surfaces of PUCs to prevent movement under the simulation, and periodic boundary conditions were applied on the lateral surfaces. 2% compressive strain was applied to PUCs by pressing a rigid plate under the assumption of linear elasticity. The used material properties, density, elastic modulus, and Poisson's ratio of PU and PS, are listed in **Table 4.4.1**.

As a result of the structural analysis, von Mises stress contours were obtained in the deformed state and the stress distribution of each PUC was visualized. For the quantitative evaluation, effective elastic modulus ( $E_{eff}$ ) of each PUC was calculated from the simulation results. The total applied stress to PUC was calculated from the magnitude of the force over the contact area of PUC. Then  $E_{eff}$  was evaluated from the linear relationship between effective stress and effective strain.

#### 4.4.4. Results and discussion

##### 4.4.4.1. Sound absorption behavior

Sound absorption performance of each SHF (syntactic hybrid foam) containing the microstructure of the designed PUCs was predicted numerically by using the multiscale poroacoustics method. The microscale simulation results for all PUCs (periodic unit cells) are shown in **Figs. 4.4.2(a-d)**. By embedding the PS beads, the streamlines in PUCs of SHFs have a more distorted shape compared to those in PUC of BF (bare foam) in both microscale analyses. The complex shape of streamlines indicates that the path of propagating sound waves in the SHFs is more intricate such as inside higher density foams [315,316]. It is meaningful that the complex inner structure can induce more powerful noise damping ability especially in low frequency ranges since the speed of sound waves becomes slower. Hence, the inner microstructure of the SHFs leads to higher flow resistivity ( $R_f$ ) and tortuosity factor ( $\tau_\infty$ ). For example, the tortuosity of BF is 1.06, but it increases to 3.47 for BCC-SHF, which is more than tripled. In other words, the complexity of a sound wave path can increase more than three times in the SHFs, as shown in the best case of BCC-SHF. The highest value of flow resistivity is  $25838 \text{ N}\cdot\text{m}^4\cdot\text{s}$  for FCC-SHF, due to their high volumetric fraction of the PS beads. Also, the characteristic lengths (thermal characteristic length and viscous characteristic length) decrease in proportional to the radius of the inserted beads in each PUC of SHFs. All calculated poroacoustics parameters are listed in Table 4.4.2.

The pressure acoustics simulation was performed at macroscale by using the poroacoustics parameters tabulated in **Table 4.4.2**. **Figure 4.4.3** displays (i) the background and (ii-v) the scattered sound pressure fields generated in the B&K standing wave tube for each foam. BF could not sufficiently attenuate sound waves at all frequencies due to its low tortuosity ( $\tau_\infty$ ) and flow resistivity ( $R_f$ ). Meanwhile, the scattered sound pressure fields by SHFs have very low intensity compared to that of BF, showing that the sound absorption performance was drastically improved. FCC-SHF and BCC-SHF showed the best sound damping efficiency among all foams since they contain the most complex internal structure described through the tortuosity. The color surfaces and line graphs of the pressure profiles in **Fig. 4.4.3** intuitively present the reduced pressure magnitude after installing the foam

domains in the tube.

Theoretical sound absorption coefficient ( $\alpha$ ) curves were obtained from the sound pressure fields as shown in **Fig. 4.4.4(a)**. The theoretical sound absorption coefficient of the 80 kg/m<sup>3</sup> PU foam (80-1) calculated in Section 4.2 was added to the figure to confirm the possibility that SHFs can overcome the density limitation and to compare sound absorption performance with each other. At first, BF exhibits poor sound absorption performance because there is no disturbance for sound propagation, as confirmed in the poroacoustics parameters evaluation. However, sound absorption performance of the SHFs is comparable to that of the 80 kg/m<sup>3</sup> foam because of its complicated sound path. The maximum peak frequency is shifted from 5744 Hz for BF to 1512 Hz for the FCC-SHF due to an increase in the tortuosity factor ( $\tau_{\infty}$ ). Moreover, the sound absorption coefficients for FCC-SHF in the overall frequency range are also much higher than those for BF. BCC-SHF also reveals the similar behavior to FCC-SHF. Stacking the PS beads in simple-cubic lattices (SC-SHF) also heightens the performance but cannot exceed the performance of the 80 kg/m<sup>3</sup> open cell foam because of the lack of complexity.

Several noise damping parameters were estimated for quantitative analyses (**Fig. 4.4.4(b)**); RMS (root mean square) and NRC (noise reduction coefficient). Three parameters, *i.e.*, RMS 0-2000 for low frequency noise damping from 0 to 2000 Hz, RMS 4000-6400 for high frequency noise damping from 4000 to 6400 Hz, and NRC, were evaluated. RMS 0-2000 and NRC have the greatest values in FCC-SHF, 7 times and 4 times higher than those of BF, respectively. In RMS 4000-6400, BCC-SHF have the highest value.

As an additional analysis, 1/3 octave band spectrogram is suggested in **Fig. 4.4.4(c)**. Octave band spectrograms are often used to quantify sound absorption performance from a human perspective. Most bands of BCC-SHF and FCC-SHF score much higher values than those of the 80 kg/m<sup>3</sup> PU foam except for few bands. These results are remarkable because the density of BF and SHFs is only 40 kg/m<sup>3</sup>, which is half of 80 kg/m<sup>3</sup>.

The reason for the enhancement of sound absorption should be investigated to explain the underlying principle enabling this. The complex parameters were calculated to suggest the principle (**Fig. 4.4.5**). All values were normalized with the basic air properties. Effective bulk density ( $\rho(\omega)$ ) and effective bulk modulus ( $K(\omega)$ ) indicate that air in the SHFs has very high effective density and low effective modulus. This trend implies that inclusion of

the PS beads in BF leads to a more complex microcellular foam, thereby slowing the phase speed of sound without increasing density of the solid frame.

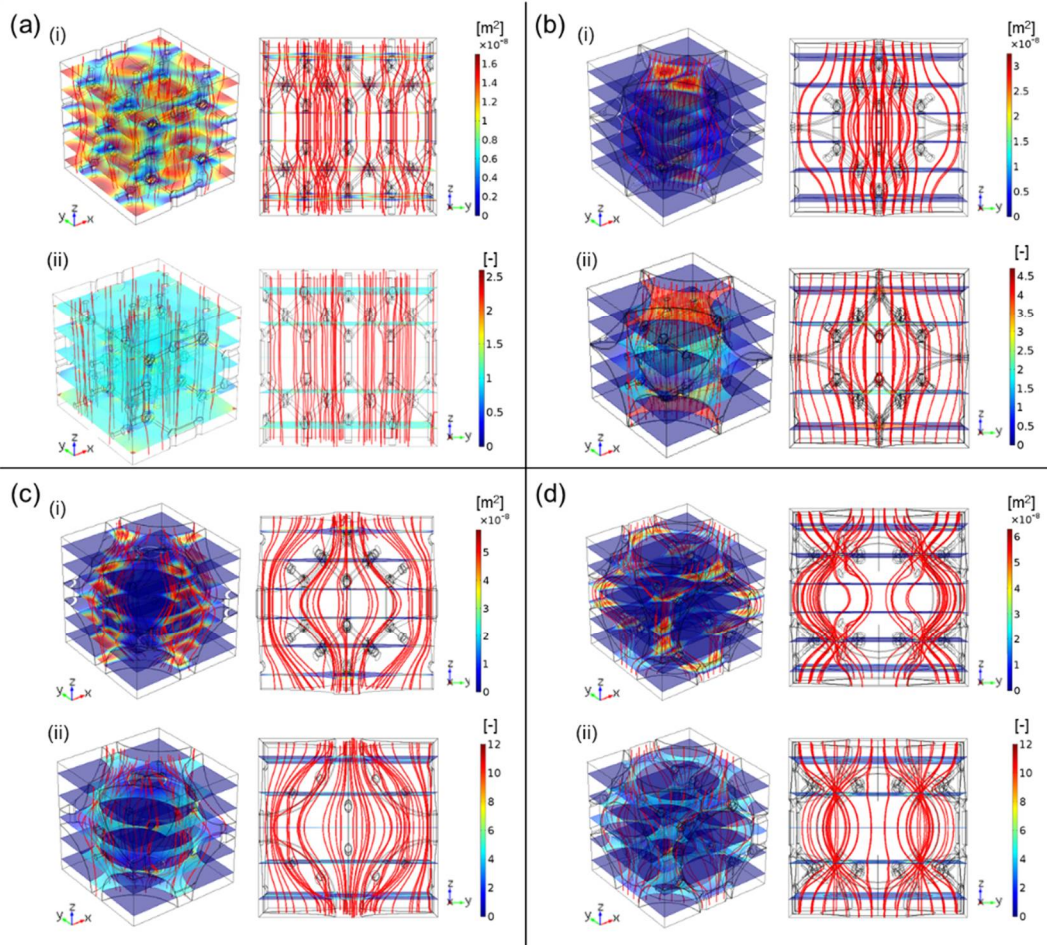


**Figure 4.4.2.** Microscale flow analysis results for PUCs of (a) BF, (b) SC-SHF, (c) BCC-SHF, and (d) FCC-SHF. (i) and (ii) show the permeability fields and the scaled electric fields as a solution to the viscous flow problem and the inertial flow problem, respectively.

**Table 4.4.2.** Calculated poroacoustics parameters for JCA model.

	BF	SC-SHF	BCC-SHF	FCC-SHF
Porosity, $\epsilon_p$ (-)	0.96	0.96	0.96	0.96
Flow resistivity, $R_f$ (N·m <sup>4</sup> ·s)	2085	5954	11209	25838
Tortuosity, $\tau_\infty$ (-)	1.06	2.59	3.47	3.31
Viscous characteristic length, $L_v$ ( $\mu\text{m}$ )	356	110	75	49
Thermal characteristic length, $L_{th}$ ( $\mu\text{m}$ )	539	220	118	127

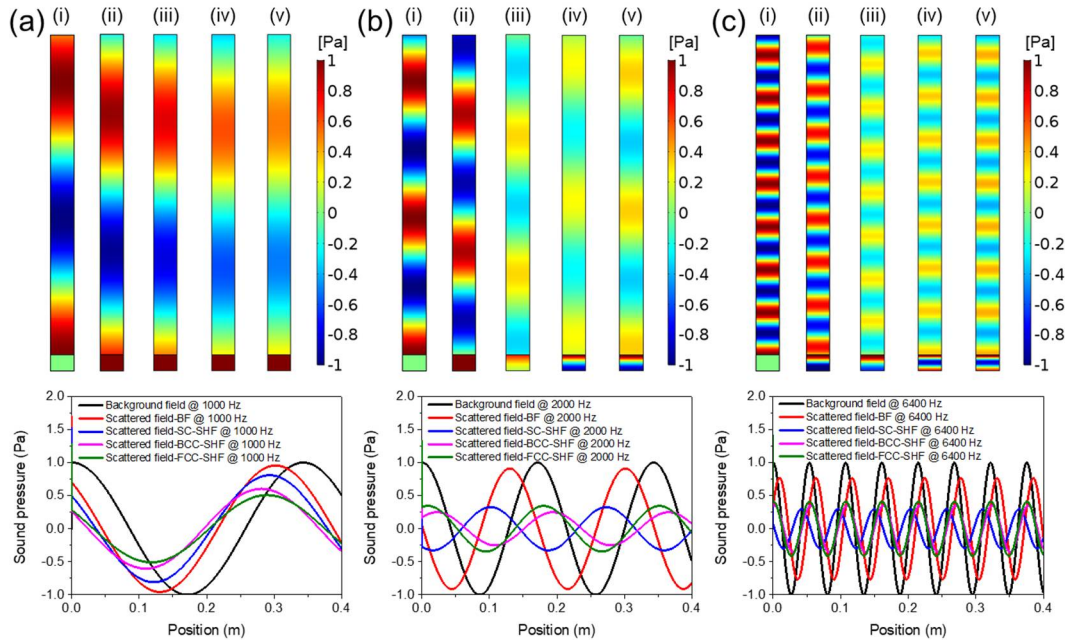


**Figure 4.4.3.** Macroscale pressure acoustics simulation results for different incident pressure wave frequencies: (a) 1000 Hz, (b) 2000 Hz, and (c) 6400 Hz. (i) shows the background pressure field and (ii-v) show the scattered pressure fields affected by BF, SC-SHF, BCC-SHF, and FCC-SHF, respectively. The line graphs below display pressure profiles for each case.

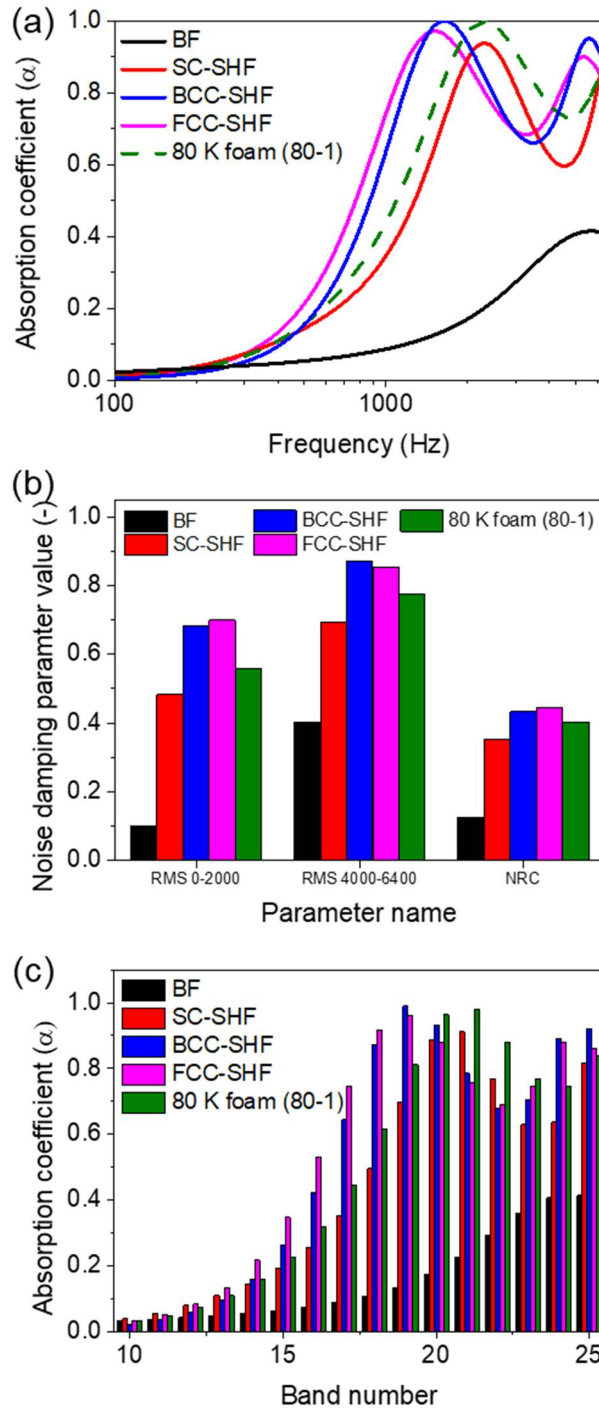


**Figure 4.4.4.** Sound absorption performance of the foams with BF, SC-SHF, BCC-SHF, and FCC-SHF. (a) Sound absorption coefficient curves. (b) Noise damping parameter values; RMS (root mean square) 0-2000, RMS 4000-6400, and NRC (noise reduction coefficient). (c) 1/3 octave band spectrograms.



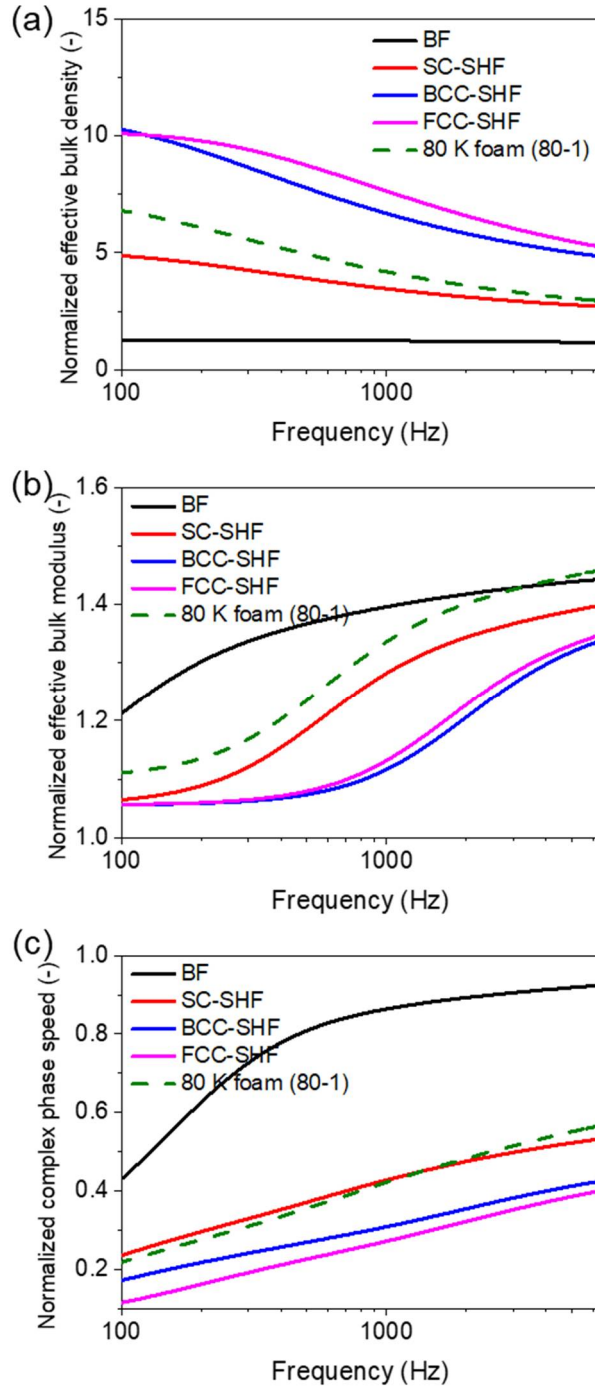


**Figure 4.4.5.** Comparison of the acoustical complex variables of the porous domain; (a) normalized effective bulk density, (b) normalized effective bulk modulus, and (c) normalized complex phase speed.

#### 4.4.4.3. Thermal and mechanical behavior

Additional numerical analyses were conducted for heat transfer and compressive mechanical behaviors. Thermal insulation characteristics of each PUC were identified by the heat transfer simulation. In general, fully open cell foams cannot elicit satisfactory thermal insulation performance compared to closed cell foams [357]. Low thermal conductivity gases (*e.g.*, carbon dioxide, butane, and cyclopentane) encapsulated in closed cells contribute to good thermal insulation of fully closed cell foams. In this sense, incorporating the PS beads, which are usually expanded with butane gas, into the PU foam can lead to the similar effect as containing closed cells because each PS bead acts as one large closed cell.

**Figures 4.4.6(a-d)** show the total heat flux magnitude of all PUCs. In the simulation, the heat radiation was considered by setting the surfaces of a solid frame as a heat source. Therefore, heat flux magnitude in the same domain varies depending on the position due to the effect of radiative heat transfer, unlike consideration of heat conduction only. That is, the closer to the hot top surface, the more heat flux is generated. Another noteworthy point in these figures is that the heat flux depends on the kind of materials, such as PU, PS, air, and butane gas. The heat flux magnitude of the SHFs is lower than that of BF since the butane gas in the PS beads has a very low thermal conductivity of 15 mW/m·K. This trend can hamper heat transfer in the SHFs more efficiently.

Effective thermal conductivity ( $k_{eff}$ ) of each PUC was calculated to quantitatively compare thermal insulation performance with each other (**Fig. 4.4.6(e)**). The effective thermal conductivity of BF was estimated to 29.8 mW/m·K, which is similar to a general thermal conductivity value of open cell PU foams in the references [359,360]. The effective thermal conductivity of the SHFs decreased due to their hybrid composite structures; 23.0 mW/m·K for SC-SHF, 20.1 mW/m·K for BCC-SHF, and 22.1 mW/m·K for FCC-SHF. Among them, the best thermal insulator was rated BCC-SHF since it has the lowest effective thermal conductivity due to the lowest cell openness. Cell openness is defined as the ratio of the area of opened cell walls to that of the entire cell walls in PUC. The cell openness of each PUC was calculated as 100% for BF, 75% for SC-SHF, 35% for BCC-SHF, and 40% for FCC-SHF. The difference in the effective thermal conductivity between BF and BCC-SHF was 10 mW/m·K, indicating 30% reduction. Furthermore, the value of

20.1 mW/m·K itself is a thermal conductivity that is very hard to reach when using ordinary thermal insulation materials.

Mechanical robustness is a significant property for enhancing durability of porous materials. Many composite foams have been reported to achieve this purpose by embedding micro-/nanoscale particles or fibers into matrices [361,362]. The mechanical properties of the PUCs were investigated by carrying out the structural analysis under the compression condition. **Figures 4.4.7(a-d)** show von Mises stress contours after applying 2% compressive strain to the PUCs. All PUCs of SHFs withstand higher stress than PUC of BF, especially in the PS domain. The quantitative comparison was possible by calculating the effective compressive modulus ( $E_{eff}$ ) for each case (**Fig. 4.4.7(e)**); 39.7 Pa for BF, 324.2 Pa for SC-SHF, 593.3 Pa for BCC-SHF, and 402.4 Pa for FCC-SHF.

There are several reasons to make the hybrid microstructures mechanically stronger. First, PS (polystyrene), which is the material of the microbeads, has about 10 times higher elastic modulus than PU (polyurethane), 3 GPa. Secondly, the enclosed shape of the microbeads can help endure more forces against the compression. The synergistic effect of these two features reinforces the hybrid microstructures and induces more than 10 times higher effective modulus. Experimental realization of these hybrid microstructures is an innovative way that can simultaneously improve both thermal insulation and sound absorption performance with high mechanical robustness.

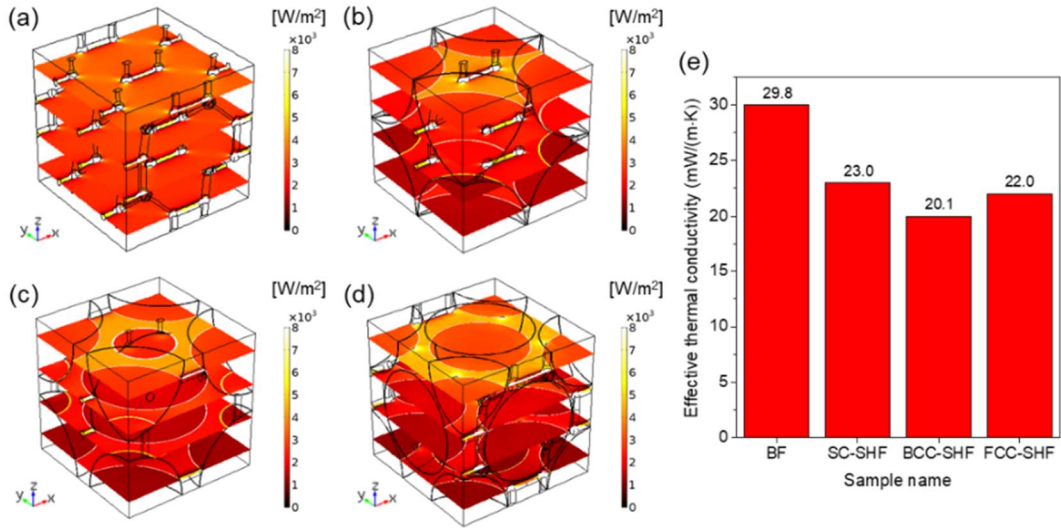


**Figure 4.4.6.** Heat transfer simulation results. Heat flux magnitude in z-direction for (a) BF, (b) SC-SHF, (c) BCC-SHF, and (d) FCC-SHF. (e) Effective thermal conductivities.

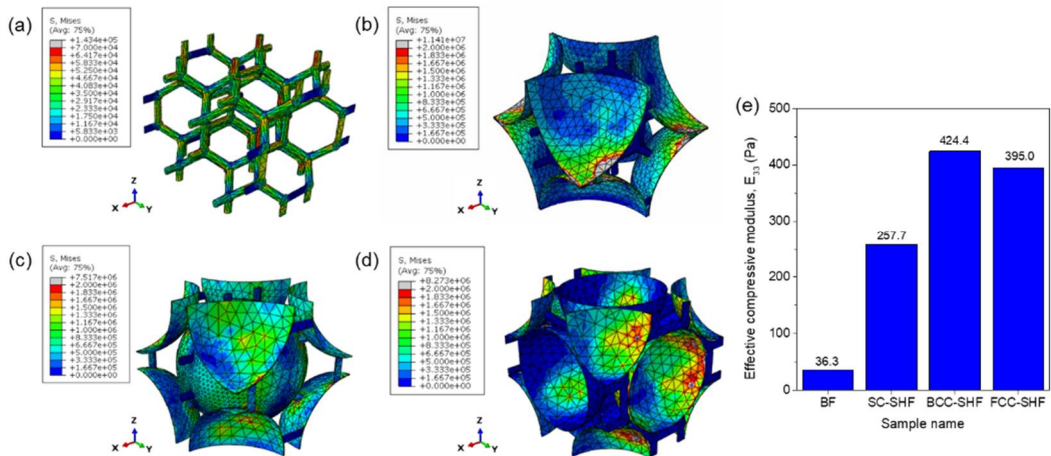


**Figure 4.4.7.** Microscale structural analysis. Mises stress contours for (a) BF, (b) SC-SHF, (c) BCC-SHF, and (d) FCC-SHF, after applying 2% compressive strain in z-direction. (e) Effective compressive moduli.

**Table 4.4.3.** Evaluated material properties calculated from poroacoustics, thermal, and mechanical simulation.

	BF	SC-SHF	BCC-SHF	FCC-SHF
Max peak frequency (Hz)	5744	2304	1640	1512
RMS 0-2000 (-)	0.099	0.483	0.683	0.699
RMS 4000-6400 (-)	0.350	0.749	0.814	0.802
NRC (-)	0.124	0.350	0.432	0.445
$\alpha$ at 1000 Hz (-)	0.086	0.346	0.636	0.742
$\alpha$ at 2000 Hz (-)	0.171	0.894	0.938	0.881
$\alpha$ at 4000 Hz (-)	0.360	0.625	0.693	0.739
$k_{eff}$ (mW/m·K)	29.8	23.0	20.1	22.0
$E_{eff}$ (MPa)	36.3	257.7	424.4	395.0

#### 4.4.5. Conclusions

The hybrid composite microstructures that present design direction for a poroacoustic meta-absorber were reported in this section. The PUC (periodic unit cell) of BF (a bare foam) was modeled under the conditions of 600  $\mu\text{m}$  cell diameter and 40  $\text{kg}/\text{m}^3$  density. The three PUCs of SHFs (syntactic hybrid foams) were constructed by resembling three different cubic unit cell lattices; SC (simple-cubic)-SHF, BCC (body-centered-cubic)-SHF, and FCC (face-centered-cubic)-SHF. The multiscale poroacoustics modeling was carried out using the modeled PUCs. Unlike the BF case, the SHFs show drastically higher sound absorbing performance which originates from the complex inner microstructure created by the embedded PS beads. The heat transfer and the structural analyses also prove the multifunctional properties of the SHFs. The underlying mechanisms for all these improvements were figured out theoretically and the reasonable cautions were also suggested. Although it is hard to produce the ideal structure proposed in this study, it is worth noting that this work opens a new chapter to design multifunctional and advanced porous materials showing high sound absorption, thermal insulation, and mechanical robustness, simultaneously, even with low density.

## 4.5. Summary

This chapter presents the strategies for the poroacoustic meta-absorbers to overcome macroscopic limitations of industrial sound absorbing PU foams, by designing and realizing desired microcellular structures. In Sections 4.2 and 4.3, the optimized microcellular structures were modeled and materialized experimentally. The optimum cell size and openness were predicted from the numerical simulation results of multiscale poroacoustics modeling and the PU foams with the optimum microstructures were fabricated by using the ultrasonic foaming method and the reactive cell opening method, respectively. In Section 4.4, the hybrid microstructures were designed by combining the open cell PU foam with the closed cell PS beads. Poroacoustic, thermal, and mechanical properties of the hybrid microstructures were examined numerically. In order to apply the developed sound absorbing metamaterials to actual industrial fields, it is necessary to study not only the mass production process but also the scale up of the foam materials. It is expected that application of the poroacoustic meta-absorbers will not only more effectively control annoying noises, but also lower the density critical point required for sound absorbing materials, thereby bringing about economic effects such as fuel reduction.

# Chapter 5.

## Concluding Remarks

The aim of this dissertation is to propose new types of polymeric metamaterials made of architected micro/nanostructures. Through a full development process of design, numerical analysis, synthesis, fabrication, and experimental analysis, three classes of polymeric metamaterials were successfully materialized; rheological metamaterials, shape memory metasurfaces, and poroacoustic meta-absorbers.

Specific polymeric materials were chemically or rheologically designed to engineer each micro/nano-architected metamaterial and fulfill the respective strategic functions. Polydimethylsiloxane (PDMS) was used to fabricate the rheological metamaterials in a microfluidic device due to its high transparency, transcription ratio, and mechanical flexibility. Shape memory copolyacrylate (SMCPA) was a specially designed smart polymer for preparing the shape memory metasurfaces, which can be triggered at body temperature and reveal high transparency. Rheologically-tuned polyurethane (PU) resin was employed to fabricate the poroacoustic meta-absorbers as a constituent material of the porous microcellular structure.

Development strategies of the metamaterials started with the design of micro/nanostructured unit cells that are capable of achieving the desired peculiar phenomena. The rheological metamaterials required the establishment of microstructured unit cells that manipulate effective viscosity of a specific medium, and the unit cells were numerically designed by installing the precisely sized micropillars. The shape memory metasurfaces were engineered by listing the unit cells of bullet-shaped nanopillars in order to realize a gradually changing subwavelength layer. The poroacoustic meta-absorbers were modeled with the unit cells consisting of tetrakaidekahedron clusters that mimic general microcellular structures. All the unit cells were drawn by using the commercial CAD programs, CATIA and AutoCAD, and subject to numerical simulations using the commercial FEM programs, COMSOL Multiphysics and ABAQUS/CAE with user



subroutines.

Based on the unit cells design and simulations, the effective medium property of each target physical phenomenon was successfully predicted, which indicates fluidic viscosity for the rheological metamaterials, a refractive index and an electrical conductivity for the shape memory metasurfaces, and a bulk modulus and a bulk density for the poroacoustic meta-absorbers. The metamaterials were designed and assembled by mapping the unit cells and were also drawn and numerically simulated by using the aforementioned commercial programs. From the results of the simulation, the performance and function of the metamaterials could be predicted theoretically in advance, and it was possible to produce the precisely-designed metamaterials by inferring what problem occurs and what the solution is.

The metamaterials with the desired micro/nanostructures were produced by using methods tailored to each material. The rheological metamaterials were fabricated by using soft lithography that replicates the elaborate patterned-masters with the PDMS chemical. Nanoscale in-mold polymerization was conducted to engineer nanopattern arrays of the shape memory metasurfaces by filling the low-viscosity SMPAC resin with the nanoheled-master and then initiating in-situ polymerization. The poroacoustic meta-absorbers were prepared using a reaction injection molding process of polyurethane foams assisted by ultrasonic waves and reactive cell openers.

Each polymeric metamaterial demonstrated in each chapter achieved the following performance improvements and showed potentials. The rheological metamaterials (*i.e.*, cloak, concentrator, and rotator) suggest the novel technologies of fluid flow control such as a drag-free space, hydrodynamic energy harvesting, and fluid flow guiding. The shape memory metasurfaces allow to preserve the nanopattern-driven functions even if the pattern is deformed by an external impact, by recovering the deformed pattern using thermal stimulation of body temperature. Specifically, the transparent SMP nanopatterns demonstrated that the damaged antireflective performance by an external impact can be restored by nanopattern recovery. And the CNT embedded nanocomposite patterns doubled the transmission of biometric information, and these patterns also own shape-recovery function. The poroacoustic meta-absorbers enabled the improved sound absorbing performance at low frequencies beyond the macroscale limitations, by designing and

manipulating theoretically optimum microcellular structures of PU foams.

Despite these successes and advancements, the current state of metamaterials faces many limitations and problems. For the rheological metamaterials, the effective viscosity control is a major issue to be pondered for practical applications. The current viscosity control method based on microscale unit cells not only requires impedance matching treatment but also has difficulty in designing complex-shaped metamaterials. Therefore, as a subsequent study, it is necessary to develop a technique for controlling fluidic viscosity itself by using external fields such as magnetic or electric fields. For the shape memory metasurfaces, research is needed to narrow the spacing between nanopatterns and increase the aspect ratio of the nanopattern height. Through such subsequent studies, high-performance techniques for antireflection and biometric information delivery can be achieved. For the poroacoustic meta-absorbers, it is essential to secure a more precise and extensive microcell structure control technology. In particular, manufacturing the designed microcellular structures using 3D printing technology is expected to ensure the production of foams with much better and more efficient sound absorption performance.

In addition to the metamaterials developed and presented in this dissertation, many types of polymer-based metamaterials have been reported. The various strategies, numerical analysis results, and experimental results established in this dissertation are anticipated to provide a plentiful source of inspiration to the researchers involved in the metamaterial field. Also, it is hoped that this dissertation paves a new way to develop unprecedented metamaterials for interdisciplinary phenomena.

## Bibliography

- [1] R.S. Kshetrimayum, A brief intro to metamaterials, *IEEE Potentials*. 23 (2004) 44–46. doi:10.1109/MP.2005.1368916.
- [2] D.R. Smith, J.B. Pendry, M.C.K. Wiltshire, Metamaterials and negative refractive index., *Science*. 305 (2004) 788–792. doi:10.1126/science.1096796.
- [3] R.A. Shelby, D.R. Smith, S. Schultz, Experimental verification of a negative index of refraction, *Science*. 292 (2001) 77–79. doi:10.1126/science.1058847.
- [4] J.B. Pendry, Negative refraction makes a perfect lens, *Phys. Rev. Lett.* 85 (2000) 3966–3969. doi:10.1103/PhysRevLett.85.3966.
- [5] N. Fang, H. Lee, C. Sun, X. Zhang, Sub-diffraction-limited optical imaging with a silver superlens, *Science*. 308 (2005) 534–537. doi:10.1126/science.1108759.
- [6] H. Tao, N.I. Landy, C.M. Bingham, X. Zhang, R.D. Averitt, W.J. Padilla, A metamaterial absorber for the terahertz regime: design, fabrication and characterization, *Opt. Express*. 16 (2008) 7181. doi:10.1364/OE.16.007181.
- [7] M.K. Hedayati, M. Javaherirahim, B. Mozooni, R. Abdelaziz, A. Tavassolizadeh, V.S.K. Chakravadhanula, V. Zaporozhchenko, T. Strunkus, F. Faupel, M. Elbahri, Design of a perfect black absorber at visible frequencies using plasmonic metamaterials, *Adv. Mater.* 23 (2011) 5410–5414. doi:10.1002/adma.201102646.
- [8] U. Leonhardt, Optical conformal mapping, *Science*. 312 (2006) 1777–1780. doi:10.1126/science.1126493.
- [9] J.B. Pendry, D. Schurig, D.R. Smith, Controlling electromagnetic fields, *Science*. 312 (2006) 1780–1782. doi:10.1126/science.1125907.
- [10] D.A. Genov, S. Zhang, X. Zhang, Mimicking celestial mechanics in metamaterials, *Nat. Phys.* 5 (2009) 687–692. doi:10.1038/nphys1338.
- [11] N. Yu, F. Capasso, Flat optics with designer metasurfaces, *Nat. Mater.* 13 (2014) 139–150. doi:10.1038/nmat3839.
- [12] A. Pors, S.I. Bozhevolnyi, Plasmonic metasurfaces for efficient phase control in reflection, *Opt. Express*. 21 (2013) 27438. doi:10.1364/OE.21.027438.
- [13] A.R. Parker, H.E. Townley, Biomimetics of photonic nanostructures, *Nat. Nanotechnol.* 2 (2007) 347–353. doi:10.1038/nano.2007.152.

- [14] J. Park, J.R. Youn, Y.S. Song, Carbon Nanotube Embedded Nanostructure for Biometrics, *ACS Appl. Mater. Interfaces*. 9 (2017) 44724–44731. doi:10.1021/acsami.7b15567.
- [15] J. Hao, J. Wang, X. Liu, W.J. Padilla, L. Zhou, M. Qiu, High performance optical absorber based on a plasmonic metamaterial, *Appl. Phys. Lett.* 96 (2010). doi:10.1063/1.3442904.
- [16] G. Zheng, H. Mühlenbernd, M. Kenney, G. Li, T. Zentgraf, S. Zhang, Metasurface holograms reaching 80% efficiency, *Nat. Nanotechnol.* 10 (2015) 308–312. doi:10.1038/nnano.2015.2.
- [17] H. Chen, C.T. Chan, P. Sheng, Transformation optics and metamaterials, *Nat. Mater.* 9 (2010) 387–396. doi:10.1038/nmat2743.
- [18] S. Brûlé, E.H. Javelaud, S. Enoch, S. Guenneau, Experiments on seismic metamaterials: Molding surface waves, *Phys. Rev. Lett.* 112 (2013). doi:10.1103/PhysRevLett.112.133901.
- [19] S. Zhang, C. Xia, N. Fang, Broadband acoustic cloak for ultrasound waves, *Phys. Rev. Lett.* 106 (2011). doi:10.1103/PhysRevLett.106.024301.
- [20] J. Mei, G. Ma, M. Yang, Z. Yang, W. Wen, P. Sheng, Dark acoustic metamaterials as super absorbers for low-frequency sound, *Nat. Commun.* 3 (2012). doi:10.1038/ncomms1758.
- [21] N. Fang, D. Xi, J. Xu, M. Ambati, W. Srituravanich, C. Sun, X. Zhang, Ultrasonic metamaterials with negative modulus, *Nat. Mater.* 5 (2006) 452–456. doi:10.1038/nmat1644.
- [22] R.S. Lakes, Foam Structures with a Negative Poisson ' s Ratio, *Science*. 235 (1987) 1038–1040. doi:10.1126/science.235.4792.1038.
- [23] J.B. Lee, S. Peng, D. Yang, Y.H. Roh, H. Funabashi, N. Park, E.J. Rice, L. Chen, R. Long, M. Wu, D. Luo, A mechanical metamaterial made from a DNA hydrogel, *Nat. Nanotechnol.* 7 (2012) 816–820. doi:10.1038/nnano.2012.211.
- [24] X. Zheng, H. Lee, T.H. Weisgraber, M. Shusteff, J. DeOtte, E.B. Duoss, J.D. Kuntz, M.M. Biener, Q. Ge, J.A. Jackson, S.O. Kucheyev, N.X. Fang, C.M. Spadaccini, Ultralight, ultrastiff mechanical metamaterials, *Science*. 344 (2014) 1373–1377. doi:10.1126/science.1252291.

- [25] R. Schittny, M. Kadic, S. Guenneau, M. Wegener, Experiments on transformation thermodynamics: Molding the flow of heat, *Phys. Rev. Lett.* 110 (2013). doi:10.1103/PhysRevLett.110.195901.
- [26] S.A. Cummer, D. Schurig, One path to acoustic cloaking, *New J. Phys.* 9 (2007). doi:10.1088/1367-2630/9/3/045.
- [27] N. Stenger, M. Wilhelm, M. Wegener, Experiments on elastic cloaking in thin plates, *Phys. Rev. Lett.* 108 (2012). doi:10.1103/PhysRevLett.108.014301.
- [28] D. Schurig, J.J. Mock, B.J. Justice, S.A. Cummer, J.B. Pendry, A.F. Starr, D.R. Smith, Metamaterial electromagnetic cloak at microwave frequencies, *Science*. 314 (2006) 977–980. doi:10.1126/science.1133628.
- [29] K. Liu, X. Zeng, S. Jiang, D. Ji, H. Song, N. Zhang, Q. Gan, A large-scale lithography-free metasurface with spectrally tunable super absorption, *Nanoscale*. 6 (2014) 5599. doi:10.1039/c4nr00747f.
- [30] T. Frenzel, M. Kadic, M. Wegener, Three-dimensional mechanical metamaterials with a twist, *Science*. 358 (2017) 1072–1074. doi:10.1126/science.aao4640.
- [31] E. Boatti, N. Vasios, K. Bertoldi, Origami Metamaterials for Tunable Thermal Expansion, *Adv. Mater.* 29 (2017). doi:10.1002/adma.201700360.
- [32] T. Bückmann, N. Stenger, M. Kadic, J. Kaschke, A. Frölich, T. Kennerknecht, C. Eberl, M. Thiel, M. Wegener, Tailored 3D mechanical metamaterials made by dip-in direct-laser-writing optical lithography, *Adv. Mater.* 24 (2012) 2710–2714. doi:10.1002/adma.201200584.
- [33] A. Einstein, The Foundation of the General Theory of Relativity, *Ann. Phys.* 49 (1916) 31. doi:10.1097/ACM.0b013e31816bf1fd.
- [34] U. Leonhardt, T.G. Philbin, General relativity in electrical engineering, *New J. Phys.* 8 (2006). doi:10.1088/1367-2630/8/10/247.
- [35] S.A. Cummer, B.I. Popa, D. Schurig, D.R. Smith, J. Pendry, Full-wave simulations of electromagnetic cloaking structures, *Phys. Rev. E - Stat. Nonlinear, Soft Matter Phys.* 74 (2006). doi:10.1103/PhysRevE.74.036621.
- [36] W. Cai, U.K. Chettiar, A. V. Kildishev, V.M. Shalaev, Optical cloaking with metamaterials, *Nat. Photonics*. 1 (2007) 224–227. doi:10.1038/nphoton.2007.28.
- [37] J. Li, J.B. Pendry, Hiding under the carpet: A new strategy for cloaking, *Phys.*

- Rev. Lett. 101 (2008). doi:10.1103/PhysRevLett.101.203901.
- [38] M. Rahm, D. Schurig, D.A. Roberts, S.A. Cummer, D.R. Smith, J.B. Pendry, Design of electromagnetic cloaks and concentrators using form-invariant coordinate transformations of Maxwell's equations, *Photonics Nanostructures - Fundam. Appl.* 6 (2008) 87–95. doi:10.1016/j.photonics.2007.07.013.
- [39] C. Navau, J. Prat-Camps, A. Sanchez, Magnetic energy harvesting and concentration at a distance by transformation optics, *Phys. Rev. Lett.* 109 (2012). doi:10.1103/PhysRevLett.109.263903.
- [40] H. Chen, C.T. Chan, Transformation media that rotate electromagnetic fields, *Appl. Phys. Lett.* 90 (2007). doi:10.1063/1.2748302.
- [41] H. Chen, B. Hou, S. Chen, X. Ao, W. Wen, C.T. Chan, Design and experimental realization of a broadband transformation media field rotator at microwave frequencies, *Phys. Rev. Lett.* 102 (2009). doi:10.1103/PhysRevLett.102.183903.
- [42] S.A. Cummer, B.I. Popa, D. Schurig, D.R. Smith, J. Pendry, M. Rahm, A. Starr, Scattering theory derivation of a 3D acoustic cloaking shell, *Phys. Rev. Lett.* 100 (2008). doi:10.1103/PhysRevLett.100.024301.
- [43] M. Farhat, S. Guenneau, S. Enoch, Ultrabroadband elastic cloaking in thin plates, *Phys. Rev. Lett.* 103 (2009). doi:10.1103/PhysRevLett.103.024301.
- [44] S. Zhang, D.A. Genov, C. Sun, X. Zhang, Cloaking of matter waves, *Phys. Rev. Lett.* 100 (2008). doi:10.1103/PhysRevLett.100.123002.
- [45] S. Guenneau, C. Amra, D. Veynante, Transformation thermodynamics: cloaking and concentrating heat flux, *Opt. Express.* 20 (2012) 8207. doi:10.1364/OE.20.008207.
- [46] T. Han, C.W. Qiu, Transformation Laplacian metamaterials: Recent advances in manipulating thermal and dc fields, *J. Opt.* 18 (2016). doi:10.1088/2040-8978/18/4/044003.
- [47] A. Greenleaf, M. Lassas, G. Uhlmann, Anisotropic conductivities that cannot be detected by EIT, in: *Physiol. Meas.*, 2003: pp. 413–419. doi:10.1088/0967-3334/24/2/353.
- [48] Y.A. Urzhumov, D.R. Smith, Fluid flow control with transformation media, *Phys. Rev. Lett.* 107 (2011). doi:10.1103/PhysRevLett.107.074501.

- [49] M. Farhat, S. Enoch, S. Guenneau, A.B. Movchan, Broadband cylindrical acoustic cloak for linear surface waves in a fluid, *Phys. Rev. Lett.* 101 (2008). doi:10.1103/PhysRevLett.101.134501.
- [50] F. Yang, Z.L. Mei, T.Y. Jin, T.J. Cui, Dc electric invisibility cloak, *Phys. Rev. Lett.* 109 (2012). doi:10.1103/PhysRevLett.109.053902.
- [51] T. Bückmann, M. Thiel, M. Kadic, R. Schittny, M. Wegener, An elasto-mechanical unfeelability cloak made of pentamode metamaterials, *Nat. Commun.* 5 (2014). doi:10.1038/ncomms5130.
- [52] T. Bückmann, M. Kadic, R. Schittny, M. Wegener, Mechanical cloak design by direct lattice transformation, *Proc. Natl. Acad. Sci.* 112 (2015) 4930–4934. doi:10.1073/pnas.1501240112.
- [53] T. Han, J. Zhao, T. Yuan, D.Y. Lei, B. Li, C.-W. Qiu, Theoretical realization of an ultra-efficient thermal-energy harvesting cell made of natural materials, *Energy Environ. Sci.* 6 (2013) 3537. doi:10.1039/c3ee41512k.
- [54] F. Chen, D. Yuan Lei, Experimental Realization of Extreme Heat Flux Concentration with Easy-to-Make Thermal Metamaterials, *Sci. Rep.* 5 (2015) 11552. doi:10.1038/srep11552.
- [55] W.X. Jiang, C.Y. Luo, H.F. Ma, Z.L. Mei, T.J. Cui, Enhancement of current density by dc electric concentrator, *Sci. Rep.* 2 (2012). doi:10.1038/srep00956.
- [56] X. Jiang, B. Liang, X.Y. Zou, L.L. Yin, J.C. Cheng, Broadband field rotator based on acoustic metamaterials, *Appl. Phys. Lett.* 104 (2014). doi:10.1063/1.4866333.
- [57] S. Narayana, Y. Sato, Heat flux manipulation with engineered thermal materials, *Phys. Rev. Lett.* 108 (2012). doi:10.1103/PhysRevLett.108.214303.
- [58] M.D. Hager, S. Bode, C. Weber, U.S. Schubert, Shape memory polymers: Past, present and future developments, *Prog. Polym. Sci.* 49–50 (2015) 3–33. doi:10.1016/j.progpolymsci.2015.04.002.
- [59] R. Kempaiah, Z. Nie, From nature to synthetic systems: shape transformation in soft materials, *J. Mater. Chem. B.* 2 (2014) 2357–2368. doi:10.1039/C3TB21462A.
- [60] M.A.C. Stuart, W.T.S. Huck, J. Genzer, M. Müller, C. Ober, M. Stamm, G.B. Sukhorukov, I. Szleifer, V. V. Tsukruk, M. Urban, F. Winnik, S. Zauscher, I.

- Luzinov, S. Minko, Emerging applications of stimuli-responsive polymer materials, *Nat. Mater.* 9 (2010) 101–113. doi:10.1038/nmat2614.
- [61] L.B.V.E.T. Al, B. Vernon, H.M. Vernon, Process of manufacturing articles of thermoplastic synthetic resins, US Pat. (1941).
- [62] J. Hu, Y. Zhu, H. Huang, J. Lu, Recent advances in shape-memory polymers: Structure, mechanism, functionality, modeling and applications, *Prog. Polym. Sci.* 37 (2012) 1720–1763. doi:10.1016/j.progpolymsci.2012.06.001.
- [63] O. Emile, A. Le Floch, F. Vollrath, Shape memory in spider draglines, *Nature.* 440 (2006) 621. doi:10.1038/440621a.
- [64] I.A. Rousseau, P.T. Mather, Shape Memory Effect Exhibited by Smectic-C Liquid Crystalline Elastomers, *J. Am. Chem. Soc.* 125 (2003) 15300–15301. doi:10.1021/ja039001s.
- [65] A. Lendlein, S. Kelch, Shape-Memory Polymers, *Angew. Chemie.* 41 (2002) 2034–2057.
- [66] A. Lendlein, H. Jiang, O. Jünger, R. Langer, Light-induced shape-memory polymers, *Nature.* 434 (2005) 879–882. doi:10.1038/nature03496.
- [67] Y. Zhu, J. Hu, H. Luo, R.J. Young, L. Deng, S. Zhang, Y. Fan, G. Ye, Rapidly switchable water-sensitive shape-memory cellulose/elastomer nano-composites, *Soft Matter.* 8 (2012) 2509. doi:10.1039/c2sm07035a.
- [68] J. Hu, S. Chen, A review of actively moving polymers in textile applications, *J. Mater. Chem.* 20 (2010) 3346. doi:10.1039/b922872a.
- [69] C. Liu, S.B. Chun, P.T. Mather, L. Zheng, E.H. Haley, E.B. Coughlin, Chemically cross-linked polycyclooctene: Synthesis, characterization, and shape memory behavior, *Macromolecules.* 35 (2002) 9868–9874. doi:10.1021/ma021141j.
- [70] C.M. Yakacki, R. Shandas, D. Safranski, A.M. Ortega, K. Sassaman, K. Gall, Strong, tailored, biocompatible shape-memory polymer networks, *Adv. Funct. Mater.* 18 (2008) 2428–2435. doi:10.1002/adfm.200701049.
- [71] A. Lendlein, A.M. Schmidt, R. Langer, AB-polymer networks based on oligo(-caprolactone) segments showing shape-memory properties, *Proc. Natl. Acad. Sci.* 98 (2001) 842–847. doi:10.1073/pnas.98.3.842.
- [72] X. Zheng, S. Zhou, X. Li, J. Weng, Shape memory properties of poly(d,l-



- lactide)/hydroxyapatite composites, *Biomaterials*. 27 (2006) 4288–4295.  
doi:10.1016/j.biomaterials.2006.03.043.
- [73] M.K. Jang, A. Hartwig, B.K. Kim, Shape memory polyurethanes cross-linked by surface modified silica particles, *J. Mater. Chem.* 19 (2009) 1166.  
doi:10.1039/b816691a.
- [74] E.D. Rodriguez, X. Luo, P.T. Mather, Linear/network poly( $\epsilon$ -caprolactone) blends exhibiting shape memory assisted self-healing (SMASH), *ACS Appl. Mater. Interfaces*. 3 (2011) 152–161. doi:10.1021/am101012c.
- [75] D. Ratna, J. Karger-Kocsis, Shape memory polymer system of semi-interpenetrating network structure composed of crosslinked poly (methyl methacrylate) and poly (ethylene oxide), *Polymer*. 52 (2011) 1063–1070.  
doi:10.1016/j.polymer.2010.12.054.
- [76] S. Zhang, Y. Feng, L. Zhang, J. Sun, X. Xu, Y. Xu, Novel interpenetrating networks with shape-memory properties, *J. Polym. Sci. Part A Polym. Chem.* 45 (2007) 768–775. doi:10.1002/pola.21832.
- [77] H. Zhang, H. Wang, W. Zhong, Q. Du, A novel type of shape memory polymer blend and the shape memory mechanism, *Polymer*. 50 (2009) 1596–1601.  
doi:10.1016/j.polymer.2009.01.011.
- [78] S.C. Li, L. Tao, Melt rheological and thermoresponsive shape memory properties of HDPE/PA6/POE-g-MAH blends, *Polym. - Plast. Technol. Eng.* 49 (2010) 218–222. doi:10.1080/03602550903147320.
- [79] F.L. Ji, J.L. Hu, T.C. Li, Y.W. Wong, Morphology and shape memory effect of segmented polyurethanes. Part I: With crystalline reversible phase, *Polymer*. 48 (2007) 5133–5145. doi:10.1016/j.polymer.2007.06.032.
- [80] S. Chen, J. Hu, Y. Liu, H. Liem, Y. Zhu, Y. Liu, Effect of SSL and HSC on morphology and properties of PHA Based SMPU synthesized by bulk polymerization method, *J. Polym. Sci. Part B Polym. Phys.* 45 (2007) 444–454.  
doi:10.1002/polb.21046.
- [81] J. Li, J.A. Viveros, M.H. Wrue, M. Anthamatten, Shape-memory effects in polymer networks containing reversibly associating side-groups, *Adv. Mater.* 19 (2007) 2851–2855. doi:10.1002/adma.200602260.

- [82] M. Behl, M.Y. Razzaq, A. Lendlein, Multifunctional shape-memory polymers, *Adv. Mater.* 22 (2010) 3388–3410. doi:10.1002/adma.200904447.
- [83] V. Kafka, Shape memory polymers: A mesoscale model of the internal mechanism leading to the SM phenomena, *Int. J. Plast.* 24 (2008) 1533–1548. doi:10.1016/j.ijplas.2007.11.001.
- [84] Y. Liu, K. Gall, M.L. Dunn, A.R. Greenberg, J. Diani, Thermomechanics of shape memory polymers: Uniaxial experiments and constitutive modeling, *Int. J. Plast.* 22 (2006) 279–313. doi:10.1016/j.ijplas.2005.03.004.
- [85] H.J. Qi, T.D. Nguyen, F. Castro, C.M. Yakacki, R. Shandas, Finite deformation thermo-mechanical behavior of thermally induced shape memory polymers, *J. Mech. Phys. Solids.* 56 (2008) 1730–1751. doi:10.1016/j.jmps.2007.12.002.
- [86] J. Diani, K. Gall, Molecular dynamics simulations of the shape-memory behaviour of polyisoprene, *Smart Mater. Struct.* 16 (2007) 1575–1583. doi:10.1088/0964-1726/16/5/011.
- [87] C. Zhang, J. Hu, S. Chen, F. Ji, Theoretical study of hydrogen bonding interactions on MDI-based polyurethane, *J. Mol. Model.* 16 (2010) 1391–1399. doi:10.1007/s00894-010-0645-4.
- [88] V. Srivastava, S.A. Chester, N.M. Ames, L. Anand, A thermo-mechanically-coupled large-deformation theory for amorphous polymers in a temperature range which spans their glass transition, *Int. J. Plast.* 26 (2010) 1138–1182. doi:10.1016/j.ijplas.2010.01.004.
- [89] J. Hyun Kim, T. Jin Kang, W.R. Yu, Simulation of mechanical behavior of temperature-responsive braided stents made of shape memory polyurethanes, *J. Biomech.* 43 (2010) 632–643. doi:10.1016/j.jbiomech.2009.10.032.
- [90] W.M. Huang, B. Yang, Y.Q. Fu, *Polyurethane Shape Memory Polymers*, 2011. doi:10.1201/b11209-2.
- [91] B. Dietsch, T. Tong, A review - Features and benefits of shape memory polymers (SMPs), *J. Adv. Mater.* 39 (2007) 3–12.
- [92] Y. Liu, H. Du, L. Liu, J. Leng, Shape memory polymers and their composites in aerospace applications: A review, *Smart Mater. Struct.* 23 (2014). doi:10.1088/0964-1726/23/2/023001.

- [93] X. Lan, Y. Liu, H. Lv, X. Wang, J. Leng, S. Du, Fiber reinforced shape-memory polymer composite and its application in a deployable hinge, *Smart Mater. Struct.* 18 (2009). doi:10.1088/0964-1726/18/2/024002.
- [94] R. Zhang, X. Guo, Y. Liu, J. Leng, Theoretical analysis and experiments of a space deployable truss structure, *Compos. Struct.* 112 (2014) 226–230. doi:10.1016/j.compstruct.2014.02.018.
- [95] W. Small Iv, T. Wilson, W. Benett, J. Loge, D. Maitland, Laser-activated shape memory polymer intravascular thrombectomy device., *Opt. Express.* 13 (2005) 8204–8213. doi:10.1364/OPEX.13.008204.
- [96] R. Mohr, K. Kratz, T. Weigel, M. Lucka-Gabor, M. Moneke, A. Lendlein, Initiation of shape-memory effect by inductive heating of magnetic nanoparticles in thermoplastic polymers, *Proc. Natl. Acad. Sci.* 103 (2006) 3540–3545. doi:10.1073/pnas.0600079103.
- [97] J. Leng, H. Lv, Y. Liu, S. Du, Electroactivate shape-memory polymer filled with nanocarbon particles and short carbon fibers, *Appl. Phys. Lett.* 91 (2007). doi:10.1063/1.2790497.
- [98] L. De Nardo, R. Alberti, A. Cigada, L. Yahia, M.C. Tanzi, S. Farè, Shape memory polymer foams for cerebral aneurysm reparation: Effects of plasma sterilization on physical properties and cytocompatibility, *Acta Biomater.* 5 (2009) 1508–1518. doi:10.1016/j.actbio.2008.11.017.
- [99] S. Farè, V. Valtulina, P. Petrini, E. Alessandrini, G. Pietrocola, M.C. Tanzi, P. Speziale, L. Visai, In vitro interaction of human fibroblasts and platelets with a shape-memory polyurethane, *J. Biomed. Mater. Res. - Part A.* 73 (2005) 1–11. doi:10.1002/jbm.a.30193.
- [100] A. Metcalfe, A.C. Desfaits, I. Salazkin, L. Yahia, W.M. Sokolowski, J. Raymond, Cold hibernated elastic memory foams for endovascular interventions, *Biomaterials.* 24 (2003) 491–497. doi:10.1016/S0142-9612(02)00362-9.
- [101] M. Enriquez-Sarano, H. V Schaff, T.A. Orszulak, A.J. Tajik, K.R. Bailey, R.L. Frye, Valve repair improves the outcome of surgery for mitral regurgitation. A multivariate analysis., *Circulation.* 91 (1995) 1022–8. doi:10.1161/01.cir.91.4.1022.

- [102] D.J. Maitland, M.F. Metzger, D. Schumann, A. Lee, T.S. Wilson, Photothermal properties of shape memory polymer micro-actuators for treating stroke, *Lasers Surg. Med.* 30 (2002) 1–11. doi:10.1002/lsm.10007.
- [103] W. Small IV, T.S. Wilson, P.R. Buckley, W.J. Benett, J.M. Loge, J. Hartman, D.J. Maitland, Prototype fabrication and preliminary In Vitro testing of a shape memory endovascular thrombectomy device, *IEEE Trans. Biomed. Eng.* 54 (2007) 1657–1666. doi:10.1109/TBME.2007.892921.
- [104] H.M. Wache, D.J. Tartakowska, A. Hentrich, M.H. Wagner, Development of a polymer stent with shape memory effect as a drug delivery system, in: *J. Mater. Sci. Mater. Med.*, 2003: pp. 109–112. doi:10.1023/A:1022007510352.
- [105] C.M. Yakacki, R. Shandas, C. Lanning, B. Rech, A. Eckstein, K. Gall, Unconstrained recovery characterization of shape-memory polymer networks for cardiovascular applications, *Biomaterials*. 28 (2007) 2255–2263. doi:10.1016/j.biomaterials.2007.01.030.
- [106] S.H. Ajili, N.G. Ebrahimi, M. Soleimani, Polyurethane/polycaprolactane blend with shape memory effect as a proposed material for cardiovascular implants, *Acta Biomater.* 5 (2009) 1519–1530. doi:10.1016/j.actbio.2008.12.014.
- [107] L. Song, W. Hu, G. Wang, G. Niu, H. Zhang, H. Cao, K. Wang, H. Yang, S. Zhu, Tailored (Meth)Acrylate Shape-Memory Polymer Networks for Ophthalmic Applications, *Macromol. Biosci.* 10 (2010) 1194–1202. doi:10.1002/mabi.201000028.
- [108] J.M. Ortega, W. Small IV, T.S. Wilson, W.J. Benett, J.M. Loge, D.J. Maitland, A shape memory polymer dialysis needle adapter for the reduction of hemodynamic stress within arteriovenous grafts, *IEEE Trans. Biomed. Eng.* 54 (2007) 1722–1724. doi:10.1109/TBME.2007.892927.
- [109] A.A. Sharp, H. V. Panchawagh, A. Ortega, R. Artale, S. Richardson-Burns, D.S. Finch, K. Gall, R.L. Mahajan, D. Restrepo, Toward a self-deploying shape memory polymer neuronal electrode, *J. Neural Eng.* 3 (2006). doi:10.1088/1741-2560/3/4/L02.
- [110] A. Lendlein, R. Langer, Biodegradable, elastic shape-memory polymers for potential biomedical applications, *Science*. 296 (2002) 1673–1676.

doi:10.1126/science.1066102.

- [111] X. Xiao, T. Xie, Y.-T. Cheng, Self-healable graphene polymer composites, *J. Mater. Chem.* 20 (2010) 3508. doi:10.1039/c0jm00307g.
- [112] C.M. Chen, S. Yang, Directed water shedding on high-aspect-ratio shape memory polymer micropillar arrays, *Adv. Mater.* 26 (2014) 1283–1288. doi:10.1002/adma.201304030.
- [113] C.M. Chen, C.L. Chiang, S. Yang, Programming Tilting Angles in Shape Memory Polymer Janus Pillar Arrays with Unidirectional Wetting against the Tilting Direction, *Langmuir.* 31 (2015) 9523–9526. doi:10.1021/acs.langmuir.5b02622.
- [114] T. Xie, X. Xiao, J. Li, R. Wang, Encoding localized strain history through wrinkle based structural colors, *Adv. Mater.* 22 (2010) 4390–4394. doi:10.1002/adma.201002825.
- [115] H. Xu, C. Yu, S. Wang, V. Malyarchuk, T. Xie, J.A. Rogers, Deformable, programmable, and shape-memorizing micro-optics, *Adv. Funct. Mater.* 23 (2013) 3299–3306. doi:10.1002/adfm.201203396.
- [116] E. Lee, M. Zhang, Y. Cho, Y. Cui, J. Van Der Spiegel, N. Engheta, S. Yang, Tilted pillars on wrinkled elastomers as a reversibly tunable optical window, *Adv. Mater.* 26 (2014) 4127–4133. doi:10.1002/adma.201400711.
- [117] M. Ebara, K. Uto, N. Idota, J.M. Hoffman, T. Aoyagi, Shape-memory surface with dynamically tunable nano-geometry activated by body heat, *Adv. Mater.* 24 (2012) 273–278. doi:10.1002/adma.201102181.
- [118] M. Ebara, M. Akimoto, K. Uto, K. Shiba, G. Yoshikawa, T. Aoyagi, Focus on the interlude between topographic transition and cell response on shape-memory surfaces, *Polymer.* 55 (2014) 5961–5968. doi:10.1016/j.polymer.2014.09.009.
- [119] D. Mosqueira, S. Pagliari, K. Uto, M. Ebara, S. Romanazzo, C. Escobedo-Lucea, J. Nakanishi, A. Taniguchi, O. Franzese, P. Di Nardo, M.J. Goumans, E. Traversa, P. Pinto-Do-Ó, T. Aoyagi, G. Forte, Hippo pathway effectors control cardiac progenitor cell fate by acting as dynamic sensors of substrate mechanics and nanostructure, *ACS Nano.* 8 (2014) 2033–2047. doi:10.1021/nn4058984.
- [120] X. Tao, X. Xingcheng, Self-peeling reversible dry adhesive system, *Chem. Mater.* 20 (2008) 2866–2868. doi:10.1021/cm800173c.

- [121] L.F. Boesel, C. Cremer, E. Arzt, A. Del Campo, Gecko-inspired surfaces: A path to strong and reversible dry adhesives, *Adv. Mater.* 22 (2010) 2125–2137. doi:10.1002/adma.200903200.
- [122] J.D. Eisenhaure, T. Xie, S. Varghese, S. Kim, Microstructured shape memory polymer surfaces with reversible dry adhesion, *ACS Appl. Mater. Interfaces.* 5 (2013) 7714–7717. doi:10.1021/am402479f.
- [123] L.M. Castano, A.B. Flatau, Smart fabric sensors and e-textile technologies: A review, *Smart Mater. Struct.* 23 (2014). doi:10.1088/0964-1726/23/5/053001.
- [124] J.E. Marshall, S. Gallagher, E.M. Terentjev, S.K. Smoukov, Anisotropic colloidal micromuscles from liquid crystal elastomers, *J. Am. Chem. Soc.* 136 (2014) 474–479. doi:10.1021/ja410930g.
- [125] D.L. Thomsen, P. Keller, J. Naciri, R. Pink, H. Jeon, D. Shenoy, B.R. Ratna, Liquid crystal elastomers with mechanical properties of a muscle, *Macromolecules.* 34 (2001) 5868–5875. doi:10.1021/ma001639q.
- [126] A. Tadeu, J. António, D. Mateus, Sound insulation provided by single and double panel walls - A comparison of analytical solutions versus experimental results, *Appl. Acoust.* 65 (2004) 15–29. doi:10.1016/j.apacoust.2003.07.003.
- [127] J. Zhao, X.M. Wang, J.M. Chang, Y. Yao, Q. Cui, Sound insulation property of wood-waste tire rubber composite, *Compos. Sci. Technol.* 70 (2010) 2033–2038. doi:10.1016/j.compscitech.2010.03.015.
- [128] A.C. Nilsson, Wave propagation in and sound transmission through sandwich plates, *J. Sound Vib.* 138 (1990) 73–94. doi:10.1016/0022-460X(90)90705-5.
- [129] K. Ghorbani, H. Hasani, M. Zarrebini, R. Saghafi, An investigation into sound transmission loss by polypropylene needle-punched nonwovens, *Alexandria Eng. J.* 55 (2016) 907–914. doi:10.1016/j.aej.2016.02.012.
- [130] C. Zwicker, J. V.D. Eijk, C.W. Kosten, Absorption of sound by porous materials II, *Physica.* 8 (1941) 469–476. doi:10.1016/S0031-8914(41)90087-3.
- [131] C. Perrot, F. Chevillotte, R. Panneton, Bottom-up approach for microstructure optimization of sound absorbing materials, *J. Acoust. Soc. Am.* 124 (2008) 940–948. doi:10.1121/1.2945115.
- [132] O. Doutres, N. Atalla, K. Dong, A semi-phenomenological model to predict the

- acoustic behavior of fully and partially reticulated polyurethane foams, *J. Appl. Phys.* 113 (2013). doi:10.1063/1.4789595.
- [133] S. Amares, E. Sujatmika, T.W. Hong, R. Durairaj, H.S.H.B. Hamid, A Review : Characteristics of Noise Absorption Material, *J. Phys. Conf. Ser.* 908 (2017). doi:https://doi.org/10.1088/1742-6596/908/1/012005.
- [134] H.S. Seddeq, Factors Influencing Acoustic Performance of Sound Absorptive Materials, *Aust. J. Basic Appl. Sci.* 3 (2009) 4610–4617.
- [135] Z. Azkorra, G. Pérez, J. Coma, L.F. Cabeza, S. Bures, J.E. Álvaro, A. Erkoreka, M. Urrestarazu, Evaluation of green walls as a passive acoustic insulation system for buildings, *Appl. Acoust.* 89 (2015) 46–56. doi:10.1016/j.apacoust.2014.09.010.
- [136] S.J. Wertel, Experimental Analysis of Noise Reduction Properties of Sound Absorbing Foam, *Univ. Wisconsin-Stout.* (2000) 66.
- [137] F. Shahani, P. Soltani, M. Zarrebini, The Analysis of Acoustic Characteristics and Sound Absorption Coefficient of Needle Punched Nonwoven Fabrics, *J. Eng. Fiber. Fabr.* 9 (2014) 84–92.
- [138] U. Leonhardt, T. Tyc, Broadband invisibility by non-Euclidean cloaking, *Science.* 323 (2009) 110–112. doi:10.1126/science.1166332.
- [139] L. Zigoneanu, B.I. Popa, S.A. Cummer, Three-dimensional broadband omnidirectional acoustic ground cloak, *Nat. Mater.* 13 (2014) 352–355. doi:10.1038/nmat3901.
- [140] A.J. Chorin, Numerical Solution of the Navier-Stokes Equations, *Math. Comput.* 22 (1968) 745. doi:10.2307/2004575.
- [141] P.U. Zhang, Theory of transformation optics and invisibility cloak design, KTH Royal Institute of Technology, 2011.
- [142] H. Young, R. Freedman, University physics with modern physics, 2007. doi:10.1038/479008b.
- [143] G.K. Batchelor, A.D. Young, An Introduction to Fluid Dynamics, *J. Appl. Mech.* 35 (1968) 624. doi:10.1063/1.3060769.
- [144] G. Falkovich, Fluid mechanics: A short course for physicists, 2011. doi:10.1017/CBO9780511794353.

- [145] L. Sirovlch, S. Karlsson, Turbulent drag reduction by passive mechanisms, *Nature*. 388 (1997) 753–755. doi:10.1038/41966.
- [146] R.G. Bill, W.F. Herrnkind, Drag reduction by formation movement in spiny lobsters., *Science*. 193 (1976) 1146–8. doi:10.1126/science.193.4258.1146.
- [147] M.R. Driels, S. Ayyash, Drag reduction in laminar flow, *Nature*. 259 (1976) 389–390. doi:10.1038/259389a0.
- [148] R. Liu, C. Ji, J.J. Mock, J.Y. Chin, T.J. Cui, D.R. Smith, Broadband ground-plane cloak, *Science*. 323 (2009) 366–369. doi:10.1126/science.1166949.
- [149] T. Ergin, N. Stenger, P. Brenner, J.B. Pendry, M. Wegener, Three-dimensional invisibility cloak at optical wavelengths, *Science*. 328 (2010) 337–339. doi:10.1126/science.1186351.
- [150] F. Gömöry, M. Solovyov, J. Šouc, C. Navau, J. Prat-Camps, A. Sanchez, Experimental realization of a magnetic cloak, *Science*. 335 (2012) 1466–1468. doi:10.1126/science.1218316.
- [151] X. Ni, Z.J. Wong, M. Mrejen, Y. Wang, X. Zhang, An ultrathin invisibility skin cloak for visible light, *Science*. 349 (2015) 1310–1314. doi:10.1126/science.aac9411.
- [152] R. Schittny, M. Kadic, T. Bučkman, M. Wegener, Invisibility cloaking in a diffusive light scattering medium, *Science*. 345 (2014) 427–429. doi:10.1126/science.1254524.
- [153] F.J. Valdes-Parada, J. Alberto Ochoa-Tapia, J. Alvarez-Ramirez, On the effective viscosity for the Darcy-Brinkman equation, *Phys. A Stat. Mech. Its Appl.* 385 (2007) 69–79. doi:10.1016/j.physa.2007.06.012.
- [154] V.M. Starov, V.G. Zhdanov, Effective viscosity and permeability of porous media, *Colloids Surfaces A Physicochem. Eng. Asp.* 192 (2001) 363–375. doi:10.1016/S0927-7757(01)00737-3.
- [155] R.E.R. Larson, J.J.L. Higdon, Microscopic flow near the surface of two-dimensional porous media. Part 1. Axial flow, *J. Fluid Mech.* 166 (1986) 449–472. doi:10.1017/S0022112087001149.
- [156] R.E. Larson, J.J.L. Higdon, Microscopic flow near the surface of two-dimensional porous media. Part 2. Transverse flow, *J. Fluid Mech.* 178 (1987) 119–136.



doi:10.1017/S0022112087001149.

- [157] K. Yazdchi, S. Srivastava, S. Luding, Microstructural effects on the permeability of periodic fibrous porous media, *Int. J. Multiph. Flow.* 37 (2011) 956–966.  
doi:10.1016/j.ijmultiphaseflow.2011.05.003.
- [158] R.S. Hale, R.T. Bonnecaze, C.H. Hidrovo, Optimization of capillary flow through square micropillar arrays, *Int. J. Multiph. Flow.* 58 (2014) 39–51.  
doi:10.1016/j.ijmultiphaseflow.2013.08.003.
- [159] W.P. Breugem, The effective viscosity of a channel-type porous medium, *Phys. Fluids.* 19 (2007). doi:10.1063/1.2792323.
- [160] J. Yao, Z. Liu, Y. Liu, Y. Wang, C. Sun, G. Bartal, A.M. Stacy, X. Zhang, Optical negative refraction in bulk metamaterials of nanowires, *Science.* 321 (2008) 930.  
doi:10.1126/science.1157566.
- [161] N.I. Landy, S. Sajuyigbe, J.J. Mock, D.R. Smith, W.J. Padilla, Perfect metamaterial absorber, *Phys. Rev. Lett.* 100 (2008).  
doi:10.1103/PhysRevLett.100.207402.
- [162] E.E. Narimanov, A. V. Kildishev, Optical black hole: Broadband omnidirectional light absorber, *Appl. Phys. Lett.* 95 (2009). doi:10.1063/1.3184594.
- [163] Y. Luo, H. Chen, J. Zhang, L. Ran, J.A. Kong, Design and analytical full-wave validation of the invisibility cloaks, concentrators, and field rotators created with a general class of transformations, *Phys. Rev. B - Condens. Matter Mater. Phys.* 77 (2008). doi:10.1103/PhysRevB.77.125127.
- [164] W. Wang, L. Lin, J. Ma, C. Wang, J. Cui, C. Du, X. Luo, Electromagnetic concentrators with reduced material parameters based on coordinate transformation, *Opt. Express.* 16 (2008) 11431–7. doi:10.1364/OE.16.011431.
- [165] G. Park, S. Kang, H. Lee, W. Choi, Tunable multifunctional thermal metamaterials: Manipulation of local heat flux via assembly of unit-cell thermal shifters, *Sci. Rep.* 7 (2017). doi:10.1038/srep41000.
- [166] S. Guenneau, C. Amra, Anisotropic conductivity rotates heat fluxes in transient regimes, *Opt. Express.* 21 (2013) 6578–83. doi:10.1364/OE.21.006578.
- [167] S. Guenneau, D. Petiteau, M. Zerrad, C. Amra, T. Puvirajesinghe, Transformed Fourier and Fick equations for the control of heat and mass diffusion, *AIP Adv.* 5

- (2015). doi:10.1063/1.4917492.
- [168] T. Xie, Tunable polymer multi-shape memory effect, *Nature*. 464 (2010) 267–270. doi:10.1038/nature08863.
- [169] D.Y. Wu, S. Meure, D. Solomon, Self-healing polymeric materials: A review of recent developments, *Prog. Polym. Sci.* 33 (2008) 479–522. doi:10.1016/j.progpolymsci.2008.02.001.
- [170] K.S. Toohey, N.R. Sottos, J.A. Lewis, J.S. Moore, S.R. White, Self-healing materials with microvascular networks, *Nat. Mater.* 6 (2007) 581–585. doi:10.1038/nmat1934.
- [171] P. Cordier, F. Tournilhac, C. Soulié-Ziakovic, L. Leibler, Self-healing and thermoreversible rubber from supramolecular assembly, *Nature*. 451 (2008) 977–980. doi:10.1038/nature06669.
- [172] R. Yang, Y. Qin, L. Dai, Z.L. Wang, Power generation with laterally packaged piezoelectric fine wires, *Nat. Nanotechnol.* 4 (2009) 34–39. doi:10.1038/nnano.2008.314.
- [173] S.A. McDonald, G. Konstantatos, S. Zhang, P.W. Cyr, E.J.D. Klem, L. Levina, E.H. Sargent, Solution-processed PbS quantum dot infrared photodetectors and photovoltaics, *Nat. Mater.* 4 (2005) 138–142. doi:10.1038/nmat1299.
- [174] Z. Fan, H. Razavi, J.W. Do, A. Moriwaki, O. Ergen, Y.L. Chueh, P.W. Leu, J.C. Ho, T. Takahashi, L.A. Reichertz, S. Neale, K. Yu, M. Wu, J.W. Ager, A. Javey, Three-dimensional nanopillar-array photovoltaics on low-cost and flexible substrates, *Nat. Mater.* 8 (2009) 648–653. doi:10.1038/nmat2493.
- [175] G. Zhu, G. Liang, Q. Xu, Q. Yu, Shape-memory effects of radiation crosslinked Poly( $\epsilon$ -caprolactone), *J. Appl. Polym. Sci.* 90 (2003) 1589–1595. doi:10.1002/app.12736.
- [176] S.H. Lee, J.W. Kim, B.K. Kim, Shape memory polyurethanes having crosslinks in soft and hard segments, *Smart Mater. Struct.* 13 (2004) 1345–1350. doi:10.1088/0964-1726/13/6/007.
- [177] H. Tobushi, S. Hayashi, K. Hoshio, N. Miwa, Influence of strain-holding conditions on shape recovery and secondary-shape forming in polyurethane-shape memory polymer, *Smart Mater. Struct.* 15 (2006) 1033–1038. doi:10.1088/0964-

1726/15/4/016.

- [178] G.H. Pan, W.M. Huang, Z.C. Ng, N. Liu, S.J. Phee, The glass transition temperature of polyurethane shape memory polymer reinforced with treated/non-treated attapulgite (playgorskite) clay in dry and wet conditions, *Smart Mater. Struct.* 17 (2008). doi:10.1088/0964-1726/17/4/045007.
- [179] C. Min, W. Cui, J. Bei, S. Wang, Biodegradable shape-memory polymer—polylactide-co-poly(glycolide-co-caprolactone) multiblock copolymer, *Polym. Adv. Technol.* 16 (2005) 608–615. doi:10.1002/pat.624.
- [180] D. Pérez-Foullerat, S. Hild, A. Mücke, B. Rieger, Synthesis and properties of poly(ketone-co-alcohol) materials: Shape memory thermoplastic elastomers by control of the glass transition process, *Macromol. Chem. Phys.* 205 (2004) 374–382. doi:10.1002/macp.200300155.
- [181] J. Leng, X. Wu, Y. Liu, Effect of a linear monomer on the thermomechanical properties of epoxy shape-memory polymer, *Smart Mater. Struct.* 18 (2009). doi:10.1088/0964-1726/18/9/095031.
- [182] C. Liu, H. Qin, P.T. Mather, Review of progress in shape-memory polymers, *J. Mater. Chem.* 17 (2007) 1543. doi:10.1039/b615954k.
- [183] W. Chen, C. Zhu, X. Gu, Thermosetting polyurethanes with water-swollen and shape memory properties, *J. Appl. Polym. Sci.* 84 (2002) 1504–1512. doi:10.1002/app.10357.
- [184] J. Chen, L. Liu, Y. Liu, J. Leng, Thermoviscoelastic shape memory behavior for epoxy-shape memory polymer, *Smart Mater. Struct.* 23 (2014). doi:10.1088/0964-1726/23/5/055025.
- [185] T. Ware, K. Hearon, A. Lonnecker, K.L. Wooley, D.J. Maitland, W. Voit, Triple-shape memory polymers based on self-complementary hydrogen bonding, *Macromolecules.* 45 (2012) 1062–1069. doi:10.1021/ma202098s.
- [186] S. Chena, J. Hua, C.W. Yuena, L. Chana, H. Zhuoa, Triple shape memory effect in multiple crystalline polyurethanes, *Polym. Adv. Technol.* 21 (2010) 377–380. doi:10.1002/pat.1523.
- [187] N.S. Goo, I.H. Paik, K.J. Yoon, The durability of a conducting shape memory polyurethane actuator, *Smart Mater. Struct.* 16 (2007). doi:10.1088/0964-

1726/16/4/N01.

- [188] S. V. Ahir, A.R. Tajbakhsh, E.M. Terentjev, Self-assembled shape-memory fibers of triblock liquid-crystal polymers, *Adv. Funct. Mater.* 16 (2006) 556–560. doi:10.1002/adfm.200500692.
- [189] K. Hiraoka, W. Sagano, T. Nose, H. Finkelmann, Biaxial shape memory effect exhibited by monodomain chiral smectic C elastomers, *Macromolecules*. 38 (2005) 7352–7357. doi:10.1021/ma050642c.
- [190] A. Lendlein, J. Zotzman, Y. Feng, A. Alteheld, S. Kelch, Controlling the switching temperature of biodegradable, amorphous, shape-memory poly(rac-lactide)urethane networks by incorporation of different comonomers, *Biomacromolecules*. 10 (2009) 975–982. doi:10.1021/bm900038e.
- [191] C. Liu, P.T. Mather, Thermomechanical characterization of a tailored series of shape memory polymers, *J. Appl. Med. Polym.* 6 (2002) 47–52.
- [192] A. Alteheld, Y. Feng, S. Kelch, A. Lendlein, Biodegradable, amorphous copolyester-urethane networks having shape-memory properties, *Angew. Chemie - Int. Ed.* 44 (2005) 1188–1192. doi:10.1002/anie.200461360.
- [193] J.H. Yang, B.C. Chun, Y.C. Chung, J.H. Cho, Comparison of thermal/mechanical properties and shape memory effect of polyurethane block-copolymers with planar or bent shape of hard segment, *Polymer*. 44 (2003) 3251–3258. doi:10.1016/S0032-3861(03)00260-X.
- [194] G. Barot, I.J. Rao, Constitutive modeling of the mechanics associated with crystallizable shape memory polymers, *Zeitschrift Fur Angew. Math. Und Phys.* 57 (2006) 652–681. doi:10.1007/s00033-005-0009-6.
- [195] G. Barot, I.J. Rao, K.R. Rajagopal, A thermodynamic framework for the modeling of crystallizable shape memory polymers, *Int. J. Eng. Sci.* 46 (2008) 325–351. doi:10.1016/j.ijengsci.2007.11.008.
- [196] J.S. Sodhi, P.R. Cruz, I.J. Rao, Inhomogeneous deformations of Light Activated Shape Memory Polymers, *Int. J. Eng. Sci.* 89 (2015) 1–17. doi:10.1016/j.ijengsci.2014.11.010.
- [197] G. Barot, Constitutive modeling of the thermo-mechanics associated with crystallizable shape memory polymers, New Jersey Institute of Technology, 2006.

- [198] M. Khanolkar, Constitutive modeling of glassy shape memory polymers, New Jersey Institute of Technology, 2010.
- [199] D.T. Clark, H.R. Thomas, Applications of ESCA to polymer chemistry. XVII. Systematic investigation of the core levels of simple homopolymers, *J. Polym. Sci. Polym. Chem. Ed.* 16 (1978) 791–820. doi:10.1002/pol.1978.170160407.
- [200] X. Luo, P.T. Mather, Conductive shape memory nanocomposites for high speed electrical actuation, *Soft Matter*. 6 (2010) 2146. doi:10.1039/c001295e.
- [201] V. V. Gite, P.P. Mahulikar, D.G. Hundiware, Preparation and properties of polyurethane coatings based on acrylic polyols and trimer of isophorone diisocyanate, *Prog. Org. Coatings*. 68 (2010) 307–312. doi:10.1016/j.porgcoat.2010.03.008.
- [202] G. Kister, G. Cassanas, M. Vert, Effects of morphology, conformation and configuration on the IR and Raman spectra of various poly(lactic acid)s, *Polymer*. 39 (1998) 267–273. doi:10.1016/S0032-3861(97)00229-2.
- [203] K.M. Shakesheff, C. Evora, I. Soriano, R. Langer, The adsorption of poly(vinyl alcohol) to biodegradable microparticles studied by X-ray photoelectron spectroscopy (XPS), *J. Colloid Interface Sci.* 185 (1997) 538–547. doi:10.1006/jcis.1996.4637.
- [204] M.C. Davies, R.D. Short, M.A. Khan, J.F. Watts, A. Brown, A.J. Eccles, P. Humphrey, J.C. Vickerman, M. Vert, An XPS and SIMS analysis of biodegradable biomedical polyesters, *Surf. Interface Anal.* 14 (1989) 115–120. doi:10.1002/sia.740140304.
- [205] L.J. Gerenser, XPS Studies Of In Situ Plasma-Modified Polymer Surfaces, *J. Adhes. Sci. Technol.* 7 (1993) 1019–1040. doi:10.1163/156856193X00556.
- [206] S. Krause, J.J. Gormley, N. Roman, J. a Shetter, W.H. Watanabe, Glass Temperatures of Some Acrylic Polymers, *J. Polym. Sci., Part A.* 3 (1965) 3573–3586. doi:10.1002/pol.1965.100031020.
- [207] L.A. Wood, Glass transition temperatures of copolymers, *J. Polym. Sci.* 28 (1958) 319–330. doi:10.1002/pol.1958.1202811707.
- [208] W. Bushuk, H. Benoit, Light-scattering Studies of Copolymers: I. Effect of Heterogeneity of Chain Composition on the Molecular Weight, *Can. J. Chem.* 36

- (1958) 1616–1626. doi:10.1139/v58-235.
- [209] Y. Jiang, I. Almansouri, S. Huang, T. Young, Y. Li, Y. Peng, Q. Hou, L. Spiccia, U. Bach, Y.-B. Cheng, M.A. Green, A. Ho-Baillie, Optical analysis of perovskite/silicon tandem solar cells, *J. Mater. Chem. C* 4 (2016) 5679–5689. doi:10.1039/C6TC01276K.
- [210] W.U. Huynh, J.J. Dittmer, A.P. Alivisatos, Hybrid nanorod-polymer solar cells, *Science* 295 (2002) 2425–2427. doi:10.1126/science.1069156.
- [211] F. Xia, T. Mueller, Y.M. Lin, A. Valdes-Garcia, P. Avouris, Ultrafast graphene photodetector, *Nat. Nanotechnol.* 4 (2009) 839–843. doi:10.1038/nnano.2009.292.
- [212] E.E. Narimanov, Far-field superlens: Optical nanoscope, *Nat. Photonics* 1 (2007) 260–261. doi:10.1038/nphoton.2007.57.
- [213] H.K. Raut, V.A. Ganesh, A.S. Nair, S. Ramakrishna, Anti-reflective coatings: A critical, in-depth review, *Energy Environ. Sci.* 4 (2011) 3779. doi:10.1039/c1ee01297e.
- [214] X. Li, X. Yu, Y. Han, Polymer thin films for antireflection coatings, *J. Mater. Chem. C* 1 (2013) 2266. doi:10.1039/c2tc00529h.
- [215] T. V. Teperik, F.J. García De Abajo, A.G. Borisov, M. Abdelsalam, P.N. Bartlett, Y. Sugawara, J.J. Baumberg, Omnidirectional absorption in nanostructured metal surfaces, *Nat. Photonics* 2 (2008) 299–301. doi:10.1038/nphoton.2008.76.
- [216] J. Hiller, J.D. Mendelsohn, M.F. Rubner, Reversibly erasable nanoporous anti-reflection coatings from polyelectrolyte multilayers, *Nat. Mater.* 1 (2002) 59–63. doi:10.1038/nmat719.
- [217] K.C. Park, H.J. Choi, C.H. Chang, R.E. Cohen, G.H. McKinley, G. Barbastathis, Nanotextured silica surfaces with robust superhydrophobicity and omnidirectional broadband supertransmissivity, *ACS Nano* 6 (2012) 3789–3799. doi:10.1021/nn301112t.
- [218] W.K. Kuo, J.J. Hsu, C.K. Nien, H.H. Yu, Moth-eye-inspired biophotonic surfaces with antireflective and hydrophobic characteristics, *ACS Appl. Mater. Interfaces* 8 (2016) 32021–32030. doi:10.1021/acsami.6b10960.
- [219] H.K. Raut, S.S. Dinachali, Y.C. Loke, R. Ganesan, K.K. Ansh-Antwi, A. Góra, E.H. Khoo, V.A. Ganesh, M.S.M. Saifullah, S. Ramakrishna, Multiscale

- ommatidial arrays with broadband and omnidirectional antireflection and antifogging properties by sacrificial layer mediated nanoimprinting, *ACS Nano*. 9 (2015) 1305–1314. doi:10.1021/nn5051272.
- [220] L. Xu, Z. Geng, J. He, G. Zhou, Mechanically Robust, Thermally Stable, Broadband Antireflective, and Superhydrophobic Thin Films on Glass Substrates, *ACS Appl. Mater. Interfaces*. 6 (2014) 9029–9035. doi:10.1021/am5016777.
- [221] S. Jeon, J.Y. Jang, J.R. Youn, J.H. Jeong, H. Brenner, Y.S. Song, Fullerene embedded shape memory nanolens array, *Sci. Rep.* 3 (2013). doi:10.1038/srep03269.
- [222] T. Pretsch, M. Ecker, M. Schildhauer, M. Maskos, Switchable information carriers based on shape memory polymer, *J. Mater. Chem.* 22 (2012) 7757. doi:10.1039/c2jm16204k.
- [223] Y. Mao, K. Yu, M.S. Isakov, J. Wu, M.L. Dunn, H. Jerry Qi, Sequential Self-Folding Structures by 3D Printed Digital Shape Memory Polymers, *Sci. Rep.* 5 (2015). doi:10.1038/srep13616.
- [224] I.H. Paik, N.S. Goo, Y.C. Jung, J.W. Cho, Development and application of conducting shape memory polyurethane actuators, *Smart Mater. Struct.* 15 (2006) 1476–1482. doi:10.1088/0964-1726/15/5/037.
- [225] A.T. Neffe, B.D. Hanh, S. Steuer, A. Lendlein, Polymer networks combining controlled drug release, biodegradation, and shape memory capability, *Adv. Mater.* 21 (2009) 3394–3398. doi:10.1002/adma.200802333.
- [226] Y. Fang, S.Y. Leo, Y. Ni, L. Yu, P. Qi, B. Wang, V. Basile, C. Taylor, P. Jiang, Optically Bistable Macroporous Photonic Crystals Enabled by Thermoresponsive Shape Memory Polymers, *Adv. Opt. Mater.* 3 (2015) 1509–1516. doi:10.1002/adom.201500277.
- [227] A. Espinha, M.C. Serrano, Á. Blanco, C. López, Thermoresponsive Shape-Memory Photonic Nanostructures, *Adv. Opt. Mater.* 2 (2014) 516–521. doi:10.1002/adom.201300532.
- [228] J.H. Park, H. Kim, J.R. Youn, Y.S. Song, Strategic design and fabrication of acrylic shape memory polymers, *Smart Mater. Struct.* 26 (2017) 085026.

doi:10.1088/1361-665X/aa7224.

- [229] D.J. Lee, Y.S. Song, Anomalous water drop bouncing on a nanotextured surface by the Leidenfrost levitation, *Appl. Phys. Lett.* 108 (2016).  
doi:10.1063/1.4948769.
- [230] K. Choi, S.H. Park, Y.M. Song, Y.T. Lee, C.K. Hwangbo, H. Yang, H.S. Lee, Nano-tailoring the surface structure for the monolithic high-performance antireflection polymer film, *Adv. Mater.* 22 (2010) 3713–3718.  
doi:10.1002/adma.201001678.
- [231] S. Jeon, J. Jeong, Y.S. Song, W.-I. Jeong, J.-J. Kim, J.R. Youn, Vacuum nano-hole array embedded organic light emitting diodes, *Nanoscale.* 6 (2014) 2642–8.  
doi:10.1039/c3nr05331h.
- [232] G.A. Niklasson, C.G. Granqvist, O. Hunderi, Effective medium models for the optical properties of inhomogeneous materials, *Appl. Opt.* 20 (1981) 26.  
doi:10.1364/AO.20.000026.
- [233] S. Ji, K. Song, T.B. Nguyen, N. Kim, H. Lim, Optimal moth eye nanostructure array on transparent glass towards broadband antireflection, *ACS Appl. Mater. Interfaces.* 5 (2013) 10731–10737. doi:10.1021/am402881x.
- [234] P. Spinelli, M.A. Verschuuren, A. Polman, Broadband omnidirectional antireflection coating based on subwavelength surface Mie resonators, *Nat. Commun.* 3 (2012). doi:10.1038/ncomms1691.
- [235] J. Cai, L. Qi, Recent advances in antireflective surfaces based on nanostructure arrays, *Mater. Horiz.* 2 (2015) 37–53. doi:10.1039/C4MH00140K.
- [236] Y.C. Chen, Z.S. Huang, H. Yang, Cicada-Wing-Inspired Self-Cleaning Antireflection Coatings on Polymer Substrates, *ACS Appl. Mater. Interfaces.* 7 (2015) 25495–25505. doi:10.1021/acsami.5b08743.
- [237] D.J. Lee, H.M. Kim, Y.S. Song, J.R. Youn, Water droplet bouncing and superhydrophobicity induced by multiscale hierarchical nanostructures, *ACS Nano.* 6 (2012) 7656–7664. doi:10.1021/nn3032547.
- [238] A.K. Jain, Technology: biometric recognition, *Nature.* 449 (2007) 38–40.  
doi:10.1007/978-3-642-35136-5.
- [239] D.R. Ifa, N.E. Manicke, A.L. Dill, R.G. Cooks, Latent fingerprint chemical



- imaging by mass spectrometry, *Science*. 321 (2008) 805.  
doi:10.1126/science.1157199.
- [240] M. Wadman, Hand and eye security systems in growing use, *Nature*. 398 (1999) 451.
- [241] I. Cohen, W. Giles, D. Noble, Cellular basis for the T wave of the electrocardiogram, *Nature*. 262 (1976) 657–661. doi:10.1038/262657a0.
- [242] H.P. Dietz, C. Shek, B. Clarke, Biometry of the pubovisceral muscle and levator hiatus by three-dimensional pelvic floor ultrasound, *Ultrasound Obstet. Gynecol.* 25 (2005) 580–585. doi:10.1002/uog.1899.
- [243] P. Metherall, D.C. Barber, R.H. Smallwood, B.H. Brown, Three-dimensional electrical impedance tomography, *Nature*. 380 (1996) 509–512.  
doi:10.1038/380509a0.
- [244] T.W. Shen, W.J. Tompkins, Biometric statistical study of one-lead ECG features and body mass index (BMI), 2005 27th Annu. Int. Conf. Ieee Eng. Med. Biol. Soc. Vols 1-7. (2005) 1162–1165. doi:10.1109/Iembs.2005.1616629.
- [245] N. Hogan, *Controlling Impedance at the Man / Machine Interface*, IEEE. (1989).
- [246] R.Z. Li, A. Hu, T. Zhang, K.D. Oakes, Direct writing on paper of foldable capacitive touch pads with silver nanowire inks, *ACS Appl. Mater. Interfaces*. 6 (2014) 21721–21729. doi:10.1021/am506987w.
- [247] M. Santhiago, J. Bettini, S.R. Araújo, C.C.B. Bufon, Three-Dimensional Organic Conductive Networks Embedded in Paper for Flexible and Foldable Devices, *ACS Appl. Mater. Interfaces*. 8 (2016) 10661–10664. doi:10.1021/acsami.6b02589.
- [248] Y. Liu, S. Kumar, Polymer/carbon nanotube nano composite fibers-A review, *ACS Appl. Mater. Interfaces*. 6 (2014) 6069–6087. doi:10.1021/am405136s.
- [249] H. Ogihara, H. Kibayashi, T. Saji, Microcontact printing for patterning carbon nanotube/polymer composite films with electrical conductivity, *ACS Appl. Mater. Interfaces*. 4 (2012) 4891–4897. doi:10.1021/am3012214.
- [250] S. Iijima, Helical microtubules of graphitic carbon, *Nature*. 354 (1991) 56–58.  
doi:10.1038/354056a0.
- [251] Y.S. Song, J.R. Youn, Influence of dispersion states of carbon nanotubes on physical properties of epoxy nanocomposites, *Carbon N. Y.* 43 (2005) 1378–1385.

doi:10.1016/j.carbon.2005.01.007.

- [252] K. Liu, Y. Sun, X. Lin, R. Zhou, J. Wang, S. Fan, K. Jiang, Scratch-resistant, highly conductive, and high-strength carbon nanotube-based composite yarns, *ACS Nano*. 4 (2010) 5827–5834. doi:10.1021/nn1017318.
- [253] H. Koerner, G. Price, N.A. Pearce, M. Alexander, R.A. Vaia, Remotely actuated polymer nanocomposites - Stress-recovery of carbon-nanotube-filled thermoplastic elastomers, *Nat. Mater.* 3 (2004) 115–120. doi:10.1038/nmat1059.
- [254] Z. He, N. Satarkar, T. Xie, Y.T. Cheng, J.Z. Hilt, Remote controlled multishape polymer nanocomposites with selective radiofrequency actuations, *Adv. Mater.* 23 (2011) 3192–3196. doi:10.1002/adma.201100646.
- [255] D.H. Lee, H.J. Oh, S.J. Bai, Y.S. Song, Photosynthetic solar cell using nanostructured proton exchange membrane for microbial biofilm prevention, *ACS Nano*. 8 (2014) 6458–6465. doi:10.1021/nn502033f.
- [256] H.J. Oh, Y.S. Song, Precise nanoinjection molding through local film heating system, *RSC Adv.* 5 (2015) 99797–99805. doi:10.1039/C5RA20206J.
- [257] J. Park, J.R. Youn, Y.S. Song, Sustainable antireflection using recoverable nanopattern arrays, *J. Mater. Chem. C.* (2017). doi:10.1039/C7TC02942J.
- [258] P. Spinelli, M. Hebbink, R. De Waele, L. Black, F. Lenzmann, A. Polman, Optical impedance matching using coupled plasmonic nanoparticle arrays, *Nano Lett.* 11 (2011) 1760–1765. doi:10.1021/nl200321u.
- [259] R. Gholipur, Z. Khorshidi, A. Bahari, Enhanced Absorption Performance of Carbon Nanostructure Based Metamaterials and Tuning Impedance Matching Behavior by an External AC Electric Field, *ACS Appl. Mater. Interfaces.* 9 (2017) 12528–12539. doi:10.1021/acsami.7b02270.
- [260] G. Ma, M. Yang, S. Xiao, Z. Yang, P. Sheng, Acoustic metasurface with hybrid resonances, *Nat. Mater.* 13 (2014) 873–878. doi:10.1038/nmat3994.
- [261] T. Xie, Recent advances in polymer shape memory, *Polymer.* 52 (2011) 4985–5000. doi:10.1016/j.polymer.2011.08.003.
- [262] B.Q.Y. Chan, Z.W.K. Low, S.J.W. Heng, S.Y. Chan, C. Owh, X.J. Loh, Recent Advances in Shape Memory Soft Materials for Biomedical Applications, *ACS Appl. Mater. Interfaces.* 8 (2016) 10070–10087. doi:10.1021/acsami.6b01295.

- [263] W. Sokolowski, A. Metcalfe, S. Hayashi, L. Yahia, J. Raymond, Medical applications of shape memory polymers, *Biomed. Mater.* 2 (2007). doi:10.1088/1748-6041/2/1/S04.
- [264] O. Regev, P.N.B. ElKati, J. Loos, C.E. Koning, Preparation of conductive nanotube-polymer composites using latex technology, *Adv. Mater.* 16 (2004) 248–251. doi:10.1002/adma.200305728.
- [265] T. Chatterjee, R. Krishnamoorti, Steady shear response of carbon nanotube networks dispersed in poly(ethylene oxide), *Macromolecules.* 41 (2008) 5333–5338. doi:10.1021/ma800640w.
- [266] C. Kim, D.S. Kim, G.H. Ko, K. Lee, K. Heo, M. Choi, Y. Sohn, An experimental study on the pressure drop of nanofluids containing carbon nanotubes in a horizontal tube, *Int. J. Heat Mass Transf.* 50 (2007) 4749–4753.
- [267] D.R. Barbero, N. Boulanger, M. Ramstedt, J. Yu, Nano-engineering of SWNT networks for enhanced charge transport at ultralow nanotube loading, *Adv. Mater.* 26 (2014) 3111–3117. doi:10.1002/adma.201305843.
- [268] K. Yu, Y. Liu, J. Leng, Shape memory polymer/CNT composites and their microwave induced shape memory behaviors, *RSC Adv.* 4 (2014) 2961–2968. doi:10.1039/C3RA43258K.
- [269] W. Bauhofer, J.Z. Kovacs, A review and analysis of electrical percolation in carbon nanotube polymer composites, *Compos. Sci. Technol.* 69 (2009) 1486–1498. doi:10.1016/j.compscitech.2008.06.018.
- [270] M.E. Bryan, A tentative criterion for acceptable noise levels in passenger vehicles, *J. Sound Vib.* 48 (1976) 525–535. doi:10.1016/0022-460X(76)90554-X.
- [271] T. Yano, H. Ma, Standardized noise annoyance scales in chinese, korean and vietnamese, *J. Sound Vib.* 277 (2004) 583–588. doi:10.1016/j.jsv.2004.03.020.
- [272] H. Krebs, M. Macht, P. Weyers, H.G. Weijers, W. Janke, Effects of stressful noise on eating and non-eating behavior in rats, *Appetite.* 26 (1996) 193–202. doi:10.1006/appe.1996.0015.
- [273] W. Wd, Noise nuisance caused by road traffic in residential areas: Part II, *J. Sound Vib.* 47 (1976) 265–282.
- [274] J.H.B. Zarek, Sound absorption in flexible porous materials, *J. Sound Vib.* 61

- (1978) 205–234. doi:10.1016/0022-460X(78)90004-4.
- [275] M.T. Hoang, G. Bonnet, H. Tuan Luu, C. Perrot, Linear elastic properties derivation from microstructures representative of transport parameters, *J. Acoust. Soc. Am.* 135 (2014) 3172–3185. doi:10.1121/1.4872296.
- [276] X. Sagartzazu, L. Hervella-Nieto, J.M. Pagalday, Review in sound absorbing materials, *Arch. Comput. Methods Eng.* 15 (2008) 311–342. doi:10.1007/s11831-008-9022-1.
- [277] D. Lafarge, P. Lemarinier, J.F. Allard, V. Tarnow, Dynamic compressibility of air in porous structures at audible frequencies, *J. Acoust. Soc. Am.* 102 (1997) 1995–2006. doi:10.1121/1.419690.
- [278] D.L. Johnson, J. Koplik, R. Dashen, Theory of dynamic permeability and tortuosity in fluid-saturated porous media, *J. Fluid Mech.* 176 (1987) 379. doi:10.1017/S0022112087000727.
- [279] Y. Champoux, J.F. Allard, Dynamic tortuosity and bulk modulus in air-saturated porous media, *J. Appl. Phys.* 70 (1991) 1975–1979. doi:10.1063/1.349482.
- [280] M.A. Biot, Theory of Propagation of Elastic Waves in a Fluid-Saturated Porous Solid. I. Low-Frequency Range, *J. Acoust. Soc. Am.* 28 (1956) 168–178. doi:10.1121/1.1908239.
- [281] M.A. Biot, Generalized Theory of Acoustic Propagation in Porous Dissipative Media, *J. Acoust. Soc. Am.* 34 (1962) 1254–1264. doi:10.1121/1.1918315.
- [282] M.M. Farag, Quantitative methods of materials substitution: Application to automotive components, *Mater. Des.* 29 (2008) 374–380. doi:10.1016/j.matdes.2007.01.028.
- [283] J.P. Arenas, M.J. Crocker, Recent Trends in Porous Sound-Absorbing Materials, *Sound Vib.* (2010) 12–17.
- [284] H. Park, J.R. Youn, Study of reaction injection molding of polyurethane microcellular foam, *Polym. Eng. Sci.* 35 (1995) 1899–1906. doi:10.1002/pen.760352310.
- [285] D. Seo, J.R. Youn, C.L. Tucker, Numerical simulation of mold filling in foam reaction injection molding, *Int. J. Numer. Methods Fluids.* 42 (2003) 1105–1134. doi:10.1002/flid.582.

- [286] M.S. Koo, K. Chung, J.R. Youn, Reaction injection molding of polyurethane foam for improved thermal insulation, *Polym. Eng. Sci.* 41 (2001).  
doi:10.1002/pen.10819.
- [287] T. Yamashita, K. Suzuki, H. Adachi, S. Nishino, Y. Tomota, Effect of Microscopic Internal Structure on Sound Absorption Properties of Polyurethane Foam by X-ray Computed Tomography Observations, *Mater. Trans.* 50 (2009) 373–380. doi:10.2320/matertrans.MRA2008207.
- [288] T. Yamashita, K. Suzuki, S. Nishino, Y. Tomota, Relationship between Sound Absorption Property and Microscopic Structure Determined by X-ray Computed Tomography in Urethane Foam Used as Sound Absorption Material for Automobiles, *Mater. Trans.* 49 (2008) 345–351.  
doi:10.2320/matertrans.MRA2007234.
- [289] N. Broner, The effects of low frequency noise on people-A review, *J. Sound Vib.* 58 (1978) 483–500. doi:10.1016/0022-460X(78)90354-1.
- [290] K. Persson Wayne, R. Rylander, The prevalence of annoyance and effects after long-term exposure to low-frequency noise, *J. Sound Vib.* 240 (2001) 483–497.  
doi:10.1006/jsvi.2000.3251.
- [291] A. Gonzalez, M. Ferrer, M. De Diego, G. Piñero, J.J. Garcia-Bonito, Sound quality of low-frequency and car engine noises after active noise control, *J. Sound Vib.* 265 (2003) 663–679. doi:10.1016/S0022-460X(02)01462-1.
- [292] R. Verdejo, R. Stämpfli, M. Alvarez-Lainez, S. Mourad, M.A. Rodriguez-Perez, P.A. Brühwiler, M. Shaffer, Enhanced acoustic damping in flexible polyurethane foams filled with carbon nanotubes, *Compos. Sci. Technol.* 69 (2009) 1564–1569.  
doi:10.1016/j.compscitech.2008.07.003.
- [293] W. Jiejun, L. Chenggong, W. Dianbin, G. Manchang, Damping and sound absorption properties of particle reinforced Al matrix composite foams, *Compos. Sci. Technol.* 63 (2003) 569–574. doi:10.1016/S0266-3538(02)00215-4.
- [294] Z. Li, M.J. Crocker, Effects of thickness and delamination on the damping in honeycomb-foam sandwich beams, *J. Sound Vib.* 294 (2006) 473–485.  
doi:10.1016/j.jsv.2005.11.024.
- [295] J. Lee, G.H. Kim, C.S. Ha, Sound absorption properties of polyurethane/nano-

- silica nanocomposite foams, *J. Appl. Polym. Sci.* 123 (2012) 2384–2390.  
doi:10.1002/app.34755.
- [296] W. Zhai, J. Yu, L. Wu, W. Ma, J. He, Heterogeneous nucleation uniformizing cell size distribution in microcellular nanocomposites foams, *Polymer*. 47 (2006) 7580–7589. doi:10.1016/j.polymer.2006.08.034.
- [297] C. Kim, J.R. Youn, Environmentally friendly processing of polyurethane foam for thermal insulation, *Polym. - Plast. Technol. Eng.* 39 (2000) 163–185.  
doi:10.1081/PPT-100100022.
- [298] J. Wang, W. Zhai, J. Ling, B. Shen, W. Zheng, C.B. Park, Ultrasonic irradiation enhanced cell nucleation in microcellular poly(lactic acid): A novel approach to reduce cell size distribution and increase foam expansion, *Ind. Eng. Chem. Res.* 50 (2011) 13840–13847. doi:10.1021/ie201643j.
- [299] W. Zhai, J. Yu, J. He, Ultrasonic irradiation enhanced cell nucleation: An effective approach to microcellular foams of both high cell density and expansion ratio, *Polymer*. 49 (2008) 2430–2434. doi:10.1016/j.polymer.2008.04.002.
- [300] A. Gandhi, N. Asija, H. Chauhan, N. Bhatnagar, Ultrasound-induced nucleation in microcellular polymers, *J. Appl. Polym. Sci.* 131 (2014) 9076–9080.  
doi:10.1002/app.40742.
- [301] C. Torres-Sanchez, J.R. Corney, Effects of ultrasound on polymeric foam porosity, *Ultrason. Sonochem.* 15 (2008) 408–415.  
doi:10.1016/j.ultsonch.2007.05.002.
- [302] C. Torres-Sanchez, J.R. Corney, Toward Functionally Graded Cellular Microstructures, *J. Mech. Des.* 131 (2009) 091011. doi:10.1115/1.3158985.
- [303] Y.J. Kang, B.K. Gardner, J.S. Bolton, An axisymmetric poroelastic finite element formulation, *J. Acoust. Soc. Am.* 106 (1999) 565–574. doi:10.1121/1.428041.
- [304] T.G. Zieliński, Microstructure-based calculations and experimental results for sound absorbing porous layers of randomly packed rigid spherical beads, *J. Appl. Phys.* 116 (2014). doi:10.1063/1.4890218.
- [305] C. Perrot, F. Chevillotte, R. Panneton, J.-F. Allard, D. Lafarge, On the dynamic viscous permeability tensor symmetry, *J. Acoust. Soc. Am.* 124 (2008) EL210-EL217. doi:10.1121/1.2968300.

- [306] T.G. Zieliński, Generation of random microstructures and prediction of sound velocity and absorption for open foams with spherical pores, *J. Acoust. Soc. Am.* 137 (2015) 1790–1801. doi:10.1121/1.4915475.
- [307] C. Perrot, F. Chevillotte, M. Tan Hoang, G. Bonnet, F.X. Bécot, L. Gautron, A. Duval, Microstructure, transport, and acoustic properties of open-cell foam samples: Experiments and three-dimensional numerical simulations, *J. Appl. Phys.* 111 (2012). doi:10.1063/1.3673523.
- [308] A.F. Seybert, Notes on Absorption and Impedance Measurements, *Astm E1050*. (2010) 1–6.
- [309] M.D. Montminy, A.R. Tannenbaum, C.W. MacOsko, The 3D structure of real polymer foams, *J. Colloid Interface Sci.* 280 (2004) 202–211. doi:10.1016/j.jcis.2004.07.032.
- [310] H.X. Zhu, J.F. Knott, N.J. Mills, Analysis of the elastic properties of open-cell foams with tetrakaidecahedral cells, *J. Mech. Phys. Solids.* 45 (1997) 319–343. doi:10.1016/S0022-5096(96)00090-7.
- [311] L. Gong, S. Kyriakides, W.Y. Jang, Compressive response of open-cell foams. Part I: Morphology and elastic properties, *Int. J. Solids Struct.* 42 (2005) 1355–1379. doi:10.1016/j.ijsolstr.2004.07.023.
- [312] X.H. Yang, S.W. Ren, W.B. Wang, X. Liu, F.X. Xin, T.J. Lu, A simplistic unit cell model for sound absorption of cellular foams with fully/semi-open cells, *Compos. Sci. Technol.* 118 (2015) 276–283. doi:10.1016/j.compscitech.2015.09.009.
- [313] J.S. Lee, Y.Y. Kim, J.S. Kim, Y.J. Kang, Two-dimensional poroelastic acoustical foam shape design for absorption coefficient maximization by topology optimization method, *J. Acoust. Soc. Am.* 123 (2008) 2094–2106. doi:10.1121/1.2839001.
- [314] C. Perrot, F. Chevillotte, R. Panneton, Dynamic viscous permeability of an open-cell aluminum foam: Computations versus experiments, *J. Appl. Phys.* 103 (2008). doi:10.1063/1.2829774.
- [315] J.H. Park, S.H. Yang, H.R. Lee, C. Bin Yu, S.Y. Pak, C.S. Oh, Y.J. Kang, J.R. Youn, Optimization of low frequency sound absorption by cell size control and

- multiscale poroacoustics modeling, *J. Sound Vib.* 397 (2017) 17–30.  
doi:10.1016/j.jsv.2017.03.004.
- [316] J.H. Park, K.S. Minn, H.R. Lee, S.H. Yang, C. Bin Yu, S.Y. Pak, C.S. Oh, Y.S. Song, Y.J. Kang, J.R. Youn, Cell openness manipulation of low density polyurethane foam for efficient sound absorption, *J. Sound Vib.* 406 (2017) 224–236. doi:10.1016/j.jsv.2017.06.021.
- [317] M.J. Swift, P. Briš, K. V. Horoshenkov, Acoustic absorption in re-cycled rubber granulate, *Appl. Acoust.* 57 (1999) 203–212. doi:10.1016/S0003-682X(98)00061-9.
- [318] J.R. Youn, H. Park, Bubble growth in reaction injection molded parts foamed by ultrasonic excitation, *Polym. Eng. Sci.* 39 (1999) 457–468.  
doi:10.1002/pen.11435.
- [319] S. Ersoy, H. Küçük, Investigation of industrial tea-leaf-fibre waste material for its sound absorption properties, *Appl. Acoust.* 70 (2009) 215–220.  
doi:10.1016/j.apacoust.2007.12.005.
- [320] D. Chen, J. Li, J. Ren, Study on sound absorption property of ramie fiber reinforced poly(l-lactic acid) composites: Morphology and properties, *Compos. Part A Appl. Sci. Manuf.* 41 (2010) 1012–1018.  
doi:10.1016/j.compositesa.2010.04.007.
- [321] P.H.T. Zannin, F.B. Diniz, W.A. Barbosa, Environmental noise pollution in the city of Curitiba, Brazil, *Appl. Acoust.* 63 (2002) 351–358. doi:10.1016/S0003-682X(01)00052-4.
- [322] S.A. Stansfeld, M.P. Matheson, Noise pollution: Non-auditory effects on health, *Br. Med. Bull.* 68 (2003) 243–257. doi:10.1093/bmb/ldg033.
- [323] M.F. Sonnenschein, Polyurethane flexible foams, *Polyurethanes.* (2014) 235–254.  
doi:10.1002/9781118901274.
- [324] D. Wee, D.G. Seong, J.R. Youn, Processing of microcellular nanocomposite foams by using a supercritical fluid, *Fibers Polym.* 5 (2004) 160–169.  
doi:10.1007/BF02902932.
- [325] W.J. Cho, H. Park, J.R. Youn, Ultrasonic bubble nucleation in reaction injection moulding of polyurethane, *Proc. Inst. Mech. Eng. Part B J. Eng. Manuf.* 208



- (1994) 121–128. doi:10.1243/PIME\_PROC\_1994\_208\_068\_02.
- [326] T.J. Lu, F. Chen, D. He, Sound absorption of cellular metals with semiopen cells, *J. Acoust. Soc. Am.* 108 (2000) 1697–1709. doi:10.1121/1.1286812.
- [327] D. Guan, J.H. Wu, J. Wu, J. Li, W. Zhao, Acoustic performance of aluminum foams with semiopen cells, *Appl. Acoust.* 87 (2015) 103–108. doi:10.1016/j.apacoust.2014.06.016.
- [328] A. Sharma, E. Ruckenstein, Stability, Critical Thickness, and the Time of Rupture of Thinning Foam and Emulsion Films, *Langmuir.* 3 (1987) 760–768. doi:10.1021/la00077a033.
- [329] G. Rossmly, H.J. Kollmeier, W. Lidy, H. Schator, M. Wiemann, Mechanism of the Stabilization of Flexible Polyether Polyurethane Foams by Silicone-Based Surfactants, *J. Cell. Plast.* 17 (1981) 319–327. doi:10.1177/0021955X8101700602.
- [330] G.C. Frye, J.C. Berg, Mechanisms for the synergistic antifoam action by hydrophobic solid particles in insoluble liquids, *J. Colloid Interface Sci.* 130 (1989) 54–59. doi:10.1016/0021-9797(89)90077-5.
- [331] D.R. Ekserova, P.M. Krugliakov, Foam and foam films: theory, experiment, application, 1998. doi:10.1016/S1383-7303(98)80004-5.
- [332] A.K. Malhotra, D.T. Wasan, Effects of surfactant adsorption-desorption kinetics and interfacial rheological properties on the rate of drainage of foam, *Chem. Eng. Commun.* (1987).
- [333] K. Yasunaga, R.A. Neff, X.D. Zhang, C.W. Macosko, Study of Cell Opening in Flexible Polyurethane Foam, *J. Cell. Plast.* 32 (1996) 427–448. doi:10.1177/0021955X9603200502.
- [334] X.D. Zhang, C.W. Macosko, H.T. Davis, A.D. Nikolov, D.T. Wasan, Role of silicone surfactant in flexible polyurethane foam, *J. Colloid Interface Sci.* 215 (1999) 270–279. doi:10.1006/jcis.1999.6233.
- [335] W. Ahn, Open-Cell Rigid Polyurethane Foam Using Reactive Cell Opening Agents, *J. Korea Acad. Ind. Coop. Soc.* 14 (2013) 2524–2528.
- [336] Y.T. Kiyohiro Yuge, Hitoshi Muramatsu, Yasuto Masuda, Kazutaka Uekado, Production and use of open cell rigid polyurethane foam, United States Pat.

(1994).

- [337] S.S. Mi-seon Jang, Jin-Taek Hwang, Open cell rigid polyurethane foam and method for producing the same and method for making vacuum insulation panel using same, United States Pat. (1999).
- [338] K.C. Song, S.M. Lee, D.H. Lee, Cell opening of high resilience polyurethane foam II. Structure effect of polyether type cell opener, *Polym.* 26 (2002) 218–226.
- [339] F. Chevillotte, R. Panneton, Elastic characterization of closed cell foams from impedance tube absorption tests, *J. Acoust. Soc. Am.* 122 (2007) 2653. doi:10.1121/1.2783126.
- [340] A. Craggs, A finite element model for rigid porous absorbing materials, *J. Sound Vib.* 61 (1978) 101–111. doi:10.1016/0022-460X(78)90044-5.
- [341] C. Zhang, J. Li, Z. Hu, F. Zhu, Y. Huang, Correlation between the acoustic and porous cell morphology of polyurethane foam: Effect of interconnected porosity, *Mater. Des.* 41 (2012) 319–325. doi:10.1016/j.matdes.2012.04.031.
- [342] E.A. Moreira, J.R. Coury, The influence of structural parameters on the permeability of ceramic foams, *Brazilian J. Chem. Eng.* 21 (2004) 23–33. doi:10.1590/S0104-66322004000100004.
- [343] N. V. Gama, B. Soares, C.S.R. Freire, R. Silva, C.P. Neto, A. Barros-Timmons, A. Ferreira, Bio-based polyurethane foams toward applications beyond thermal insulation, *Mater. Des.* 76 (2015) 77–85. doi:10.1016/j.matdes.2015.03.032.
- [344] F. Chevillotte, C. Perrot, R. Panneton, Microstructure based model for sound absorption predictions of perforated closed-cell metallic foams, *J. Acoust. Soc. Am.* 128 (2010) 1766–1776. doi:10.1121/1.3473696.
- [345] Z. Hong, L. Bo, H. Guangsu, Sound absorption behavior of multiporous hollow polymer micro-spheres, *Mater. Lett.* 60 (2006) 3451–3456. doi:10.1016/j.matlet.2006.03.030.
- [346] C.H. Sung, K.S. Lee, K.S. Lee, S.M. Oh, J.H. Kim, M.S. Kim, H.M. Jeong, Sound damping of a PU foam nanocomposite, in: *Proc. IFOST-2008 - 3rd Int. Forum Strateg. Technol.*, 2008: pp. 181–185. doi:10.1109/IFOST.2008.4602982.
- [347] M. Bandarian, A. Shojaei, A.M. Rashidi, Thermal, mechanical and acoustic damping properties of flexible open-cell polyurethane/multi-walled carbon

- nanotube foams: Effect of surface functionality of nanotubes, *Polym. Int.* 60 (2011) 475–482. doi:10.1002/pi.2971.
- [348] J.G. Gwon, S.K. Kim, J.H. Kim, Sound absorption behavior of flexible polyurethane foams with distinct cellular structures, *Mater. Des.* 89 (2016) 448–454. doi:http://dx.doi.org/10.1016/j.matdes.2015.10.017.
- [349] S. Basirjafari, R. Malekfar, S. Esmailzadeh Khadem, Low loading of carbon nanotubes to enhance acoustical properties of poly(ether)urethane foams, *J. Appl. Phys.* 112 (2012). doi:10.1063/1.4765726.
- [350] C. Swetha, R. Kumar, Quasi-static uni-axial compression behaviour of hollow glass microspheres/epoxy based syntactic foams, *Mater. Des.* 32 (2011) 4152–4163. doi:10.1016/j.matdes.2011.04.058.
- [351] M. Dimchev, R. Caeti, N. Gupta, Effect of carbon nanofibers on tensile and compressive characteristics of hollow particle filled composites, *Mater. Des.* 31 (2010) 1332–1337. doi:10.1016/j.matdes.2009.09.007.
- [352] L. Wang, J. Zhang, X. Yang, C. Zhang, W. Gong, J. Yu, Flexural properties of epoxy syntactic foams reinforced by fiberglass mesh and/or short glass fiber, *Mater. Des.* 55 (2014) 929–936. doi:10.1016/j.matdes.2013.10.065.
- [353] X.F. Tao, L.P. Zhang, Y.Y. Zhao, Al matrix syntactic foam fabricated with bimodal ceramic microspheres, *Mater. Des.* 30 (2009) 2732–2736. doi:10.1016/j.matdes.2008.11.005.
- [354] I.N. Orbulov, K. Májlinger, Description of the compressive response of metal matrix syntactic foams, *Mater. Des.* 49 (2013) 1–9. doi:10.1016/j.matdes.2013.02.007.
- [355] M. Taherishargh, I. V. Belova, G.E. Murch, T. Fiedler, On the mechanical properties of heat-treated expanded perlite-aluminium syntactic foam, *Mater. Des.* 63 (2014) 375–383. doi:10.1016/j.matdes.2014.06.019.
- [356] L. Glicksman, M. Schuetz, M. Sinofsky, Radiation heat transfer in foam insulation, *Int. J. Heat Mass Transf.* 30 (1987) 187–197. doi:10.1016/0017-9310(87)90071-8.
- [357] M. Wang, N. Pan, Modeling and prediction of the effective thermal conductivity of random open-cell porous foams, *Int. J. Heat Mass Transf.* 51 (2008) 1325–

1331. doi:10.1016/j.ijheatmasstransfer.2007.11.031.

- [358] K. Boomsma, D. Poulikakos, On the effective thermal conductivity of a three-dimensionally structured fluid-saturated metal foam, *Int. J. Heat Mass Transf.* 44 (2001) 827–836. doi:10.1016/S0017-9310(00)00123-X.
- [359] J.-W. Wu, W.-F. Sung, H.-S. Chu, Thermal conductivity of polyurethane foams, *Int. J. Heat Mass Transf.* 42 (1999) 2211–2217. doi:10.1016/S0017-9310(98)00315-9.
- [360] W.-H. Tao, H.-C. Hsu, C.-C. Chang, C.-L. Hsu, Y.-S. Lin, Measurement and Prediction of Thermal Conductivity of Open Cell Rigid Polyurethane Foam, *J. Cell. Plast.* 37 (2001) 310–332. doi:10.1106/1X25-NV25-LUA2-GHR3.
- [361] L.J. Lee, C. Zeng, X. Cao, X. Han, J. Shen, G. Xu, Polymer nanocomposite foams, *Compos. Sci. Technol.* 65 (2005) 2344–2363. doi:10.1016/j.compscitech.2005.06.016.
- [362] X. Cao, L. James Lee, T. Widya, C. Macosko, Polyurethane/clay nanocomposites foams: Processing, structure and properties, *Polymer.* 46 (2005) 775–783. doi:10.1016/j.polymer.2004.11.028.

## Korean Abstract

### 초 록

메타물질은 인류의 상상력을 사로 잡을 수 있도록 인공적으로 설계된 물질이다. 다양한 메타물질이 수학적, 물리화학적 배경지식에 근거하여 정교한 마이크로/나노구조로 설계되어 왔다. 메타물질은 일반적으로 복합 재료 특성을 위한 유효 매질을 이끌어 낼 수 있는 마이크로/나노 크기의 단위 셀을 사용하여 설계된다. 메타물질은 실제 장치로 제작되어 왔으며, 자연의 법칙을 따르지 않는 전례 없는 현상들을 구현 시켜 왔다. 본 논문에서는 전략적 설계, 화학적 합성, 제작 및 실험적 분석에 의하여 세 종류의 메타물질이 제안된다; 고분자 유연학적 메타물질, 형상 기억 고분자 메타표면, 고분자 다공성 메타흡음재.

제 1 장에서는 메타물질이란 무엇이고 어떤 종류의 메타물질이 지금까지 보고되어 왔는지에 대하여 설명된다. 또한, 본 논문을 이해하는 데에 요구되는 배경지식들이 서술된다. 변환 광학 이론과 그에 기초한 메타물질이 설계 전략과 직면 과제들과 함께 소개된다. 형상기억고분자의 정의, 원리 및 응용들이 특정 예시들과 함께 설명된다. 흡음 현상과 그 이론적 모델들이 설명되고, 흡음재 성능의 일반적 경향에 대하여 검토된다. 본 논문의 전체적인 목표가 간략하게 제시된다.

제 2 장에서는 가상 유체 공간 설계를 통해 전례 없는 유동을 가능하게 하는 고분자 유연학적 메타물질의 개발이 서술된다. 변환 광학은 전자기파를 제어하는 정밀한 방법을 제시해 왔다. 이 이론을 사용하여, 특정 전자기적 공간을 압축, 팽창 혹은 회전시키는 유클리드 공간 하 좌표 변환이 고안되었다. 변환된 좌표계들은 메타물질 접근법에 기초하여 실험적으로 구현되어 왔다. 메타물질 설계 과정에서 특이한 재료 물성을 구현시킬 수 있는 마이크로/나노 크기의 단위 셀이 유효 매체 이론에 기초하여 제작되고,

이들의 나열을 통해 통합 메타물질 복합체가 제조된다. 본 연구에서는, 유체 역학 현상의 조작을 위해 변환 광학을 유변학적 관점으로 재해석하는 발상을 고안하였다. 변환 유변학이 나비에-스토크스식의 좌표 변환에 기반하여 최초로 수학적 수립되었고 그에 따라 유체의 유변 물성인 점도가 자코비안 변환 행렬과 함께 텐서 형태로 변환되어야 가상 유체 공간을 유도할 수 있는 것이 확인되었다. 유변학적 메타물질은 유효 점도 단위 셀의 설계 및 나열을 통해 제작되었고, 수치모사를 통해 이론적으로 분석되었다. 본 메타물질은 폴리다이메틸실록세인으로 구성된 미세유체 장치로 제작되었다. 해당 메타물질이 설계 된 대로 적절하게 작동하는 것을 실험적 분석을 통해 확인하였다.

제 3 장에서는 손상된 구조를 회복시켜 지속 가능한 나노 효과를 수반하는 형상기억 고분자 메타표면의 개발 과정이 설명된다. 고분자 나노 구조체는 반사방지, 태양 에너지 수확, 광학 센서 등 다양한 응용을 위하여 연구되어 왔다. 나노 구조체의 서브 파장 특성이 전자기학적 메타 특성들을 가능하게 한다. 이러한 구조적 특징은 나노 구조체가 재료 구성 그 자체가 아니라 유효 재료 매체로서 기능하게 해 준다. 하지만, 기계적 변형에 대한 취약성은 이러한 나노구조체의 실제 응용에 있어서 장애물로 지적되어 왔다. 본 연구에서는, 이러한 단점을 극복하기 위하여 나노구조체의 구성 물질을 형상기억고분자로 변경하는 전략을 수립하였다. 아크릴 화학물질로 구성 된 형상기억고분자가 체온에 의해 구동될 수 있도록 화학적으로 설계되고 합성되었다. 설계 된 형상기억고분자로 구성된 나노 패턴 나열을 통해 반사방지와 생체인식을 위한 기능성 메타표면이 시편 표면에 가공되었고, 메타 특성들이 실험적으로 확인되었다. 나노 패턴들이 외력에 의하여 변형되었을 지라도, 열 자극을 통해 원래의 형상으로 회복될 수 있다. 그에 따라 각 메타 특성의 손실되었던 성능이 원래대로 회복되는 것이 확인되었다.

제 4 장에서는 거시적 인자의 한계를 극복하여 뛰어난 소음 에너지 소실을 가능하게 하는 고분자 다공성 메타 흡음재가 소개된다. 흡음재는 우수한 흡음 성능을 달성하기 위하여 이론적, 실험적으로 연구되어 왔다.

이론적 연구들에서 폼의 내부 미세 구조가 흡음 성능에 대한 주된 기여 인자로 밝혀졌다. 하지만, 미세 구조의 제어가 매우 어렵기 때문에 기존의 대부분의 연구들에서는 흡음재의 두께, 구성 성분 및 밀도와 같은 거시적 인자들을 주로 제어하여 왔다. 따라서 일반 상식 하에서는 흡음재의 주요 작동 주파수와 성능은 거시적 인자에 강력하게 연관되어 있고 그에 비례하는 경향을 보인다. 본 연구에서는, 내부 미세구조를 조정하여 흡음에 대한 메타 흡수체를 획득하는 전략적 접근을 시도하였다. 최적의 셀 크기와 셀 개폐도를 지니는 폴리우레탄폼이 다중 스케일 수치모사와 유변제어 발포 방법을 통해 제작되었다. 제작된 폴리우레탄 폼은 밀도 조건의 한계를 넘어서는 우수한 저주파 소음 흡음 성능을 보여주었다. 또한, 탁월한 흡음 성능과 더불어 좋은 단열 성능 및 기계적 물성을 지니는 새로운 하이브리드 미세 구조체가 설계되었다.

제 5 장에서는 본 논문의 결론이 서술된다. 본 연구의 최종 목표가 제 2 장부터 4 장까지의 요약과 함께 제시된다. 사용된 고분자, 설계 전략, 가공 방법 및 특이한 메타물질의 기능 등이 순서대로 요약되고 이들의 잠재적 응용 분야가 제시된다. 현 기술들의 문제점과 한계들이 논의되고 그들에 대한 해결책들이 제안된다. 본 논문에서 개발 된 메타물질에 대한 후속 연구들이 추천된다.

**주요어:** 메타물질, 고분자, 지능성 재료, 다공성 재료, 재료 설계, 유변학, 임피던스 매칭, 흡음, 수치모사.

**학 번:** 2013-23040